Photoproduction of Inelastic and Elastic J/ψ Vector Mesons

by

Audrius Bronius Stundžia

A thesis submitted in conformity with the requirements
of the Degree of Doctor of Philosophy,
Graduate Department of Physics,
in the University of Toronto

1992

Abstract

Results and analysis on the inelastic and elastic photoproduction of J/ψ vector mesons by Fermilab experiment E691 are presented. The inelastic, deep inelastic, coherent elastic and incoherent elastic cross sections were measured at $\langle E_\gamma \rangle = 145$ GeV. The $d\sigma/dzdp_T^2$ distribution and the photon energy dependence of the cross sections for these production processes were also measured. The deep inelastic J/ψ was analyzed in the colour–singlet photon–gluon–fusion model. It was found that the $d\sigma/dzdp_T^2$ distribution and the the rise of the cross section with E_γ are both well described by a relatively soft gluon distribution [$xG(x) \propto (1-x)^{n_g}$, where $n_g = 6.5 \pm 1.1$ (stat.) $^{+1.0}_{-0.6}$ (syst.)].

Acknowledgements

Current HEP experiments are large in both scale and complexity, requiring dedicated teamwork to build and run. Thus, I would first like to gratefully acknowledge the contributions of all the members of our collaboration, listed below, in making E691 a success.

The Tagged Photon Spectrometer Collaboration

J.C. Anjos[3], J.A. Appel[6], A. Bean[1], S.B. Bracker[11], T.E. Browder[1],[a], L.M. Cremaldi[7], J.E. Duboscq[1], J.R. Elliott[5],[b], C.O. Escobar[10], P. Estabrooks[2], M.C. Gibney[5],[c], G.F. Hartner[11], P.E. Karchin[12], B.R. Kumar[11], M.J. Losty[8], G.J. Luste[11], P.M. Mantsch[6], J.F. Martin[11], S. McHugh[1], S.R. Menary[11],[d], R.J. Morrison[1], T. Nash[6], J. Pinfold[2], G. Punkar[1],[e], M.V. Purohit[9], W.R. Ross[12], A.F.S. Santoro[3], A.L. Shoup[4],[f], D.M. Schmidt[1], J.S. Sidhu[2],[g], K. Sliwa[6],[h], M.D. Sokoloff[4], M.H.G. Souza[3], W.J. Spalding[6], M.E. Streetman[6], A.B. Stundžia[11],[i], M.S. Witherell[1]

1. University of California, Santa Barbara, CA 93106, USA

2. Carleton University, Ottawa, Ontario K1S 5B6, Canada

3. Centro Brasileiro de Pesquisas Físicas, Rio de Janeiro CEP 22290, Brasil

4. University of Cincinnati, Cincinnati OH 45221, USA

5. University of Colorado, Boulder, CO 80309, USA

6. Fermi National Accelerator Laboratory, Batavia, IL 60510, USA

7. University of Mississippi, University, MS 38677, USA

8. National Research Council, Ottawa, Ontario K1S 5B6, Canada

9. Princeton University, Princeton, N.J. 08544, USA

10. Universidade de São Paolo, São Paolo BR-01498, Brasil

11. University of Toronto, Toronto, Ontario M5S 1A7, Canada

12. Yale University, New Haven, CT 06511, USA

I would like to thank, in particular,

- my advisor, Dr. George J. Luste, for his support and encouragement
- Steve Bracker for his guidance during my work on the Online Monitoring System
- Dr. Mike Witherell for his guidance during my work on the Dimuon Trigger

My principal association has been with Dr. Milind Purohit who carried out the open–charm photoproduction analysis. I am indebted to him for countless enlightening physics discussions and data analysis insights.

Many friends, colleagues and fellow graduate students helped make the years spent at Fermilab not only productive but also enjoyable. I would like to explicitly thank

- Homaira Akbari and Kimberly Frame,
- Dr. Algis and Vija Paulius,
- Steve Bracker, Milind Purohit and David Salopek,
- the crew of the Fox River (Aurora) Rowing Club and
- the crews of the yachts *Audra* and *Baltija*

The contribution of the Canadian taxpaying citizenry, who payed for my research and stay, is gratefully acknowledged.

My thesis was completed back in Toronto and I would like to especially thank my love, Kelly Lynn Akers, for being so accommodating during the writing.

Finally, I would like to thank my parents, Bronius and Marija, for their steadfast and patient support in all my endeavors.

a. Now at Cornell University, Ithaca N.Y. 14853, USA.

b. Now at Electromagnetic Applications, Denver, CO 80226, USA.

c. Now at Nichols Research, Inc., Colorado Springs, CO 80226, USA.

d. Now at the University of California, Santa Barbara, CA 93106, USA.

e. Now at SLAC, Stanford, CA 94309, USA.

f. Now at the University of California, Irvine, CA 92716, USA.

g. Deceased.

h. Now at Tufts University, Medford, MA 02155, USA.

i. Now at the Membrane Biology Group, Faculty of Medicine, University of Toronto, Toronto, M5S 1A8.

Contents

List of Figures

List of Tables

Chapter 1

Introduction

1.1 Physics Motivation

Scattering experiments have played a central role in the development of our understanding of the fundamental particles that constitute the physical universe and the forces through which they interact. The Rutherford α–gold foil scattering experiment revealed the existence of the positively charged nucleus [Rut 11]. Elastic electron–proton scattering experiments using a 188 MeV electron beam on a liquid hydrogen target were pioneered at SLAC by Hofstader and others [Mca 56]. They measured the proton form factor from which the root–mean–square proton radius was extracted. In 1967, a SLAC-MIT group began a study of electron scattering from protons in the 4.5 GeV to 20 GeV energy range at two different angles, $\theta = 6°$ and $\theta = 10°$, relative to the incident electron beam [Pou 74]. As the scattered electron energy was decreased at a fixed angle, the cross–section exhibited an elastic peak and resonances as expected. Inelastic scattering was observed as the 4–momenta transfer Q^2 was increased beyond the last resonance causing the proton to fragment. The differential cross-section for inelastic electron–proton scattering in the lab frame is

$$\frac{d\sigma}{d\Omega dE'} = \frac{\alpha^2 \cos^2(\theta/2)}{4E^2 \sin^4(\theta/2)} \left[W_2(\nu, Q^2) + 2W_1(\nu, Q^2) \tan^2(\theta/2)\right] \tag{1.1}$$

where E is the electron beam energy, E' is the scattered electron energy, $\nu = E - E'$ and θ is the electron scattering angle with respect to the beam axis. It was observed that at large Q^2 the form factors

$$MW_1(\nu, Q^2) \rightarrow F_1(x) \tag{1.2}$$

$$\nu W_2(\nu, Q^2) \rightarrow F_2(x) \tag{1.3}$$

scale; are independent of Q^2 at a given value of $x = Q^2/2M\nu$. This $1/\sin^4(\theta/2) \propto 1/Q^4$ Rutherford scattering behaviour in the inelastic cross–section indicated that the proton has substructure consisting of point scatterers; the partons. Scaling had been predicted by Bjorken and Paschos [Bjo 69] and was explained by Feynman [Fey 72] in terms of the parton model with x interpreted as the fraction of the proton's momentum carried by the struck constituent pointlike parton, Bjorken x. The structure functions have a direct physical interpretation in terms of up, down and strange quark (q) and antiquark ($\bar{q}$) densities. For electron–nucleon (or muon–nucleon) scattering

$$F_1^{eN}(x) = \left(\frac{5}{18}\right)[u(x) + \bar{u}(x)] + \left(\frac{5}{18}\right)\left[d(x) + \bar{d}(x)\right] + \left(\frac{1}{9}\right)[s(x) + \bar{s}(x)] \tag{1.4}$$

$$F_2^{eN}(x) = 2xF_1^{eN}(x) \tag{1.5}$$

where the fractional coefficients correspond to the squares of the fractional quark electric charges, averaged over an isoscalar target. The Callan–Gross relation [Cal 69] given by Equation 1.5 is a consequence of taking the quarks to be point–like Dirac (spin 1/2) particles. All quarks possess the same weak charge, thus the differential cross–section for neutrino–nucleon scattering is

$$\frac{d\sigma^{\nu N, \bar{\nu} N}}{dxdy} = \frac{G^2 ME}{\pi}\left[(1-y)F_2^{\nu N}(x) + \frac{y^2}{2}2xF_1^{\nu N}(x) \pm y\left(1 - \frac{y}{2}\right)xF_3^{\nu N}(x)\right] \tag{1.6}$$

where

- $\nu = E - E'$
- $y = \frac{\nu}{E}$
- $x = \frac{Q^2}{2ME\nu}$
- $Q^2 = -(p_\nu - p'_{\nu,\mu})^2$ (allowing for both neutral and charged current scattering)

and the deep inelastic neutrino–nucleon scattering form factors in Equation 1.6, expressed in terms of the quark and antiquark densities, are

$$F_1^{\nu N}(x) = [u(x) + \bar{u}(x)] + \left[d(x) + \bar{d}(x)\right] + [s(x) + \bar{s}(x)] \quad (1.7)$$

$$F_2^{\nu N}(x) = 2xF_1^{\nu N}(x) \quad (1.8)$$

$$F_3^{\nu N}(x) = [u(x) - \bar{u}(x)] + \left[d(x) - \bar{d}(x)\right] + [s(x) - \bar{s}(x)] \quad (1.9)$$

The proton quantum numbers require that

$$\int dx[u(x) - \bar{u}(x)] = 2 \quad (1.10)$$

$$\int dx[d(x) - \bar{d}(x)] = 1 \quad (1.11)$$

$$\int dx[s(x) - \bar{s}(x)] = 0 \quad (1.12)$$

generalizing the valence quark model of Gell-Mann [Gel 64] and Zweig [Zwe 64].

Progress in the development of a gauge theory of the strong interaction, using quantum electrodynamics (QED) as a model, culminated in the formulation of quantum chromodynamics (QCD) [Gro 73, Wei 73, Fri 73]. In this theory, the strong interaction between quarks is mediated by the exchange of gluons, vector particles that unlike the electrically neutral photon possess colour; the strong interaction charge [Nam 66]. Indirect evidence for electrically neutral partons came from the observation that the quarks account for only about 50% of the proton's momentum in electron–proton scattering

$$\int_0^1 dx\ x(u+\bar{u}+d+\bar{d}+s+\bar{s}) = 0.54 \pm 0.05 \tag{1.13}$$

for values of Q^2 from 1 to 10 GeV^2 [Clo 79]. The gluon colour charge gives rise to asymptotic freedom, the charge anti-screening property of QCD [Gro 73, Pol 73] in contradistinction to the charge screening of QED. To first order, the strong force coupling constant runs as

$$\alpha_S(Q^2) = \frac{12\pi}{(33-2n_f)\ln(Q^2/\Lambda)} \tag{1.14}$$

where $\Lambda \simeq 200$ MeV and n_f is the number of quark flavours. At sufficiently short distances or equivalently at large $Q^2 s$, as in asymptotically free deep inelastic scattering, α_S is small enough that perturbative QCD calculations are valid. Thus, at large Q^2 the quarks are weakly bound by gluon exchange. These quark–gluon and gluon–gluon interactions violate scaling; the quark (q) and gluon (G) densities are weak (logarithmically varying) functions of Q^2 as well as x,

$$q = q(x,Q^2) \tag{1.15}$$

$$G = G(x,Q^2) \tag{1.16}$$

The QCD scaling violations are described by the Altarelli–Parisi evolution equations [Alt 77]

$$\frac{dq_i(x,Q^2)}{d\log Q^2} = \frac{\alpha_s}{2\pi}\int_x^1 \frac{dy}{y}\left[q_i(y,Q^2)P_{qq}\left(\frac{x}{y}\right) + G(y,Q^2)P_{qg}\left(\frac{x}{y}\right)\right] \tag{1.17}$$

$$\frac{dG(x,Q^2)}{d\log Q^2} = \frac{\alpha_s}{2\pi}\int_x^1 \frac{dy}{y}\left[\sum_i q_i(y,Q^2)P_{gq_i}\left(\frac{x}{y}\right) + G(y,Q^2)P_{gg}\left(\frac{x}{y}\right)\right] \tag{1.18}$$

where the sum $i = 1,...,2n_f$ runs over quarks and antiquarks of all flavours. The splitting function $P_{qg}(z)$ gives the probability density of a quark emitting a gluon with a fraction z of its momentum to first order in α_S. The other three splitting

functions are analogous. F_2 and xF_3 scaling violations consistent with QCD were observed in deep inelastic neutrino scattering by the CCFRR, CDHSW and CHARM collaborations [CCF 84, CDH 84, CHA 83]. These scaling violations are shown in Figure 1.1. The quark and antiquark structure functions (momentum distributions) of the nucleon have been measured directly by deep inelastic neutrino–nucleon and muon–nucleon electroweak scattering. These momentum distributions of quarks q and antiquarks $\bar{q}$ in the nucleon (at 10 GeV$^2 \leq Q^2 \leq$ 100 GeV^2) are shown in Figure 1.2. The first direct evidence for gluons was the three jet events

$$e^+e^- \rightarrow gq\bar{q} \rightarrow 3 \; hadronic \; jets \tag{1.19}$$

observed by the TASSO, PLUTO, MARK J and JADE collaborations at PETRA, a 30 GeV centre–of–mass e^+e^- collider, located at DESY [JAD 79, MAR 79, PLU 79, TAS 79].

As gluons are electroweakly neutral, the gluon structure function cannot be measured directly by lepton–parton scattering. One method for obtaining a direct measurement of $G(x)$ is to employ heavy quark photoproduction. The tree level perturbative QCD deep inelastic charm photoproduction diagrams are shown in Figure 1.3. In order to measure the fraction of the nucleon momentum carried by the gluon, it is sufficient to measure the photon beam momentum and the momentum of the D ($\bar{D}$) meson produced via hadronization of the c ($\bar{c}$) quark or the momentum of the J/ψ produced via coupling of the c and $\bar{c}$ to form a bound state.

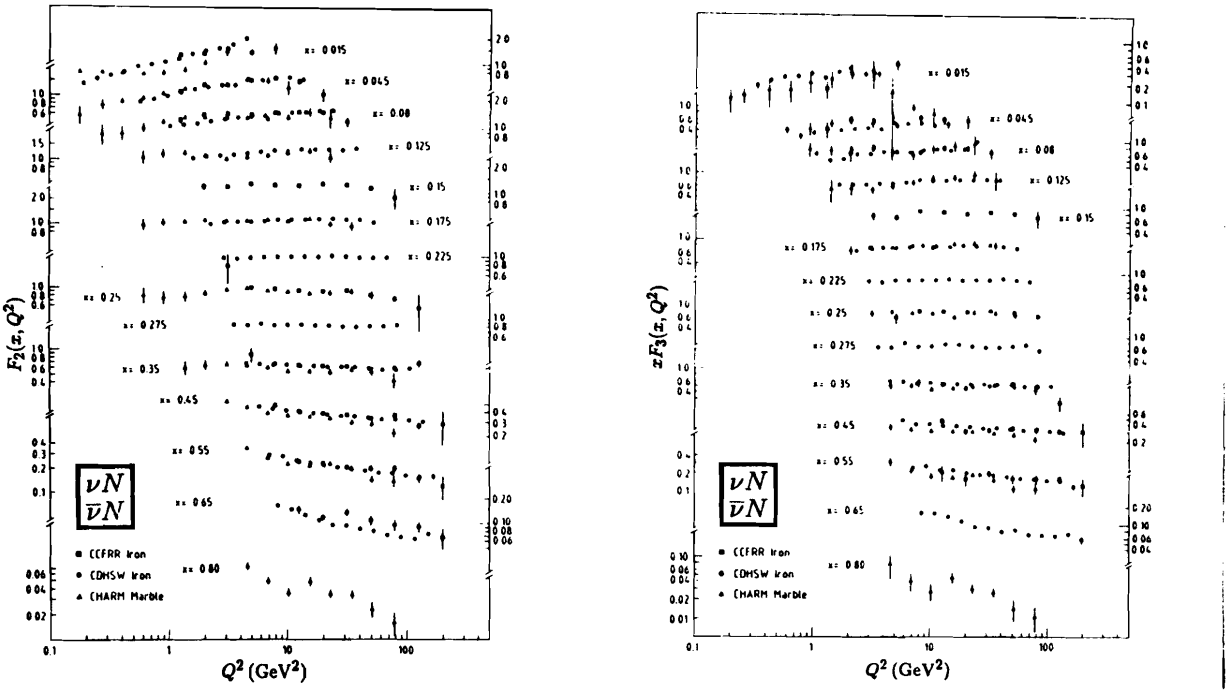

Figure 1.1: The F_2 and xF_3 scaling violations with Q^2 measured in charged-current neutrino and antineutrino scattering on iron (CCFRR, CDHWS) and marble (CHARM) targets, for fixed bins of x. Adapted from the Particle Data Group compilation (1990).

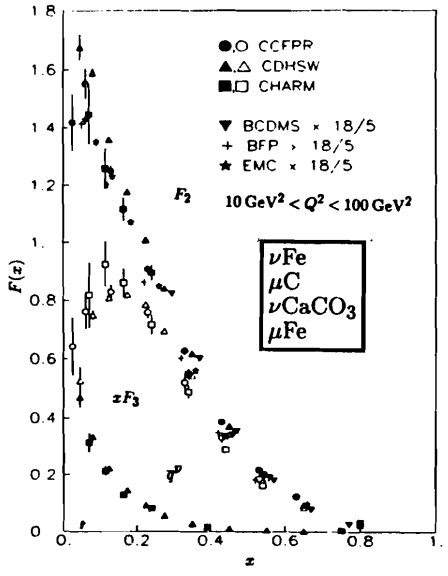

Figure 1.2: The momentum distributions of quarks q and antiquarks $\bar{q}$ in the nucleon measured by deep–inelastic lepton–nucleon scattering on isoscalar targets. Adapted from the Particle Data Group compilation (1990).

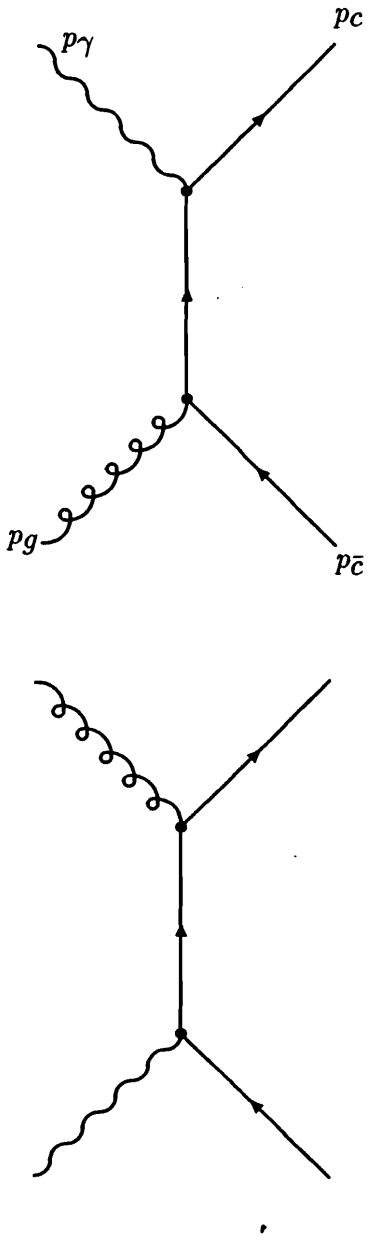

Figure 1.3: The tree level perturbative QCD diagrams for charm photoproduction.

1.2 Outline of Thesis

This thesis documents the measurement of the gluon structure function using the E691 deep inelastic J/ψ photoproduction data. In addition, the z, p_T^2 and E_γ dependence of the deep inelastic and coherent and incoherent elastic cross sections are presented. Summaries of the development of deep inelastic scattering and the properties of the bound–state vectors mesons, J/ψ and ψ', are contained in Chapter 1 along with a brief description of the E691 spectrometer. The Standard Model of particle physics is reviewed in Chapter 2, followed by a summary of the strong force, quantum chromodynamics. Furthermore, deep inelastic J/ψ photoproduction is discussed in terms of the photon–gluon–fusion model, as calculated to next–to–leading order in perturbation theory by Berger and Jones. Next a phenomenological model of elastic J/ψ photoproduction from nuclear targets is presented. Finally, fragmentation is discussed. The E691 beamline, target and spectrometer are summarized in Chapter 3. A detailed description is provided in Appendix E and references contained therein. The experiment triggers, data acquisition, online monitoring and offline reconstruction are discussed in Chapter 4. The J/ψ photoproduction analysis is presented in Chapter 5 and compared with previous data. The conclusions are presented in Chapter 6.

1.3 The Charm Quark and the J/ψ Vector Meson

The charm quark was independently discovered in 1974 by a collaboration at SLAC led by B. Richter [Aug 74] and by a collaboration at Brookhaven led by S. Ting [Aub 74]. The SLAC group, working at the SPEAR e^+e^- collider, observed a resonance at 3.1 GeV

$$e^+e^- \rightarrow J/\psi \rightarrow e^+e^-,\ \mu^+\mu^- \tag{1.20}$$

At the Brookhaven AGS, 30 GeV protons were directed at a beryllium target. The same resonance was observed in the reaction

$$pBe \rightarrow J/\psi X \rightarrow e^+e^-X \tag{1.21}$$

The $J/\psi(3069)$ resonance was subsequently identified as a bound charm–anticharm ($c\bar{c}$) vector meson. Discovery of a more massive $c\bar{c}$ vector meson state, the $\psi(3685)$ or ψ' soon followed. The properties of the J/ψ and ψ' are listed in Table 1.1

Table 1.1: The J/ψ and ψ' vector mesons. The J/ψ is the S–wave ($L = 0$) $c\bar{c}$ ground state and the ψ' is the first radial excitation. The decay modes listed are the ones observed by experiment E691.

Meson	Mass (GeV)	Width (keV)	$^{2S+1}L_J$	J^{PC}	Decay Mode	B. R. (%)
J/ψ	3.09693 ± 0.00009	68 ± 10	$^3 1S_1$	1^{--}	$\mu^+\mu^-$	6.9 ± 0.9
ψ'	3.68600 ± 0.00010	243 ± 43	$^3 2S_1$	1^{--}	$\mu^+\mu^-\pi^+\pi^-$	16.2 ± 1.6

The existence of a fourth quark – charm, forming a doublet with the strange quark, had been predicted by S. Glashow, J. Iliopoulos and L. Maiani in 1970 [Gla 70]. The d', s' weak interaction (left–handed) eigenstates are rotations of the d, s mass eigenstates [Cab 63]

$$\begin{pmatrix} d' \\ s' \end{pmatrix}_L = \begin{pmatrix} \cos\theta_C & \sin\theta_C \\ -\sin\theta_C & \cos\theta_C \end{pmatrix}_L \begin{pmatrix} d \\ s \end{pmatrix}_L \tag{1.22}$$

The first quark generation consists of a left–handed doublet

$$\begin{pmatrix} u \\ d' \end{pmatrix}_L = \begin{pmatrix} u \\ d\cos\theta_C + s\sin\theta_C \end{pmatrix}_L \tag{1.23}$$

and the three weakly non–interacting singlets u_R, d_R and s_R. The hadronic part of the effective weak neutral–current Lagrangian is

$$L_{eff}(x) = -\frac{G_F}{\sqrt{2}} J^0_\mu(x) J^{0\mu}(x) + h.c. \tag{1.24}$$

where the neutral–current coupling is of the form

$$J^0_\mu J^{0\mu} \propto \underbrace{u\bar{u} + (d\bar{d}\cos^2\theta_C + s\bar{s}\sin^2\theta_C)}_{\Delta S=0} + \underbrace{(s\bar{d} + \bar{s}d)\sin\theta_C\cos\theta_C}_{\Delta S=1} \tag{1.25}$$

The second term in Equation 1.25 gives rise to $O(G_F)$ $\Delta S = 1$ strangeness changing neutral–current processes. Thus the branching ratio for the weak neutral–current decay $K^0_L \to \mu^+\mu^-$ should be of the same order as for the weak charge–current decay $K^+ \to \mu^+\nu_\mu$. Experimentally, the measured branching ratios differ by 10 orders of magnitude

$$BR(K^+ \to \mu^+\nu_\mu) = 63.51 \pm 0.19\% \tag{1.26}$$

$$BR(K^0_L \to \mu^+\mu^-) = (6.3 \pm 1.1) \times 10^{-9}\% \tag{1.27}$$

To account for the suppression of strangeness–changing neutral current processes, Glashow *et al.* proposed the existence of the charm quark. The charm quark forms a left–handed doublet with the strange quark weak eigenstate

$$\begin{pmatrix} c \\ s' \end{pmatrix}_L = \begin{pmatrix} c \\ s\cos\theta_C - d\sin\theta_C \end{pmatrix}_L \tag{1.28}$$

(with s'_L orthogonal to d'_L) and a right–handed singlet c_R. This introduces new terms in the neutral–current coupling

$$\begin{aligned} J^0_\mu J^{0\mu} \propto\ & \underbrace{u\bar{u} + c\bar{c} + (d\bar{d} + s\bar{s})\cos^2\theta_C + (s\bar{s} + d\bar{d})\sin^2\theta_C}_{\Delta S=0} \\ & + \underbrace{(s\bar{d} + \bar{s}d - s\bar{d} - \bar{s}d)\sin\theta_C\cos\theta_C}_{\Delta S=1} \end{aligned} \tag{1.29}$$

strongly suppressing the $\Delta S = 1$ neutral currents. If the masses of the down and strange quarks were identical, then the cancellation in the $\Delta S = 1$ term of Equation 1.29 would be exact. This suppression scheme has subsequently become know as

the GIM mechanism, after Glashow, Iliopoulos and Maiani. While the discovery of charm, in 1974, was widely considered to be a surprise, it is interesting to note that the GIM mechanism had, in 1970, predicted the existence of a fourth quark with the charm quantum numbers.

1.4 Experiment E691

Experiment E691 was performed during 1985 at the Tagged Photon Spectrometer of the Fermi National Accelerator Laboratory (Batavia, Illinois). A photon beam was directed at a beryllium target. The photon beam had a bremsstrahlung spectrum with a maximum energy of 250 GeV. During the run about 100 million photoproduced events were recorded. Immediately downstream of the target was the high resolution silicon microstrip detector (SMD) consisting of 9 50 μm pitch silicon microstrip planes. The SMD enabled the reconstruction algorithm to separate the primary interaction vertex from the downstream open–charm decay vertex on an event–by–event basis. This reduced the combinatoric background in the open–charm reconstruction by a large factor of about 300 to 500. Following the SMD was a fully instrumented downstream spectrometer consisting of 35 drift chamber planes, 2 momentum analyzing magnets, 2 threshold Cherenkov counters and electromagnetic and hadronic calorimeters followed by a steel wall and a wall of segmented scintillation counters, the back muon wall.

It is important for the study of the production dynamics to have an unbiased trigger. Yet at the same time, it is necessary to reduce the high rate of non–charm background events. For the J/ψ, a dimuon trigger was chosen utilizing the segmentation of the threshold Cherenkov counters and back muon wall to provide a fast signal for the presence of a dimuon pair in an event. For the open–charm, a global transverse energy trigger E_T was chosen utilizing the segmentation of the electromagnetic and hadronic calorimeters to provide a fast measure of the global transverse energy for hadronic events.

Chapter 2

Theory

2.1 Introduction

2.1.1 The Standard Model

Our understanding of the fundamental particles and forces of Nature is summarized by the Standard Model (SM). The modern development of the SM began approximately with the discovery of the electron by J.J. Thompson in 1897, while the most recent addition to this model is a limit on the number of neutrino generations, obtained by measuring the Z^0 resonance width [PDG 90].

The SM consists of three generations of matter interacting via three forces. Each generation contains two leptons and two quarks. The quarks interact via the electromagnetic, weak and strong forces but the leptons interact only via the electromagnetic and weak forces. All fundamental interactions are described as an exchange of a quanta of the field of force between the matter particles. Both the matter fields and the force fields are quantized. All (known) matter fields are spin – 1/2 fermions obeying Fermi–Dirac statistics and all (known) force fields are integer spin bosons obeying Bose–Einstein statistics. The quanta of the electromagnetic force (the photons) the weak force (the intermediate vector bosons) and the strong force (the gluons) are all spin–1 bosons. Gravitons are the spin-2 quanta of gravity. The SM provides a

unifying description of Nature via the principle of local gauge invariance for the electromagnetic, weak and strong forces (although classical general relativity may also be obtained using local gauge invariance, no self–consistent theory of quantum gravity has yet been formulated). Interactions are described by the direct product of the three Lie groups

$$\mathrm{SU(3)}_C \times \mathrm{SU(2)}_L \times \mathrm{U(1)}_Y \tag{2.1}$$

where $\mathrm{SU(3)}_C$ corresponds to quantum chromodynamics, the theory of the strong force [Gro 73, Wei 73, Fri 73], and $\mathrm{SU(2)}_L \times \mathrm{U(1)}_Y$ corresponds to the electroweak unification of quantum electrodynamics and quantum flavourdynamics, the theories of the electromagnetic and weak forces [Gla 61, Wei 67, Sal 68]. The intrinsic good quantum numbers of the fermions are summarized in Table 2.1 and those of the bosons in Table 2.2.

The strong and electromagnetic interactions conserve parity, whereas the weak interaction is maximally parity violating [Lee 56] in that an equal mixture of polar and axial currents is involved

$$J_\mu = V_\mu - A_\mu \tag{2.2}$$

Under parity inversion P, the polar components transform as

$$PV_0 = V_0 \tag{2.3}$$

$$P\boldsymbol{V} = -\boldsymbol{V} \tag{2.4}$$

$$\tag{2.5}$$

whereas the axial components transform as

$$PA_0 = -A_0 \tag{2.6}$$

Table 2.1: Intrinsic quantum numbers of the three quark and lepton generations. The top quark, t, and the tau neutrino, ν_τ, have been predicted but as yet have not been directly observed.

	Quarks					
	$1st$		$2nd$		$3rd$	
Quantum Number	d	u	s	c	b	t
S – Spin	1/2	1/2	1/2	1/2	1/2	1/2
Q – Electric Charge	−1/3	+2/3	−1/3	+2/3	−1/3	+2/3
B – Baryon Number	1/3	1/3	1/3	1/3	1/3	1/3
I_z – Isospin z–component	−1/2	1/2	0	0	0	0
S – Strange	0	0	−1	0	0	0
C – Charm	0	0	0	1	0	0
B – Bottom	0	0	0	0	−1	0
T – Top	0	0	0	0	0	1
	Leptons					
	$1st$		$2nd$		$3rd$	
Quantum Number	e	ν_e	μ	ν_μ	τ	ν_τ
S – Spin	1/2	1/2	1/2	1/2	1/2	1/2
Q – Electric Charge	−1	0	−1	0	−1	0
L_e – Electron Lepton Number	1	1	0	0	0	0
L_μ – Muon Lepton Number	0	0	1	1	0	0
L_μ – Tau Lepton Number	0	0	0	0	1	1

Table 2.2: Intrinsic quantum numbers of the four fundamental force quanta: Electromagnetic , Weak, Strong and Gravitational.

Force	E.M.	Weak			Strong			Gravity
Quanta	Photon	Intermediate Vector Bosons			Gluons			Graviton
Quantum Number	γ	Z^0	W^+	W^-	G_1	...	G_8	g
S – Spin	1	1	1	1	1	...	1	2
Q – Electric Charge	0	0	+1	−1	0	...	0	0
RBG – Colour Charge	0	0	0	0	$R\overline{G}$	...	$G\overline{R}$	0

$$PA = A \tag{2.7}$$

(2.8)

and thus parity is not conserved

$$PJ_\mu \neq \pm J_\mu \tag{2.9}$$

In the SM, the left–handed fermions form doublets whose interactions are described by the weak isospin group $SU(2)_L$ whereas the right–handed fermions form singlets whose interactions are described by the weak hypercharge group $U(1)_Y$. The weak isospin operators T and T_3 and their eigenvalues are directly analogous to the nuclear isopin operators I and I_3. Weak hypercharge, weak isospin and electric charge are related by

$$Q = T_3 + \frac{1}{2}Y \tag{2.10}$$

The intrinsic weak quantum numbers are listed in Table 2.3.

Table 2.3: Weak isospin and hypercharge quantum numbers of the first fermion generation.

Particle	T	T_3	Y
ν_{eL}	1/2	+1/2	–1
e_L	1/2	–1/2	–1
u_L	1/2	+1/2	–1/3
d_L	1/2	–1/2	+1/3
e_R	0	0	–2
u_R	0	0	+4/3
d_R	0	0	–2/3

The quark mass eigenstates listed in Table 2.1 are not the electroweak eigenstates of $SU(2)_L \times U(1)_Y$ listed in Table 2.3. These two set of states are related by the unitary Cabibbo–Kobayashi–Maskawa (CKM) transformation; a 3×3 matrix giving the couplings between different quark generations [Kob 73]. With the primed quark fields representing the electroweak eigenstates and (V_{ij}) the CKM matrix is

$$\begin{pmatrix} d' \\ s' \\ b' \end{pmatrix}_L = \begin{pmatrix} V_{ud} & V_{us} & V_{ub} \\ V_{cd} & V_{cs} & V_{cb} \\ V_{td} & V_{ts} & V_{tb} \end{pmatrix}_L \begin{pmatrix} d \\ s \\ b \end{pmatrix}_L \tag{2.11}$$

and may be parameterized in terms of three real angles and one phase. A non–zero value of the phase is a possible source of the observed CP violation in the K meson system and predicts CP violation in the B meson system.

As presented, the SM Langrangian does not admit mass terms. Mass terms are of the form

$$\mathcal{L}_{SM} = ... + \frac{1}{2} m_\psi \psi^\mu \psi_\mu \tag{2.12}$$

where ψ represents a intermediate vector boson, quark or charged lepton field. Such terms are not local $SU(2)_L \times U(1)_Y$ gauge invariant. Thus a new idea is required to give mass to fundamental fields without violating local gauge invariance. One proposal is to introduce a new doublet of complex scalar (spin–0) fields – the Higgs field [Hig 66]

$$\phi = \begin{pmatrix} \phi^+ \\ \phi^0 \end{pmatrix} \tag{2.13}$$

with the electroweak intrinsic quantum numbers listed in Table 2.4

Table 2.4: Electroweak intrinsic quantum numbers of the complex scalar Higgs doublet.

Particle	T	T_3	Y	Q
ϕ^+	1/2	+1/2	-1	+ 1
ϕ^0	1/2	-1/2	+1	0

and add the $SU(2)_L \times U(1)_Y$ gauge invariant coupling

$$\mathcal{L}_{Higgs} = (D_\mu \phi)^\dagger (D^\mu \phi) - V(\phi^\dagger \phi) \tag{2.14}$$

to the SM Lagrangian. The potential V is chosen so as to have a minimum at some non–zero radius in the (ϕ^+, ϕ^0) space. A typical form is

$$V(\phi^\dagger\phi) = -\mu\phi^\dagger\phi + \lambda(\phi^\dagger\phi)^2 \tag{2.15}$$

with a minimum value at the radius

$$\phi^\dagger\phi = \frac{\mu^2}{2\lambda} \tag{2.16}$$

The local gauge symmetry is broken by the neutral scalar developing a non–zero vacuum expectation value

$$\langle 0|\phi|0\rangle = \begin{pmatrix} 0 \\ v/\sqrt{2} \end{pmatrix} \tag{2.17}$$

with $v = \sqrt{\mu^2/\lambda}$ by choosing one of the infinite equivalent ground states or vacua on the minima radius. The SM Lagrangian is still local $\mathrm{SU}(2)_L \times \mathrm{U}(1)_Y$ gauge invariant. However, the chosen ground state or vacuum does not possess this invariance. This phenomena, known as spontaneous symmetry breaking (SSB), gives mass to the intermediate vector bosons, quarks and charged leptons while preserving the local gauge invariance of the SM Lagrangian. Consider the electroweak sector, before SSB there existed

- four massless vector gauge bosons with two spin degrees of freedom each
- four scalar Higgs fields with a single degree of freedom each

for a total of twelve degrees of freedom. After SSB, one finds

- three massive vector gauge bosons ($W^\pm, Z^0$) with three spin degrees of freedom each
- one massless gauge boson (γ) with two degrees of freedom
- one massive scalar Higgs field (H^0) with a single degree of freedom.

The total number of degrees of freedom is still twelve, but three scalar degrees of freedom have become the longitudinal polarization states of the three massive intermediate vector bosons.

2.1.2 Feynman Diagrams

The fundamental interactions are most easily visualized (and calculated) using perturbative Feynman diagrams [Fey 49]. A prototypical example, the two leading order Feynman amplitudes for muon pair production, $\gamma\gamma \rightarrow \mu^+\mu^-$, are shown in Figure 2.1.

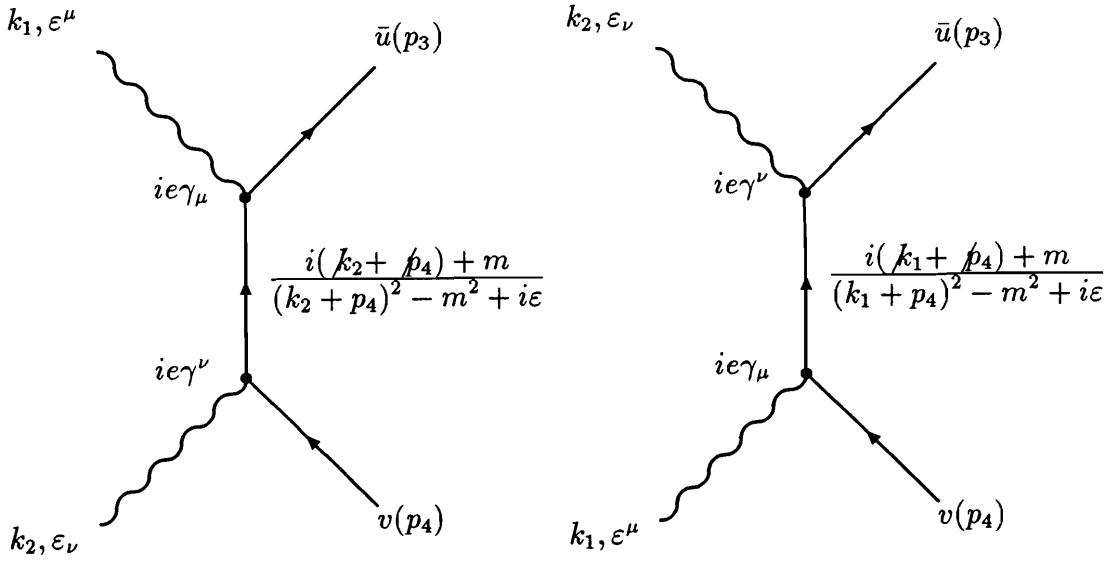

Figure 2.1: The leading order Feynman diagrams for muon pair production.

The transition amplitude for this process (in the momentum–space representation) is

$$\begin{aligned} T_{fi} &= \{\bar{u}(p_3)(ie\gamma_\mu)\varepsilon^\mu \left[\frac{i(\not{k}_2 + \not{p}_4) + m}{(k_2+p_4)^2 - m^2 + i\varepsilon}\right] \varepsilon_\nu (ie\gamma^\nu) v(p_4) \\ &\quad + \bar{u}(p_3)(ie\gamma^\nu)\varepsilon_\nu \left[\frac{i(\not{k}_1 + \not{p}_4) + m}{(k_1+p_4)^2 - m^2 + i\varepsilon}\right] \varepsilon^\mu (ie\gamma_\mu) v(p_4)\} \\ &\quad \times (2\pi)^4 \delta(k_1 + k_2 - p_3 - p_4) \\ &= (\mathcal{M}_1 + \mathcal{M}_2) \times (2\pi)^4 \delta(k_1 + k_2 - p_3 - p_4) \end{aligned}$$

$$= \mathcal{M} \times (2\pi)^4 \delta(k_1 + k_2 - p_3 - p_4) \tag{2.18}$$

consisting of the following components

- k_1, $\varepsilon^\mu \equiv$ the first incoming free photon 4–momentum and polarization
- k_2, $\varepsilon_\nu \equiv$ the second incoming free photon 4–momentum and polarization
- $ie\gamma_\mu \equiv$ the polar vector muon–photon vertex coupling
- $\frac{i(\not{k}_2 + \not{p}_4) + m}{(k_2 + p_4)^2 - m^2 + i\varepsilon} \equiv$ the spin-1/2 fermion propagator for the first amplitude (the Dirac wave equation in the momentum representation)
- $\frac{i(\not{k}_1 + \not{p}_4) + m}{(k_1 + p_4)^2 - m^2 + i\varepsilon} \equiv$ the spin-1/2 fermion propagator for the second amplitude
- $\bar{u}(p_3) \equiv$ the outgoing free muon Dirac spinor
- $v(p_4) \equiv$ the outgoing free antimuon Dirac spinor
- $ie\gamma^\nu \equiv$ the polar vector antimuon–photon vertex coupling
- $\delta(k_1 + k_2 - p_3 - p_4) \equiv$ the 4–momentum conservation

The differential cross-section $d\sigma$ is then given by

$$d\sigma = \frac{1}{(2s_1 + 1)(2s_2 + 1)} \sum_{spin\ states} \frac{|\mathcal{M}|^2}{F} d\text{Lips} \tag{2.19}$$

where

- the modulus of $\mathcal{M}$ squared is averaged over the initial photon spin states ($s_1 = s_2 = 1$) and summed over the final muon and antimuon spin states
- $F \equiv$ the incident particle flux
- dLips $\equiv$ the Lorentz invariant phase space: number of final states accessible in phase space.

In a scattering experiment, measuring the differential cross-section with respect to the kinematic variables of interest and the flux gives information about the dynamics of the underlying fundamental process represented by $|\mathcal{M}|^2$.

2.1.3 Quantum Chromodynamics

Quantum chromodynamics (QCD) is the local quantum field theory of the strong force. The QCD Lagrangian is modelled upon the Lagrangian of quantum electrodynamics (QED)

$$\mathcal{L}_{QED}(x) = \bar{\psi}(x)(\gamma^\mu D_\mu - m)\psi(x) - \frac{1}{4}F_{\mu\nu}F^{\mu\nu} \tag{2.20}$$

The covariant derivative $iD_\mu \equiv i\partial_\mu - eA_\mu(x)$ is defined in order to make the Dirac Lagrangian for a free moving particle of mass m invariant under the *local* U(1) Abelian (commutative) Lie group symmetry transformation.

Quantum chromodynamics was developed by extending the principle of local gauge invariance to the non–Abelian (noncommutative) group SU(3) [Gro 73, Wei 73, Fri 73]. A group element g of SU(3) may be written as

$$g = \exp\left(-i\lambda^a\theta^a\right) \quad , a = 1, ..., 8 \tag{2.21}$$

where the θ^as are the continuos real parameters for labelling the group elements and the λ^as are the generators of this Lie group. For infinitesimal θ^a the set of λ^a form an algebra

$$[\lambda^a, \lambda^b] = if^{abc}\lambda^c \tag{2.22}$$

where the f^{abc}, $a, b, c = 1, ..., 8$ are the structure constants. For SU(N), the quark fermion field with mass m has N components in the fundamental representation,

$\psi_i(x), i = 1, ..., N$. Thus, for SU(3), the quark field has three components with the transformation property

$$\psi_i' = U_{ij}\psi_j \tag{2.23}$$

$$U = \exp(-i\lambda^a\theta^a) \tag{2.24}$$

The QCD Lagrangian is

$$\mathcal{L}_{QCD}(x) = \bar{\psi}_i(x)[\gamma^\mu(D_\mu)_{ij} - m\delta_{ij}]\psi_j(x) - \frac{1}{4}F^a_{\mu\nu}F^{a\mu\nu} \tag{2.25}$$

with the covariant derivative

$$iD_\mu \equiv i\partial_\mu - g\lambda^a A^a_\mu(x) \tag{2.26}$$

or, in component form,

$$i(D_\mu)_{ij} \equiv i\delta_{ij}\partial_\mu - g\lambda^a_{ij}A^a_\mu(x) \tag{2.27}$$

where λ^a_{ij} is the representation of λ^a in the fundamental representation. The covariant derivative has been constructed so as to now be invariant under the *local* SU(3) symmetry transformation

$$iD_\mu\psi(x) \overset{SU(3)}{\rightarrow} \exp[iq\lambda^a\theta^a(x)][iD_\mu\psi(x)] = i(D_\mu)'\psi(x) \tag{2.28}$$

$$\lambda^a A^a_\mu(x) \overset{SU(3)}{\rightarrow} U[\lambda^a A^a_\mu(x) - \frac{1}{q}U^{-1}\partial_\mu U]U^{-1} = \lambda^a A'^a_\mu(x) \tag{2.29}$$

$$\mathcal{L}(x) \overset{SU(3)}{\rightarrow} \bar{\psi}(x)e^{-i\lambda^a\theta^a(x)}e^{i\lambda^a\theta^a(x)}(i\gamma^\mu D_\mu - m)\psi(x) \tag{2.30}$$

$$= \bar{\psi}(x)(\gamma^\mu D_\mu - m)\psi(x) \tag{2.31}$$

$$= \mathcal{L}'(x) \tag{2.32}$$

In analogy to QED, the gauge invariance of the Dirac Lagrangian under the local SU(3) symmetry transformation requires the introduction of 8 new gauge fields $A^a_\mu(x)$. These fields are identified with the *physical* chromatic vector potential. The free Lagrangian of A^a_μ is

$$\mathcal{L}(x) = -\frac{1}{4} G^a_{\mu\nu} G^{a\mu\nu} \tag{2.33}$$

where

$$G^a_{\mu\nu}(x) = \partial_\mu A^a_\nu(x) - \partial_\nu A^a_\mu(x) + g f^{abc} A^b_\mu A^c_\nu \tag{2.34}$$

is the chromatic field tensor and is also invariant under the local SU(3) transformation. This tensor may be generated from the commutator of covariant derivatives

$$[D_\mu, D_\nu] = -ig\lambda^a G^a_{\mu\nu} \tag{2.35}$$

The last term in the chromatic field strength tensor $G^a_{\mu\nu}$ is a consequence of the non–Abelian nature of the SU(3) gauge group. Such a term has no analogue in QED. If the Lagrangian is rewritten in the symbolic form

$$\mathcal{L} = \bar{q}q + G^2 + g\bar{q}qG + gG^3 + g^2G^4, \tag{2.36}$$

then the first three terms have QED analogues and describe the free propagation of quarks and gluons and the quark–gluon interaction, respectively. The last two terms represent the gluon–gluon three and four vertex interactions in QCD, respectively. Asymptotic freedom, the charge anti–screening property of QCD [Gro 73, Pol 73] in contradistinction to the charge screening of QCD, is a consequence of the colour charged gluon–gluon interactions. To first order, the strong force coupling constant runs as

$$\alpha_S(Q^2) = \frac{12\pi}{(33 - 2n_f)\ln(Q^2/\Lambda)} \tag{2.37}$$

where $\Lambda \simeq 200$ MeV and n_f is the number of quark flavours. At sufficiently short distances or equivalently at large $Q^2 s$, as in asymptotically free deep inelastic scattering, α_S is small enough that perturbative QCD calculations are valid. The quanta of A^a_μ – the gluons– must be massless as a mass term

$$\mathcal{L}(x) = \frac{1}{2} m_g^2 A^a_\mu A^{a\mu} \tag{2.38}$$

would violate the requirement of local SU(3) invariance.

The Feynman rules for QCD may be derived via either path–integral or canonical quantization.

2.2 Theory of J/ψ Photoproduction

2.2.1 Introduction

The photoproduction of J/ψ vector mesons on a nuclear target consists of three distinct processes: inelastic, coherent elastic and incoherent elastic. The kinematics of such events are described by the incident photon energy, E_γ, the transverse momentum squared, p_T^2, of the J/ψ relative to the photon beam and the inelasticity, z, a Lorentz invariant given by

$$z \equiv \frac{p_\psi \cdot p_N}{p_\gamma \cdot p_N} \tag{2.39}$$

where p_γ, p_N and p_ψ denote the incident photon, target nucleon and J/ψ 4–momenta, respectively. The symbol $\cdot$ denotes the Lorentz 4–product. In the lab frame z corresponds to the fraction of the photon beam energy transferred to the J/ψ

$$z = \frac{E_\psi}{E_\gamma} \tag{2.40}$$

Refer to Appendix A for a complete discussion of the kinematics of J/ψ photoproduction. Elastic events are those in which most of the photon energy is transferred to the the J/ψ corresponding to a very high elasticity, $z > 0.99$. Such events are characterized by low p_T^2 and for scattering from a nuclear target occur via two distinct processes: coherent scattering from the nucleus as a whole ($\langle p_T^2 \rangle \sim 0.07$ GeV$^2/c^2$) or incoherent scattering from a nucleon within the nucleus ($\langle p_T^2 \rangle \sim 0.6$ GeV$^2/c^2$). For $z < 0.99$, the production is inelastic. Deep inelastic production occurs for $m_\psi/E_\gamma < z < 0.90$, well away from $z \rightarrow 1$ and is characterized by significantly higher p_T^2, ($\langle p_T^2 \rangle \sim 1.2$ GeV$^2/c^2$). Perturbative QCD is valid for deep inelastic production and the the colour–singlet photon–gluon–fusion (PGF) model [Ber 81] is used to describe the QCD process $\gamma g_1 \rightarrow (J/\psi) g_2$.

A QCD description of elastic production does not as yet exist and we use the phenomenological vector–meson–dominance (VMD) model [Bau 78, Hol 85] with the Glauber model [Gla 70] of elastic hadron scattering from a nuclear target. The VMD model is based on the observation that the photon and the J/ψ vector meson have the same quantum numbers,

$$J^{PC} = 1^{--} \tag{2.41}$$

There is an appreciable probability for a real photon to fluctuate into a virtual J/ψ. By scattering from the target, the virtual J/ψ becomes real via the 4–momentum transferred. To describe the elastic J/ψ–nucleus and J/ψ–nucleon scattering we use the Glauber model of hadron elastic scattering from $A > 1$ nuclei. This model is an extension of optical diffraction theory. When the J/ψ scatters from the whole nucleus, it is not possible in principle to know which of the A nucleons was struck. The amplitudes for scattering by all the nucleons must be added coherently to form the nuclear scattering amplitude. The incoherent elastic $d\sigma/dp_T^2$ is obtained by subtracting the

coherent elastic $d\sigma/dp_T^2$ from the summed differential cross sections corresponding to scattering from all possible nuclear final states (neglecting excitations from the small 4–momentum transfer).

Inelastic photoproduction occurs at the parton scale via the quantum chromodynamic (QCD) process of photon–gluon fusion (PGF). In analogy to e^+e^- pair production, there is an appreciable probability for a real photon to fluctuate into a virtual quark–antiquark pair, $(q\bar{q})$. Unlike the charged leptons, the quarks interact via the strong force through gluon exchange. Inelastic photoproduction occurs when a gluon from the target nucleon transfers sufficient 4–momenta to convert the virtual charm–anticharm pair into a real $c\bar{c}$ pair. The gluon carries a fraction, $m_\psi^2/s \leq x \leq 1$, of the target nucleon 4–momentum. For $E_\gamma \sim 145\ GeV$, the strong coupling constant α_S is about 0.2. Thus the leading leading order photon–gluon diagram $(\alpha\alpha_S^2)$ dominates over the leading order photon–photon diagram (α^2). Unlike the electrically neutral photons mediating quantum–electrodynamics (QED) gluons carry colour–charge. The c and $\bar{c}$ quarks have an overall non–zero colour charge as do the fragments of the target nucleon. In nature, only particles with zero colour charge have been observed. Thus $c\bar{c}$ pair must shed its colour to the target fragments and combine each other or with quarks from the vacuum to form colour–singlet (zero colour charge) hadrons. This process is called hadronization or fragmentation.

2.2.2 Deep Inelastic J/ψ Photoproduction and the Photon–Gluon–Fusion Model

Deep inelastic J/ψ photoproduction has been predicted, by Berger and Jones [Ber 81], to occur via the QCD process of photon–gluon fusion (PGF), $\gamma g_1 \rightarrow J/\psi g_2$, where g_1 and g_2 are the incident and radiated gluons, respectively. The next–to–leading order (NLO) Feynman diagrams for this process are shown in Figure 2.3. All six diagrams are required in order to satisfy gauge invariance. Colour is explicitly conserved. The total amplitude is

$$\mathcal{M} = AF_c e_q g^2 \Big(\mathcal{M}_1^{\mu\beta\alpha} + \mathcal{M}_2^{\mu\beta\alpha} + \mathcal{M}_3^{\mu\beta\alpha} + \mathcal{M}_4^{\mu\beta\alpha} + \mathcal{M}_5^{\mu\beta\alpha} + \mathcal{M}_6^{\mu\beta\alpha} \Big) \epsilon_\mu(\gamma) \epsilon_\beta(g_1) \epsilon_\alpha(g_2) \tag{2.42}$$

As the amplitudes occur in pairs, with $\mathcal{M}_1 = \mathcal{M}_6$, $\mathcal{M}_2 = \mathcal{M}_5$ and $\mathcal{M}_3 = \mathcal{M}_4$, the total amplitude reduces to

$$\mathcal{M} = 2AF_c e_q g^2 \Big(\mathcal{M}_1^{\mu\beta\alpha} + \mathcal{M}_2^{\mu\beta\alpha} + \mathcal{M}_3^{\mu\beta\alpha} \Big) \epsilon_\mu(\gamma) \epsilon_\beta(g_1) \epsilon_\alpha(g_2) \tag{2.43}$$

where

- $\mathcal{M}_{i=1,\ldots,6} \equiv$ the six photon–gluon–fusion amplitudes shown in Figure 2.2.
- $A =$ the coupling strength of the J/ψ to the $c\bar{c}$ pair obtained from the value of the orbital $S-$wave function in momentum space.
- $F_c = \delta_{ab}/2\sqrt{3}$ is the colour factor, where a is the colour index for the initial gluon, g_1 and b is the colour index for the final gluon, g_2. Thus colour is explicitly conserved and all six amplitudes are proportional to the same colour factor.
- $e_q =$ the electric charge proportional to the coupling strength, α, at the QED vertex.
- $g =$ the colour charge proportional to the coupling strength, α_S, at each QCD vertex.
- $\epsilon_\nu(V = \gamma, g_1, g_2) =$ the spin states of the V vector boson.

The explicit expression for $\mathcal{M}_1$, shown in Figure 2.2, is

$$\mathcal{M}_1^{\mu\beta\alpha} = \frac{4}{\sqrt{2}} \mathrm{Tr} \left[\not{\epsilon}(\psi)(\not{p} + m_c)\gamma^\mu \frac{(\not{p} - \not{p}_\gamma) + m_c}{(\hat{t} - m_\psi^2)} \gamma^\beta \frac{(-\not{p} - \not{p}_{g2}) + m_c}{(\hat{s} - m_\psi^2)} \gamma^\alpha \right] \tag{2.44}$$

where

- $p = p_\psi/2$.
- $\hat{s} = (p_\gamma + p_{g1})^2 = (p_\psi + p_{g2})^2$.
- $\hat{t} = (p_\gamma - p_\psi)^2 = (p_{g2} - p_{g1})^2$.
- $\epsilon_\nu(\psi)$ = the spin states of the J/ψ vector boson.

In this calculation the $c\bar{c}$ binding energy is ignored to leading order and the J/ψ is treated as an S–wave system with each spin–1/2 constituent carrying one-half the mass, $m_c^{eff.} = m_\psi/2 \equiv m_c$ and one half the 4–momenta, $p_c = p_{\bar{c}} = p_\psi/2$, of the J/ψ. The three helicity states of the $J^P = 1^-$ charm–anticharm fermion pair are thus represented using the spinors

$$v(\uparrow)\bar{u}(\uparrow) = \frac{1}{\sqrt{2}} \not{\epsilon}(\uparrow)\frac{\not{p}_\psi + m_\psi}{2} \tag{2.45}$$

$$v(\downarrow)\bar{u}(\downarrow) = \frac{1}{\sqrt{2}} \not{\epsilon}(\downarrow)\frac{\not{p}_\psi + m_\psi}{2} \tag{2.46}$$

$$\frac{1}{\sqrt{2}}\Big[v(\uparrow)\bar{u}(\downarrow) + v(\downarrow)\bar{u}(\uparrow)\Big] = \frac{1}{\sqrt{2}} \not{\epsilon}(0)\frac{\not{p}_\psi + m_\psi}{2} \tag{2.47}$$

The coupling strength of the J/ψ to the $c\bar{c}$ pair is given in terms of an overall constant, A, related to the value of the orbital wave function at the origin in momentum space. The constant A may be determined from the the electronic width of the J/ψ

$$\Gamma_{ee}^{\psi} = \frac{A^2 e_q^2 e^2}{2\pi m_\psi} \tag{2.48}$$

where it has been assumed that the coupling of the virtual ($Q^2 > 0$) photon to the real $c\bar{c}$ pair in a electronic J/ψ decay is the same as the coupling of the real ($Q^2 = 0$) photon to the virtual $c\bar{c}$ pair in J/ψ photoproduction. The measured electronic width is 4.72 ± 0.35 keV (assuming $\Gamma_{ee}^{\psi} = \Gamma_{\mu\mu}^{\psi}$) [PDG 90].

Summing over the spin states of a massless vector boson gives

$$\sum \epsilon_\mu(V)\epsilon_\nu(V) = -g_{\mu\nu} \tag{2.49}$$

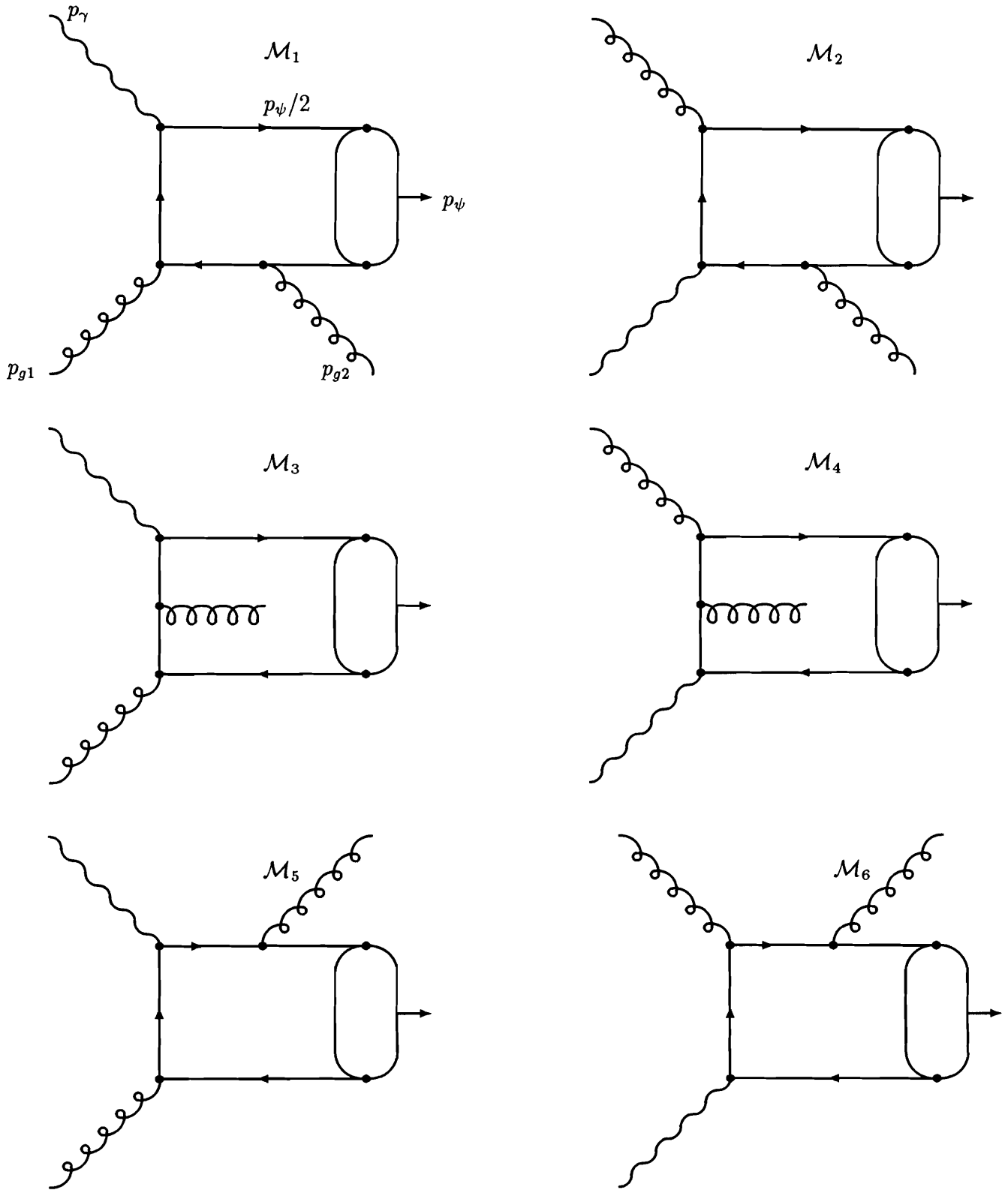

Figure 2.2: The six next-to-leading order ($\alpha\alpha_S^2$) Feynman diagrams of the photon-gluon-fusion model for the subprocess $\gamma g_1 \rightarrow J/\psi g_2$. All six diagrams are required to satisfy gauge invariance. Note that colour is explicitly conserved.

where $V =$ one of γ, g_1 or g_2 in Figure 2.2, whereas summing over the spin states of the massive J/ψ vector meson gives

$$\sum \epsilon_\mu(\psi)\epsilon_\nu(\psi) = -g_{\mu\nu} + \frac{(p_\psi)_\mu(p_\psi)_\nu}{m_\psi^2} \tag{2.50}$$

Thus summing the amplitudes, averaging over the spins of the incident photon and initial gluon and summing over the spins of the J/ψ and radiated gluon yields the $Ed\sigma/d^3p$ cross section. In analogy to the spin, the colour degrees of freedom of the initial gluon are averaged over and those of the radiated gluon are also summed over. In terms of the traditional Lorentz invariant J/ψ photoproduction variables, z and p_T^2, $Ed\sigma/d^3p = zd\sigma/\pi dz dp_T^2$ where

$$\frac{d\sigma}{dz dp_T^2} = \frac{xG(x)z(1-z)m_\psi^4 B}{[m_\psi^2(1-z)+p_T^2]^2} f(z, p_T^2) \tag{2.51}$$

with

- $h = c = 1$
- $f(z, p_T^2) = \frac{1}{(m_\psi^2 + p_T^2)^2} + \frac{(1-z)^4}{[p_T^2 + m_\psi^2(1-z)^2]^2} + \frac{z^4 p_T^4}{(m_\psi^2 + p_T^2)^2[p_T^2 + m_\psi^2(1-z)^2]^2}$
- $B = \frac{8\pi\alpha_S^2\Gamma_{ee}^\psi}{3\alpha m_\psi}$

Finiteness for $d\sigma/dz dp_T^2$ is satisfied by the total energy constraint which requires that $p_T^2 \to 0$ as $z \to 1$. The J/ψ momentum is constrained to the interval

$$0 \leq p_T^2 \leq z(1-z)xs - m_\psi^2(1-z) \tag{2.52}$$

Counting rules and momentum constraints, [Far 74] and [Gun 74], suggest

$$xG(x) = 3(1-x)^{n_g} \tag{2.53}$$

$$n_g \sim 5 \tag{2.54}$$

$$p_{g1} = xp_N \tag{2.55}$$

For $(p_T^2 + m_{psi}^2)/(zE_\gamma) \ll 1$, the gluon momentum fraction is well approximated by

$$x \simeq \frac{1}{s}\left[\frac{m_\psi^2}{z} + \frac{p_T^2}{z(1-z)}\right] \tag{2.56}$$

The strong coupling constant, α_S, is given by

$$\alpha_S(\mu^2) = \frac{12\pi}{(33 - 2n_f)ln(\mu^2/\lambda^2)} \tag{2.57}$$

to leading order, where n_f is the number of quark flavours with mass less than the energy scale μ and $\lambda \sim 200$ MeV [PDG 90]. The only scale in the deep inelastic colour singlet PGF process shown in Figure 2.2 is $\hat{s}$. Thus $\hat{s}$ was taken to be the argument of the strong coupling constant, α_S, giving

$$\begin{aligned} \mu^2 &= \hat{s} \\ &= (p_\gamma + p_{g1})^2 \\ &= 2xm_N E_\gamma \end{aligned} \tag{2.58}$$

first in terms of Lorentz invariant quantities and then in the lab frame. A scaling distribution was assumed for $xG(x)$ at least in part because the accessible range of μ^2 is narrow, as shown in the Monte Carlo generated Figure 2.6, where the invariant mass of the produced J/ψ plus radiated gluon peaks sharply near threshold. The $\langle s^2 \rangle$ was estimated, from the Monte Carlo, to be 22 GeV^2 with a $\pm\sigma$ range of [16, 26] GeV^2. Thus, for deep inelastic J/ψ photoproduction, with $n_f = 4$,

$$\alpha_S(\mu^2 = 22\text{GeV}^2) \simeq 0.24 \tag{2.59}$$

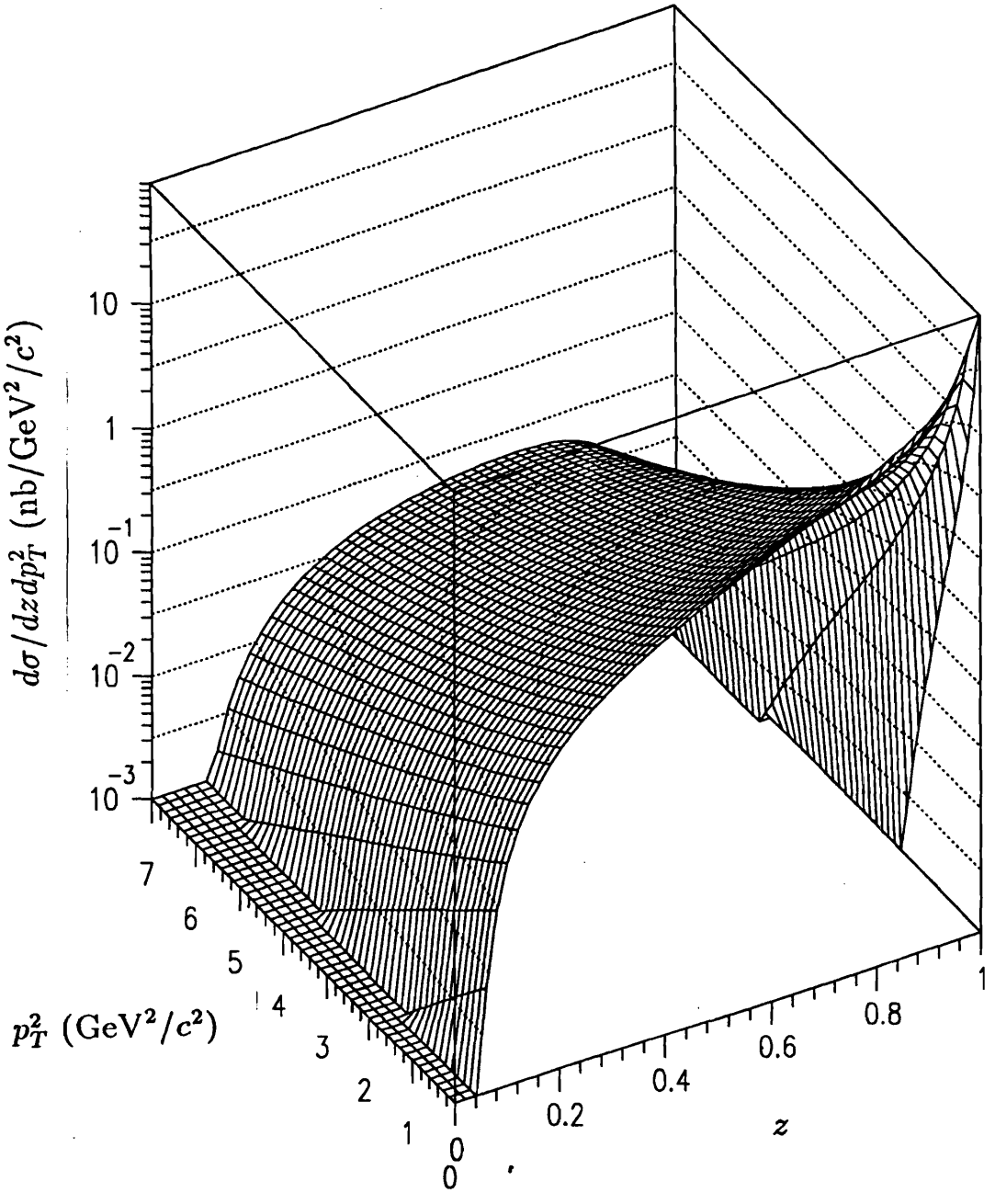

Figure 2.3: The z and p_T^2 dependence of the J/ψ cross section in the photon–gluon-fusion model for $E_\gamma = 145$ GeV and $n_g = 5$. The model is applicable over the kinematic region bounded by $z < 0.90$.

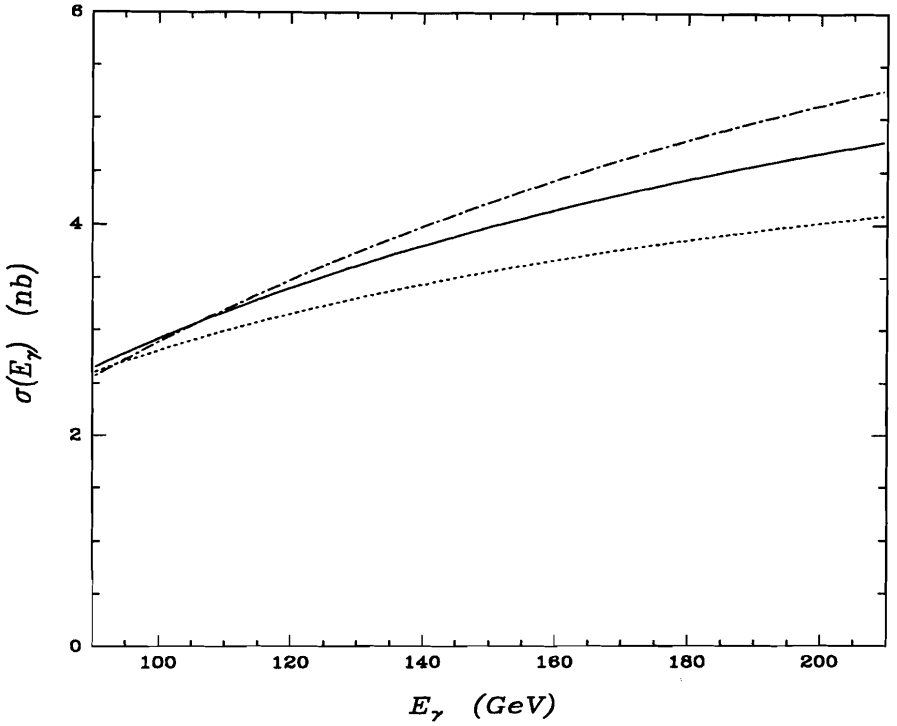

Figure 2.4: The incident photon energy dependence of the J/ψ cross section in the photon gluon fusion model for the three values of $n_g = 5$ $(\cdots)$, 7 (——) and 9 $(-\cdot-)$.

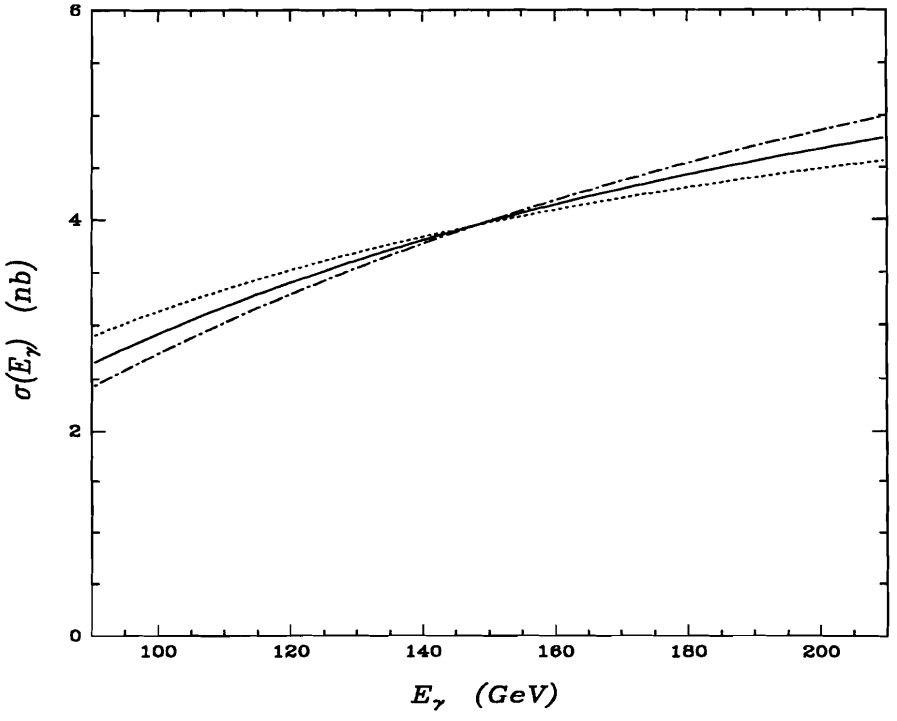

Figure 2.5: The above J/ψ cross section photon energy dependence curves all normalized to the $n_g = 7$ cross section to show only the change in the slope $d\sigma/dE_\gamma$ due to the variation in n_g.

$$\alpha_S(\mu^2 = 22\text{GeV}^2) \simeq 0.24 \tag{2.59}$$

As α_S varies logarithmically, it was taken to be a constant over the small accessible range of μ^2.

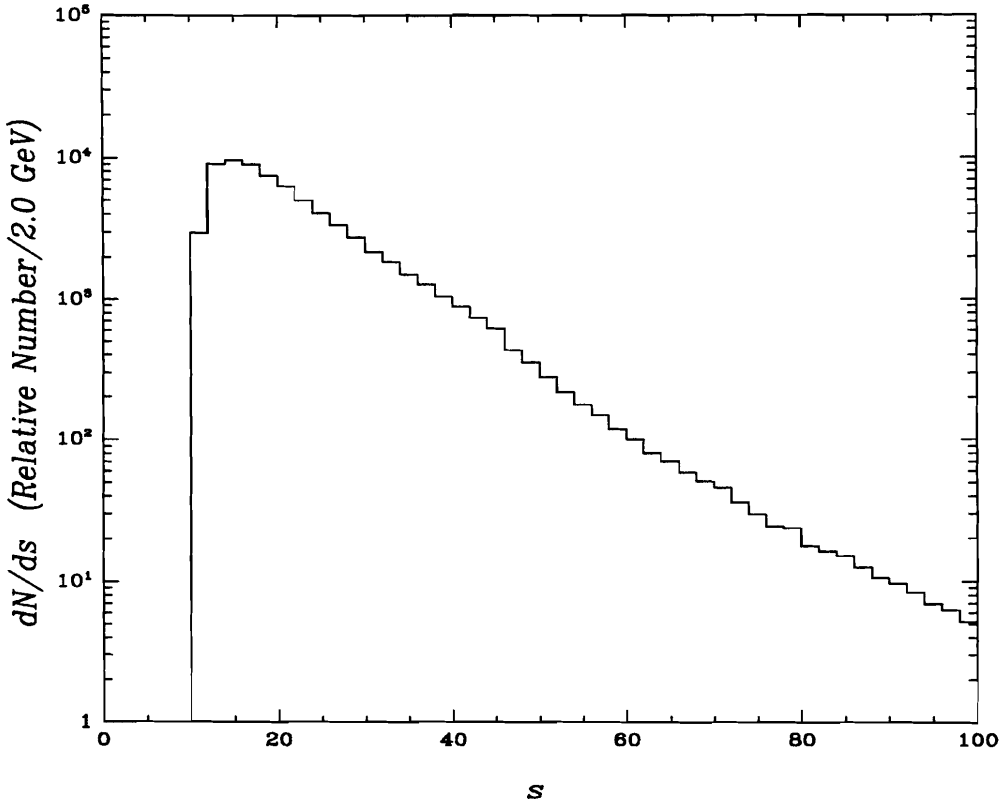

Figure 2.6: The Monte Carlo generated $\hat{s}$ distribution.

It is important to determine the region of phase space over which this model is valid. In deep inelastic lepton–nucleon scattering processes, for example,

$$eN \rightarrow eX \tag{2.60}$$

$$\nu N \rightarrow \mu X \tag{2.61}$$

the parton model is restricted to the region of phase space where the invariant mass

of the target nucleon fragments, $m_X^2 \equiv W^2$, is greater than $W_0^2 = 4$ GeV^2. For the $\gamma N \rightarrow J/\psi X$ process

$$\begin{aligned} m_X^2 &= \left[(1-x)p_N + g_2\right] \\ &= \left[\frac{(1-x)}{x} g1 + g2\right] \\ &= \frac{(1-x)}{x}\hat{t} \end{aligned} \tag{2.62}$$

and

$$\hat{t} = (1-z)\hat{s} = (1-z)xs. \tag{2.63}$$

At large s, using Equations 2.62 and 2.63, the restriction $m_X^2 > W_0^2$ gives

$$1 - z > \left(\frac{p_T^2 + W_0^2}{s}\right) \tag{2.64}$$

and z is bounded away from 1 as $p_T^2 \rightarrow 0$.

In lepton–nucleon deep inelastic scattering, the constituent parton densities are measured at a momentum scale set by the 4–momentum, Q^2, of the virtual γ, Z or W. The parton model is conventionally restricted to the region of phase space where the Q^2 of the virtual vector boson is greater than $Q_0^2 = 1$ GeV^2. The quantity analogous to Q^2 in deep inelastic $\gamma g_1 \rightarrow J/\psi g_2$ scattering is $|t|$.

Again, for large s, using Equations 2.56 and 2.63, the restriction $|t| > Q_0^2$ gives

$$1 - z > \left(\frac{Q_0^2 + p_T^2}{Q_0^2 + m_\psi^2}\right). \tag{2.65}$$

Thus the J/ψ colour–singlet photon–gluon–fusion model is applicable to the region of phase space within $z < 0.9$ (see Figure 2.3).

2.2.3 Elastic J/ψ Photoproduction from a Nuclear Target

As elastic J/ψ production is outside the region of phase space where PGF perturbation theory is valid, a QCD description does not as yet exist. The phenomenological vector–meson–dominance (VMD) model [Bau 78, Hol 85] along with the Glauber model of elastic hadron scattering [Gla 69] is used. The VMD model, shown in Figure 2.7, is based on the observation that the photon and the J/ψ vector meson have the same quantum numbers,

$$J^{PC} = 1^{--}. \tag{2.66}$$

Thus, there is an appreciable probability for a real photon to fluctuate into a virtual J/ψ^*. The virtual J/ψ^* scatters from the target nucleus, Be, or nucleon, N, via the exchange of a Pomeron. The Pomeron is postulated to have the quantum numbers of the vacuum

$$J^P = 0^+,\ I = 0,\ B = 0. \tag{2.67}$$

The 4-momentum transferred via the Pomeron puts the J/ψ^* on the mass shell, creating a real J/ψ.

To describe the coherent $J/\psi^* Be \rightarrow J/\psi Be$ and incoherent $J/\psi^* N \rightarrow J/\psi N, N^*$ elastic and quasi–elastic scattering the Glauber model of hadron elastic scattering from $A > 1$ nuclei is used. This model is an extension of optical diffraction theory. Normalizing the nuclear density function $\rho(x)$ to satisfy $\int \rho(x)\, dx = 1$, the nuclear form factor is then the Fourier transform of $\rho(x)$.

$$F(q^2) = \int e^{iq \cdot x} \rho(x)\, dx \tag{2.68}$$

If the amplitude for scattering from a single nucleon is $f(t)$ then, in the single scattering approximation, the intensity scattered coherently by the nucleus is

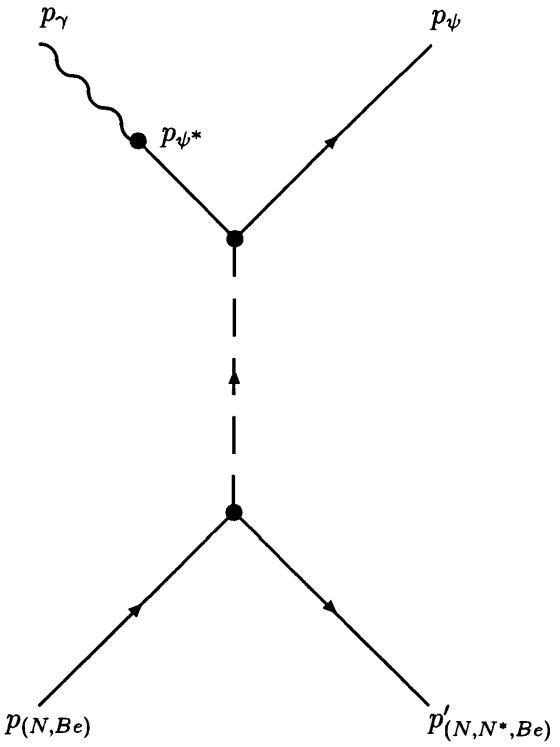

Figure 2.7: The Vector Meson Dominance amplitude for elastic J/ψ scattering. The scalar propagator is the Pomeron, having the quantum number of the vacuum, $J^P = 0^+$, $I = 0$, $B = 0$.

$$\left(\frac{d\sigma}{d\Omega}\right)_{coh.\ el.} \propto (\sigma_0)_{coh.\ el.} A^2 \, |f(t)|^2 \, |F(t)|^2 \tag{2.69}$$

where σ_0 is the coherent elastic cross section per nucleon. The nuclear amplitude $F(t)$ is responsible for the rapid decrease of the coherent elastic distribution with t and for the diffractive shape. When the J/ψ scatters from the nucleus as a whole it is not possible in principle to know which of the A nucleons was struck. The amplitudes for scattering by all the nucleons must be added coherently to form the nuclear scattering amplitude. That the entire volume of the nucleus contributes coherently to the scattering results in a forward peak in the angular distribution of the scattering. The coherent intensity is collimated within a narrow cone whose angle is of the order of the ratio of the incident particle wavelength to the nuclear radius.

The elastic collision between a hadron and nucleus produces a large number of final states, both bound and unbound, for the nuclear system. The momentum transferred to the nucleus in the collision is small relative to the incident J/ψ energy. To good accuracy the energies transferred may be ignored and the closure approximation may be invoked to sum the differential elastic cross sections corresponding to all possible nuclear final states. The incoherent elastic differential cross section is obtained by subtracting the coherent elastic cross section from the summed scattering. Continuing with the single scattering approximation and assuming that the nucleons are not significantly position correlated within the nucleus, the intensity scattered incoherently by a nucleon is

$$\left(\frac{d\sigma}{d\Omega}\right)_{incoh.\ el.} \propto (\sigma_0)_{incoh.\ el.} A\ |f(t)|^2[1 - |F(t)|] \tag{2.70}$$

where σ_0 is the incoherent elastic cross section per nucleon. In incoherent scattering, the final nuclear state is orthogonal to the initial nuclear ground state. It is not possible for a collision in the limit of t_{min} to induce such a transition; the scattering matrix element vanishes due to the orthogonality of the initial and final states. The incoherent scattering near the forward direction is correspondingly small and vanishes in the single scattering approximation at the limit $t \rightarrow t_{min}$.

A large body of hadron – nucleon elastic scattering data is well parametrized by the nucleon form factor

$$|f(t)|^2 = e^{bt} \tag{2.71}$$

in the small t region [Per 74]. Such a fit is usually good for $t \leq 0.5\ GeV^2/c^2$.

The beryllium nucleus has the proton configuration $(1s)^2(1p)^2$. From nuclear scattering of electrons it has been shown that for nuclei of the first p–shell a nuclear form factor

$$|F(t)| = \left[1 - \left(\frac{\alpha a_0^2 t}{4+6\alpha}\right)\right] \exp\left(\frac{a_0^2 t}{4}\right) \tag{2.72}$$

with $\alpha = (Z-2)/3$, derived from the independent–particle nuclear shell model with an infinite harmonic well, reproduces the experimental electron scattering data remarkably well [Hof 63]. For beryllium, with $Z = 4$ and $\alpha = 2/3$, the above nuclear form factor is

$$|F(t)| = \left(1 - \frac{a_0^2}{12} t\right) \exp\left(\frac{a_0^2 t}{4}\right) \tag{2.73}$$

If cylindrical symmetry about the beam axis is assumed, then the differential cross section is independent of ϕ and the t dependence of the cross section is related to the solid angle dependence by

$$\begin{aligned} \frac{d\sigma}{dt} &= \frac{\pi}{|\overrightarrow{p_\gamma}||\overrightarrow{p_\psi}|} \frac{d\sigma}{d\Omega} \\ &\simeq \frac{\pi}{E_\gamma^2} \frac{d\sigma}{d\Omega} \end{aligned} \tag{2.74}$$

In the elastic limit $z \rightarrow z_{max}$ for real photoproduction the 4–momentum transfer is well approximated by

$$t \simeq -p_T^2 \tag{2.75}$$

The dependence of the coherent elastic cross section on p_T^2 for scattering from a beryllium nucleus is

$$\begin{aligned} \left(\frac{d\sigma}{dp_T^2}\right)_{coh.\ el.} &\propto (\sigma_0)_{coh.\ el.} A^2 \frac{\pi}{E_\gamma^2} \exp\left(-bp_T^2\right) \left(1 + \frac{a_0^2}{12} p_T^2\right)^2 \exp\left(-\frac{a_0^2 p_T^2}{2}\right) \\ &\sim \left(\sigma_0 A^2\right)_{coh.\ el.} \frac{\pi}{E_\gamma^2} \exp\left(-ap_T^2\right) \end{aligned} \tag{2.76}$$

and the incoherent elastic p_T^2 differential cross section for scattering from a constituent nucleon in the beryllium nucleus is

$$\left(\frac{d\sigma}{dp_T^2}\right)_{incoh.\ el.} \propto (\sigma_0)_{incoh.\ el.} A\frac{\pi}{E_\gamma^2}\exp\left(-bp_T^2\right)\left[1-\left(1+\frac{a_0^2}{12}p_T^2\right)\exp\left(-\frac{a_0^2p_T^2}{4}\right)\right] \quad (2.77)$$

The 4–momentum conservation equations for elastic scattering are

$$p_\gamma + p_{Be} = p_\psi + p'_{Be} \quad \text{coherent elastic} \quad (2.78)$$

$$p_\gamma + p_N = p_\psi + p'_N \quad \text{incoherent elastic} \quad (2.79)$$

$$p_\gamma + p_N = p_\psi + p'_{N^*} \quad \text{incoherent quasi–elastic} \quad (2.80)$$

Energy and momentum conservation constrains z and p_T^2. Thus, for a fixed E_γ, there is only one independent variable, z or p_T^2. This constraint is is well approximated (to second order) by

$$z \simeq 1-\frac{p_T^2}{2m_{(N,Be)}E_\gamma}-\frac{1}{8m_{(N,Be)}E_\gamma^3}(p_T^2+m_\psi^2)^4 \quad (2.81)$$

$$z_{max} \simeq 1-\frac{m_\psi^4}{8m_{(N,Be)}E_\gamma^3} < 1 \quad (2.82)$$

For $\langle E_\gamma\rangle = 145$ GeV and $\langle p_T^2\rangle_{coh.el.} \sim 0.07$ GeV$^2/c^2$,

$$\langle z\rangle_{coh.el.} > 0.99 \quad (2.83)$$

and for $\langle p_T^2\rangle_{incoh.el.} \sim 0.6$ GeV$^2/c^2$,

$$\langle z\rangle_{incoh.el.} > 0.99 \quad (2.84)$$

Thus, elastic J/ψ photoproduction is well separated in z from deep inelastic J/ψ photoproduction.

2.3 Fragmentation

In the photon–gluon centre–of–mass frame the charm and anticharm quarks have opposite momenta. One can picture the strong field between the $c\bar{c}$ pair semi–classically as compressed into a colour flux tube or string due to the three gluon coupling. The potential energy of the c string $\bar{c}$ system is modelled by

$$V(r) = -\frac{4}{3}\frac{\alpha_S^2}{r} + \kappa r \tag{2.85}$$

where the string energy density, κ, has been determined to be about 0.2 GeV/fm by fitting to the experimental charmonium and bottomonium spectroscopy data. Thus the first term in Equation 2.85 is the QCD analogue to the electrostatic QED potential while the second linear term parametrizes the empirical observation of parton confinement within colour neutral hadrons.

For open–charm production, the $c\bar{c}$ pair moves apart increasing the potential energy of the system by stretching the string until there is enough energy available to create one or more new $q\bar{q}$ pairs ($u\bar{u}$, $d\bar{d}$ *or* $s\bar{s}$) from the vacuum. The c quark combines with such an antiquark $\bar{u}, \bar{d}$ or $\bar{s}$ to produce a D meson and the $\bar{c}$ quark combines with a u or d to form a $\bar{D}$ meson, with the remaining $q\bar{q}$ pairs typically combining to form pions and kaons. This process is referred to as fragmentation or hadronization. The one or more soft (low momentum) gluons radiated by the $c\bar{c}$ system are reabsorbed by the target fragments to make the entire system colour neutral. The scaling function $f(z)dz$ represents the probability to find a hadron containing the original quark q_0 carrying a fraction between z and $z+dz$ of $W = (E+p_{\|})_{\text{quark}}$. Thus

$$z \equiv \frac{(E + p_{\parallel})_{\text{hadron}}}{(E + p_{\parallel})_{\text{quark}}} \tag{2.86}$$

where $\parallel$ is defined by the initial direction of motion of q_0.

A string fragmentation model has been developed by the LUND group [And 83, Sjo 84] and has been implemented as a Monte Carlo package [Sjo 85] where an initial $q_0\bar{q}_0$ pair is fragmented iteratively according to the left–right symmetric scaling function

$$f(z) = N\frac{1}{z}(1-z)^a \exp\left(-\frac{bm_\perp}{z}\right) \tag{2.87}$$

$m_\perp^2 = m_q^2 + p_T^2$ is the transverse mass and the a and b parameters are determined from experiment. The origin of the exponential component is the probability for the vacuum $q\bar{q}$ pair to tunnel outside the linear colour flux tube with a given p_T^2. Thus fragmentation induces a smearing of the initial charm quark 4–momenta in open–charm production.

The string fragmentation model has several conceptual advantages over the independent fragmentation (IF) model [Fie 78]. In the IF model the two initial quarks, $q_0\bar{q}_0$, do not interact via any QCD based mechanism, such as a string, and thus fragment independently of one another. Thus in the IF model, unlike the string model, 4–momentum is not naturally conserved.

With respect to fragmentation, deep inelastic J/ψ production is qualitatively different from open–charm production. The c and $\bar{c}$ quarks form a colour–singlet bound state instead of binding with the $\bar{q}$ and q from the vacuum. Thus, *unlike open–charm production, the initial J/ψ 4–momentum is not smeared via fragmentation.* To form the bound $c\bar{c}$ state in J/ψ production one of the charm or anticharm quarks must radiate a sufficiently hard (large momentum) gluon such that the probability of the overlap of the charm and anticharm wavefunctions is appreciable for bound state formation (see Figure 2.2). The radiated gluon recombines with the nucleon target partons and this system fragments into a hadron shower denoted by X. Thus colour

is conserved and the overall final state, $J/\psi X$, is colour neutral as was the overall initial state, γN.

In the LUND string model a gluon is treated as a kink, or a transverse excitation, of the colour force field tube between a quark and an antiquark. A one–dimensional linear force field can be generalized, in a relativistic manner, to three dimensions by the dynamics of the massless relativistic string [Art 83]. On such a string it is possible for a pointlike part (away from the endpoints) to carry energy and momentum. Such a localization, a kink, moves with the velocity of light and is pulled back by the string with a force which is twice as strong as the one acting on a endpoint quark. The kink thus acts much like a gluon.

Chapter 3

The Tagged Photon Experiment E691

3.1 Overview

Experiment E691 was performed during 1985 at the Tagged Photon Spectrometer of the Fermi National Accelerator Laboratory (Batavia, Illinois). A diagram of the experiment is shown in Figure 3.1 A photon beam, with a bremsstrahlung energy spectrum from 80 GeV to 250 GeV, was directed at the beryllium target. Immediately downstream of the target was the high resolution silicon microstrip detector (SMD) consisting of 9 50 μm pitch silicon microstrip planes. The SMD enabled the reconstruction algorithm to separate the primary interaction vertex from the downstream open–charm decay vertex on an event–by–event basis. This reduced the combinatoric background in the open–charm reconstruction by a factor of about 300 to 500. Following the SMD was a fully instrumented downstream spectrometer consisting of 35 drift chamber planes, 2 momentum analyzing magnets, 2 threshold Cherenkov counters, electromagnetic and hadronic calorimeters followed by a hadron absorbing steel wall and a back wall of segmented scintillation counters to detect muons, the back muon wall. A summary of the Tagged Photon Spectrometer is contained in this chapter while a detailed description may be found in Appendix E and references therein.

It is important for the study of the production dynamics to have an unbiased trigger. Yet, it is also necessary to reduce the high rate of non–charm events. For the J/ψ production, a dimuon trigger was chosen utilizing the segmentation of the threshold Cherenkov counters and back muon wall to provide a fast signal for the presence of a $\mu\mu$ pair in an event. For the open–charm production, a global transverse energy trigger E_T was chosen utilizing the segmentation of the electromagnetic and hadronic calorimeters to provide a fast measure of the transverse energy for hadronic events. During the run about 100 million photoproduced events were recorded of which about 2.5 million fired the dimuon trigger.

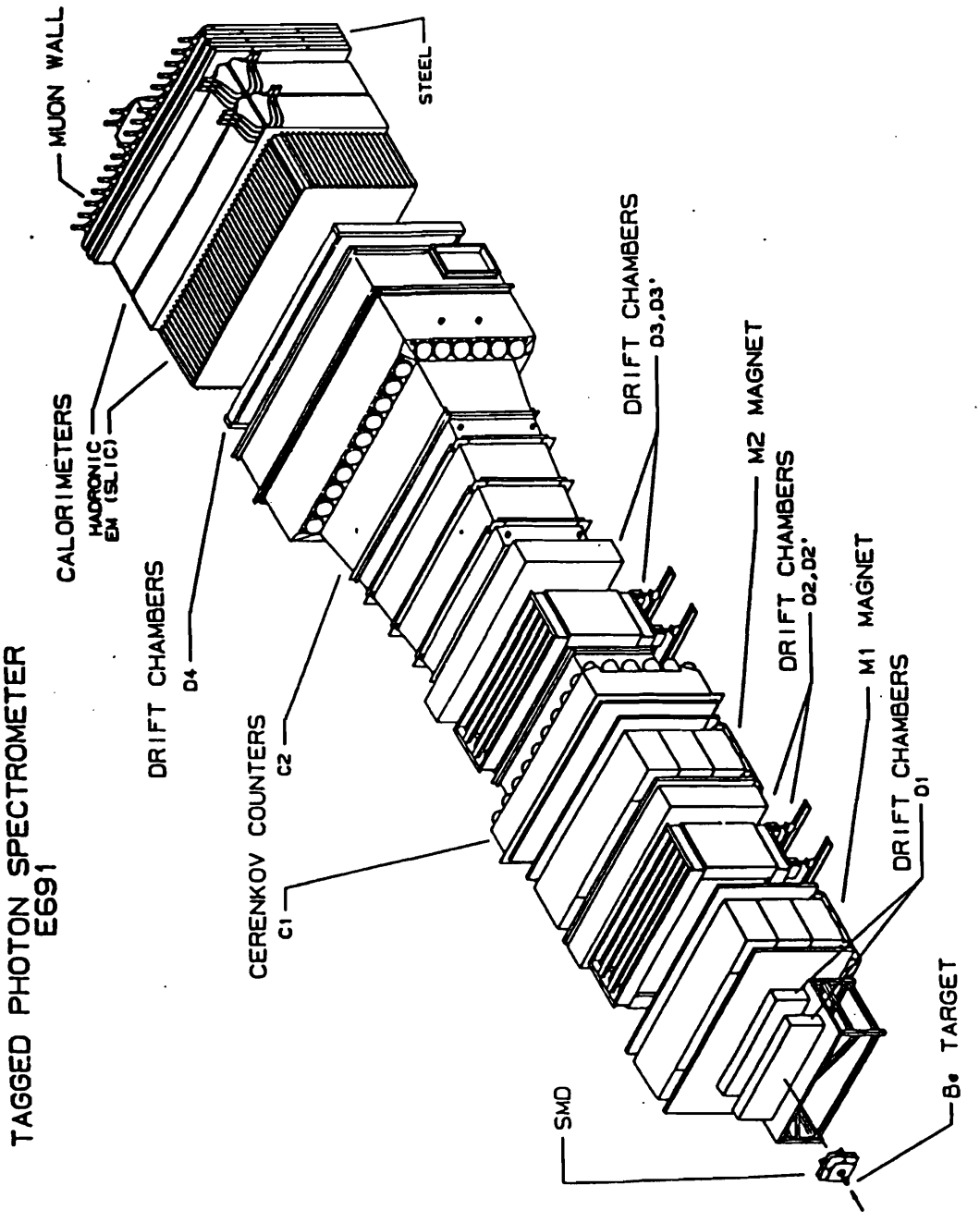
TAGGED PHOTON SPECTROMETER
E691
MUON WALL
STEEL
CALORIMETERS
HADRONIC
EM (SLIC)
DRIFT CHAMBERS
D4
CERENKOV COUNTERS
C2
C1
DRIFT CHAMBERS
D3,D3'
M2 MAGNET
DRIFT CHAMBERS
D2,D2'
M1 MAGNET
DRIFT CHAMBERS
D1
SMD
Be TARGET

Figure 3.1:

3.2 The Tagged Photon Beam, the Target and the B Counter

The FNAL TEVATRON accelerator, shown in Figure 3.2 provides a high energy 800 GeV proton beam to numerous beamlines for fixed target physics. In the PROTON area, the proton beam is split vertically into three beams which are then bent vertically into the PWest, PCentre and PEast beam lines. The Tagged Photon Lab is located on the PE beamline. This beamline receives typically 2×10^{12} protons per spill.

The PE primary beam is used to produce a secondary electron beam of known energy. The 800 GeV proton beam is directed onto a 30 cm long beryllium primary target to produce both charged and neutral secondary particles. Only the neutrals exit from the target box, the charged secondaries are swept out by a magnet to a beam dump. The neutral secondary beam (consisting primarily of neutrons, K_L^0 and photons from π^0 decays) strikes a 0.75 radiation length lead converter 12 metres downstream. Approximately 40% of the photons produce e^-e^+ pairs in the converter, while only 1.5% of the neutrons and kaons produce hadrons, mainly pions. The secondary beam then enters the electron transport system, a two–stage beam line. Each line consists of of a set of quadrupole magnets to focus the charged beam , a set of dipole magnets to bend the beam and vertical and horizontal collimators to select a momentum interval. In the first stage, the undeflected neutral hadrons and photons pass into a beam dump. The beamline can then be tuned to transport an electron beam with momentum from 10 GeV to 300 GeV. The momentum bite of the beam is about 3.4%. The momentum selection reduces the electron beam hadronic contamination, consisting predominantly of π^-, to less than 2%. During the E691 run, the beam was tuned to 250 GeV. The 250 GeV electron yield per 800 GeV proton was measured to be about $e/p = 2.6 \times 10^{-5}$. During optimum accelerator performance about 5% of the buckets contained electrons. This gave 5×10^7 electrons per spill. About 1/2% of the buckets contained 2 or more electrons.

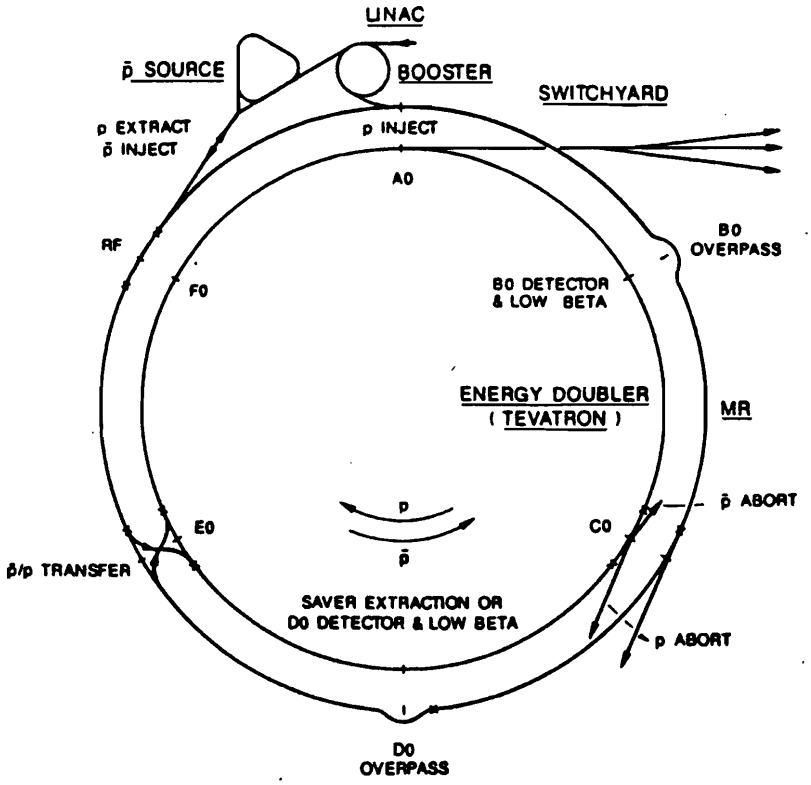

Figure 3.2: The FNAL accelerator. The acceleration is accomplished in five stages. Protons are accelerated to 750 keV in the Cockcroft–Walton, to 200 MeV in the LINAC and to 8 GeV in the Booster (synchrotron) Ring before injection into the Main (synchrotron) Ring (MR). The MR operates as a 150 GeV injector for the 800 GeV superconducting magnet TEVATRON synchrotron.

The momentum selected electron beam was used to produce a photon beam with a bremsstrahlung energy spectrum. The electrons strike a 0.2 radiation length tungsten radiator. On average, every electron produces 0.183 photons with an energy above 80 GeV. The integrated luminosity for the run was 1.5×10^{12} photons. In the thin radiator approximation, the photon spectrum is given by

$$N(k)dkdx = \frac{dk}{k}\left[\frac{4}{3} - \frac{4}{3}\left(\frac{k}{E_e}\right) + \left(\frac{k}{E_e}\right)^2\right] \tag{3.1}$$

where $N(k)$ is the number of photons within the energy interval $k + dk$, dx is the

radiator thickness in radiation lengths and E_e is the incident electron beam energy. The radiator thickness was determined by the need to maximize the photon flux while keeping pair production and multiple bremsstrahlung down to an acceptably low level. A Monte Carlo was written to do a QED simulation of the electron beam bremsstrahlung. This simulation took into account the finite radiator thickness, Z dependence and inclination (with respect to the electron beam), multiple electron bremsstrahlung and pair production. The photon energy spectrum from 80 GeV to 250 GeV is shown in Figure 3.3.

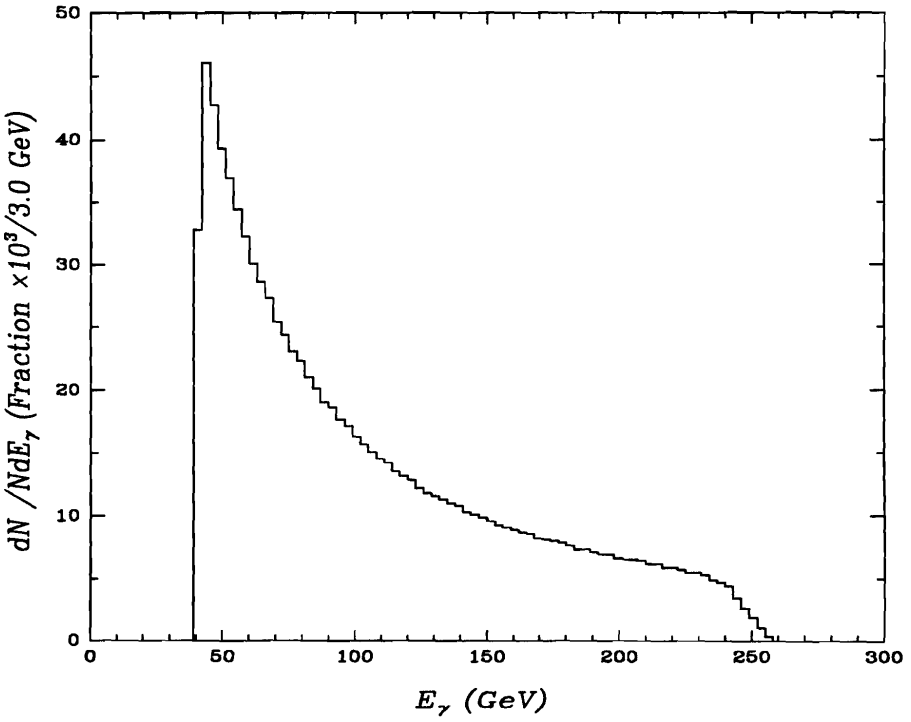

Figure 3.3: The photon energy spectrum from the bremsstrahlung of a 250 GeV electron beam on a 0.2 radiation length radiator.

After the radiator, the electron–photon beam passes through a set of dipole magnets which horizontally bend the electrons, leaving a photon beam which enters the Tagged Photon Lab. Electrons that radiate are bent into the tagging system and the rest go into a beam dump.

A schematic of the tagging system is shown in Figure 3.4. The tagging system

was used to measure the electron energy E'_e after bremsstrahlung and thereby tag the photon energy $E_{\gamma\ tag}$

$$E_{\gamma\ tag} = E_e - E'_e \tag{3.2}$$

The tagging system consisted of 8 lead–lucite (L1 through L8) and 5 lead–glass (L9 through L13) shower counters.

The electron momentum acceptances of the shower counters are listed in Table 3.1.

Table 3.1: The electron momentum acceptance of the tagging system shower counters.

Shower Counter	p'_e Momentum Acceptance (GeV)
L1	181 – 156
L2	156 – 129
L3	129 – 109
L4	109 – 95
L5	95 – 83
L6	83 – 75
L7	75 – 70
L8	70 – 64
L9	64 – 57
L10	57 – 52
L11	52 – 47
L13	42 – 31

The tagging system smearing was parametrized using elastic ρ production. In

$$\gamma Be \rightarrow \rho Be \rightarrow \pi^+\pi^- Be \tag{3.3}$$

the photon converts into the ρ with negligible energy transfer to the beryllium nucleus. The tagging system resolution as a function of photon beam energy is listed in Table 3.2.

The relative photon flux as measured by the tagging system and corrected for smearing is shown in Figure 3.5.

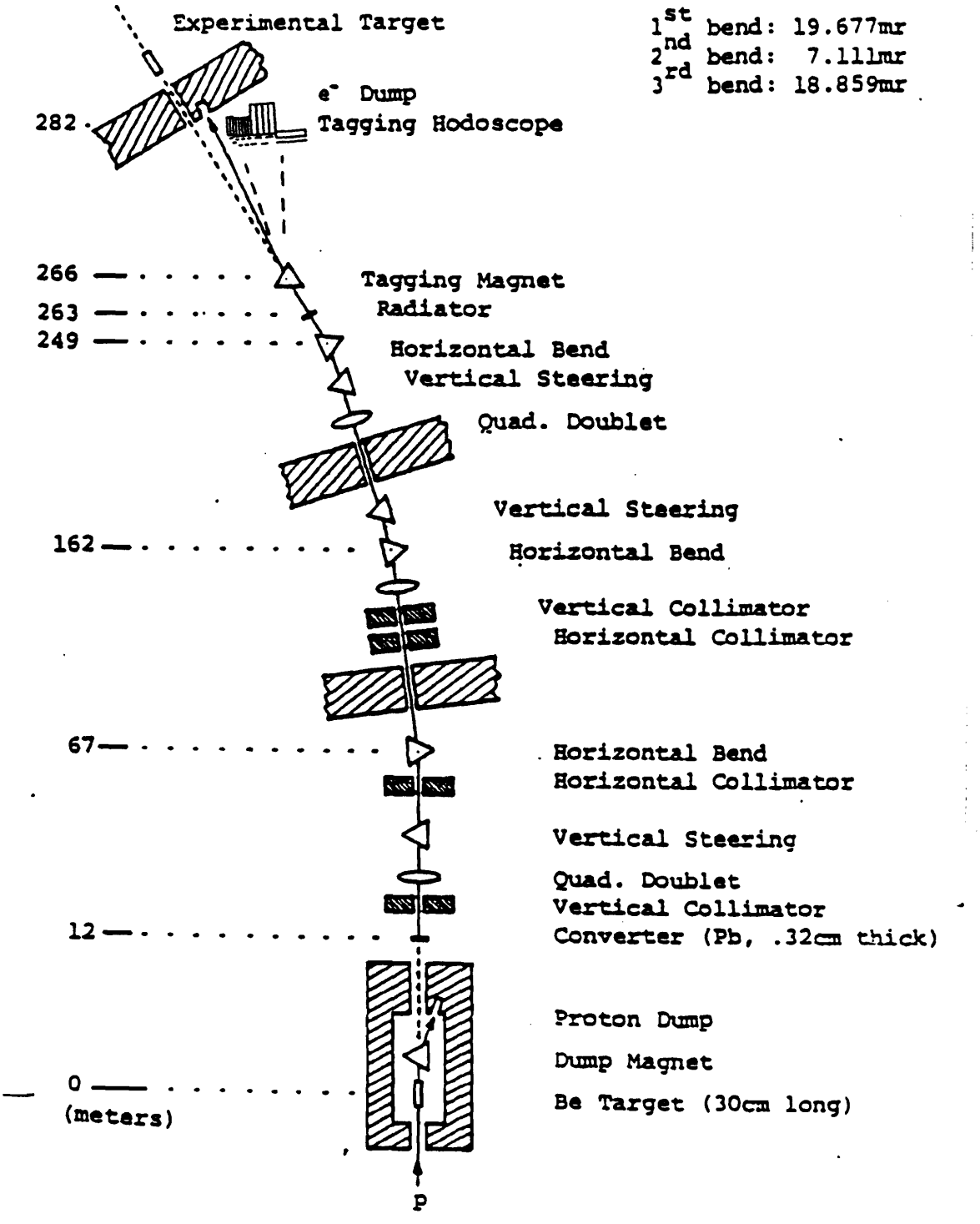

Figure 3.4: The E691 beamline and tagging system.

Table 3.2: The elastic ρ parametrization of the tagging system resolution.

E_γ (GeV)	$< E_{\gamma\ tag} - E_\rho >$ (GeV)	$\sigma(E_{\gamma\ tag} - E_\rho)$ (GeV)	$\sigma/E_{\gamma\ tag}$ (%)
100 – 110	8.39	32.2	30.7
110 – 120	6.03	30.1	26.2
120 – 130	3.13	27.4	21.9
130 – 140	1.13	25.8	19.1
140 – 150	-3.09	23.9	16.5
150 – 160	-3.89	23.0	14.8
160 – 170	-5.67	21.5	13.0
170 – 180	-8.90	20.1	11.5
180 – 190	-10.7	18.6	10.1
190 – 200	-13.2	17.9	9.2

A compact target was required in order to utilize the open–charm decay vertex resolving capability of the SMD. The target also had to maximize the ratio of hadronic interactions (including charm events) with respect to e^+e^- pair production background. The beryllium target optimized these dialectic requirements. It had a 1.905×1.905 cm^2 cross-section (large enough to contain the beam spot) and was 5.08 cm long. This length corresponded to 0.142 radiation lengths and 0.123 nuclear interaction lengths.

The target was immediately followed by an interaction counter called the B counter, a required component of all the physics triggers. The B counter was a 2.54 cm wide, 2.54 cm high and 0.159 cm thick strip of plastic scintillator. The discriminator threshold of the B counter was set between the one charged track and two charged track signal levels. The threshold was set below the two charged track signal level so as to accept muon pairs from J/ψ decays. The B counter was a component of both the dimuon and E_T triggers.

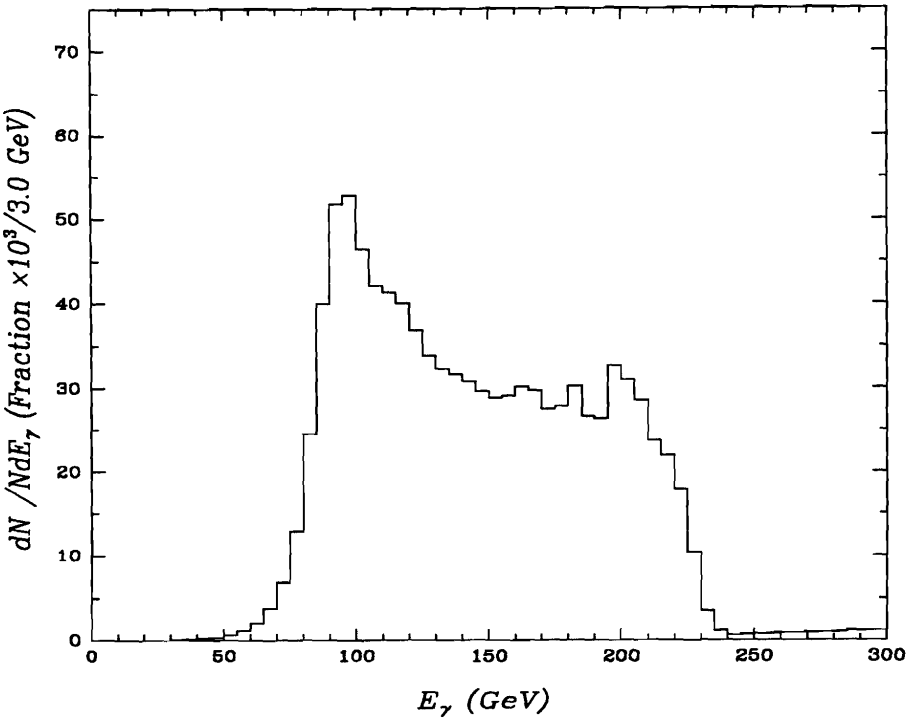

Figure 3.5: The smearing corrected flux distribution of photons accepted by the tagging system.

3.3 Vertex Identification in the Primary Interaction Region

For a 145 GeV photon beam, the energy of a forward D meson is typically greater than 50 GeV giving a mean decay path $\gamma c\tau$ in the lab of several millimetres. Therefore a vertex detector with a two–vertex resolution of several hundred microns was required. The E691 silicon microstrip detector (SMD) met this criteria, revolutionizing fixed–target open–charm physics [Raa 88].

The $c\tau$ values of the J/ψ, D^0, D^+ and D_S^+ are (2.91×10^{-9}) microns, 126 microns, 318 microns and 133 microns. Thus, unlike the open–charm production, the J/ψ vertex obviously cannot be separated from the primary production vertex. Primary interaction region vertexing, which was essential for the extraction of the open–charm

signal by resolving between the (primary) production vertex and the charm decay (secondary) vertex, was of no use in obtaining the J/ψ signal. With respect to the J/ψ analysis, the SMD was useful only by providing additional space points for the track reconstruction. The background in the $\mu^+\mu^-$ channel was quite small in the large invariant J/ψ mass region enabling the signal to be obtained by a series of simple cuts.

3.4 Charged Track Momentum Measurement

Two large aperture copper coil magnets were used to bend the charged particle paths in order to measure their momenta. These analyzing magnets, M1 and M2, gave a charged particle a p_T kick of 0.29 GeV/c and 0.32 GeV/c, respectively. The magnetic fields were in the $-y$ direction and bent positive charged particles in the $+x$ direction (towards the right side of the spectrometer looking downstream).

The charged particle tracking and momentum analysis was performed using the SMD and the four drift chamber (DC) stations (D1, D2, D3 and D4) consisting of 35 planes. These planes were grouped into assemblies, an assembly being a set of planes which completely determines the (x, y, z) co-ordinates of a single point on a charged particle trajectory. The time information could not differentiate as to whether the charge cloud drifted to a sense wire from the right–hand or left–hand side. To resolve this left–right ambiguity, two planes U and V tilted $\mp 20.5°$ with respect to the vertical (looking downstream) were used. These three planes formed a D2, D3 or D4 UXV triplet assembly. In D1 an additional X′ plane, identical to the X plane but offset by half a cell, was added to help resolve the right–left ambiguities in the highest track density region. These four planes formed a XX′UV quadruplet assembly.

The momentum resolution for a particle trajectory bent by a magnetic field is

$$\frac{\Delta p}{p} = \frac{\Delta \theta}{\theta} \tag{3.4}$$

with

$$\theta = \frac{p_T}{p} \tag{3.5}$$

$$\Delta\theta = \frac{\Delta x}{l} \tag{3.6}$$

Δx is the uncertainty in the displacement of the trajectory along the horizontal and l is the length over which the measurement is made, the lever arm. As more chambers are used or the length of the lever arm is increased Δx decreases. For the approximation of N equally spaced chambers each with a position resolution δ_x

$$\sigma(\theta) = \frac{\delta_x}{l}\sqrt{\frac{12}{N}} \tag{3.7}$$

For two sets of chambers, one upstream and one downstream of the the analyzing magnet, the total angular resolution is

$$\delta\theta = \sqrt{\sigma^2(\theta_d) + \sigma^2(\theta_u)} \tag{3.8}$$

giving a momentum resolution

$$\frac{\Delta p}{p} = \frac{\delta\theta p}{p_T} \simeq \frac{p}{q\int B \cdot dl}\sqrt{12\left(\frac{\delta_d^2}{N_d l_d^2} + \frac{\delta_u^2}{N_u l_u^2}\right)} \tag{3.9}$$

The p_T kick is given by $q\int B \cdot dl$ where the elementary charge q is 0.2998 GeV/Tm. For D2, D3 and M2, l = 118.5 cm and N = 12 giving $\Delta p/p \simeq 0.1\%\ p$ (GeV). For one magnet (M1) tracks the resolution was measured to be $\Delta p/p \simeq 0.1\%\ p\ + 0.5\%$ and for two magnet (M1 and M2) tracks the resolution was measured to be $\Delta p/p \simeq 0.05\%\ p\ + 0.5\%$. The second constant term is the multiple Coulomb scattering contribution.

At high energies, $E \simeq p \gg m$, the mass resolution is determined by the momentum resolution. For a two–body decay (m_1, m_2) of a particle of mass M

$$M^2 = m_1^2 + m_2^2 + 2E_1E_2 - 2p_1p_2\cos\theta \quad (3.10)$$

$$\simeq m_1^2 + m_2^2 + p_1p_2\theta^2 \quad (3.11)$$

In a fixed target experiment, the lab opening angle θ is small so $\cos\theta \simeq 1 - \theta^2/2$ giving the invariant mass approximation of Equation 3.11. Thus the experimental mass resolution is well approximated by

$$\frac{\Delta M}{M} \simeq \frac{1}{2}\sqrt{\left(\frac{\Delta p_1}{p_1}\right)^2 + \left(\frac{\Delta p_2}{p_2}\right)^2 + 4\left(\frac{\Delta\theta}{\theta}\right)^2} \quad (3.12)$$

The E691 mass resolution was measured to be 27 MeV for $J/\psi \rightarrow \mu^+\mu^-$ and 10.3 MeV for $D^0 \rightarrow K^-\pi^+$.

3.5 Charged Hadron Identification

Two gas–filled Cherenkov threshold detectors, C1 and C2, were used to distinguish between the charged π, K and p hadrons. The upstream counter, C1, was located behind and partly inside the second analyzing magnet M2 and the downstream counter, C2, was located behind the third drift chamber station D3 [Bar 87].

The half–angle θ_C of the Cherenkov light cone for a particle with velocity β in a medium with index of refraction n is

$$\theta_C = \cos^{-1}\left(\frac{1}{n\beta}\right) \quad (3.13)$$

giving a threshold velocity $\beta_t = 1/n$ for Cherenkov light production. The number of Cherenkov photons, N_γ, produced per interval of path length is

$$\frac{dN_\gamma}{dl} = 2\pi\alpha\int\left[1 - \frac{1}{\beta^2 n^2(\lambda)}\right]\frac{d\lambda}{\lambda^2} \quad (3.14)$$

where λ is the emitted photon wavelength.

Table 3.3 lists whether Cherenkov light is emitted, C, or not, $\overline{C}$, for a particle in a given momentum interval. In the 20 – 36 GeV momentum interval pions, kaons and protons are uniquely identified as the two counter combinations are distinct for each of these three particles.

Table 3.3: C1 and C2 threshold counter states for charged particle momentum ranges.

Momentum (GeV/c)	$\pi^{\pm}$	$K^{\pm}$	$p^{\pm}$	$e^{\pm}$ or $\mu^{\pm}$
0 – 6	$\overline{C}_1 \cdot \overline{C}_2$	$\overline{C}_1 \cdot \overline{C}_2$	$\overline{C}_1 \cdot \overline{C}_2$	$C_1 \cdot C_2$
6 – 9	$C_1 \cdot \overline{C}_2$	$\overline{C}_1 \cdot \overline{C}_2$	$\overline{C}_1 \cdot \overline{C}_2$	$C_1 \cdot C_2$
9 – 20	$C_1 \cdot C_2$	$\overline{C}_1 \cdot \overline{C}_2$	$\overline{C}_1 \cdot \overline{C}_2$	$C_1 \cdot C_2$
20 – 36	$C_1 \cdot C_2$	$C_1 \cdot \overline{C}_2$	$\overline{C}_1 \cdot \overline{C}_2$	$C_1 \cdot C_2$
36 – 38	$C_1 \cdot C_2$	$C_1 \cdot C_2$	$C_1 \cdot \overline{C}_2$	$C_1 \cdot C_2$
38 – 69	$C_1 \cdot C_2$	$C_1 \cdot C_2$	$C_1 \cdot \overline{C}_2$	$C_1 \cdot C_2$
69 – ∞	$C_1 \cdot C_2$	$C_1 \cdot C_2$	$C_1 \cdot C_2$	$C_1 \cdot C_2$

The two detectors each contained a set of primary mirrors, 28 in C1 and 32 in C2. Each mirror focussed and reflected the Cherenkov light into a Winston cone. The Winston cones were used to collect the light from the primary mirrors and transmit it to the phototubes. The partial insertion of C1 into M2 made it necessary to collect the light from the downstream end of the counter. A set of secondary plane mirrors was used to reflect the light from the primary mirrors to the downstream Winston cones.

Both sets of primary mirrors possessed quadrant symmetry with each C1 quadrant containing seven mirrors and each C2 quadrant containing eight mirrors. The layouts of the C1 and C2 primary mirrors are shown in Figures 3.6 and 3.7. These C1 and C2 mirror segmentations were an optimization of these two opposing constraints, that the light from a single particle be completely collected in a single mirror and that the number of Cherenkov rings overlapping at a mirror be minimal.

Both C1 and C2 were components of the dimuon trigger.

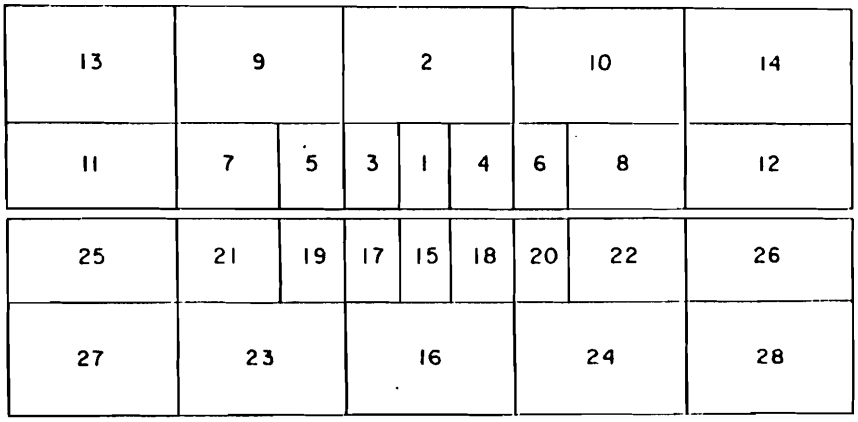

Figure 3.6: The C1 primary mirror segmentation.

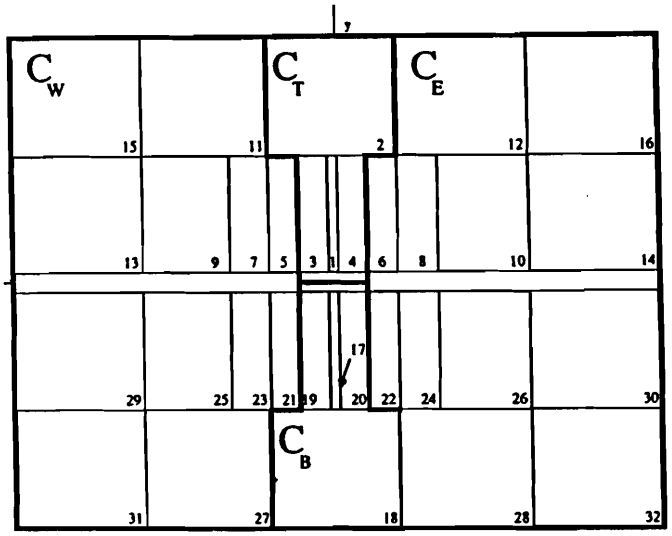

Figure 3.7: The C2 mirror segmentation.

3.6 Electron and Photon Identification

The electromagnetic calorimeter, the Scintillator Lead Interleaved Calorimeter (SLIC) [Bha 85], was used to measure the energy, position and direction of electromagnetic showers produced by photons, electrons and positrons. Shower centroids were resolved to about 3 mm and had a fractional energy resolution of about $21\%/\sqrt{E}$ (GeV). Mass resolutions were typically 8 MeV/c^2 and 12 MeV/c^2 for K^0_Ss and π^0s. The SLIC was also used in conjunction with the hadronic calorimeter, situated immediately downstream, to detect hadronic showers produced by neutral hadrons. A particle travelling parallel to the z–axis penetrated 21.5 radiation lengths and 2.07 interaction lengths of material. Both the SLIC and the hadronic calorimeter were used in the global transverse energy (E_T) trigger.

3.7 Neutral Hadron Identification

The hadronic calorimeter, the Hadrometer [App 86], was designed to measure that part of the energy from hadronic showers that was not measured by the SLIC. Less than 1% of the energy of electromagnetic showers from the SLIC reached the Hadrometer. The Hadrometer had a fractional energy resolution of about $75\%/\sqrt{E}$ (GeV) and an intrinsic position resolution less than 5 cm. With the broad with and large energy fluctuations characteristic of hadronic showers, the Hadrometer did not provide useful energy and angle measurements of neutral hadrons in multiparticle events. Thus the Hadrometer reconstruction information was mainly used as an additional constraint for the SLIC reconstruction. An electromagnetic shower deposits virtually all its energy in the SLIC. Thus a large signal in the Hadrometer indicated that the shower was hadronic and not electromagnetic in origin. The Hadrometer was also a component, along with the SLIC, of the total hadronic cross-section trigger ($B \cdot H$) and the global transverse energy (E_T) trigger.

3.8 Muon Identification

A plane of segmented scintillation counters, the back muon wall, was located downstream of the Hadrometer. It was designed to primarily detect $\mu^+\mu^-$ pairs from J/ψ decays. Situated between the Hadrometer and the muon wall was a 1.22 m thick wall of steel. The steel wall together with the steel in the Hadrometer constituted 13.12 interaction lengths parallel to the z–axis. This was sufficient to absorb and range out almost all the particles from hadronic showers. Thus the particles that penetrated all the way through the steel wall were primarily muons. The minimum momentum for muons to pass through the calorimeters and the steel wall was about 3 GeV.

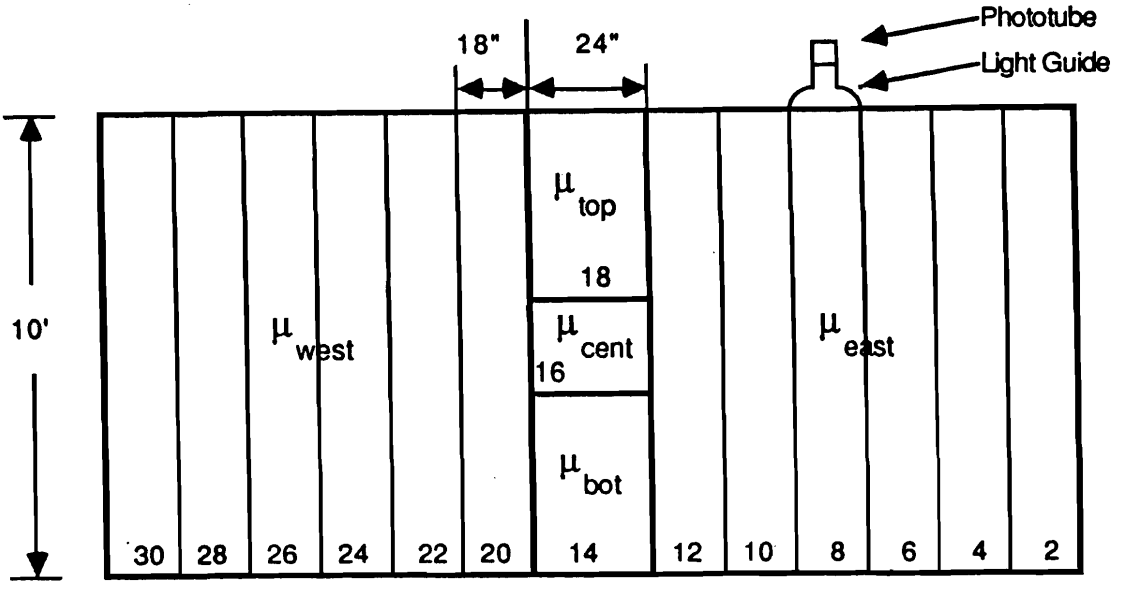

Figure 3.8: The Back Muon Wall.

3.9 Tagged Photon Spectrometer Summary

A schematic of the E691 Tagged Photon Spectrometer is shown in Figure 3.9 and a summary of the detector parameters is given in Table 3.4

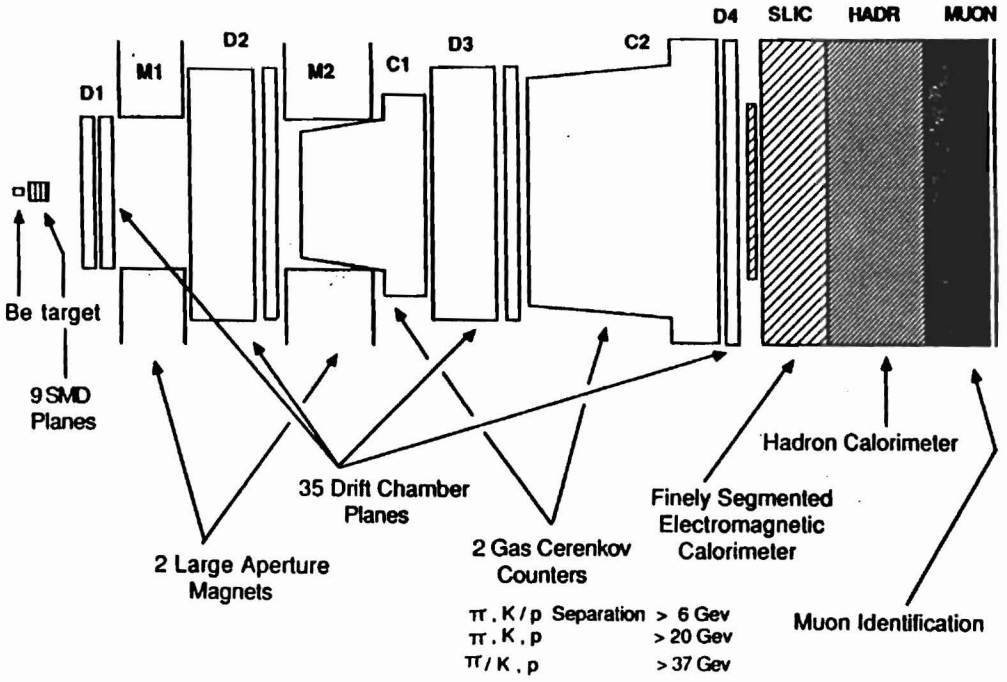

Figure 3.9: A schematic diagram of the E691 Tagged Photon Spectrometer.

Table 3.4: A summary of the Tagged Photon Spectrometer detector parameters.

Detector Component	z Position (cm)	Active Area $x \times y$ (cm)^2	Resolution
Target upstream downstream	-5.8 -0.8	1.25 × 2.5	
B counter	0.0	2.5 × 2.5	
SMD–1 SMD–2 SMD–3	3.0 11.3 20.3	2.6 × 2.6 5.0 × 5.0 5.0 × 5.0	16 μm
D1–A D1–B	156.0 192.0	86. × 65. 114. × 65.	350 μm
M1 (centre)	286.6	174. × 86.	$\Delta p/p \sim 0.1\%p$
D2 – 1 D2 – 2 D2 – 3 D2 – 4	384.0 426.0 468.0 499.0	182. × 130. 182. × 130. 210. × 130. 228. × 130.	300 μm
M2 (centre)	620.6	171. × 88.	$\Delta p/p \sim 0.05\%p$
C1 mirror plane	866.0	250. × 130.	
D3 – 1 D3 – 2 D3 – 3 D3 – 4	930.0 972.0 1014.0 1046.0	254. × 130. 254. × 130. 254. × 130. 302. × 130.	300 μm
C2 mirror plane	1653.0	465. × 240.	
D4	1744.0	508. × 240.	800 μm
SLIC upstream downstream	1849.0 1951.0	490. × 240.	$\Delta E/E \sim 21\%/\sqrt{E}$
Hadrometer upstream downstream	1962.0 1951.0	490. × 270.	$\Delta E/E \sim 75\%/\sqrt{E}$
Muon Wall	2235.0	547. × 305.	

Chapter 4

The Event Triggers and Data Acquistion Systems

4.1 Introduction

In a high energy particles physics experiment, such as E691, many others types of (background) physics events are produced besides the events of interest. To enhance the number of events of interest recorded relative to the total number of events, specialized fast electronic triggers are employed. These digital logic triggers flag the data acquisition system to record an event if its particles produce a particular combination of signals in the detector components above some set of thresholds. As the fixed target data rate is too high for online (realtime) event reconstruction, the data acquisition system packages the digitized events according to a specified format and records them onto some media, typically magnetic tape, to be read later for offline data reconstruction.

4.2 The Dimuon Trigger

The dimuon trigger was designed to fire on $\mu^+\mu^-$ pairs from J/ψ decays. It consisted of four subtriggers: the muon telescope ($MUTS$), the muon top–bottom trig-

ger ($MTBT$), the muon east–west trigger ($MEWT$) and the muon diagonal trigger (MDT).

The analog signals from the back muon wall counters were combined into five sections, labelled MW_{TOP}, MW_{BOTTOM}, MW_{EAST} and MW_{WEST}, before discrimination. The analog signals from the $C2$ mirror–phototube assemblies were also combined, before discrimination, into four sections labelled $C2_{EAST}$, $C2_{WEST}$, $C2_{TOP}$ and $C2_{BOTTOM}$. The back muon wall sections are shown in Figure 3.8 and the $C2$ sections are shown in Figure 3.7. The partitioning of $C2$ was chosen to shadow that of the back muon wall so that a muon passing through a given section of $C2$ would also pass through the corresponding section of the back muon wall.

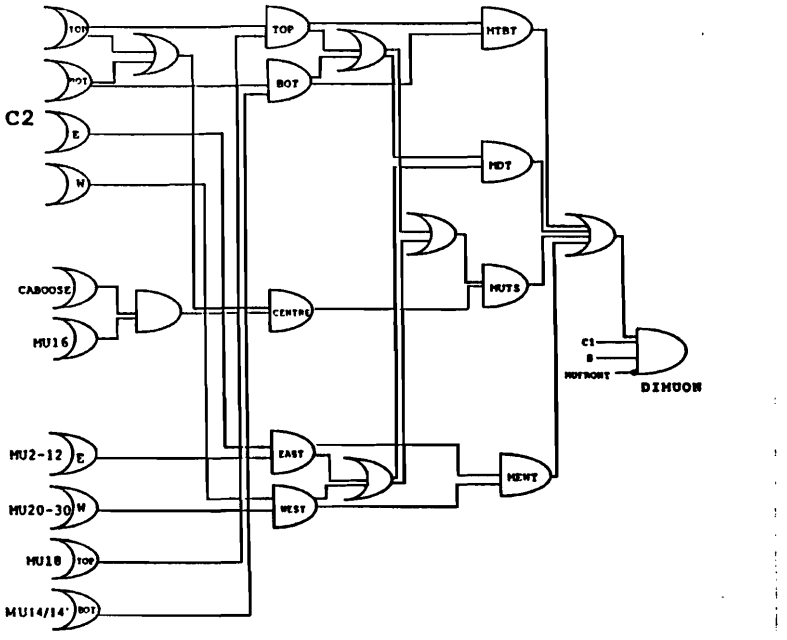

Figure 4.1: The dimuon trigger logic diagram.

Two small scintillation paddle counters called the caboose were mounted 1.5 m downstream of the central counter ($\mu 16$) in the muon wall. The coincidence between the caboose and $\mu 16$ was used to reduce the high rate of accidentals in $\mu 16$. The lucite

light pipe connecting $\mu 14$ with its photomultiplier tube overlapped $\mu 16$. This was a major source of fake dimuon trigger firings. To eliminate these fake firings a pair of small scintillation counters called MW'_{BOTTOM} were used to form a coincidence with $\mu 14$. MW'_{BOTTOM} was the same width as $\mu 14$ and covered the upper 61 cm of $\mu 14$. The subtrigger logic was (expressed in Boolean notation)

$$\begin{aligned} MUTS &= (MW_{CENTRE} \cdot CABOOSE) \cdot (C2_{TOP} + C2_{BOTTOM}) \\ &\cdot ((MW_{TOP} \cdot C2_{TOP}) + (MW_{BOTTOM} \cdot MW'_{BOTTOM} \cdot C2_{BOTTOM}) \\ &+ (MW_{EAST} \cdot C2_{EAST}) + (MW_{WEST} \cdot C2_{WEST})) \end{aligned} \tag{4.1}$$

$$\begin{aligned} MTBT &= (MW_{BOTTOM} \cdot MW'_{BOTTOM} \cdot C2_{BOTTOM}) \\ &+ (MW_{TOP} \cdot C2_{TOP}) \end{aligned} \tag{4.2}$$

$$MEWT = (MW_{EAST} \cdot C2_{EAST}) \cdot (MW_{WEST} \cdot C2_{WEST}) \tag{4.3}$$

$$\begin{aligned} MDT &= ((MW_{TOP} \cdot C2_{TOP}) + (MW_{BOTTOM} \cdot MW'_{BOTTOM} \cdot C2_{BOTTOM})) \\ &\cdot ((MW_{EAST} \cdot C2_{EAST}) + (MW_{WEST} \cdot C2_{WEST})) \end{aligned} \tag{4.4}$$

as shown in the dimuon trigger logic diagram in Figure 4.1. The four dimuon subtriggers were combined using a logical OR (fan–in) whose output was called $DIMUON$. The final stage of the dimuon trigger was a five–fold coincidence, $DIMUON \cdot B \cdot \Sigma C1 \cdot \overline{\sum frontMW}$, whose output went into the beam trigger fan–in. The components of this coincidence were

$$DIMUON = MUTS + MEWT + MTBT + MDT$$

$\overline{\sum frontMW}$ = the front muon wall component that vetoed stray halo muons coming down the beam line

$B =$ the B scintillation counter discriminator threshold requiring at least one charged track from the interaction in the target

$\Sigma C1 =$ the summed $C1$ discriminator threshold requiring the total amount of light in $C1$ to be at least that of two muons.

The dimuon trigger geometric acceptance $\times$ efficiency is a function of four parameters. One intuitive choice for these parameters is the set of opening angles and longitudinal momenta of the dimuon pair with respect to the photon beam (z) axis

$$(\theta_{fast},\ \theta_{slow},\ p_{z\ fast},\ p_{z\ slow}) \tag{4.5}$$

where $p_{z\ fast} > p_{z\ slow}$. However, if the Monte Carlo event generation and detector simulation are well tuned, the acceptance can be parametrized in terms of the kinematic variable(s) of interest. All other parameters are then properly integrated out. Thus, in Figure 4.2, the dimuon trigger geometric acceptance $\times$ efficiency is shown as a function of the J/ψ energy, E_ψ, superimposed over the (normalized) J/ψ energy distribution (solid line —) corrected for smearing and overall acceptance (geometric acceptance $\times$ efficiency). In Figures 4.3 to 4.6, the contributions of the four dimuon subtriggers to the overall acceptance are shown. Detailed geometry and efficiency measurements of the dimuon trigger components were made and incorporated into the Monte Carlo. Using the Monte Carlo, the dimuon trigger was thus determined to have a large $\langle$ geometric acceptance $\times$ efficiency $\rangle$ of $55 \pm 9\%$. For exclusively deep inelastic and elastic events the $\langle$ trigger geometric acceptance $\times$ trigger $\rangle$ efficiencies were $49 \pm 8\%$ and $58 \pm 10\%$, respectively.

As a check of the detailed Monte Carlo dimuon trigger simulation, one can estimate whether the two muons from the J/ψ decay will both pass through the central muon counter ($\mu 16$) as the photon beam energy is increased. The angular decay distribution in the centre–of–mass frame for elastic J/ψs produced with a transverse (photon) polarization is

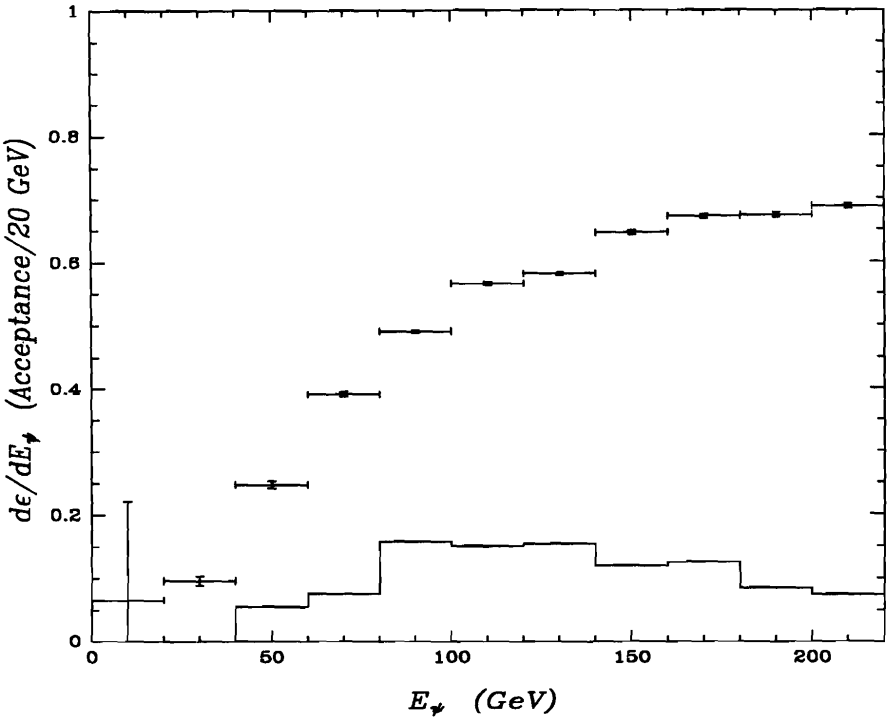

Figure 4.2: The dimuon trigger geometric acceptance × efficiency as a function of the J/ψ energy, E_ψ superimposed over the (normalized) J/ψ energy distribution (solid line —) corrected for smearing and overall acceptance.

$$p(\theta) \propto 1 + \cos^2\theta \tag{4.6}$$

and the average decay angle with respect to the z–axis is

$$\langle \cos\theta \rangle = \frac{\int_0^{\pi/2} d\cos\theta \ \cos\theta(1+\cos^2\theta)}{\int_0^{\pi/2} d\cos\theta \ (1+\cos^2\theta)} = \frac{9}{16} \tag{4.7}$$

In the centre–of–mass frame the momentum of the two decay muons is 1.545 GeV and their energy is 1.549 GeV. Their longitudinal and transverse momenta components are

$$p_{z(1,2)} = \pm\, p\langle\cos\theta\rangle = \pm\, 0.8691 \ GeV \tag{4.8}$$

$$p_T = p\langle\sin\theta\rangle = 1.277 \ GeV \tag{4.9}$$

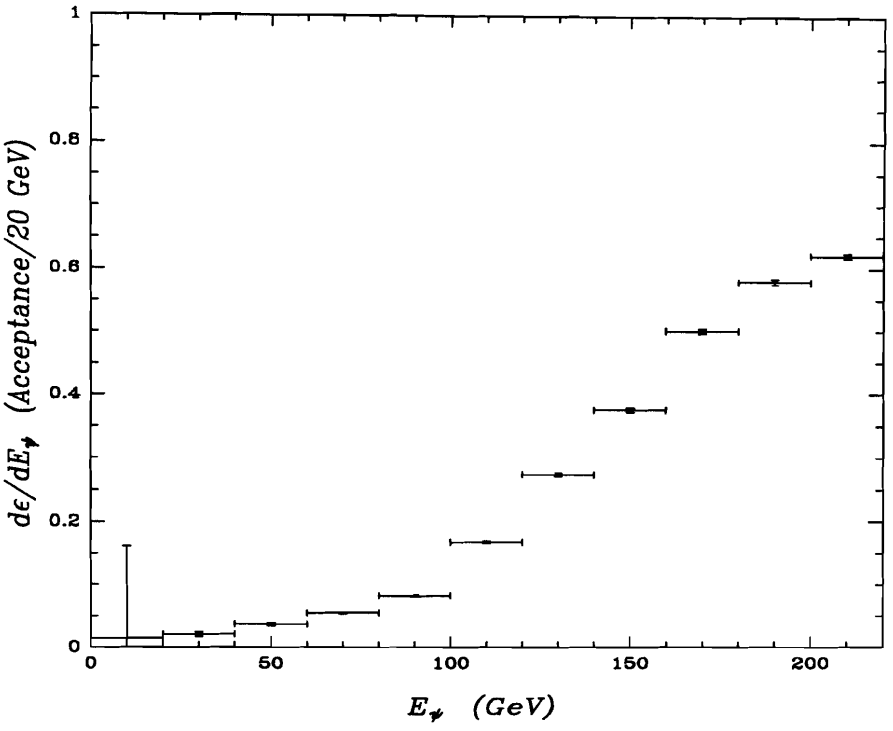

Figure 4.3: The muon telescope subtrigger (MUTS) geometric acceptance × efficiency.

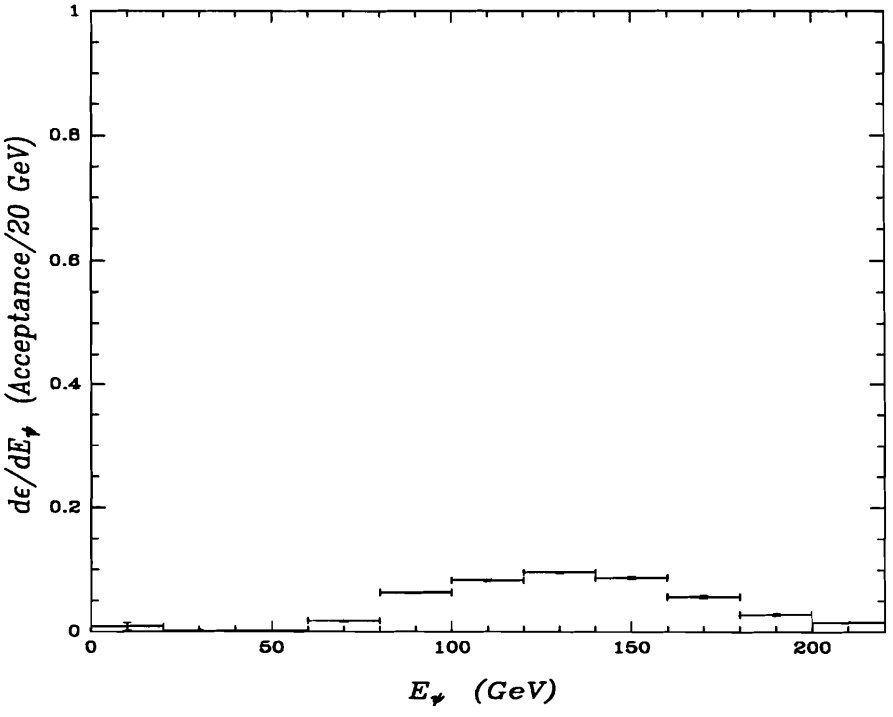

Figure 4.4: The muon top–bottom subtrigger (MTBT) geometric acceptance × efficiency.

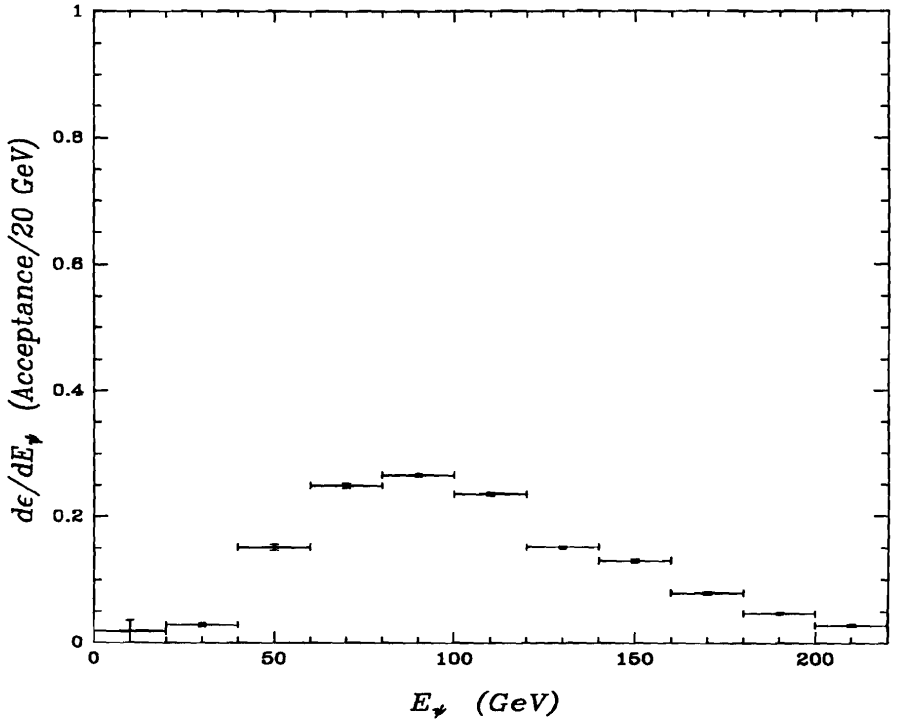

Figure 4.5: The muon east–west subtrigger (MEWT) geometric acceptance × efficiency.

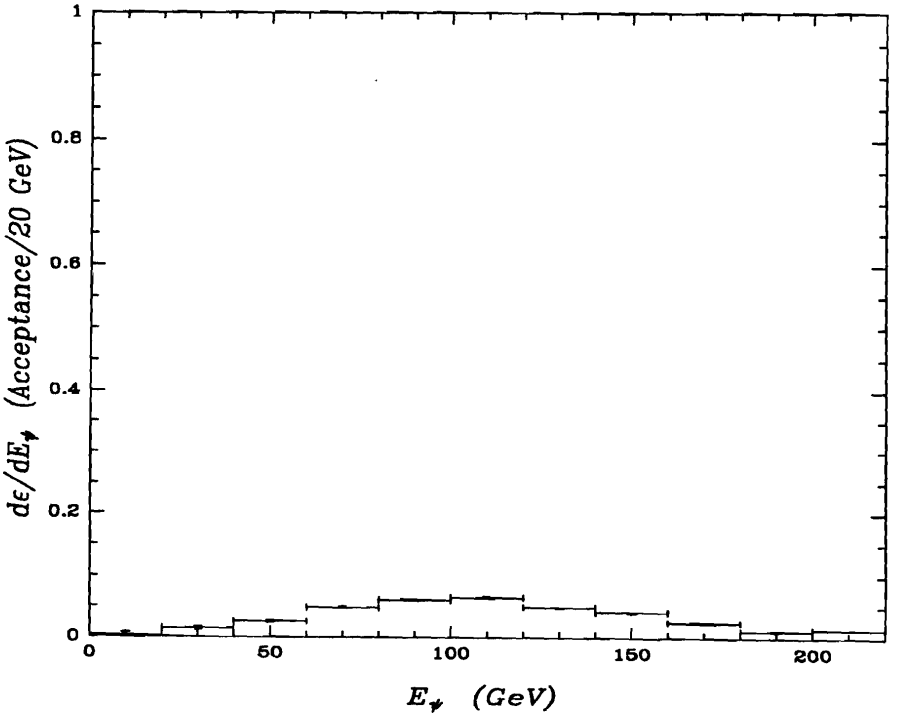

Figure 4.6: The muon diagonal subtrigger (MDT) geometric acceptance × efficiency.

Taking the J/ψ to be elastic ($z \rightarrow 1$) and the photon beam energy to be 200 GeV gives

$$E_\psi = 200\ GeV \tag{4.10}$$

Now $\gamma = E_\psi/m_\psi = 64.58$ giving $\beta = 0.99988$. Boosting to the lab frame

$$p'_{z1} = \gamma(p_{z1} + \beta E_1) = 156.1\ GeV \tag{4.11}$$

$$p'_{z2} = \gamma(p_{z2} + \beta E_2) = 44.10\ GeV \tag{4.12}$$

$$p_T = 1.277\ GeV \tag{4.13}$$

The lab frame opening angles for the two muons are

$$\theta'_1 = \sin^{-1}\left(\frac{p_T}{p_{z1}}\right) = 8.1\ mrad \tag{4.14}$$

$$\theta'_2 = \sin^{-1}\left(\frac{p_T}{p_{z2}}\right) = 29.\ mrad \tag{4.15}$$

The target to back muon wall lever arm l along the z–axis is 2235. cm. Taking the decay to be in the yz–plane, the displacements along y from the beam axis for the two muons at the back muon wall are

$$\Delta y_1 = l \sin\theta'_1 = 18.28\ cm \tag{4.16}$$

$$\Delta y_2 = l \sin\theta'_2 = 65.01\ cm \tag{4.17}$$

The height of the central muon counter from its centre to its edge along the y–axis is 30.48 cm. Thus on average only one of the muons from a J/ψ decay passes through the central muon counter at $E_\psi = 200$ GeV in agreement with the detailed Monte Carlo simulation.

4.3 The $B \cdot H$ and E_T Triggers

In fixed target high energy photoproduction and hadroproduction experiments the open charm production rates are quite high, typically 1 to 100 events per second at FNAL energies. However, at these energies the hadronic background of light quark flavours (u, d and s) is larger by a factor of 100 to 1000. Thus the problem was to trigger specifically on the open charm events by rejecting the hadronic background events. The distinguishing feature of open charm events is their high mass which means a high transverse energy, E_T.

A hadronic interaction trigger, denoted by $B \cdot H$, was designed to obtain an sample of hadronic events not biased by a transverse energy cut. A photoproduced open charm event had an average E_T of 3.1 GeV, while the non–charm hadronic background had an average E_T of 1.5 GeV. An E_T trigger was designed to trigger on high transverse energy events, defined as events with a transverse energy greater than 2.4 GeV, while rejecting low transverse energy events. Figures 4.7 and 4.8 show the E_T distributions for all hadronic events and for open–charm events, respectively, in the $B \cot H$ data. For an E_T dial setting of 4.5, corresponding to a 2.4 GeV cut, about 34% of the hadronic events survived the cut and about 68% of the charm events survived. This gave a charm signal enhancement factor of about 2. The charm enhancement factor as a function of the E_T cut is shown in Figure 4.9.

A diagram of the logic of the $B \cdot H$ and E_T triggers is shown in Figure 4.10. A trigger module was defined as one–eighth of a Le Croy 628 NIM module. At the first level 42 trigger modules summed the SLIC dynode signals and 21 trigger modules summed the hadrometer dynode signals. Each of the 63 modules, labelled Level 1, summed up to eight dynode signals. The inputs to the trigger modules from the calorimeters were arranged so that the counters feeding into any trigger module were approximately equidistant from the centres of the calorimeters. All input signals into these modules were unweighted. These Level 1 fan–ins served three purposes: they summed the signals for further use by the E_T and $B \cdot H$ triggers and for online

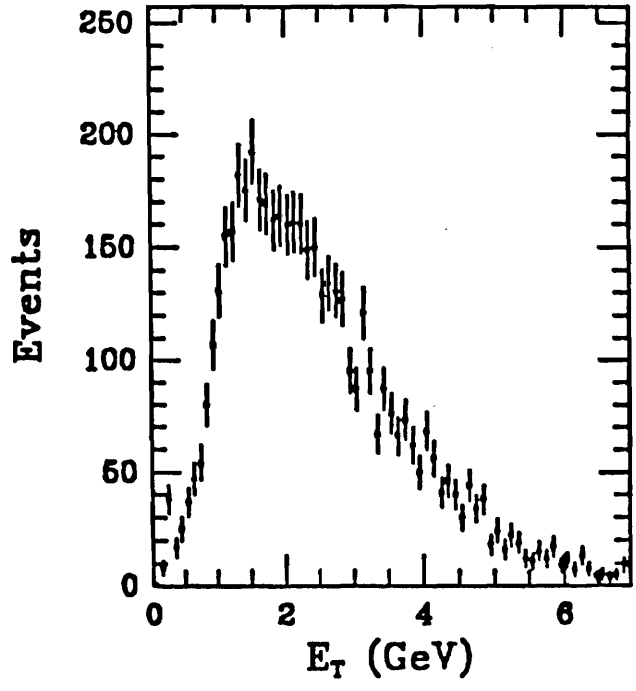

Figure 4.7: The E_T distribution for all hadronic events in the minimum bias $B \cdot H$ data.

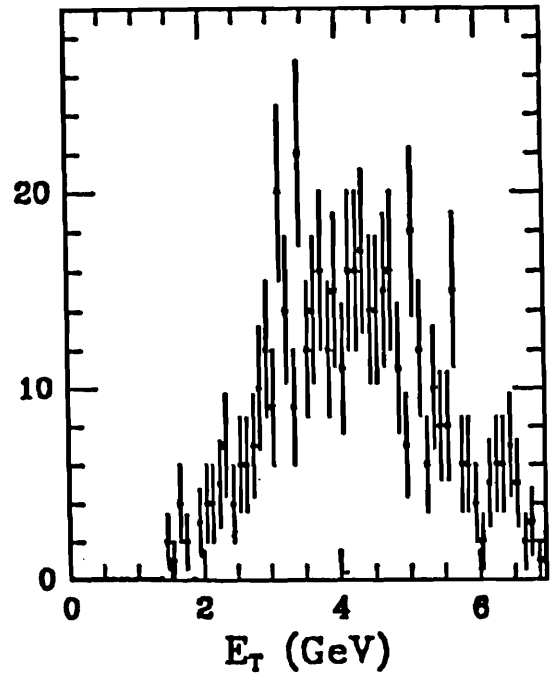

Figure 4.8: The E_T distributions for open–charm events in the minimum bias $B \cdot H$ data.

monitoring of the E_T trigger performance. Since the Le Croy 628 modules had only two outputs per fan–in, a 50 Ohm splitter was used on each channel to split one of the output signals for use by the $B \cdot H$ trigger and for monitoring. This splitter was a resistive network and was designed to split fast pulses. It had no observable cross–talk for phototube output pulses with risetimes on the order of nanoseconds.

The first of the two outputs from each Level 1 module fed into one of nine Level 2 trigger modules. The inputs to these Level 2 modules were attenuated with a set of resistors to give an effective transverse energy. The attenuation of a Level 2 input signal was linearly proportional to its distance from the centre of the SLIC or hadrometer. The six SLIC and three hadrometer Level 2 modules were numbered 64–69 and 70–72 respectively. The one SLIC and one hadrometer Level 3 trigger modules numbered 73 and 74 respectively completed the summing of the SLIC and hadrometer transverse energies. The one Level 4 trigger module number 75 summed the SLIC and hadrometer transverse energy signals to give the E_T signal.

It was not feasible to discriminate on the E_T signal pulse height for two reasons. The E_T signal had a large intrinsic time jitter due to the length of the counters in the SLIC and hadrometer. Also, the E_T signal due to the Level 2 attenuation of the SLIC and hadrometer signals was of the order of a few mV/GeV and the noise level was on the order of 0.3–0.5 mV. The solution was to integrate the charge of the E_T signals that arrived at different times over a 100 ns gate and to discriminate on the total integrated charge. Also, by integrating the signal over a time interval much larger than the characteristic periods of the noise the charge fluctuations averaged out leaving only the charge of the E_T signal. For a gate of 100 ns the integrated charge of the E_T signal for a typical hadronic event was found to be about 10–15 picocoulombs. To discriminate on such a small amount of charge required the development of a very low noise charge discriminator. This charge discriminator was able to discriminate on integrated charge levels between 4 and 48 pc. The gate for this module was provided by discriminating on the total energy in the calorimeters, denoted by H.

The first set of the two SLIC and hadrometer outputs from the splitter were

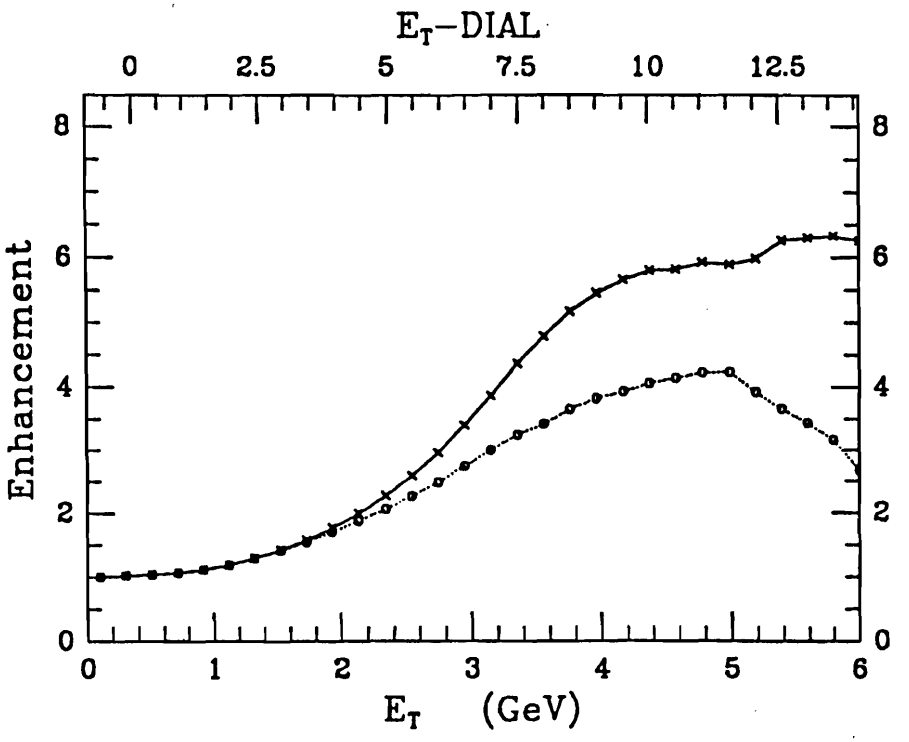

Figure 4.9: The charm enhancement factor as a function of the E_T cut for the recorded ($\times$) and reconstructed (o) open–charm data.

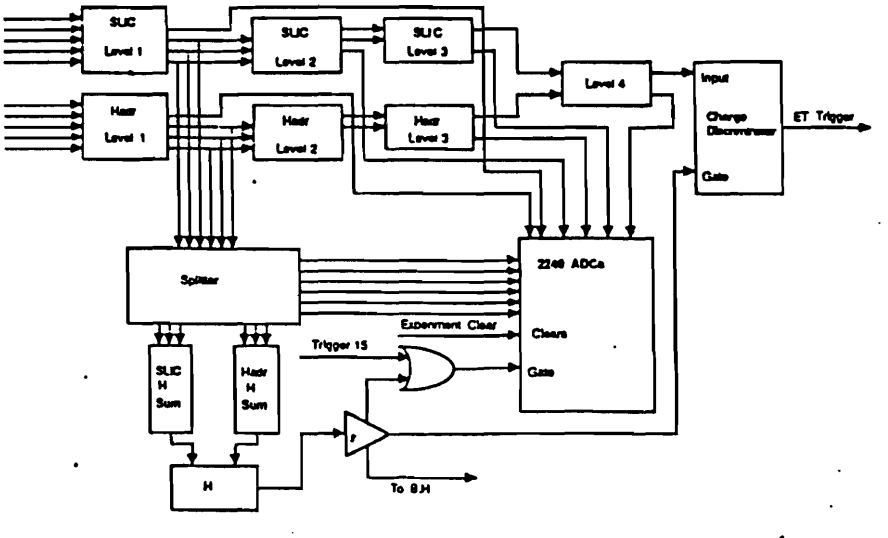

Figure 4.10: A schematic of the E_T and $B \cdot H$ trigger logic. A good parametrization of the 50% efficiency point in terms of the dial setting is $E_{T0} = 0.36 + 0.4x\ GeV$.

summed separately to give the total SLIC energy and the total hadrometer energy. The SLIC energy and the hadrometer energy were then summed to give H. The H signal was discriminated on its pulse height. A minimum of 40 GeV was required in order for H to fire the discriminator. The hadronic energy trigger, $B \cdot H$, was formed by requiring a coincidence with the logic signal from the B counter.

The second set of the SLIC and hadrometer outputs from the splitter were digitized by a set of Le Croy 2249 ADCs. The outputs from the Level 2, Level 3 and Level 4 trigger modules were also digitized. The digitized output signals from the ADCs were used to monitor the trigger performance online.

The SLIC signal level was calibrated using 200 GeV electron beam and the hadrometer signal level was calibrated using a 200 GeV pion beam. The result was to attenuate the SLIC signals by 12 dB before combining them with the hadrometer signals in the $B \cdot H$ and E_T triggers.

The E_T trigger efficiency, ϵ, was defined as the fraction of $B \cdot H$ events that the E_T trigger accepted and was determined by collecting $B \cdot H$ data with the trigger module dial set to various values in the range 0 to 10. The resulting efficiency curves were parametrized by the form

$$\epsilon = \frac{1 + \tanh[a(E_T - E_{T\emptyset})]}{2} \tag{4.18}$$

where $E_{T\emptyset}$ denoted the 50% efficiency point. The slope, a, was well fit by

$$a = \frac{16.69}{x + 2.42} \ \ GeV^{-1} \tag{4.19}$$

where x denoted the E_T trigger module dial setting. A good parametrization of the 50% efficiency point in terms of the the dial setting was found to be

$$E_{T\emptyset} = 0.36 + 0.4x \ \ GeV \tag{4.20}$$

4.4 The Calibration Triggers and Special Physics Trigger

The calibration and special physics triggers used are

γ Trigger This trigger required a coincidence between a photon TAG and a large energy deposit in the C–counter. It was used for calibration of the tagging system.

e^+e^- Trigger A set of two triggers. The first trigger was used to calibrate the pair plane by requiring an energy deposit in the pair plane counters with the 6 inner counters prescaled down due to the high pair flux in the central region of the pair plane. For the SLIC calibration, the pair plane countered was lowered out of the pair plane. The second trigger required a TAG in coincidence with an energy deposit in the central SLIC counter. This trigger was vetoed if there was a significant energy deposit in the hadrometer. It utilized two long scintillation counters, located on the east and west sides of the C–counter, to enhance the acceptance of pairs outside the central region.

Trigger 13 This was a generic trigger that included the DC paddle trigger, the halo muon trigger for drift chamber calibration, DA test trigger, $\mu_{front} \cdot \mu_{back}$ triggers that required a coincidence between the front and back muon walls for SLIC and hadrometer calibration, and a SMD trigger that required a $B \cdot B' \cdot \mu_{front}$ coincidence. Each of these triggers could be separately turned on.

Trigger 15 The second generic trigger used for non–beam related calibration events such as drift chamber pulsing, laser pulsing of the Cherenkov, SLIC and hadrometer phototubes and pedestal events. These triggers were DA generated between beam spills.

High E_γ Trigger A special physics trigger that triggered on high energy electrons. This trigger was used to obtain the total cross–section in a limited region of the

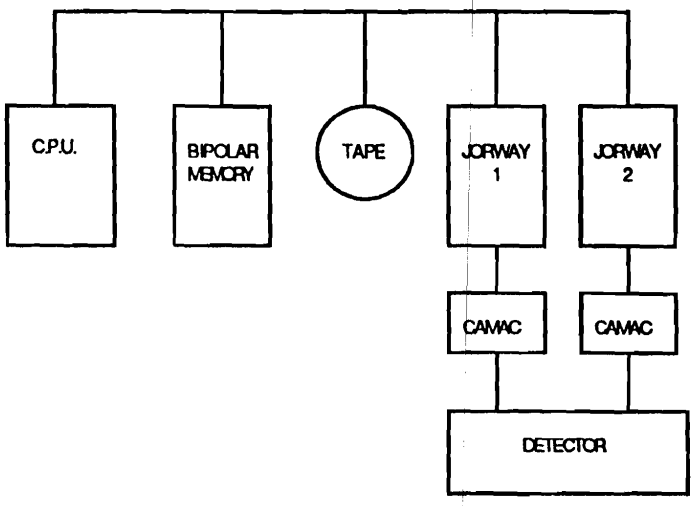

Figure 4.11: The configuration of the E691 Data Acquisition System.

photon spectrum.

4.5 The Data Acquisition System

The E691 data acquisition system software was an improved version of the RSX–11 Data Acquisition Program provided by the FNAL Computing Department. This program was installed on a PDP–11 computer. The configuration of the data acquisition system (DA) is shown in Figure 4.11.

Each device of the PDP–11 computer communicated with the others along a dataway called the UNIBUS. On one end of the UNIBUS was the PDP–11 CPU, next was the fast Bipolar memory. Following the memory was the 6250 BPI, 75 IPS tape drive (Storage Technology Corporation). The tape drive was followed in turn by two CAMAC branch drivers (Jorway 411). The data from the spectrometer was

digitized by the ADCs, TDCs and latches in the two CAMAC branches. The data words in the CAMAC crates were extracted in parallel by the two CAMAC branch drivers and placed in the memory. The tape drive then fetched the data words from the memory and wrote them on to tape. For block data transfers the devices closest to the CPU on the UNIBUS had priority.

When an event trigger occurred the DA deadened the CAMAC system to further event triggers until the event data had been stored in the PDP–11 memory. This resulted in deadtime during a spill. Also if the PDP–11 memory was filled then the DA did not allow the CAMAC system to accept any more event data until part of the data in the memory had been written to tape. This was an additional source of deadtime. The data acquisition system had a deadtime of about 3 1/2 ms per event which increased to about 4 1/2 ms per event with increasing beam intensity and event multiplicity. The maximum data acquisition rate was about 100 events per second with about 30% deadtime. Above this rate the DA system became saturated.

4.6 The Online Monitoring System

During data taking the DA transmitted about 1% of the physics and calibration events from the PDP-11 to the VAX via a high speed DR11-W data link. The E691 Online Monitoring System (E691 OLMS) then used these events to monitor the performance of the spectrometer. A schematic of the E691 OLMS is shown in Figure 4.12.

A detached process called the Event Pool Builder (EPB) stored the incoming events in an event pool. The detached EPB was created and controlled by the user–run Event Pool Builder Control Display Program (EPBCDP). The EPBCDP controlled the EPB by writing control words into a global common section that the two processes shared. The event pool was a global common section that was capable of storing 500 events at any given time. The EPB stored the events sequentially and continuously updated the pool; as new events came across the link the oldest event

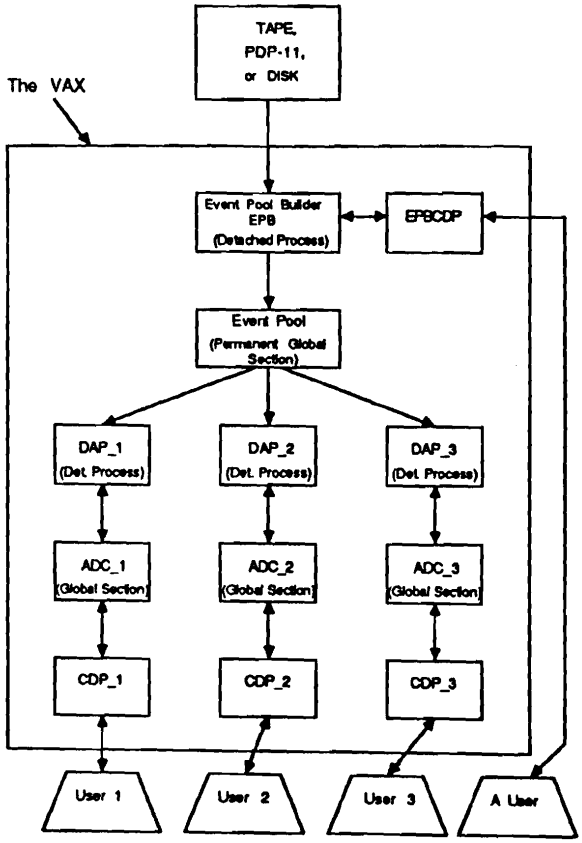

Figure 4.12: A schematic of the E691 Online Monitoring System.

that was not being read was discarded from the pool and the new event was inserted. The events in the event pool were read by a set of Data Analysis Processes (DAPs). To circumvent software integration problems each component of the spectrometer had its own set of DAPs. The performances of the tagging system, the SMD, the analyzing magnets, the threshold Cherenkov counters, the drift chambers, the SLIC, the hadrometer, the $B \cdot H$ trigger, the E_T trigger and the dimuon trigger were all independently monitored by their respective DAPs. The DAPs were detached processes that scanned the event pool, chose events of interest and analyzed them. The DAPs could scan the events in the event pool either from the oldest to the newest event or from the newest to the oldest event. More than one DAP could read an event at one time. However, the EPB could not discard an event while it was being used by a DAP. The detached DAPs were created and controlled by user–run Control/Display Processes (CDPs). A user controlled a DAP by instructing the CDP to write control words into the global common section that the two processes shared. The DAP responded by writing status words into the shared common which the CDP then read. The DAP also wrote the results of its analysis into the shared common which the user then viewed via the CDP. The DAP could also write its results to disk. Analogous EPBs were available to create event pools from events on disk or tape which could then be analyzed by the same DAPs.

Several special CDP/DAPs were written. An E691 online interactive plotting package called GPIG, the E691 General Purpose Interactive Package, was used to produce histograms and scatter plots for online monitoring purposes. An alarm package and a scaler display package were used to notify the people on shift of potential problems with the spectrometer or the electronics. Finally, an event display package was written which gave displays of an event in the spectrometer; the hits in the SMD, drift chambers and muon wall, the light in the Cherenkovs, and the energy deposited in the SLIC and hadrometer. The event display also provided more detailed displays of an event in each of the above mentioned components of the spectrometer.

4.7 Offline Reconstruction

The event reconstruction consisted of two sequential stages called PASS1 and PASS2. The PASS1 stage consisted of the algorithms that performed the SMD and drift chamber charged track reconstruction. The PASS2 stage consisted of the algorithms that performed the Cherenkov particle identification, SLIC and hadrometer energy reconstruction and SMD vertex reconstruction. Detailed descriptions of the reconstruction algorithms are contained in Appendix E and references therein. Approximately 20% of the PASS1 reconstruction was performed on the FNAL CYBER computer cluster. The remaining PASS1 reconstruction was carried out on the FNAL Advanced Computing Project (ACP) 32-bit microprocessor based parallel computing system. PASS2 was run entirely on the CYBER cluster. The J/ψ production analysis was started on the CYBER and completed on the replacement AMDAHL.

Chapter 5

The J/ψ Photoproduction Analysis

5.1 Introduction

The photoproduction of J/ψ vector mesons on a nuclear target consists of three distinct processes: inelastic, coherent elastic and incoherent elastic. The kinematics of such an event are described by the incident photon energy, E_γ, the transverse momentum squared, p_T^2, of the J/ψ relative to the photon beam and the inelasticity, z, a Lorentz invariant given by

$$z \equiv \frac{E_\psi}{E_\gamma} \tag{5.1}$$

in the lab frame. Elastic events are those in which most of the photon energy is transferred to the the J/ψ corresponding to a very high elasticity, $z > 0.99$. Such events are characterized by low p_T^2 and for scattering from a nuclear target occur via two distinct processes: coherent scattering from the nucleus as a whole ($\langle p_T^2 \rangle \sim 0.07$ GeV$^2/c^2$) or incoherent scattering from a nucleon within the nucleus ($\langle p_T^2 \rangle \sim 0.6$ GeV$^2/c^2$). For $z < 0.99$, the production is inelastic. Deep inelastic production occurs for $m_\psi/E_\gamma < z < 0.90$, well away from $z \rightarrow 1$ and is characterized by significantly higher p_T^2, ($\langle p_T^2 \rangle \sim 1.2$ GeV$^2/c^2$). Perturbative QCD is valid for deep inelastic production and the the colour–singlet photon–gluon–fusion (PGF) model [Ber 81] is used to describe the QCD process $\gamma g_1 \rightarrow (J/\psi) g_2$.

A QCD description of elastic production does not as yet exist and we use the phenomenological vector–meson–dominance (VMD) model [Bau 78, Hol 85] with the Glauber model [Gla 70] of elastic hadron scattering from a nuclear target. The VMD model is based on the observation that the photon and the J/ψ vector meson have the same quantum numbers,

$$J^{PC} = 1^{--} \tag{5.2}$$

There is an appreciable probability for a real photon to fluctuate into a virtual J/ψ. By scattering from the target, the virtual J/ψ becomes real via the 4–momentum transferred. To describe the elastic J/ψ–nucleus and J/ψ–nucleon scattering we use the Glauber model of hadron elastic scattering from $A > 1$ nuclei. This model is an extension of optical diffraction theory. When the J/ψ scatters from the whole nucleus, it is not possible in principle to know which of the A nucleons was struck. The amplitudes for scattering by all the nucleons must be added coherently to form the nuclear scattering amplitude. The incoherent elastic $d\sigma/dp_T^2$ is obtained by subtracting the coherent elastic $d\sigma/dp_T^2$ from the summed differential cross sections corresponding to scattering from all possible nuclear final states (neglecting excitations from the small 4–momentum transfer).

Compared with charm and direct photon hadroproduction, the underlying quantities of physics interest, such as the $xG(x)$, are easier to extract from the study of deep inelastic charm photoproduction. The backgrounds in the $J/\psi \to \mu^+\mu^-$ channel are quite small compared to the large backgrounds in charm and direct photon hadroproduction from fragmentation and radiative processes. In the PGF model only the gluon structure function of the target nucleon is involved and only to first order, whereas in hadroproduction the target nucleon gluon structure function is convoluted with either the gluon or quark structure function of the beam hadron. Also, in PGF there is only one tree–level diagram, $\gamma + g \to c + \bar{c}$, whereas hadroproduction has two tree–level diagrams, $q + \bar{q} \to c + \bar{c}$ plus $g + g \to c + \bar{c}$ for charm and $q + \bar{q} \to \gamma + g$ plus $g + q \to \gamma + q$ for direct photon. Further, the next–to–leading order corrections

for PGF are smaller than those for charm and direct photon hadroproduction [Ell 89]. In this chapter, results and analysis on the deep inelastic and elastic photoproduction of J/ψ on beryllium are presented. The fraction, x, of the nucleon momentum carried by the gluon is determined event–by–event from the kinematic quantities described above and the resulting gluon structure function distribution [Mar 88], $xG(x)$, from the deep inelastic data is fit to the form $(1-x)^{n_g}$. Reviews of previous fixed–target J/ψ photoproduction experiments are given in References [Hol 85] and [Nas 83].

5.2 Extraction of the J/ψ Signal

The J/ψ signal was obtained exclusively via the decay mode $J/\psi \rightarrow \mu^+\mu^-$ with a branching ratio of $6.9 \pm 0.9\%$ [PDG 90]. Experiment E691 recorded about 2.6×10^6 dimuon triggers. During the run, dimuon triggered events were stripped off from the raw data tapes and collected onto a separate tape set. This dimuon triggered event set was then reconstructed using the standard E691 two stage reconstruction program. The first stage performed the charged track reconstruction, then the second stage performed the charged track vertex reconstruction, the Cherenkov charged hadron identification and the electromagnetic and neutral hadronic calorimetry reconstruction.

The J/ψ lifetime is $9.7 \pm 1.4 \times 10^{-21}$ s [PDG 90] giving a value of $c\tau = 2.91 \pm 0.42 \times 10^{-13}$ cm. Thus the J/ψ decay vertex cannot be separated from the primary production vertex; the SMD vertexing, essential to the extraction of the open–charm signals by reducing the large combinatoric background, was only useful in providing additional space points for the track reconstruction. In the large invariant mass region of the J/ψ, $m_\psi = 3.0969 \pm 0.0001$ GeV/c^2 [PDG 90], the combinatoric background in the $\mu^+\mu^-$ channel was quite small compared to the high statistics open–charm production channels. The two main sources of background, generating false dimuon triggers, were random two muon combinations and Bethe–Heitler dimuon production $\gamma N \rightarrow \mu^+\mu^- N$ [Tsa 69]. The background invariant mass peaked near the dimuon rest mass and decreased rapidly with increasing $m_{\mu\mu}$. A set of simple strip and substrip cuts, listed in Table 5.1, was used to eliminate the low invariant mass background while retaining 97% of the J/ψ signal. These reconstruction cuts reduced the dimuon data sample to 2319 events, a size amenable to production analysis.

A charged track was categorized (using a binary code) according to whether or not it hit and was detected in the SMD and drift chambers D1, D2, D3 and D4. The categories are listed in Table 5.2.

Table 5.1: The efficiencies of the reconstruction cuts for the dimuon triggered events. The high invariant mass cut excluded most of the background events that fired the dimuon trigger.

Strip Background Cuts	Efficiency (%)
≥ 2 tracks with momentum ≥ 9 GeV/c and ≤ 250 GeV/c	1.1
≥ 2 tracks with reconstruction category ≥ 3 and ≤ 15	
≥ 2 tracks with degrees of freedom ≥ 20.	
$Q(\mu_1) \times Q(\mu_2) = -1$	
2.00 GeV/c^2 $< m_{\mu^+\mu^-}$	
Substrip Background Cuts	**Efficiency (%)**
≥ 2 tracks with momentum ≥ 9 GeV/c and ≤ 250 GeV/c	8.1
≥ 2 tracks with reconstruction category ≥ 3 and ≤ 15	
≥ 2 tracks with degrees of freedom ≥ 11.5	
$Q(\mu_1) \times Q(\mu_2) = -1$	
2.8469 GeV/c^2 $< m_{\mu^+\mu^-}$	
Good run	

Table 5.2: The reconstructed charged track categories. The Boolean operator notation is used.

Reconstructed Track Category	Hits in
1	SMD + D1
3	(SMD + D1) · D2
5	(SMD + D1) · D3
7	(SMD + D1) · D2 · D3
15	(SMD + D1) · D2 · D3 · D4

The number of degrees of freedom of a charged track is the number of planes minus the five parameters required to describe the track; the two intercepts x_0 and y_0, the two slopes dx/dz and dy/dz and the magnitude of the momentum p. The spectrometer had a total of 44 planes, 9 SMD planes and 35 drift chamber planes, thus a charged track had a maximum possible 39 degrees of freedom. For a charged track to be accepted it had to have hits in at least 17 of the 44 planes corresponding to 12 degrees of freedom. The charge of a track was labelled by $Q = \pm 1$.

A run was rejected due to a logbook documented problem in one of the $B \cdot H$, E_T

or dimuon triggers or in one the detector systems or due to missing or inconsistent scalar information.

Using the cuts listed in Table 5.3 yielded the J/ψ signal of 1225 ± 38 events shown in Figure 5.1. The signal was fit with a Gaussian and the background with a straight line. This maximum likelihood fit gave $\langle m_\psi \rangle = 3.0954 \pm 0.0006$ GeV/c^2, in agreement with the quoted world average value, and an experimental resolution $\sigma_{m_\psi} = 28.8 \pm 0.5$ MeV/c^2. The last analysis cut listed in Table 5.3 consisted of projecting the trajectories of the two J/ψ candidate muon tracks to the back segmented scintillator muon wall and rejecting events where the hit scintillators did not correlate to the segments that generated the dimuon trigger. This cut was quite effective as it was only $33 \pm 1\%$ efficient for background under the J/ψ signal.

Table 5.3: The efficiencies of the cuts on the $J/\psi \rightarrow \mu^+\mu^-$ signal events. The reconstruction efficiencies are normalized to events that generated a dimuon trigger. The analysis efficiencies are normalized to events that passed the reconstruction cuts.

Reconstruction × Strip Cuts × Substrip Cuts	Efficiency (%)
≥ 2 tracks with momentum ≥ 9 GeV/c and ≤ 250 GeV/c	96.
≥ 2 tracks with reconstruction category ≥ 3 and ≤ 15	
≥ 2 tracks with degrees of freedom > 11.5	
$Q(\mu_1) \times Q(\mu_2) = -1$	
2.8469 GeV/$c^2 \leq m_{\mu^+\mu^-} \leq$ 3.3469 GeV/c^2	
Analysis Cuts	**Efficiency (%)**
J/ψ $p_T^2 \leq 7.0$ GeV$^2/c^2$	99.6 ± 0.2
dimuon projection to back muon wall	76.2 ± 1.0

In the J/ψ production analysis events originating from the cascade decay $\psi' \rightarrow J/\psi\pi^+\pi^-$ were excluded using the invariant mass cut $m_{\psi\pi^+\pi^-} \leq 3.436$ GeV/c^2 or $m_{\psi\pi^+\pi^-} \geq 3.936$ GeV/c^2. The ψ' signal is shown in Figure 5.2 where the signal was fit with a Gaussian and the background with a straight line. Table 5.4 lists the cuts used where $C_{prob}(\pi)$ is the pion probability given by the threshold Cherenkov reconstruction algorithm. The invariant $\mu^+\mu^-$ mass, obtained using the J/ψ cuts of Table 5.3, was required to be within $2\sigma_\psi$ of the measured $\langle m_\psi \rangle$. These cuts yielded a ψ' signal of 9 ± 3 events. The maximum likelihood fit gave $m_{\psi'} = 3.6817 \pm 0.0059$ GeV/c^2, in

good agreement with the world average value of 3.68600 ± 0.00010 GeV/c^2 [PDG 90], and an experimental resolution $\sigma_{m_{\psi'}} = 15 \pm 4$ MeV/c^2.

Table 5.4: The cuts on the $\psi' \rightarrow J/\psi\pi^+\pi^-$ signal.

ψ' Cuts	Efficiency (%)
3.0387 GeV/$c^2 \leq m_{\mu^+\mu^-} \leq$ 3.1527 GeV/c^2	39 ± 5
$\pi_1\pi_2$ geometric acceptance $\times$ track reconstruction	83 ± 5
$C_{prob}(\pi_1) \times C_{prob}(\pi_2) \geq 0.71$	
$Q(\pi_1) \times Q(\pi_2) = -1$	
3.436 GeV/$c^2 \leq m_{\psi\pi^+\pi^-} \leq$ 3.936 GeV/c^2	

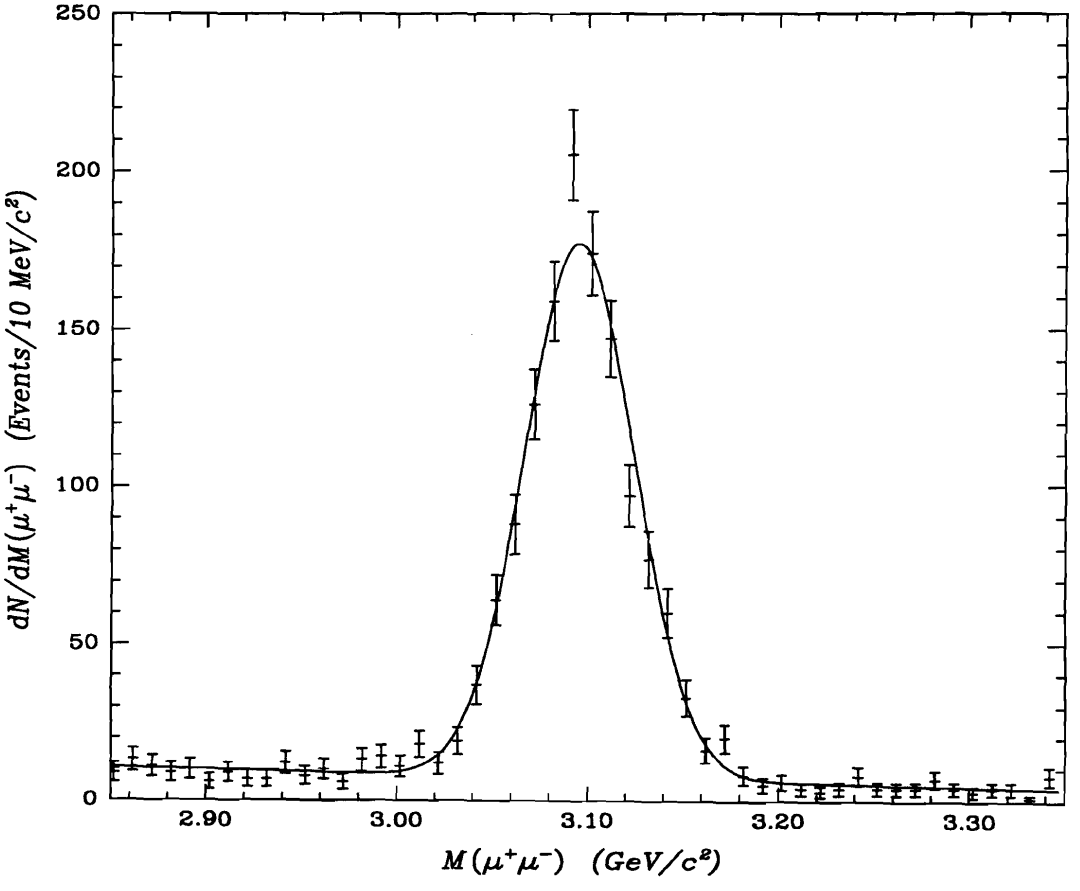

Figure 5.1: The invariant J/ψ mass distribution in the $\mu^+\mu^-$ channel. The signal is fit by a Gaussian and the background is fit by a straight line.

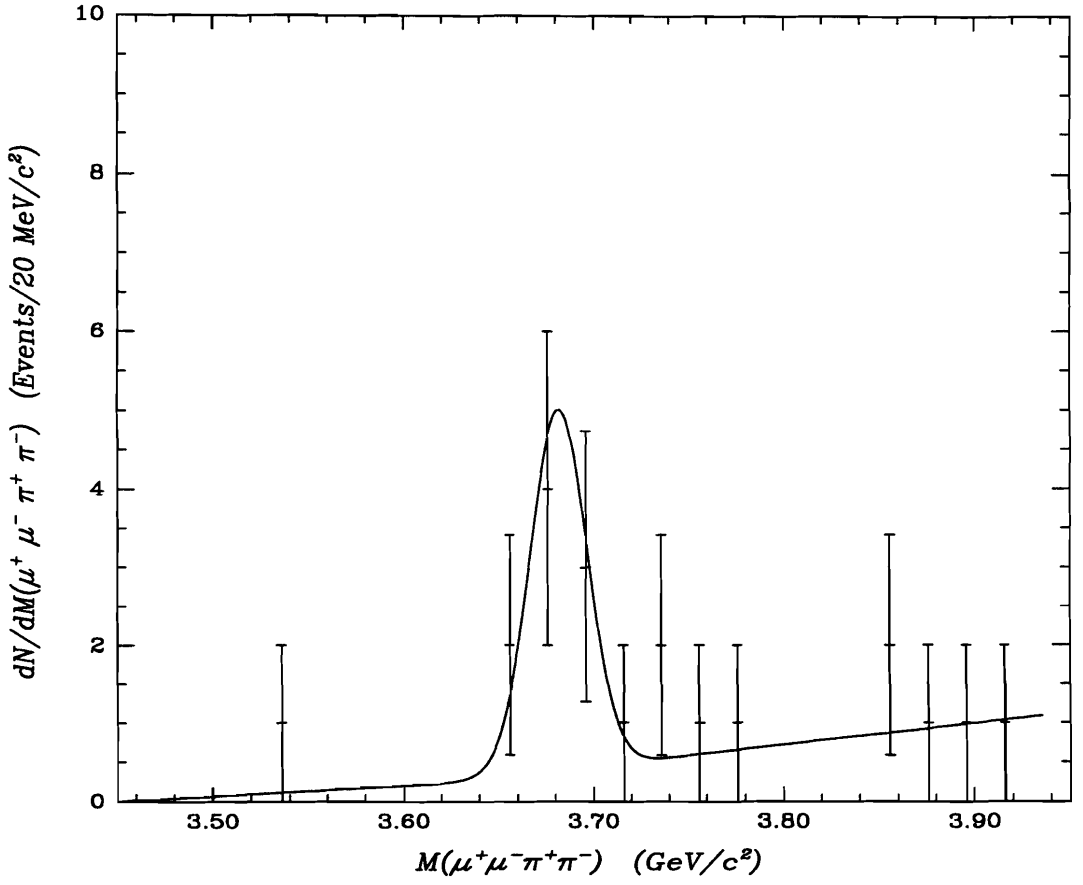

Figure 5.2: The invariant ψ' mass distribution in the $J/\psi\pi^+\pi^- \rightarrow \mu^+\mu^-\pi^+\pi^-$ channel. The signal is fit by a Gaussian and the background is fit by a straight line.

5.3 The z, p_T^2 and x Dependence of the J/ψ Cross Section

The inelasticity of an event, z, is given by the Lorentz invariant expression

$$z \equiv \frac{p_\psi \cdot p_N}{p_\gamma \cdot p_N} \tag{5.3}$$

where p_γ, p_N and p_ψ are the incident photon beam, the target nucleon and the J/ψ 4–momenta, respectively. In the lab frame, this expression is the ratio of the J/ψ energy to the photon beam energy, $z = E_\psi/E_\gamma$. The J/ψ transverse momentum squared, p_T^2, was measured with respect to the photon beam. These three variables, E_γ, z and p_T^2, describe the kinematics of a J/ψ event. A complete discussion of the J/ψ kinematics is given in Appendix A. For the discussion to follow it is useful to first define the following quantities

- $E_\psi \equiv$ the real or Monte Carlo generated J/ψ energy
- $E_X \equiv$ the true or Monte Carlo generated energy of all particles created in an event other than the J/ψ
  $= E_{Xrec} + E_{Xmiss}$
- $E_{frwrd} \equiv$ the total forward (in the lab frame) energy of all particles created in an eve
  $= E_\psi + E_X$
  $= E_\gamma + m_N$
- $E_{\psi rec} \equiv$ the reconstructed real or Monte Carlo J/ψ energy
- $E_{Xrec} \equiv$ the reconstructed real or Monte Carlo energy of all particles other than the J/ψ
- $E_{Xmiss} \equiv$ the real or Monte Carlo energy of all particles, other than J/ψ, missed by the detector

- $E_{rec} \equiv$ the reconstructed real or Monte Carlo forward energy
  $= E_{\psi rec} + E_{Xrec}$
- $(z, p_T^2) \equiv$ the true or Monte Carlo generated J/ψ inelasticity and transverse momentum squared
- $(z_{rec}, p_{Trec}^2) \equiv$ the reconstructed real or Monte Carlo J/ψ inelasticity and transverse momentum squared
- $z_{crctd} \equiv$ the real or Monte Carlo z_{rec} corrected for missing E_X
- $x \equiv$ the true or Monte Carlo generated fraction of the target nucleon momentum carried by the gluon
- $x_{rec} \equiv$ the reconstructed real or Monte Carlo gluon momentum fraction
- $x_{crctd} \equiv$ the real or Monte Carlo x_{rec} corrected for missing E_X

Deep inelastic photoproduction with the associated fragmentation producing a forward shower of invariant mass W and energy E_X is shown in Figure 5.3.

As the tagging system measurement of the photon energy was not able to resolve between elastic and inelastic events, E_{rec} was used to measure E_γ. Some part of the E_X was not detected due to particles escaping outside the detector and to detector and reconstruction inefficiencies. Thus the z distribution obtained, after just background subtraction, is given by

$$z_{rec} = \frac{E_{\psi rec}}{E_{rec}} \tag{5.4}$$

$$= \frac{E_{\psi rec}}{E_{\psi rec} + E_{Xrec}} \tag{5.5}$$

Due to the missing E_X, the z_{rec} distribution was systematically shifted towards higher values of inelasticity. Thus, in order to recover the true inelasticity distribution, the background subtracted data was corrected for missing E_X, smearing and (overall)

Table 5.5: The Monte Carlo parametrization of the average missing E_X as a function of the reconstructed z and E_ψ, $\langle E_{Xmiss}\rangle = \langle E_{Xmiss}\rangle(z_{rec}, E_{\psi rec})$. A null entry indicates a kinematically inaccessible region.

$E_{\psi rec}$ (GeV) → / z_{rec} ↓	20 – 40	40 – 60	60 – 80	80 – 100	100 – 120	120 – 140	140 – 160	160 – 180	180 – 200	200 – 220
0.10 – 0.20	$27._{-5.}^{+5.}$									
0.20 – 0.30	$40._{-10.}^{+9.}$	$24._{-7.}^{+6.}$								
0.30 – 0.40	$42._{-7.}^{+8.}$	$38._{-9.}^{+7.}$	$19._{-4.}^{+4.}$							
0.40 – 0.50	$49._{-13.}^{+3.}$	$40._{-11.}^{+4.}$	$35._{-8.}^{+6.}$	$18._{-5.}^{+5.}$						
0.50 – 0.60		$39._{-12.}^{+6.}$	$39._{-11.}^{+7.}$	$30._{-7.}^{+7.}$	$14._{-5.}^{+5.}$					
0.60 – 0.70		$32._{-8.}^{+6.}$	$39._{-10.}^{+7.}$	$34._{-8.}^{+5.}$	$27._{-6.}^{+7.}$	$15._{-5.}^{+5.}$				
0.70 – 0.80		$32._{-7.}^{+2.}$	$35._{-9.}^{+7.}$	$36._{-9.}^{+6.}$	$32._{-7.}^{+6.}$	$25._{-5.}^{+5.}$	$15._{-4.}^{+4.}$	$2._{-2.}^{+4.}$		
0.80 – 0.90		$32._{-5.}^{+2.}$	$30._{-8.}^{+4.}$	$29._{-7.}^{+5.}$	$31._{-8.}^{+5.}$	$28._{-6.}^{+4.}$	$23._{-5.}^{+5.}$	$14._{-4.}^{+4.}$	$4._{-2.}^{+2.}$	
0.90 – 0.95			$21._{-4.}^{+3.}$	$25._{-6.}^{+4.}$	$25._{-7.}^{+5.}$	$28._{-7.}^{+4.}$	$23._{-4.}^{+3.}$	$19._{-4.}^{+4.}$	$10._{-3.}^{+3.}$	
0.95 – 0.99			$20._{-4.}^{+2.}$	$17._{-5.}^{+3.}$	$17._{-5.}^{+3.}$	$18._{-5.}^{+3.}$	$20._{-6.}^{+4.}$	$16._{-4.}^{+3.}$	$11._{-4.}^{+4.}$	$2._{-2.}^{+3.}$
0.99 – 1.00			$12.9_{-3.4}^{+4.9}$	$2.7_{-1.8}^{+0.1}$	$2.6_{-1.6}^{+0.1}$	$2.1_{-1.1}^{+0.3}$	$2.2_{-1.2}^{+0.4}$	$2.3_{-1.3}^{+0.6}$	$2.0_{-1.3}^{+0.8}$	$1.1_{-1.1}^{+1.1}$

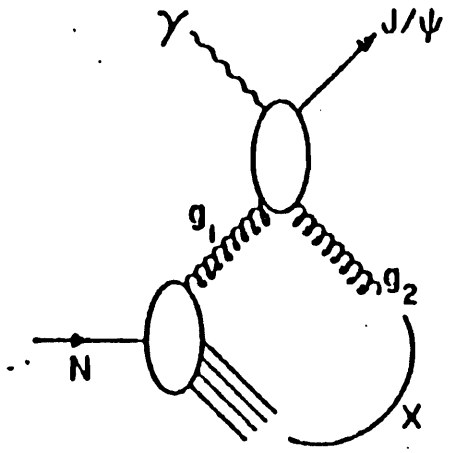

Figure 5.3: Deep inelastic J/ψ photoproduction and the associated fragmentation hadron shower, X with energy E_X.

acceptance (geometric acceptance × dimuon trigger efficiency × reconstruction efficiency × analysis cuts efficiency).

In principle, the missing E_X could be a function of all four of the reconstructed variables

$$E_{Xmiss} = E_{Xmiss}(E_{rec}, E_{\psi rec}, z_{rec}, p^2_{Trec}) \tag{5.6}$$

In practice, the missing E_X was found to be correlated with z and E_ψ and was parametrized as

$$\langle E_{Xmiss} \rangle = \langle E_{Xmiss} \rangle (z_{rec}, E_{\psi rec}) \tag{5.7}$$

using the Monte Carlo. This parametrization is shown in Table 5.5. The asymmetric systematic errors were estimated by fitting the distribution in each $(z_{rec}, E_{\psi rec})$ cell,

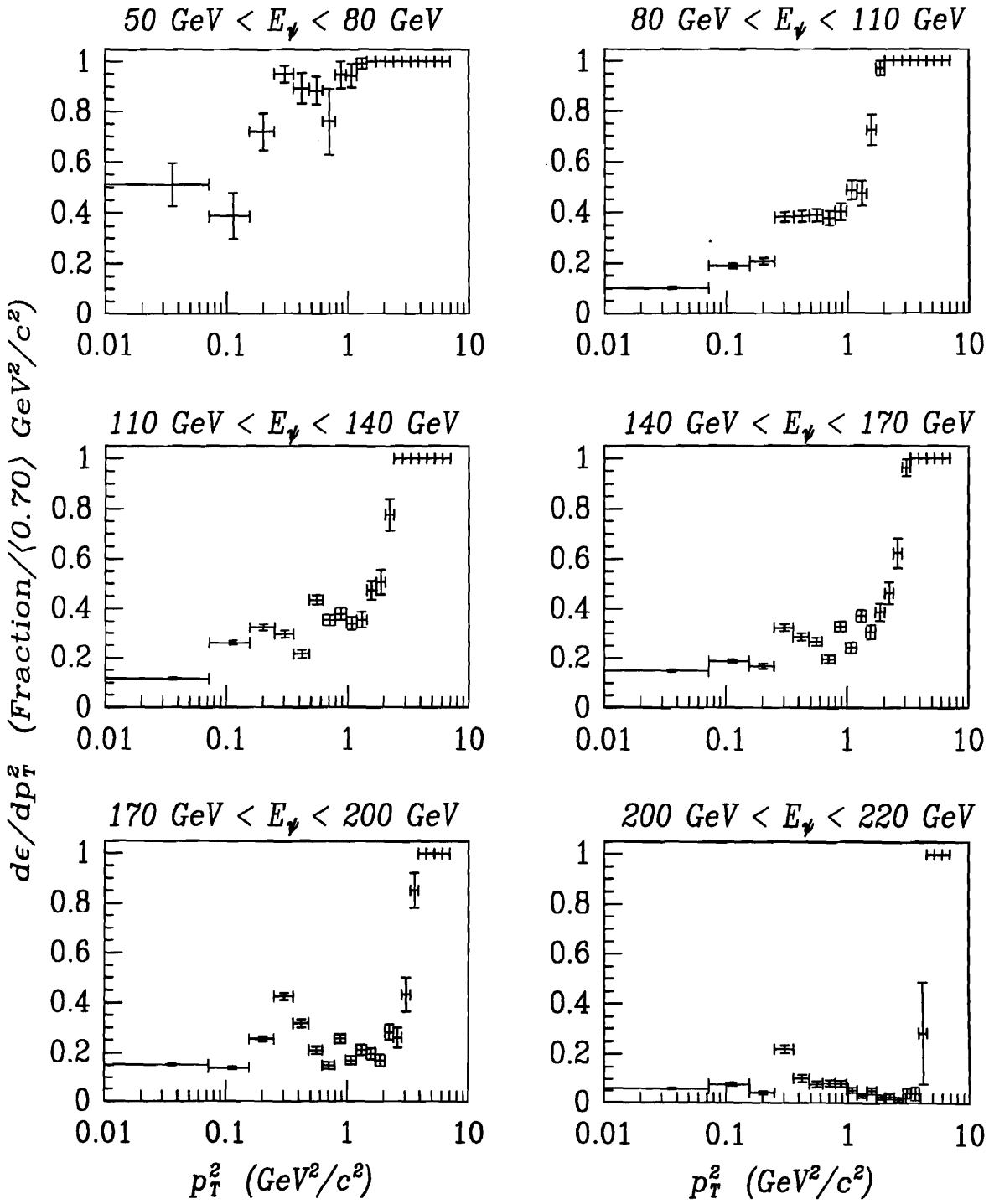

Figure 5.4: The fraction of false elastic events in bins of the J/ψ energy, E_ψ, and transverse momentum squared, p_T^2.

using a binned maximum likelihood fit (1 GeV bins for $z < 0.99$ and 0.25 GeV bins for $z \geq 0.99$). The lower error bound was determined by integrating over 34% of the area of this fit to the left of $\langle E_{Xmiss} \rangle$. Analogously, the upper error bound was determined by integrating over 34% of the area to the right of $\langle E_{Xmiss} \rangle$. As an example, the missing E_X distribution for the cell ($0.6 < z_{rec} < 0.7$, 80 GeV $< E_{\psi rec} <$ 100 GeV) is shown in Figure 5.5. To correct for the missing energy, the $\langle E_{Xmiss} \rangle$ of each $(z_{rec}, E_{\psi rec})$ cell was used as opposed to the E_X distribution. Throwing random values of E_{Xmiss} according to a distribution would have introduced an *additional* smearing to the already smeared z_{rec} distribution.

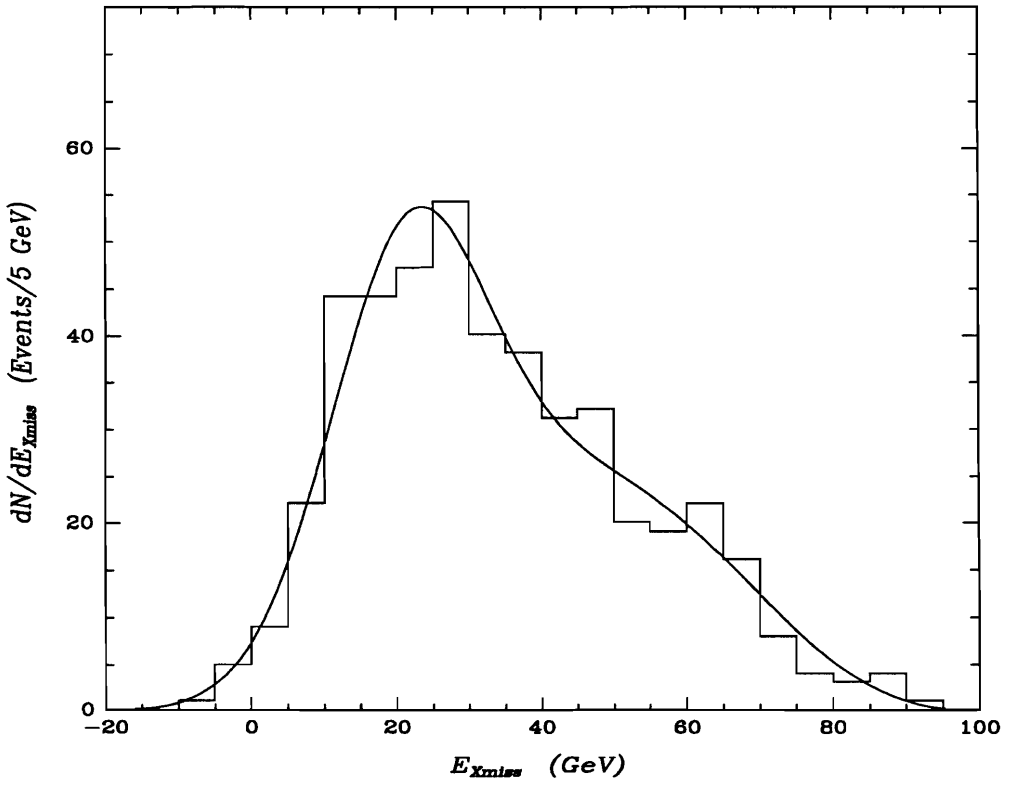

Figure 5.5: The E_{Xmiss} distribution for the cell $0.6 < z_{rec} < 0.7$, 80 GeV $< E_{\psi rec} <$ 100 GeV. Also shown is the fit used to determine the asymmetric errors about $\langle E_{Xmiss} \rangle$.

The z distribution, corrected for missing E_X, is generated by

$$z_{crctd} = \frac{E_{\psi rec}}{E_{\psi rec} + E_{Xrec} + \langle E_{Xmiss}\rangle(z_{rec}, E_{\psi rec})} \tag{5.8}$$

Note that in the region $z > 0.99$ most of the reconstructed elastic events are truly elastic and should not be corrected for missing E_X. However, some fraction of the inelastic events with z close to 0.99 were misreconstructed, due to missed forward energy, as elastic events with $E_{Xrec} \sim 0$. Using the Monte Carlo, the fraction of these false elastic events was parametrized in terms of 6 bins of $E_{\psi rec}$ and 20 bins of p_T^2. The six plots of the fractional occurrence of false elastic events as a function of $E_{\psi rec}$ and p_{Trec}^2 are shown in Figure 5.4. Thus, in the elastic region, the missing energy correction was weighted by the probability, given by Figure 5.4, that the event was inelastic.

The missing forward energy is not known event–by–event, it is known *only* statistically. For a given event, $\langle E_{Xmiss}\rangle$ is either smaller or larger than the true E_{Xmiss}. This gives a residual smearing in the z_{crctd} distribution that must be corrected for. The reconstructed z smearing matrices before and after the $\langle E_{Xmiss}\rangle$ correction, $S(z, z_{rec})$ and $S(z, z_{crctd})$, are shown in Table 5.6 and Table 5.7. The errors in the z_{crctd} smearing are dominated by the propagation of the uncertainties in the $\langle E_{Xmiss}\rangle$ values from Table 5.5. The p_T^2 smearing matrix, $S(p_T^2, p_{Trec}^2)$, is shown in Table 5.8. These matrices were obtained by using the Monte Carlo to plot z_{rec} and z_{crctd} as a function of the generated (true) z and p_{Trec}^2 as a function of the generated (true) p_T^2. Unlike the acceptance correction, the shape of a smeared distribution is a function of the shape of the true distribution. Thus each event entered in the plots was weighted by the photon flux multiplied by the theoretical (E_γ, z, p_T^2) function. The smearing matrices were then obtained by normalizing each column of the generated z in the $S(z, z_{rec})$ and $S(z, z_{crctd})$ plots by its sum and of the generated p_T^2 in the $S(p_T^2, p_{Trec}^2)$ plot by its sum. Note that after correcting the smearing in the inelasticity for $\langle E_{Xmiss}\rangle$, most of the deep inelastic data was shifted into the diagonal elements of $S(z, z_{crctd})$. The feedthrough of elastic events into the deep inelastic region was estimated, as the percentage of z_{crctd} elastic data in the $z < 0.9$ region, to be a negligible $1.3 \pm 1.0\%$.

$z \rightarrow$ / $z_{rec} \downarrow$	0.10 - 0.30	0.30 - 0.50	0.50 - 0.70	0.70 - 0.90	0.90 - 0.99	0.99 - 1.00
0.10 - 0.30	**0.20**	0.01				
0.30 - 0.50	0.68	**0.22**	0.01			
0.50 - 0.70	0.12	0.58	**0.24**	0.01		
0.70 - 0.90		0.18	0.63	**0.31**	0.01	
0.90 - 0.99		0.01	0.11	0.51	**0.31**	0.01
0.99 - 1.00			0.01	0.17	0.68	**0.99**

Table 5.6: The z_{rec} smearing matrix, $S(z, z_{rec})$, before correcting for $\langle E_{Xmiss} \rangle$.

$z \rightarrow$ / $z_{crctd} \downarrow$	0.10 – 0.30	0.30 – 0.50	0.50 – 0.70	0.70 – 0.90	0.90 – 0.99	0.99 – 1.00
0.10 – 0.30	$\mathbf{0.57}^{+0.09}_{-0.09}$	$0.03^{+0.02}_{-0.01}$				
0.30 – 0.50	$0.42^{+0.08}_{-0.09}$	$\mathbf{0.70}^{+0.05}_{-0.13}$	$0.10^{+0.04}_{-0.06}$			
0.50 – 0.70	$0.01^{+0.01}_{-0.00}$	$0.27^{+0.13}_{-0.06}$	$\mathbf{0.68}^{+0.02}_{-0.06}$	$0.15^{+0.03}_{-0.08}$		
0.70 – 0.90			$0.20^{+0.08}_{-0.06}$	$\mathbf{0.64}^{+0.04}_{-0.14}$	$0.13^{+0.16}_{-0.07}$	
0.90 – 0.99			$0.02^{+0.04}_{-0.00}$	$0.07^{+0.21}_{-0.07}$	$\mathbf{0.21}^{+0.06}_{-0.16}$	0.01
0.99 – 1.00				$0.14^{+0.02}_{-0.01}$	$0.66^{+0.01}_{-0.00}$	**0.99**

Table 5.7: The z_{crctd} smearing matrix, $S(z, z_{crctd})$, after correcting for $\langle E_{Xmiss} \rangle$. Note the shift of the deep inelastic data into the diagonal elements. The errors correspond to the propagation of the uncertainty in $\langle E_{Xmiss} \rangle$.

Table 5.8: The p^2_{Trec} smearing matrix, $S(p^2_T, p^2_{Trec})$.

$p^2_T \rightarrow$ (GeV^2/c^2)	0.00 – 0.07	0.07 – 0.16	0.16 – 0.25	0.25 – 0.36	0.36 – 0.48	0.48 – 0.63	0.63 – 0.79	0.79 – 0.98	0.98 – 1.19	1.19 – 1.44	1.44 – 1.72	1.72 – 2.04	2.04 – 2.41	2.41 – 2.83	2.83 – 3.31	3.31 – 3.86	3.86 – 4.50	4.50 – 5.22	5.22 – 6.05	6.05 – 7.00
$p^2_{Trec} \downarrow$ (GeV^2/c^2)	0.07	0.16	0.25	0.36	0.48	0.63	0.79	0.98	1.19	1.44	1.72	2.04	2.41	2.83	3.31	3.86	4.50	5.22	6.05	7.00
0.00 – 0.07	**0.98**	0.04																		
0.07 – 0.16	0.02	**0.92**	0.09																	
0.16 – 0.25		0.04	**0.87**	0.05																
0.25 – 0.36			0.04	**0.87**	0.06															
0.36 – 0.48				0.07	**0.88**	0.06														
0.48 – 0.63					0.06	**0.88**	0.06													
0.63 – 0.79						0.06	**0.88**	0.07												
0.79 – 0.98							0.06	**0.86**	0.08											
0.98 – 1.19								0.07	**0.85**	0.07										
1.19 – 1.44									0.07	**0.86**	0.07									
1.44 – 1.72										0.07	**0.85**	0.06								
1.72 – 2.04											0.08	**0.86**	0.07							
2.04 – 2.41												0.08	**0.87**	0.06						
2.41 – 2.83													0.06	**0.89**	0.07					
2.83 – 3.31														0.05	**0.87**	0.07				
3.31 – 3.86															0.06	**0.87**	0.06			
3.86 – 4.50																0.06	**0.88**	0.07		
4.50 – 5.22																	0.06	**0.86**	0.07	
5.22 – 6.05																		0.07	**0.88**	0.08
6.05 – 7.00																			0.05	**0.92**

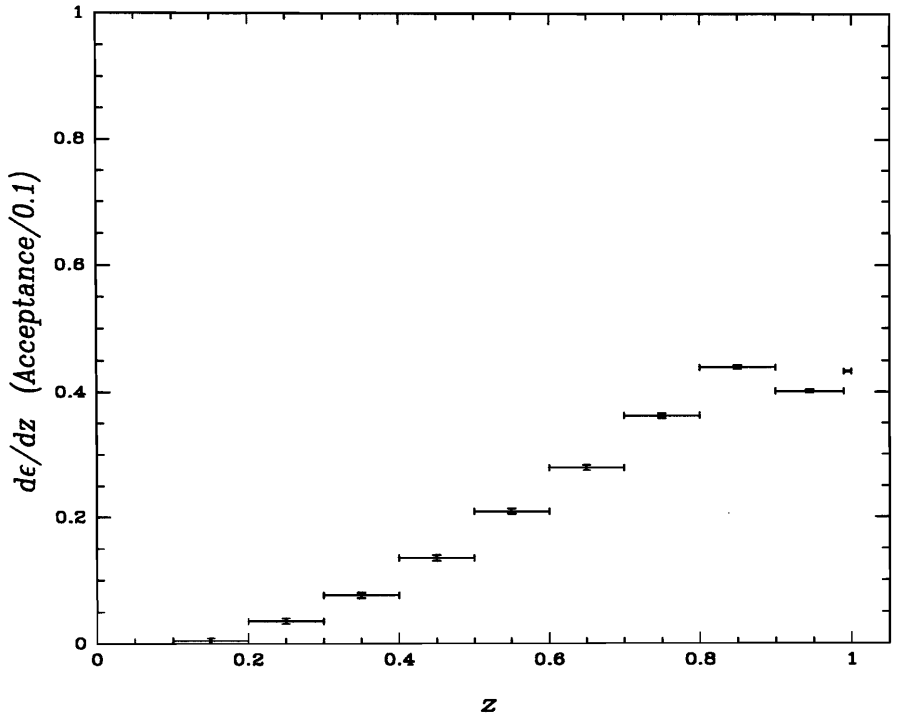

Figure 5.6: The acceptance as a function of the inelasticity, z.

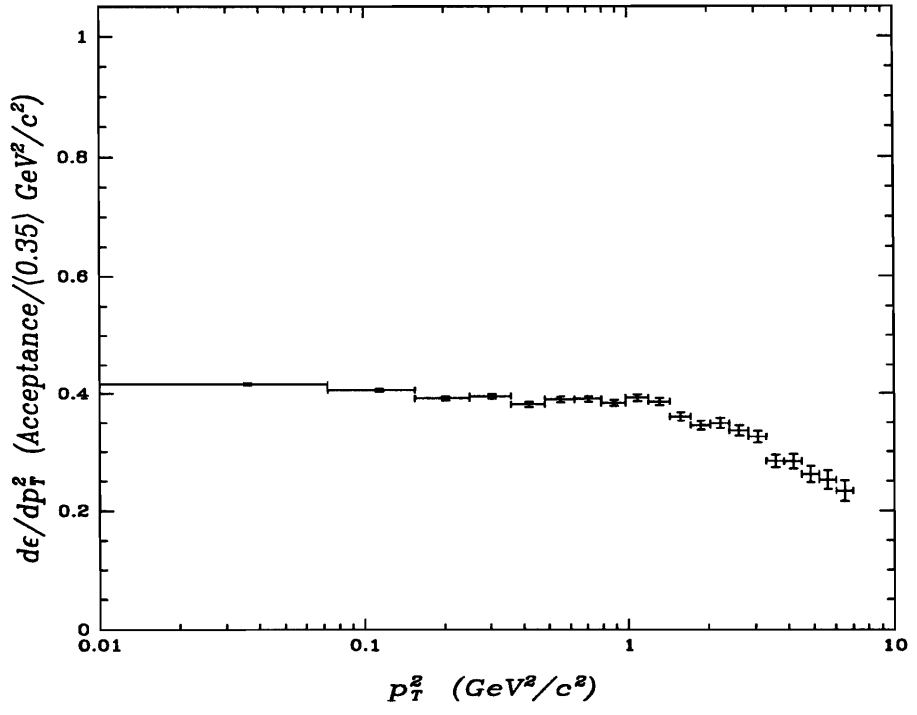

Figure 5.7: The acceptance as a function of the transverse momentum squared, p_T^2.

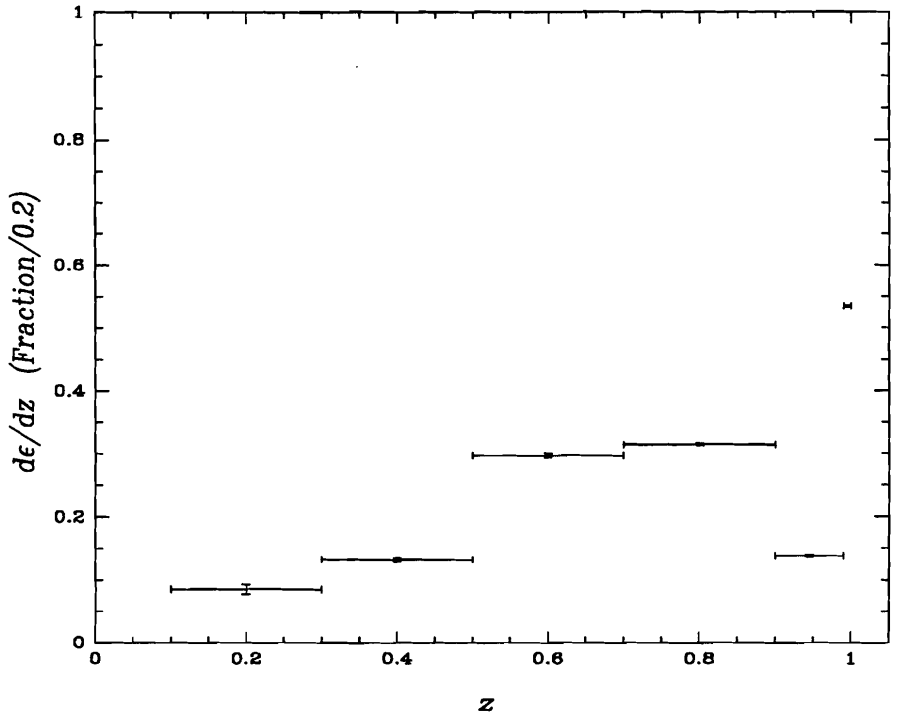

Figure 5.8: The acceptance × smearing as a function of the inelasticity, z.

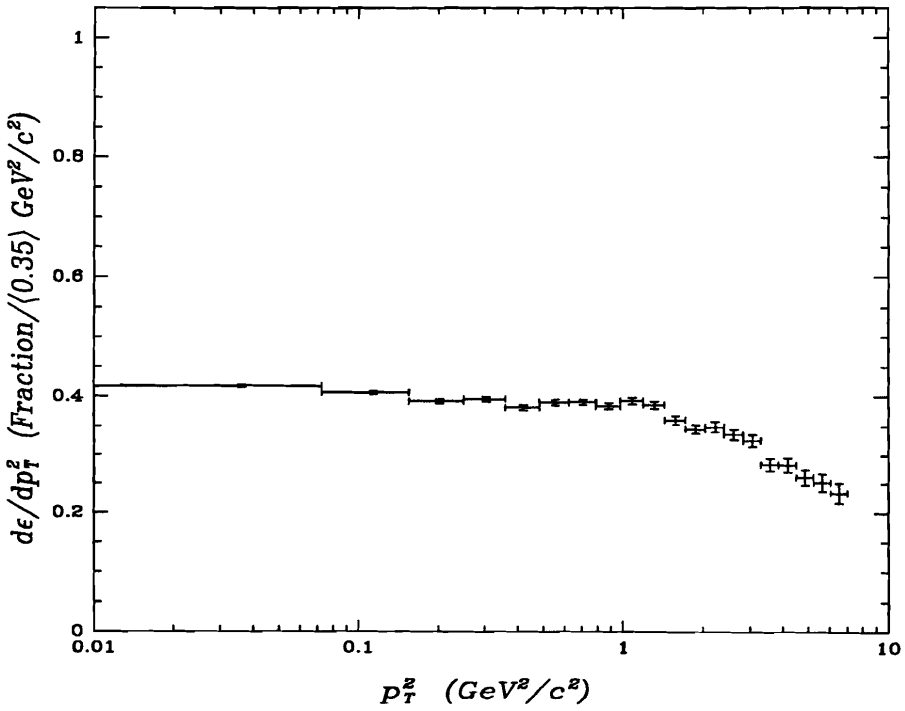

Figure 5.9: The acceptance × smearing as a function of the transverse momentum squared, p_T^2.

Although $66 \pm 1\%$ of the inelastic data from the $0.90 < z < 0.99$ region was misidentified as elastic after the E_{Xmiss} correction, this corresponded to only $16 \pm 1\%$ of the total (elastic plus feedthrough inelastic) data in the elastic region.

The (z_{crctd}, p^2_{Trec}) data was divided into 120 cells, projecting out to 6 bins in z and 20 bins in p_T^2. The dimensions of the cells were constrained by the requirement that the diagonals of the z and p_T^2 smearing matrices have probabilities greater than 0.5. Otherwise the matrices are ill-conditioned making the smearing corrections too sensitive to fluctuations in the off-diagonal elements. Conversely, binning the data entails a loss of information. Thus one attempts to bin the data with the smallest cell dimensions possible. The dimensions of the (z_{crctd}, p^2_{Trec}) cells were chosen to optimize between these two conflicting requirements.

To completely parametrize the overall acceptance for an event, two variables for each muon from the $J/\psi \rightarrow \mu^+\mu^-$ decay are needed. The overall acceptance is a convolution of the geometric acceptance, the dimuon trigger efficiency and the efficiencies of the reconstruction and analysis cuts. One intuitive choice for the dimuon variables is

$$p_{z\ fast},\ \theta_{fast},\ p_{z\ slow},\ \theta_{slow},\quad p_{z\ fast} > p_{z\ slow}, \tag{5.9}$$

the longitudinal momenta and opening angles of the two muons. However, if the Monte Carlo event generation and detector simulation are well tuned, the acceptance can be parametrized in terms of the kinematic variable(s) of interest. All other parameters are then properly integrated out. Thus the the acceptance can be parametrized as a function of z and p_T^2. The z dependence and p_T^2 dependence of the acceptance are shown in Figures 5.6 and 5.7, respectively. These plots are the projections of the (z, p_T^2) acceptance onto the z and p_T^2 axes. The acceptance was generated by dividing the (z, p_T^2) distribution of *generated* events that passed the geometric acceptance cut, fired the dimuon trigger and passed the reconstruction and analysis cuts by the (z, p_T^2) distribution of all generated events.

To correct the data for both the smearing and acceptance, the acceptance distribution was convoluted with the smearing by dividing the (z_{crctd}, p^2_{Trec}) distribution, of *reconstructed* and $\langle E_{Xmiss} \rangle$ corrected events, by the (z, p_T^2) distribution of all generated events. The z dependence and p_T^2 dependence of the acceptance $\times$ smearing convolution are shown in Figures 5.8 and 5.9, respectively. Dividing the $dN/dz_{crctd}dp^2_{Trec}$ data by this acceptance $\times$ smearing gave the $d\sigma/dzdp_T^2$ distribution.

The $d\sigma/dz$ data are displayed in Figure 5.10. In the deep inelastic region, where perturbative QCD is valid, the data are fit by the solid colour–singlet PGF curve normalized to the measured cross section. The $\langle z \rangle$ for the deep inelastic region is $0.68 \pm 0.01\ ^{+0.03}_{-0.05}$. The extrapolation of the PGF curve to the elastic region is shown by the dashed $(- - -)$ curve. Also shown is the dotted $(\cdots)$ curve of the ψ' contribution to the z distribution. To estimate the $\psi' \rightarrow (J/\psi)$ *anything* component [PDG 90] of the $d\sigma/dz$ data it was assumed that the ψ' had the same z distribution as the J/ψ. The J/ψ is the $c\bar{c}$ vector meson ground state and the ψ' is the first radially excited state. Also, both states have the same quantum numbers, $I^G(J^{PC}) = 0^-(1^{--})$. Thus the hypothesis that the J/ψ and ψ' have the same differential distributions was used. The z distribution for the ψ' was normalized to the measured cross section. For $d\sigma/dp_T^2$, the deep inelastic data are displayed in Figure 5.11 and the $\langle p_T^2 \rangle$ is listed in Table 5.10. Both distributions are well fit by the colour–singlet PGF differential equation [Ber 81]

$$\left(\frac{d\sigma}{dzdp_T^2}\right)_{deep\ inel.} = \frac{1}{N_{deep\ inel.}} \frac{xG(x)z(1-z)m_\psi^4}{[m_\psi^2(1-z)+p_T^2]^2}\left\{\frac{1}{(m_\psi^2+p_T^2)^2} + \frac{(1-z)^4}{[p_T^2+m_\psi^2(1-z)^2]^2} + \frac{z^4 p_T^4}{(m_\psi^2+p_T^2)^2[p_T^2+m_\psi^2(1-z)^2]^2}\right\} \quad (5.10)$$

where $N_{deep\ inel.}$ is the normalization to the measured deep inelastic cross section. Counting rules and momentum constraints, [Far 74] and [Gun 74], motivate a parametrization for the gluon structure function of the form

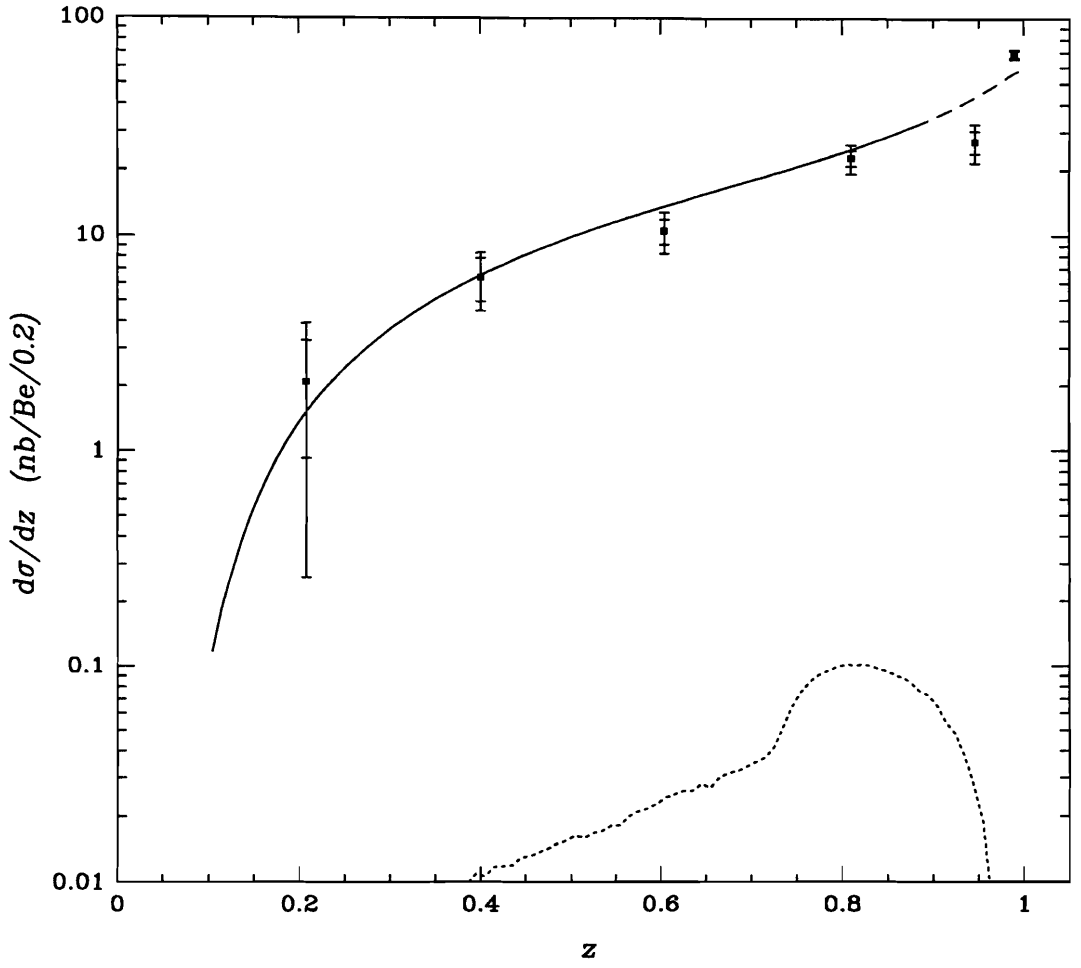

Figure 5.10: The z dependence of J/ψ cross section. The data in the in the deep inelastic region, where perturbative QCD is valid, are fit by the colour–singlet photon–gluon–fusion solid curve normalized to the measured cross–section. The inner error is statistical and the outer error includes, in quadrature, all systematic errors except those associated with the absolute scale. Also shown is the dotted $(\cdots)$ curve of the ψ' contribution to the z distribution.

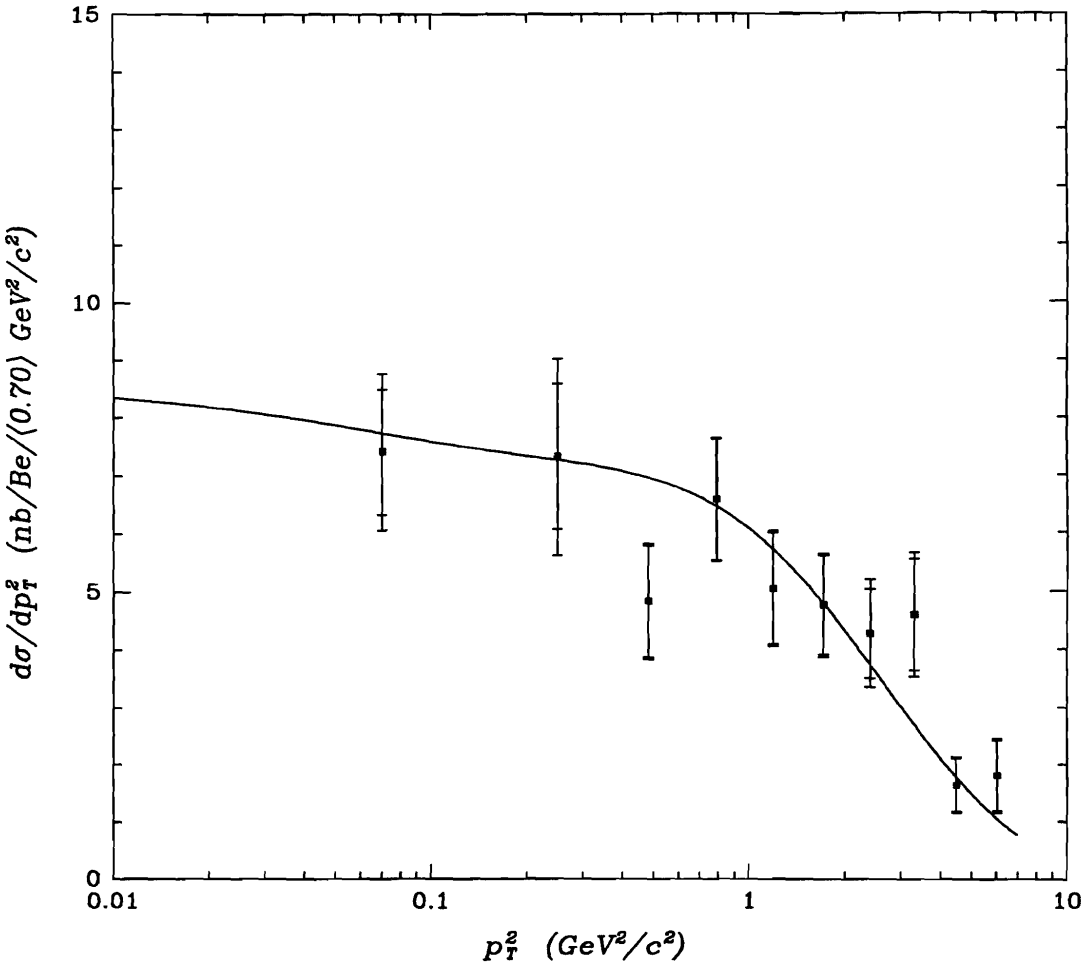

Figure 5.11: The p_T^2 dependence of the deep inelastic J/ψ cross section. The data are fit by the photon–gluon–fusion curve, described in the text, normalized to the measured cross section. The inner error is statistical and the outer error includes, in quadrature, all systematic errors except those associated with the absolute scale.

$$xG(x) = \frac{n_g + 1}{2}(1 - x)^{n_g} \tag{5.11}$$

where x is the fraction of the target nucleon 4-momentum carried by the gluon, g_1,

$$p_{g_1} = xp_N \tag{5.12}$$

and p_N is the 4–momentum of the target nucleon. Expressed first in terms of the invariant Mandelstam variables and then in the lab frame

$$x = -\frac{t}{(1-z)s} \tag{5.13}$$

$$= \frac{m_\psi^2 - 2E_\gamma\left[(E_\gamma/z) - \sqrt{(E_\gamma/z)^2 - p_T^2 - m_N^2}\right]}{(1-z)(2m_N E_\gamma + m_N^2)} \tag{5.14}$$

$$\simeq \frac{1}{2m_N E_\gamma}\left[\frac{m_\psi^2}{z} + \frac{p_T^2}{z(1-z)}\right], \quad (p_T^2 + m_N^2)/(zE_\gamma) \ll 1 \tag{5.15}$$

where kinematically allowed values of x lie within the interval $m_\psi^2/2m_N E_\gamma < x < 1$. The $xG(x)$ distribution for the deep inelastic J/ψ data is obtained from Equation 5.10 by integrating over the kinematically accessible region of the (z, p_T^2) phase space for fixed x

$$\underbrace{\int_z \int_{p_T^2}}_{fixed\ x}\left(\frac{d\sigma}{dz dp_T^2}\right)_{deep\ inel.} = xG(x)\underbrace{\int_z \int_{p_T^2}}_{fixed\ x} f(m_\psi^2, z, p_T^2) \tag{5.16}$$

The E691 data are sensitive to $xG(x)$ in the x range $[0.03, 0.25]$.

The $S(x, x_{crctd})$ smearing matrix, shown in Table 5.9, was obtained using the Monte Carlo to plot x_{crctd} as a function of the generated (true) x and normalizing each column of x in the $S(x, x_{crctd})$ plot by its sum. Recall that unlike the acceptance correction, the shape of a smeared distribution is a function of the shape of the true distribution. Thus each event entered in plot was weighted by the flux multiplied by the theoretical (E_γ, z, p_T^2) function. With the $S(x, x_{crctd})$ matrix, the $x_{crctd}G(x_{crctd})$

data was unsmeared using a χ^2 minimization method. The χ^2 expression was defined as

$$\chi^2 \equiv \sum_{i=1}^{4}\sum_{j=1}^{4} \frac{\left\{n_i - \left[S(x, x_{crctd})\right]_{ij} m_j\right\}^2}{n_i} \tag{5.17}$$

where

- $\left[S(x, x_{crctd})\right]_{ij} \equiv$ the $ijth$ element of the (x, x_{crctd}) smearing matrix
- $n_i \equiv$ the number of reconstructed events in the ith x_{crctd} bin
- $m_j \equiv$ the number of unsmeared events in the jth x bin, constrained to physical values by

$$m_i > 0, \text{ for all } i = 1,4 \tag{5.18}$$

$$m_i < \sum_i m_i \text{ for all } i = 1,4 \tag{5.19}$$

$$\sum_i m_i = \sum_i n_i \tag{5.20}$$

The number of unsmeared events in the m_i bins was varied until a minimum χ^2 value was obtained.

The acceptance as a function of x is shown in Figure 5.12. As $x \propto 1/E_\gamma$, the variation in dN_γ/dx due to the bremsstrahlung spectrum of the photon flux, shown in Figure 5.13, must also be corrected for. The $xG(x)$ dependence of the deep inelastic J/ψ data (background subtracted and corrected for $\langle E_{Xmiss}\rangle$, smearing, acceptance and flux), is displayed in Figure 5.14. The data are fit by the $xG(x)$ parametrization of Equation 5.11, normalized to 1/2.

The only scale in the deep inelastic colour–singlet PGF process shown in Figure 5.15 is $\hat{s}$. Thus $\hat{s}$ was taken to be the argument of the strong coupling constant, $\alpha_S = \alpha_S(\mu^2 = \hat{s}^2)$, giving

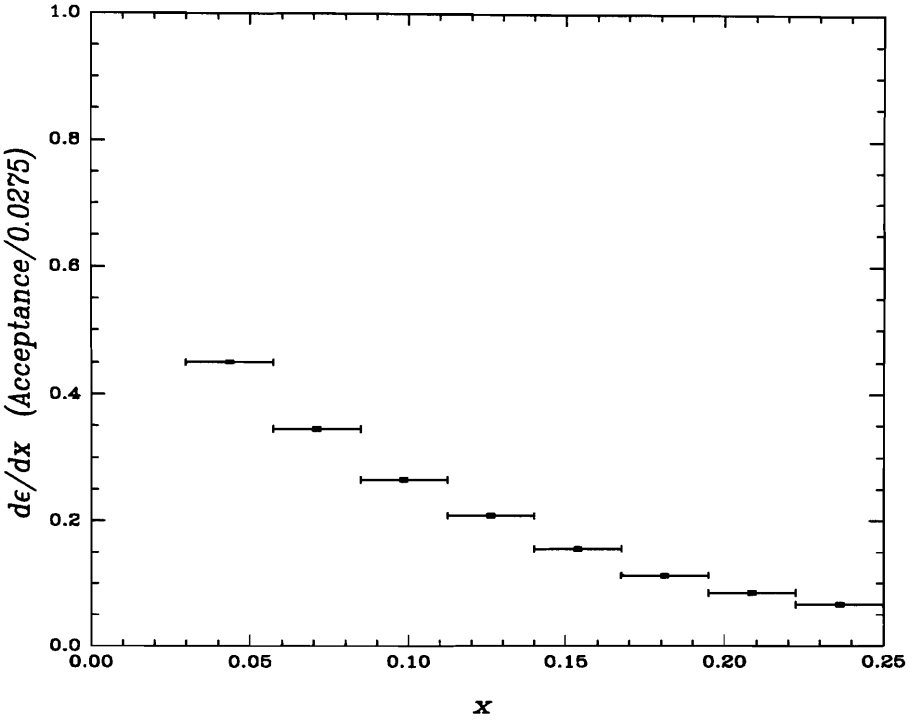

Figure 5.12: The acceptance as a function of the gluon momentum fraction, x.

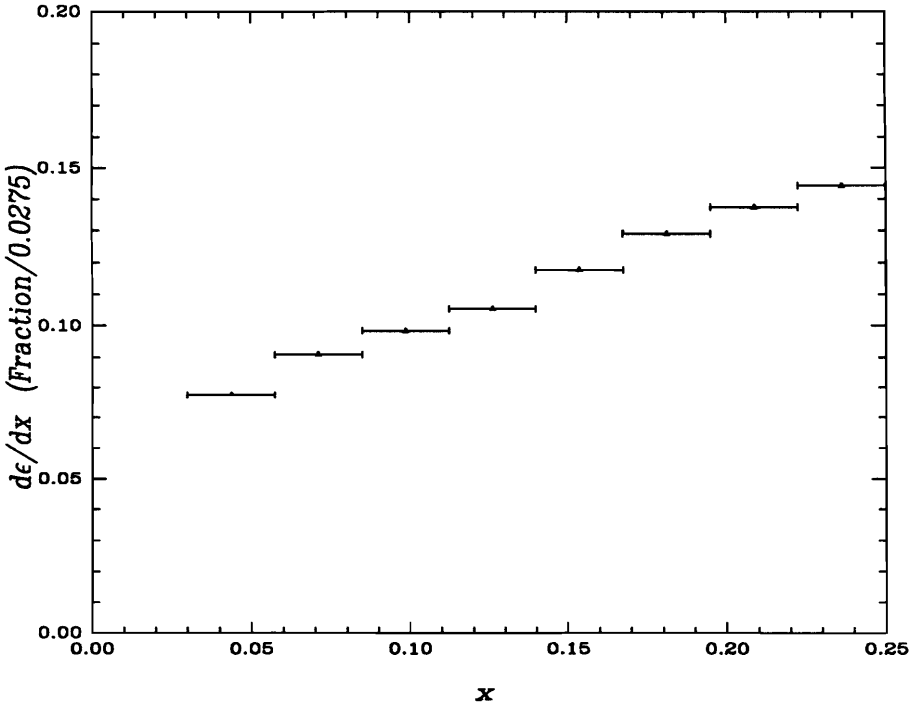

Figure 5.13: The relative flux as a function of the gluon momentum fraction, x.

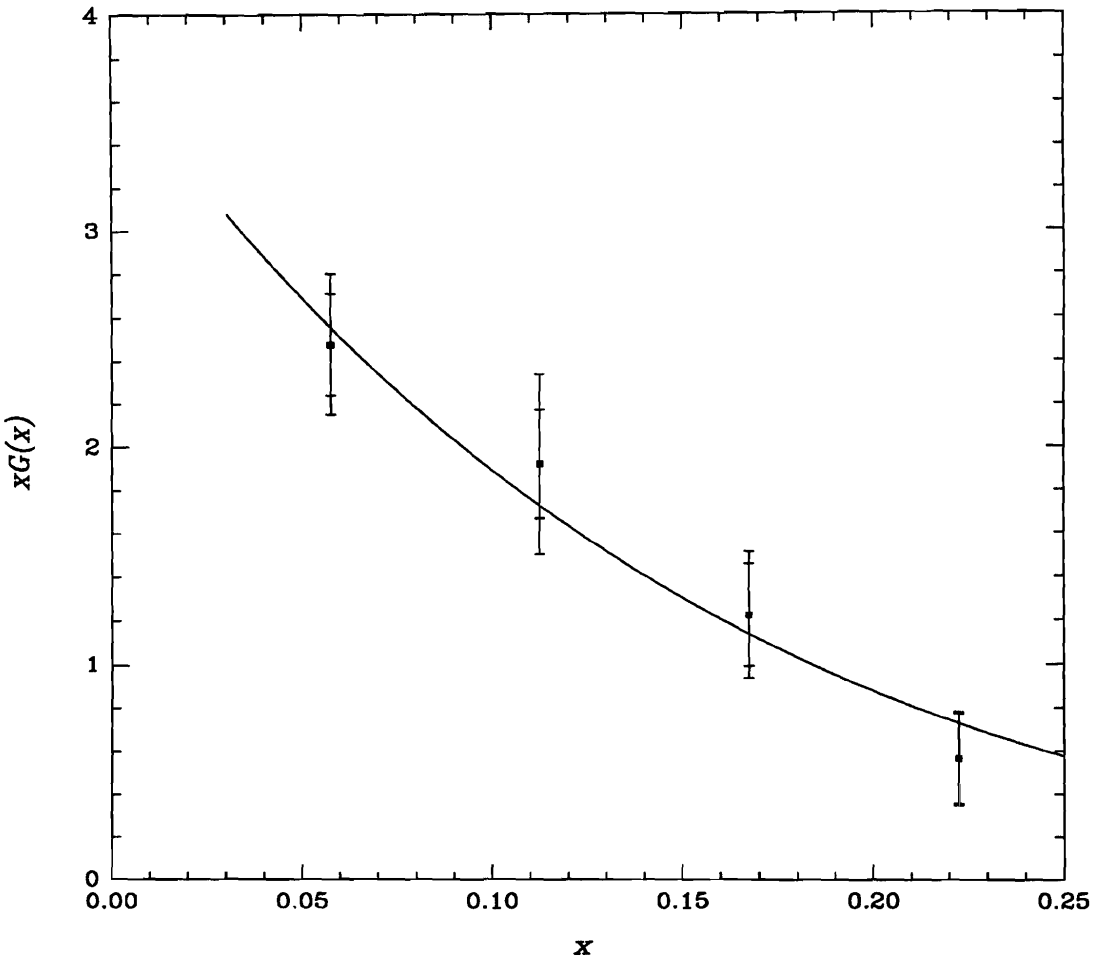

Figure 5.14: The $xG(x)$ distribution of the deep inelastic J/ψ data. The data are fit by the parametrization of the gluon structure function, described in the text, normalized to 1/2. The inner error is statistical and the outer error includes, in quadrature, all systematic errors except those associated with the absolute scale.

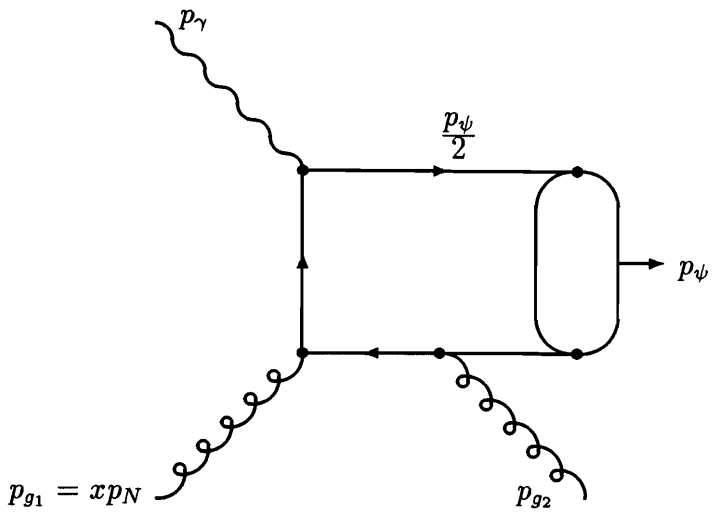

Figure 5.15: The 4–momentum flow in the lowest order diagram of the colour–singlet J/ψ photon–gluon–fusion model.

$$\mu^2 = (p_\gamma + p_{g_1})^2 \tag{5.21}$$

$$= 2xm_N E_\gamma \tag{5.22}$$

first in terms of Lorentz invariant s and then in the lab frame. Note that in Figure 5.15 the charm and anti charm quarks each carry one–half of the J/ψ 4–momentum, $p_c = p_{\bar{c}} = p_\psi/2$. A scaling distribution was assumed for $xG(x)$ at least in part because the accessible range of μ^2 is narrow, as shown in the Monte Carlo generated Figure 2.6, since the invariant mass of the produced J/ψ plus radiated gluon peaks sharply near threshold. Thus the $\langle\mu^2\rangle$ was estimated, from the Monte Carlo, to be 22 GeV^2 with a $\pm\sigma$ range of [16, 26] GeV^2. As α_S varies logarithmically with μ^2, it was taken to be a constant over the small accessible range of μ^2 with a value of 0.24.

In the elastic region, $z > 0.99$, the coherent elastic data was fit by a simple exponential [Per 74]

$$\left(\frac{d\sigma}{dp_T^2}\right)_{coh.\ el.} = \frac{1}{N_{coh.\ el}} \exp(-ap_T^2) \tag{5.23}$$

and the incoherent elastic data was fit by the single scattering approximation of the Glauber model [Gla 69]

$$\left(\frac{d\sigma}{dp_T^2}\right)_{incoh.\ el.} = \frac{1}{N_{incoh.\ el}} \exp(-bp_T^2)\left[1 - \left(1 + \frac{a_0^2 p_T^2}{12}\right)\exp(-a_0^2 p_T^2)\right] \tag{5.24}$$

where a_0^2 was taken from theory [Hof 63] to be 62.5 GeV^2. In incoherent elastic production, the final nuclear state is orthogonal to the initial nuclear ground state. It is not possible for a collision in the limit of $t \simeq p_T^2 \to 0$ to induce such a transition; the scattering matrix element vanishes due to the orthogonality of the initial and final states. As it was not possible to resolve values of z in the elastic region, the coherent and incoherent elastic $d\sigma/dz$ were taken to be uniform over this interval

$$\left(\frac{d\sigma}{dz}\right)_{elastic} = \frac{1}{N_{elastic}} \frac{1}{(1 - z_{min.\ el.})} \tag{5.25}$$

where $N_{elastic}$ is the normalization to the total (coherent plus incoherent) elastic cross section with $z_{min.\ el.} = 0.99$.

Thus, to summarize, the overall fit to the $d\sigma/dzdp_T^2$ distribution is given by

- inelastic region, $z < 0.99$,

$$\frac{1}{\sigma}\frac{d\sigma}{dzdp_T^2} = \epsilon_{inel.}\left(\frac{dP}{dzdp_T^2}\right)_{inel.} \tag{5.26}$$

- elastic region, $z > 0.99$,

$$\begin{aligned} &\frac{1}{\sigma}\frac{d\sigma}{dzdp_T^2} \\ = \quad &(1 - \epsilon_{inel.})\left(\frac{dP}{dz}\right)_{el.}\left[\epsilon_{coh.\ el.}\left(\frac{dP}{dp_T^2}\right)_{coh.\ el.} + (1 - \epsilon_{coh.\ el.})\left(\frac{dP}{dp_T^2}\right)_{incoh.\ el.}\right] \\ &+ \epsilon_{inel.}\left(\frac{dP}{dzdp_T^2}\right)_{inel.} \end{aligned} \tag{5.27}$$

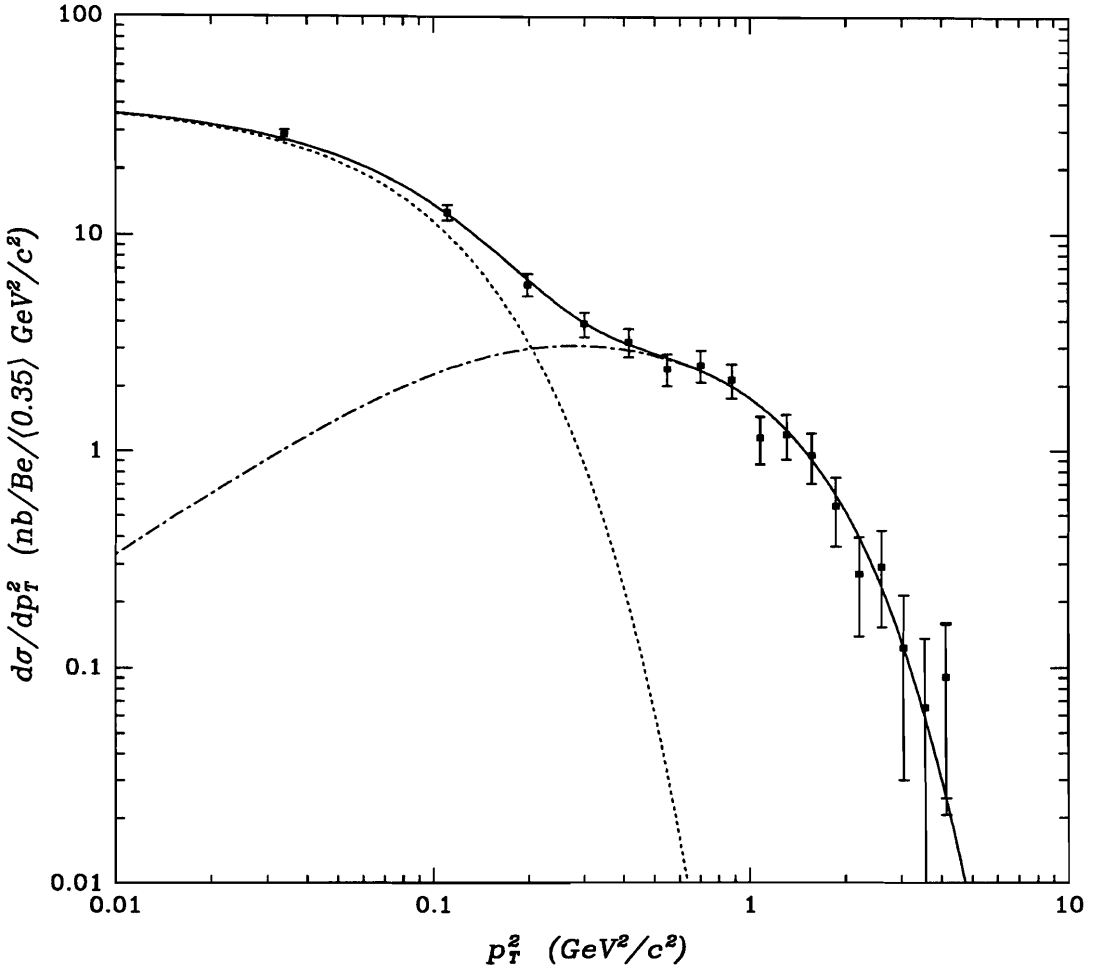

Figure 5.16: The p_T^2 dependence of the elastic J/ψ cross section. The coherent elastic production data are fit by the dotted ($\cdots$) curve and the incoherent elastic production data are fit by the dash–dotted ($-\cdot-$) curve. Both curves are described in the text. The sum of the two fits to the data is given by the solid curve. Only the total point–to–point errors are shown, not the errors associated with the absolute scale.

where the $(dP/dz)_{el.}$, $(dP/dp_T^2)_{coh.\ el.}$, $(dP/dp_T^2)_{incoh.\ el.}$ and $(dP/dzdp_T^2)_{coh.\ el.}$ are the probability densities obtained by normalizing the differential cross sections given in Equations 5.25, 5.23, 5.24 and 5.10, respectively, $\epsilon_{in} \in [0,1]$ is the inelastic fraction of the total data and $\epsilon_{ce} \in [0,1]$ is the coherent elastic fraction of the elastic data. A binned maximum likelihood fit, weighted by the acceptance $\times$ smearing, was used to fit to the 120 cells in (z, p_T^2) with 6 bins in z_{crctd} and 20 bins in p_{Trec}^2. Note that for the deep inelastic data, the value for n_g was obtained from a binned maximum likelihood fit directly to the $xG(x)$ data shown in Figure 5.14.

Systematic Errors

To ensure that the statistical uncertainty in the Monte Carlo distributions would not contribute as a source of systematic uncertainty in the corrections to the real J/ψ data sample, a sample of 200,000 Monte Carlo events was generated. After reconstruction and analysis cuts this sample yielded about 80,000 events. Thus the average statistical uncertainty in the Monte Carlo data was $\sqrt{80,000 \text{ Monte Carlo events}}/\sqrt{1225 \text{ real data events}} \sim 8$ times smaller than that of the real data.

The dominant source of systematic point–to–point errors in the differential distributions was the uncertainty in the photon energy due to the missing forward energy. Using the Monte Carlo the mean missing forward energy was parametrized in cells of inelasticity and J/ψ energy. As the missing forward energy distributions in each cell were asymmetric a set of fits was used to extract the errors corresponding to 34% of the areas above and below the mean missing forward energies. These missing forward energy corrections were incorporated into the data, with the feedthrough from the elastic region into the deep inelastic region a negligible $1.3 \pm 1.0\%$. The data were analyzed after correcting for smearing and acceptance. The results were parametrized and fed back into the Monte Carlo. This procedure was iterated until values for the mean missing forward energy and analysis results converged. The mean missing forward energy was not sensitive to variation of the Lund fragmentation function parameters within their known statistical errors. The photon beam bremsstrahlung spectrum was calculated, for our 250 GeV electron beam, using a

QED–based Monte Carlo that included the finite thickness, Z dependence and inclination (with respect to the electron beam) of the copper radiator, pair production and multiple bremsstrahlung. The Monte Carlo simulation of the detector was tuned to inelastic and elastic J/ψ, open charm and non–charm data. Particular attention was paid to the per–plane tracking efficiencies (within 1% of the data), Cherenkov identification, calorimeter simulations which used shower shapes from data and muon wall efficiencies.

The $\langle E_{X miss} \rangle$ parametrization, shown in Table 5.5, was not sensitive to the choice of the Monte Carlo fragmentation model for the X hadrons: the LUND string model, independent fragmentation or the isospin–conserving phase–space model $N^* \rightarrow N\pi$. However, there is evidence from the analysis of the E691 open charm data that the string model describes data better than independent fragmentation [Anj 90]. The fit to the $d\sigma_{c\bar{c}}/dx_F$ distribution, the distribution most sensitive to fragmentation, gave $\chi^2_{string} = 3.9$ versus $\chi^2_{indep.} = 4.8$. Thus the LUND string model was chosen for the inelastic J/ψ analysis. Note that in the case of the open charm string fragmentation, the $c\bar{c}$ pair can hadronize independently of the target or with one string between the charm quark and the target diquark and another between the anticharm quark and the target quark.

However, unlike the open charm analysis, a transverse momentum cut was not used. To compare the J/ψ p_T^2 to the open charm p_T^2, the J/ψ p_T^2 is analogous to the total p_T^2 of the two charm (mesons) in open charm production and not the p_T^2 of one of the single charm (mesons). A J/ψ may be produced through PGF with zero p_T^2, but radiate a hard recoil gluon making the event deep inelastic. However, in the gluon structure function analysis, we have to consider the uncertainty due to the *intrinsic gluon* $\langle k_T^2 \rangle$. Results from measurements of the Drell–Yan process [Con 89] are inconclusive about the magnitude of the $\langle k_T^2 \rangle$ due to higher order contributions. Nonetheless, a conservative conclusion would be that the intrinsic $\langle p_T^2 \rangle$ of the lepton pair is in the range $0.4 - 0.8$ GeV$^2/c^2$. Depending on the degree of kinematic correlation in the charm quark pair, this gives a intrinsic $\langle p_T^2 \rangle$ of $0.05 - 0.2$ GeV$^2/c^2$ for the

single charm quark. In J/ψ production the charm quark pair are completely correlated, thus we make the conservative assumption that the $\langle k_T^2 \rangle = 0.10 \pm 0.10$ GeV$^2/c^2$. This estimate of the intrinsic gluon $\langle k_T^2 \rangle$ is included, in quadrature, in the deep inelastic $\langle p_T^2 \rangle$ systematic error. Inserting the above quoted values for $\langle E_\gamma \rangle$ and deep inelastic $\langle z \rangle$ into Equation 5.15 and varying p_T^2 from zero to $\langle k_T^2 \rangle$ increases $\langle x \rangle = 0.052$ by 4% corresponding to 4% of the x bin width in Figure 5.14 and a negligible 3% change in n_g.

Table 5.9: The corrected gluon momentum fraction, x_{crctd}, smearing matrix, $S(x, x_{crctd})$, for the deep inelastic region. The errors correspond to the propagation of the uncertainty in $\langle E_{Xmiss} \rangle$.

$x \rightarrow$ / $x_{crctd} \downarrow$	0.030 – 0.085	0.085 – 0.140	0.140 – 0.195	0.195 – 0.250
0.030 - 0.085	$\mathbf{0.84}^{+0.08}_{-0.07}$	$0.07^{+0.05}_{-0.03}$	$0.01^{+0.02}_{-0.00}$	$0.02^{+0.03}_{-0.00}$
0.085 - 0.140	$0.14^{+0.07}_{-0.07}$	$\mathbf{0.78}^{+0.04}_{-0.05}$	$0.32^{+0.19}_{-0.16}$	$0.07^{+0.03}_{-0.11}$
0.140 - 0.195	$0.01^{+0.01}_{-0.00}$	$0.13^{+0.06}_{-0.08}$	$\mathbf{0.53}^{+0.06}_{-0.09}$	$0.41^{+0.16}_{-0.18}$
0.195 - 0.250	$0.01^{+0.00}_{-0.00}$	$0.02^{+0.03}_{-0.01}$	$0.14^{+0.08}_{-0.10}$	$\mathbf{0.50}^{+0.11}_{-0.28}$

Table 5.10: Results of fits to the p_T^2 dependence of coherent and incoherent elastic J/ψ photoproduction and to $xG(x)$ for deep inelastic J/ψ production. The fit parameters are discussed in the text. Unless explicitly stated, the errors on the parameters include systematic errors.

Production mechanism	$\langle p_T^2 \rangle$ (GeV$^2/c^2$)	Fit Parameter
Deep inelastic $z < 0.90$	$1.20 \pm 0.05\ ^{+0.13}_{-0.17}$	$n_g = 6.5 \pm 1.1\ ^{+1.0}_{-0.6}$ in Eq. 5.11
Coherent elastic $z > 0.99$	0.070 ± 0.007	$a = 14.3 \pm 1.5$ (GeV$^2/c^2)^{-1}$ in Eq. 5.23
Incoherent elastic $z > 0.99$	0.62 ± 0.005	$b = 1.72 \pm 0.18$ (GeV$^2/c^2)^{-1}$ in Eq. 5.24

5.4 The Energy Dependence of the J/ψ Cross Section

To measure the energy dependence of the deep inelastic and total (coherent plus incoherent) J/ψ cross sections, the reconstructed forward energy, E_{rec}, data were first separated into deep inelastic and total elastic sets using the missing forward energy corrected inelasticity, z_{crctd}. Both sets of data were background subtracted. Only the deep inelastic data were then corrected for $\langle E_{Xmiss} \rangle$ and smearing. These corrections were negligible in the elastic data. Finally, both sets of data were corrected for the energy dependence of the acceptance and the photon flux yielding the energy dependence of the cross sections.

The smearing matrices for E_{rec} were generated using the Monte Carlo. To quantify the smearing, the matrix elements, shown in Tables 5.11 and 5.12, were normalized to unity over the columns of the generated photon energy, E_γ. Recall that for inelastic J/ψ events, hadronization of the radiated gluon and the target fragments produces a shower of particles that is boosted forward, in the lab frame, into the detector. The energy of this shower is,

$$E_X = E_\gamma + m_N - E_\psi \tag{5.28}$$

The detector has a limited geometric acceptance. Within this acceptance the tracking and calorimetry have detection efficiencies less than unity. Furthermore, not all the detected particles are successfully identified by the reconstruction algorithms. Thus the true shower energy consists of a reconstructed part and a missing part,

$$E_X = E_{Xrec} + E_{Xmiss} \tag{5.29}$$

The shift of E_{rec} into the lower energy (off-diagonal) matrix elements is due to this forward energy missed by the reconstruction,

$$E_{rec} = E_\gamma - E_\psi \tag{5.30}$$

Table 5.11: The reconstructed photon energy smearing matrix, $S_{deep\ inel.}(E_\gamma, E_{rec})$, for deep inelastic production.

E_{rec} (GeV) $\rightarrow$ / E_γ (GeV) $\downarrow$	90 – 130	130 – 170	170 – 210
90 – 130	0.99	0.51	0.06
130 – 170	0.01	0.49	0.55
170 – 210	0.00	0.00	0.39

Table 5.12: The reconstructed photon energy smearing matrix, $S_{tot.\ elast.}(E_\gamma, E_{rec})$, for total elastic production.

E_{rec} (GeV) $\rightarrow$ / E_γ (GeV) $\downarrow$	90 – 130	130 – 170	170 – 210
90 – 130	1.00	0.00	0.00
130 – 170	0.00	1.00	0.00
170 – 210	0.00	0.00	1.00

To correct for the missing forward energy, the parametrization of $\langle E_{Xmiss} \rangle$ in terms of z_{rec} and $E_{\psi rec}$ in Table 5.5 was used. The smearing matrix, $S_{deep\ inel.}(E_\gamma, E_{crctd})$, for the corrected forward energy,

$$E_{crctd} = E_{rec} + \langle E_{Xmiss}(z_{rec}, E_{\psi rec}) \rangle \tag{5.31}$$

is shown in Table 5.13. The errors are the propagation of the uncertainty in the average missing energy correction. As the missing energy is not known event by event, one can only correct for E_{Xmiss} statistically. For such a statistical correction $\langle E_{Xmiss} \rangle$ was used as opposed to the E_{Xmiss} distribution in each $(z_{rec}, E_{\psi rec})$ cell. Throwing random values of E_{Xmiss} using these distributions would have introduced *additional* smearing into the E_{crctd} distribution. The deep inelastic bin size was chosen so that the diagonal elements of $S_{deep\ inel.}(E_\gamma, E_{crctd})$ would all have probabilities greater than 0.5 in order to avoid ill–conditioned matrices. The total elastic bin size was chosen

to be the same as that of the deep inelastic. As $S_{tot.\ elast.}$ is the identity matrix, no smearing corrections are necessary for the total elastic data.

Table 5.13: The corrected photon energy smearing matrix, $S_{deep\ inel.}(E_\gamma, E_{crctd})$, for deep inelastic production. The errors correspond to the uncertainty in $\langle E_{Xmiss} \rangle$.

E_{crctd} (GeV) $\rightarrow$ / E_γ (GeV) $\downarrow$	90 - 130	130 - 170	170 - 210
90 - 130	$0.70^{+0.17}_{-0.14}$	$0.17^{+0.09}_{-0.07}$	0.00
130 - 170	$0.30^{+0.14}_{-0.17}$	$0.66^{+0.01}_{-0.07}$	$0.23^{+0.09}_{-0.10}$
170 - 210	0.00	$0.17^{+0.14}_{-0.10}$	$0.77^{+0.10}_{-0.09}$

The $S_{deep\ inel.}(E_\gamma, E_{crctd})$ smearing matrix was used to unsmear the E_{crctd} data using a χ^2 minimization method. The χ^2 expression was defined as

$$\chi^2 \equiv \sum_{i=1}^{3}\sum_{j=1}^{3} \frac{\left\{ n_i - \left[S_{deep\ inel.}(E_\gamma, E_{crctd}) \right]_{ij} m_j \right\}^2}{n_i} \tag{5.32}$$

where

- $\left[S_{deep\ inel.} \right]_{ij} \equiv$ the $ijth$ element of the (E_γ, E_{crctd}) smearing matrix
- $n_i \equiv$ the number of reconstructed events in the ith E_{crctd} bin
- $m_j \equiv$ the number of unsmeared events in the jth E_γ bin, constrained to physical values by

$$m_i > 0, \text{ for all } i = 1,3 \tag{5.33}$$

$$m_i < \sum_i m_i \text{ for all } i = 1,3 \tag{5.34}$$

$$\sum_i m_i = \sum_i n_i \tag{5.35}$$

The number of unsmeared events in the m_i bins was varied until a minimum χ^2 value was obtained.

The energy dependence of the overall deep inelastic and total elastic acceptance, shown in Figures 5.17 and 5.17, is a convolution of the E_γ dependence of the geometric

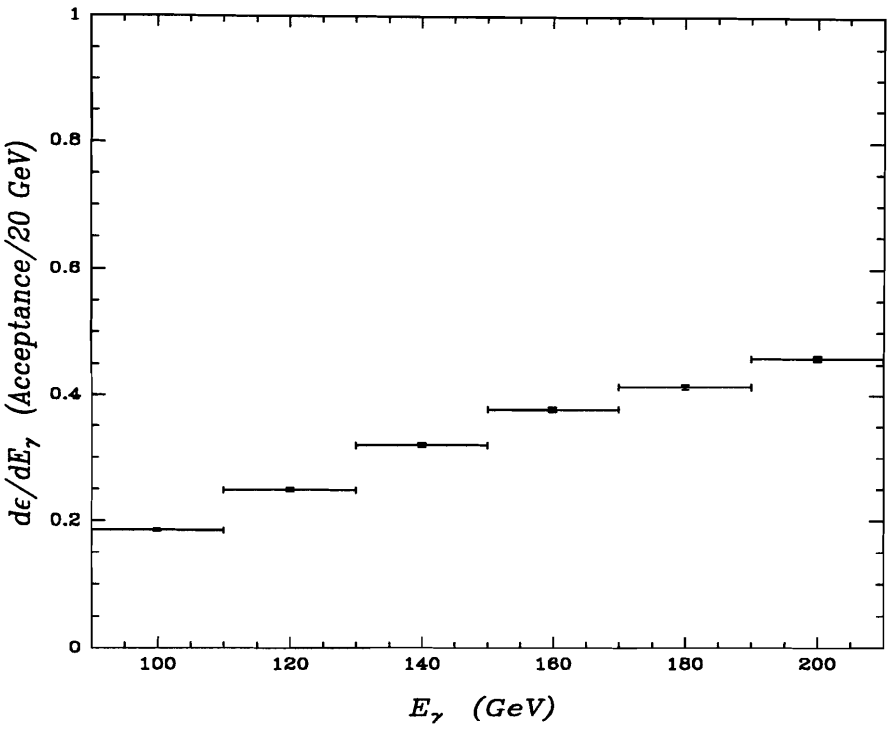

Figure 5.17: The energy dependence of the acceptance for deep inelastic events.

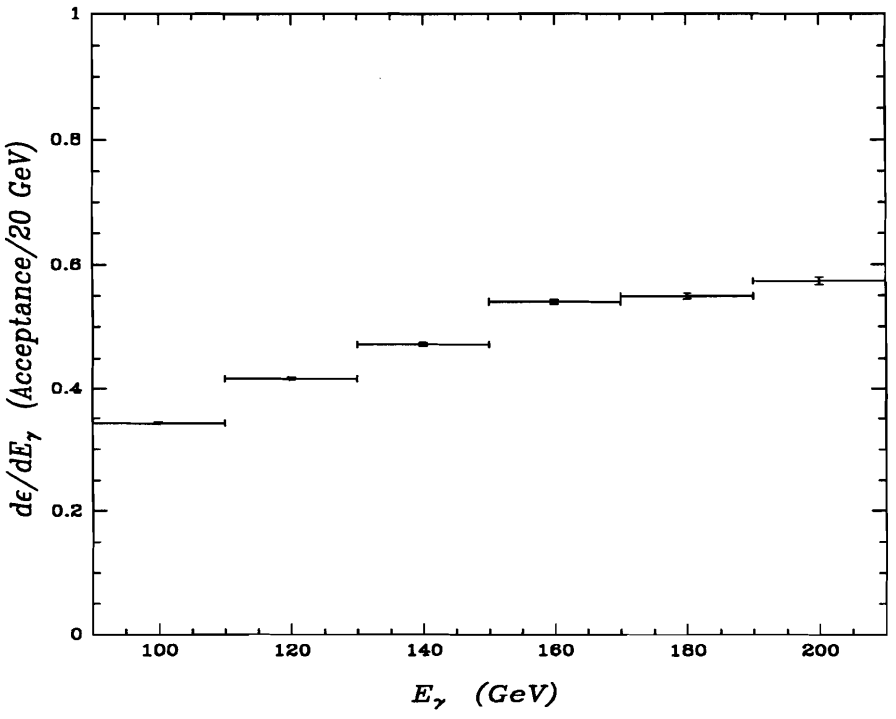

Figure 5.18: The energy dependence of the acceptance for elastic events.

acceptance, the dimuon trigger efficiency and the efficiencies of the reconstruction and analysis cuts. To obtain these acceptance curves, the Monte Carlo reconstructed, $E_{\gamma rec}$, distributions were divided by the generated, E_γ, distributions for deep inelastic and elastic production, respectively.

The photon energy dependence of the deep inelastic and total elastic J/ψ cross sections was then obtained by dividing the corrected data by the overall acceptances and the photon flux, shown in Figure 3.3. The rise of the J/ψ cross sections as a function of the photon energy was quantified as the ratio $\sigma(200\text{ GeV})/\sigma(100\text{ GeV})$. Values from the linear fits to the deep inelastic and total elastic $d\sigma/dE_\gamma$ data are listed in Table 5.14. The energy dependence of the deep inelastic cross section on beryllium is shown in Figure 5.19 along with the PGF curve obtained by integrating $d\sigma/dzdp_T^2$ for E_γ varying from 90 GeV to 210 GeV and normalized to the measured cross section. The inner error is statistical and the outer error also includes, in quadrature, all systematic errors except those associated with the absolute scale. The total elastic data along with the empirical straight line fit, normalized to the measured cross section, are shown in Figure 5.20. Only the total (statistical in quadrature with systematic) point–to–point errors are shown, not the errors associated with the absolute scale.

Table 5.14: Results of the linear fits to the photon energy dependence of the deep inelastic and total (coherent plus incoherent) elastic cross sections.

Production Mechanism	$\frac{\sigma(200\text{ GeV})}{\sigma(100\text{ GeV})}$
Deep Inelastic $z < 0.90$	$1.73 \pm 0.43^{+0.41}_{-0.26}$
Total Elastic $z > 0.99$	1.28 ± 0.15

Systematic Errors

As for the z and p_T^2 distributions, the dominant source of systematic point-to-point error of the deep inelastic E_γ distribution was the uncertainty in the photon energy

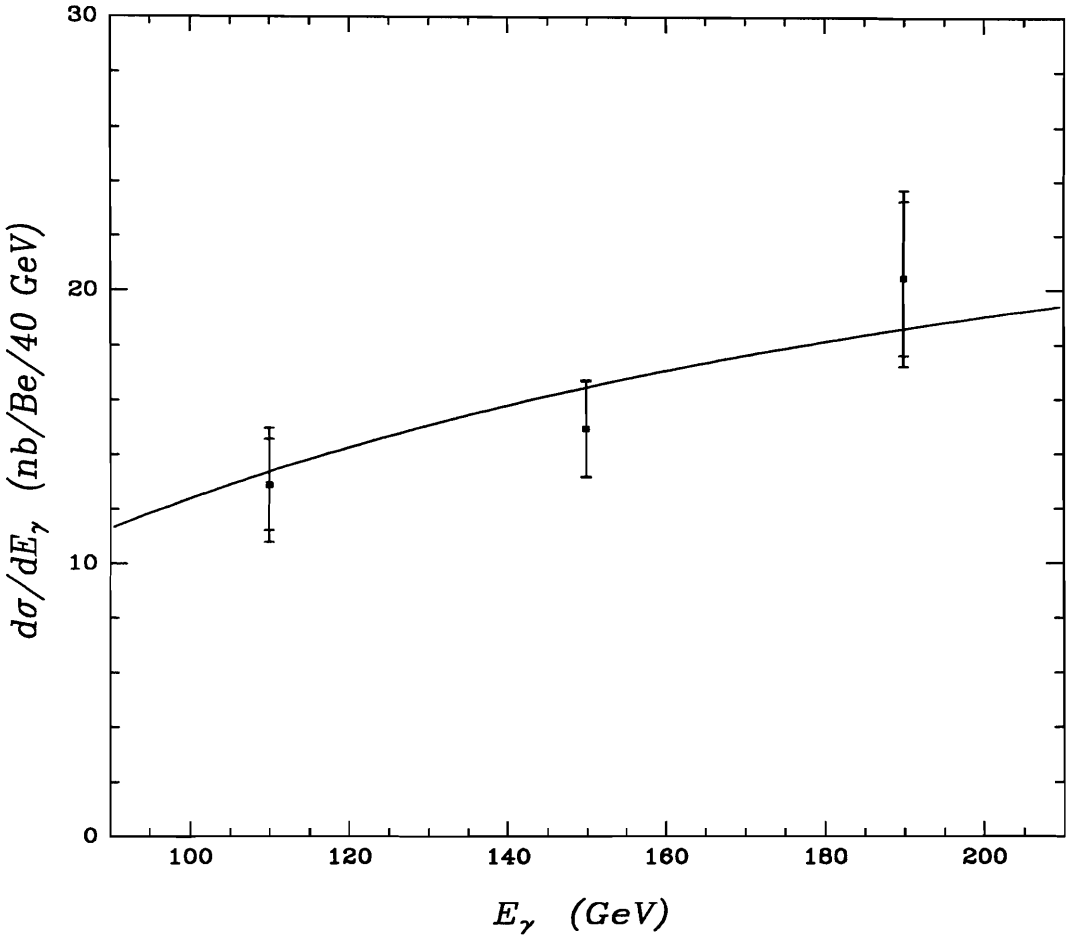

Figure 5.19: The energy dependence of the deep inelastic J/ψ cross section on beryllium. The inner error is statistical and the outer error also includes, in quadrature, all systematic errors except those associated with the absolute scale. Also shown is the photon–gluon–fusion curve, normalized to the measured cross section, described in the text.

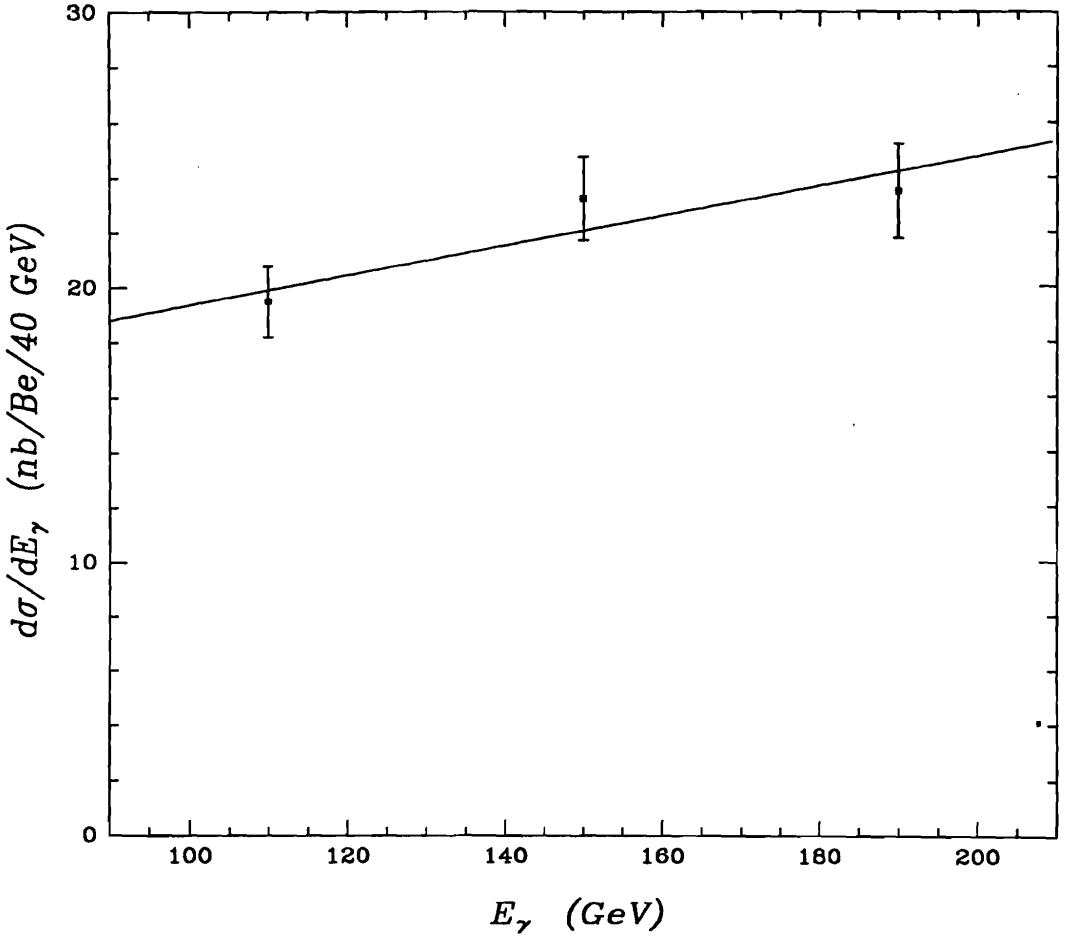

Figure 5.20: The energy dependence of the total (coherent plus incoherent) elastic J/ψ cross section on beryllium. Only the total point–to–point errors are shown, not the errors associated with the absolute scale. The fit is linear.

due to the missing forward energy, $\langle E_{X_{miss}} \rangle$. For a full discussion of this contribution to the systematic error, refer to the previous Section 5.3.

The photon beam bremsstrahlung spectrum, produced by the 250 GeV electron beam incident on the copper radiator and shown in Figure 3.3, was calculated using a QED–based Monte Carlo that included the finite thickness, inclination (with respect to the beam axis) and Z dependence of the radiator, pair production and multiple bremsstrahlung. To check this calculation of the photon flux, the energy dependence of the total hadronic cross section was measured. The tagging system smearing was parametrized using elastic J/ψs. This parametrization was then used to smear the Monte Carlo generated photon flux. Normalizing the energy dependence of hadronic events, measured using the tagging system, by the smeared Monte Carlo photon flux gave the energy dependence of the total hadronic cross section. This energy dependence was found to be essentially flat, in good agreement with previously reported measurements [PDG 90] shown in Figure 5.21.

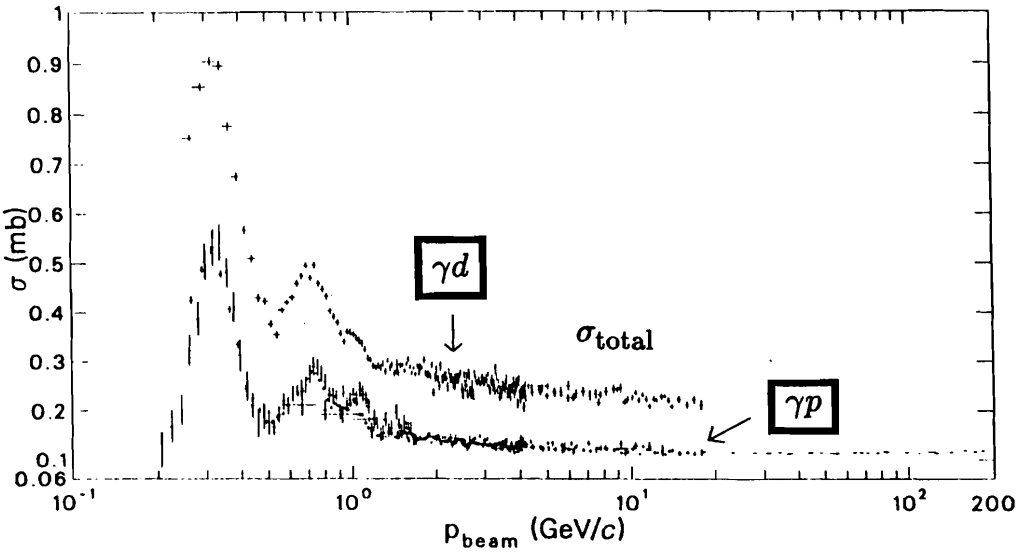

Figure 5.21: Photon total hadronic cross sections versus laboratory beam momentum p_{beam} and total centre–of–mass energy, E_{CM}. Adapted from the Particle Data Book (1990).

5.5 Measurement of the J/ψ and ψ' Cross Sections

The total J/ψ cross section on beryllium, $\sigma_{J/\psi}^{(Be)}$, may be measured by normalizing to the total hadronic photoproduction cross section on beryllium, $\sigma_{TOT}^{(Be)}$.

$$\frac{\sigma_{J/\psi}^{(Be)} \cdot BR(J/\psi \to \mu^+\mu^-)}{\sigma_{TOT}^{(Be)}} = \frac{\text{number of corrected } J/\psi \text{ events}}{\text{number of corrected hadronic events}} \tag{5.36}$$

The events were corrected for livetime and trigger efficiency as follows

$$\frac{\sigma_{J/\psi}^{(Be)} \cdot BR(J/\psi \to \mu^+\mu^-)}{\sigma_{TOT}^{(Be)}} = \frac{N_{J/\psi}^{(B\cdot H)}/(\langle f\rangle_{LT}^{(B\cdot H)}\varepsilon_{dimuon}) + N_{J/\psi}^{(E_T)}/(\langle f\rangle_{LT}^{(E_T)}\varepsilon_{dimuon})}{N_{B\cdot H}/(\langle f\rangle_{LT}^{(B\cdot H)}\varepsilon_{B\cdot H}) + N_{E_T}/(\langle f\rangle_{LT}^{(E_T)}\varepsilon_{E_T})} \tag{5.37}$$

where

- $N_{J/\psi}^{(B\cdot H)} \equiv$ number of observed J/ψ events in the $B \cdot H$ runs
- $N_{J/\psi}^{(E_T)} \equiv$ number of observed J/ψ events in the E_T runs
- $N_{B\cdot H} \equiv$ number of $B \cdot H$ triggered events
- $N_{E_T} \equiv$ number of E_T triggered events
- $\langle f\rangle_{LT}^{(B\cdot H)} \equiv$ average livetime fraction over the $B \cdot H$ runs
- $\langle f\rangle_{LT}^{(E_T)} \equiv$ average livetime fraction over the E_T runs
- $\varepsilon_{dimuon} \equiv$ geometric acceptance $\times$ absolute dimuon trigger efficiency $\times$ reconstruction efficiency $\times$ analysis cuts efficiency
- $\varepsilon_{B\cdot H} \equiv$ absolute $B \cdot H$ trigger efficiency $\times$ geometric acceptance
- $\varepsilon_{E_T} \equiv$ absolute E_T trigger efficiency $\times$ geometric acceptance
- $\sigma_{J/\psi}^{(Be)} \equiv$ total J/ψ cross section on beryllium

- $\sigma_{TOT}^{(Be)} \equiv$ total hadronic photoproduction cross section on beryllium
- $BR(J/\psi \rightarrow \mu^+\mu^-) \equiv J/\psi$ muonic branching ratio

Beginning with a set of 2549 E691 runs, 472 runs were rejected, leaving 2077 good runs. The bad runs were rejected due to problems with one of the $B \cdot H$, E_T or dimuon triggers, missing or inconsistent scaler information or a logbook documented problem in one of the detector systems.

This set of good runs was found to consist of 4.533×10^8 hadronic events corrected for the average livetime and the E_T trigger and the $B \cdot H$ trigger efficiencies. The corrections are listed in Table 5.15. When an event generates a trigger, a finite amount of time is required by the data acquisition system to process the event and write the information to tape. As the data acquisition system will not accept any new triggers during event processing, this interval of time is called the *deadtime*. The data acquisition system indicated that it was in the deadtime state by generating a logical $BUSY$ flag followed by a logical $CLEAR$ notifying that it had completed processing and was ready to accept a new event. Using the ratios of the scalers,

$$f_{DT}^{(B\cdot H)} = \frac{\sum_{run}[(B\cdot H)\cdot(BUSY)]}{\sum_{run}(B\cdot H)} \tag{5.38}$$

$$f_{DT}^{(E_T)} = \frac{\sum_{run}[(E_T)\cdot(BUSY)]}{\sum_{run}(E_T)} \tag{5.39}$$

the $B \cdot H$ and E_T trigger deadtimes for a run were calculated. The $\langle f \rangle_{DT}$ was determined by averaging the deadtime over all the good runs and the average livetime, $\langle f \rangle_{LT}$, is simply

$$\langle f \rangle_{LT} \equiv 1 - \langle f \rangle_{DT} \tag{5.40}$$

Note that the $\langle f \rangle_{LT}$ was determined by the hadronic triggers and not the dimuon trigger, as the dimuon trigger rate was less than 5% of the hadronic trigger rates. The

$B \cdot H$ trigger rejected 99.9% of the electromagnetic events, $\gamma N \rightarrow e^+e^-N$, $\mu^+\mu^-N$, but accepted essentially all the hadronic interactions [Est 86]. Openness of the $B \cdot H$ trigger to hadronic events was due to the low H threshold of 40 GeV, with $H \equiv$ energy deposited in the hadrometer + energy deposited in the SLIC weighted by 12 dB, in coincidence with a signal above the threshold of a single minimum ionizing particle passing through the B counter (the interaction counter immediately downstream of the target). An event that generated a $B \cdot H$ trigger was counted as a hadronic event. The hadronic efficiency of the global weighted transverse energy trigger, E_T, was determined by the fraction of hadronic events above the (more restrictive) E_T trigger threshold.

Table 5.15: The number of hadronic events in the good E691 runs corrected for the average livetime fraction and the trigger efficiency.

Event Type	Number of Observed Events N	Average Livetime Fraction $\langle f \rangle_{LT}$	Absolute Trigger Efficiency ε	Number of Corrected Events $N/(\langle f \rangle_{LT}\varepsilon)$
$B \cdot H$	9.641×10^6	0.3048	1.0	3.163×10^7
E_T	77.98×10^6	0.6350	0.2912	4.217×10^8
Total				4.533×10^8

The good run data set also yielded $4975 \pm 160 \pm 83$ J/ψ events corrected for the livetime, detector acceptance $\times$ dimuon trigger efficiency, reconstruction efficiency and analysis cuts efficiency. The corrections are shown in Table 5.16. Recall that the dimuon trigger consisted of the front segmented scintillator muon wall, the interaction B counter, the two Cherenkov counters and a hadron–stopping steel wall followed by the back segmented scintillator wall. Detailed geometry and efficiency measurements of these detector components were made and incorporated in the Monte Carlo. Using the Monte Carlo, the overall efficiency of the dimuon trigger was measured. For exclusively deep inelastic and elastic events, the dimuon trigger efficiencies were $49 \pm 8\%$ and $58 \pm 10\%$, respectively.

The total photoproduction hadronic cross section on beryllium has been measured

Table 5.16: The number of observed $J/\psi \to \mu^+\mu^-$ events in the good E691 runs and the average livetime fraction and the dimuon trigger, reconstruction and analysis cut efficiencies.

Run Type	Number of Observed J/ψ Events	Average Livetime Fraction $\langle f \rangle_{LT}$	Dimuon Trigger Efficiency × Geometric Acceptance	Reconstruction Efficiency	Analysis Cuts Efficiency
			ε_{dimuon}		
$B \cdot H$	53 ± 8	0.3048	0.55 ± 0.09	0.97	0.75 ± 0.01
E_T	1172 ± 37	0.6350	0.55 ± 0.09	0.97	0.75 ± 0.01
Total	1225 ± 38				

Table 5.17: The number of $\psi' \to J/\psi\pi^+\pi^- \to \mu^+\mu^-\pi^+\pi^-$ events in the good E691 runs corrected for the average livetime fraction and the overall dimuon and $\pi^+\pi^-$ acceptances.

Run Type	Number of Observed ψ' Events $N_{\psi'}$	Average Livetime Fraction $\langle f \rangle_{LT}$	Dimuon Acceptance ε_{dimuon}	$\pi^+\pi^-$ Acceptance $\varepsilon_{\pi^+\pi^-}$	Number of Corrected ψ' Events $N_{\psi'}/(\langle f \rangle_{LT}\varepsilon_{dimuon}\varepsilon_{\pi^+\pi^-})$
$B \cdot H$	1 ± 1	0.3048	0.39 ± 0.08	0.83 ± 0.05	$10 \pm 10 \pm 2$
E_T	8 ± 3	0.6350	0.39 ± 0.08	0.83 ± 0.05	$39 \pm 15 \pm 10$
Total	9 ± 3				$49 \pm 18 \pm 10$

Table 5.18: The number of $J/\psi \to \mu^+\mu^-$ events with the $\psi' \to J/\psi X \to \mu^+\mu^- X$ cascade events, where X corresponds to any allowed particle(s), subtracted and corrected for the average livetime fraction and the dimuon trigger, reconstruction and analysis cut efficiencies listed above in Table 5.16.

Run Type	$\frac{BR(\psi' \to J/\psi\pi^+\pi^-)}{BR(\psi' \to J/\psi\ anything)}$	Number of $\psi' \to J/\psi X$ Events	Number of Observed ($\psi' \to J/\psi X$ Subtracted) J/ψ Events $N_{J/\psi}$	Number of Corrected ($\psi' \to J/\psi X$ Subtracted) J/ψ Events $N_{J/\psi}/(\langle f \rangle_{LT}\varepsilon_{dimuon})$
$B \cdot H$	0.568 ± 0.061	1.8 ± 1.8	51 ± 8	$418 \pm 66 \pm 68$
E_T	0.568 ± 0.061	14.1 ± 5.2	1158 ± 37	$4557 \pm 146 \pm 746$
Total		15.9 ± 5.5	1209 ± 38	$4975 \pm 160 \pm 749$

to be $\sigma_{TOT}^{(Be)} = 861 \pm 40$ μb/Be nucleus [Cal 78, Cal 79, PDG 90]. In order to check the average livetime and absolute trigger efficiency values used in the calculations of Table 5.15, an independent E691 measurement of $\sigma_{TOT}^{(Be)}$ was performed. The value obtained using the E691 data, 834 ± 47 μb/Be nucleus [Pur 87], is in good agreement with the above quoted value.

The ψ' cascade decays $\gamma N \rightarrow \psi' X \rightarrow (J/\psi\ anything)X$ also contribute to the J/ψ cross section. To obtain the direct $\gamma N \rightarrow J/\psi X$ production cross section, these feedthrough events must be first subtracted. Thus the observed $\psi' \rightarrow J/\psi\pi^+\pi^- \rightarrow \mu^+\mu^-\pi^+\pi^-$ events, shown in Figure 5.2, were first corrected for the world average branching ratio of $32.4 \pm 2.6\%$ [PDG 90] normalized to the $\psi' \rightarrow J/\psi\ anything$ world average branching ratio of $57 \pm 4\%$ [PDG 90] and then subtracted from the total number of observed $J/\psi \rightarrow \mu^+\mu^-$ events as shown in Figure 5.18. Substituting the PDG $\sigma_{TOT}^{(Be)}$ measurement and the number of corrected hadronic and J/ψ events from Tables 5.15 and 5.18, respectively, into Equation 5.37 along with the world average $J/\psi \rightarrow \mu^+\mu^-$ branching ratio of $6.9 \pm 0.9\%$ [PDG 90] yielded the E691 total J/ψ cross section on beryllium

$$\sigma_{J/\psi}^{(Be)} = 137 \pm 4 \pm 28 \ \text{nb/Be nucleus} \tag{5.41}$$

at $\langle E_\gamma \rangle = 145$ GeV. The Tagged Photon Collaboration has reported [Sok 86] a measurement of the A^α dependencies of the coherent elastic and incoherent elastic/inelastic J/ψ cross sections to be $\alpha_{coh.\ el.} = 1.40 \pm 0.06 \pm 0.04$ and $\alpha_{incoh.\ el.,\ inelastic} = 0.94 \pm 0.02 \pm 0.03$. From the fit to the differential $d\sigma/dzdp_T^2$ data, the fractions of inelastic and deep inelastic to total production and the fractions of coherent elastic and incoherent elastic to total production were measured. These production fractions were used to determine the J/ψ inelastic and deep inelastic cross sections and the J/ψ coherent and incoherent elastic cross sections on beryllium and per nucleon as listed in Table 5.19. The sum of the inelastic and coherent plus incoherent elastic cross sections per nucleon gives the total J/ψ cross section per nucleon

$$\sigma_{J/\psi}^{(N)} = 14.0 \pm 0.5 \pm 2.3 \text{ nb/nucleon} \tag{5.42}$$

at $\langle E_\gamma \rangle = 145$ GeV.

Table 5.19: Inelastic, deep inelastic, coherent and incoherent elastic J/ψ cross sections, ψ' subtracted, on beryllium and per nucleon.

Production mechanism	Fraction of the total $\sigma_{J/\psi}$ on Be	$\sigma_{J/\psi}$ on Be (nb)	$\sigma_{J/\psi}$ per nucleon (nb)
Deep inelastic $z < 0.90$	$0.35 \pm 0.01 \,^{+0.02}_{-0.04}$	$48 \pm 2 \pm 11$	$6.1 \pm 0.3 \pm 1.5$
Inelastic $z < 0.99$	$0.52 \pm 0.01 \,^{+0.03}_{-0.01}$	$72 \pm 3 \pm 10$	$9.0 \pm 0.4 \pm 2.1$
Coherent elastic $z > 0.99$	$0.300 \pm 0.020 \,^{+0.020}_{-0.008}$	$41.0 \pm 3.0 \pm 6.5$	$1.89 \pm 0.14 \pm 0.49$
Incoherent elastic $z > 0.99$	$0.180 \pm 0.010 \,^{+0.010}_{-0.006}$	$24.7 \pm 1.6 \pm 5.2$	$3.13 \pm 0.20 \pm 0.71$
Total (Inelastic + Coh. Elastic + Incoh. Elastic)		$137 \pm 4 \pm 28$	$14.0 \pm 0.5 \pm 2.3$

The total ψ' cross section on beryllium was determined using Equation 5.43, analogous to the expression for the total J/ψ cross section on beryllium, Equation 5.37.

$$\begin{aligned} &\frac{\sigma_{\psi'}^{(Be)} \cdot BR(\psi' \to J/\psi\pi^+\pi^-) \cdot BR(J/\psi \to \mu^+\mu^-)}{\sigma_{TOT}^{(Be)}} \\ &= \frac{N_{\psi'}^{(B\cdot H)}/(\langle f \rangle_{LT}^{(B\cdot H)} \varepsilon_{dimuon}\varepsilon_{\pi^+\pi^-}) + N_{\psi'}^{(E_T)}/(\langle f \rangle_{LT}^{(E_T)} \varepsilon_{dimuon}\varepsilon_{\pi^+\pi^-})}{N_{B\cdot H}/(\langle f \rangle_{LT}^{(B\cdot H)} \varepsilon_{B\cdot H}) + N_{E_T}/(\langle f \rangle_{LT}^{(E_T)} \varepsilon_{E_T})} \end{aligned} \tag{5.43}$$

where

- $N_{\psi'}^{(B\cdot H)} \equiv$ number of observed ψ' events in the $B \cdot H$ runs
- $N_{\psi'}^{(E_T)} \equiv$ number of observed ψ' events in the E_T runs
- $N_{B\cdot H} \equiv$ number of $B \cdot H$ triggered events
- $N_{E_T} \equiv$ number of E_T triggered events

- $\langle f \rangle_{LT}^{(B\cdot H)} \equiv$ average livetime fraction over the $B \cdot H$ runs
- $\langle f \rangle_{LT}^{(E_T)} \equiv$ average livetime fraction over the E_T runs
- $\varepsilon_{dimuon} \equiv$ geometric acceptance $\times$ absolute dimuon trigger efficiency $\times$ reconstruction efficiency $\times$ analysis cuts efficiency
- $\varepsilon_{\pi^+\pi^-} \equiv$ geometric acceptance $\times$ reconstruction efficiency $\times$ analysis cuts efficiency for $\psi' \rightarrow J/\psi\pi^+\pi^-$ accepted by the dimuon trigger
- $\varepsilon_{B\cdot H} \equiv$ absolute $B \cdot H$ trigger efficiency $\times$ geometric acceptance
- $\varepsilon_{E_T} \equiv$ absolute E_T trigger efficiency $\times$ geometric acceptance
- $\sigma_{\psi'}^{(Be)} \equiv$ total ψ' cross section on beryllium
- $\sigma_{TOT}^{(Be)} \equiv$ total hadronic photoproduction cross section on beryllium
- $BR(\psi' \rightarrow J/\psi\pi^+\pi^-) \equiv \psi'$ branching ratio
- $BR(J/\psi \rightarrow \mu^+\mu^-) \equiv J/\psi$ muonic branching ratio

Substituting the PDG $\sigma_{TOT}^{(Be)}$ measurement and the number of corrected hadronic and ψ' events from Tables 5.15 and 5.18, respectively, into Equation 5.43 along with the world average $\psi' \rightarrow J/\psi\pi^+\pi^-$ and $J\psi \rightarrow \mu^+\mu^-$ branching ratios yielded the E691 total ψ' cross section on beryllium

$$\sigma_{\psi'}^{(Be)} = 4.2 \pm 1.5 \pm 1.1 \text{ nb/Be nucleus} \tag{5.44}$$

at $\langle E_\gamma \rangle = 145$ GeV. The $\psi' \rightarrow (J/\psi)$ *anything* cross section on beryllium was determined to be $2.6 \pm 0.9 \pm 0.6$ nb per beryllium nucleus.

Systematic Errors

Sources of systematic error on the total cross section on beryllium included, in quadrature, the following uncertainties

- $\Delta\varepsilon^{(J/\psi)}_{dimuon\ trigger} \equiv$ the uncertainty in the absolute dimuon trigger efficiency for direct $\gamma N \rightarrow J/\psi X$ production
- $\Delta\varepsilon^{(\psi')}_{dimuon\ trigger} \equiv$ the uncertainty in the absolute dimuon trigger efficiency for cascade $\gamma N \rightarrow \psi' X \rightarrow J/\psi\ anything\ X$ production
- $\Delta\varepsilon_{polarization} \equiv$ the uncertainty in the elastic and inelastic J/ψ and ψ' polarization
- $\Delta BR(J/\psi \rightarrow \mu^+\mu^-) \equiv$ the uncertainty in the world average branching ratio
- $\Delta BR(\psi' \rightarrow J/\psi\ anything) \equiv$ the uncertainty in the world average branching ratio
- $\Delta BR(\psi' \rightarrow J/\psi\pi^+\pi^-) \equiv$ the uncertainty in the world average branching ratio
- $\Delta\sigma^{(Be)}_{TOT} \equiv$ the uncertainty in the total photoproduction hadronic cross section on beryllium

The contributions to the dimuon trigger systematic error of the individual Cherenkov components were estimated by varying, in the Monte Carlo, the 2 photoelectron thresholds by ± 1 photoelectron. This variation in the photoelectron thresholds was performed independently for each of the 28 $C1$ and 32 $C2$ (mirror–plane, Winston cone and phototube) assemblies. To estimate the contributions to the systematic errors of the individual scintillator segments of the back muon wall, the efficiency of each of the 15 scintillators was independently lowered by 5%. From these studies, the maximum systematic variation in the dimuon trigger efficiency from an individual component for direct J/ψ production was found to be no more than $\pm 2.0\%$. This is due, in part, to the combinatoric redundancy of the dimuon trigger. The agreement between the Monte Carlo and the real average absolute efficiency for detection of Cherenkov photons from muons with a momentum distribution from the $J/\psi \rightarrow \mu^=\mu^-$ decay was estimated to be on the order of $\pm 14\%$. For the muon wall, the agreement between the Monte Carlo and the real average absolute efficiency for muon

detection was estimated to be on the order of $\pm 5\%$. These systematic errors taken in quadrature gave an uncertainty, $\Delta\varepsilon^{(J/\psi)}_{dimuon\ trigger}$, in the absolute dimuon trigger efficiency of $\pm 15\%$. The dimuon trigger efficiency was insensitive to the variation, within their respective statistical errors, of the ratio of inelastic to elastic production, n_G (which determines the inelastic $\langle z \rangle$ and $\langle p_T^2 \rangle$), the ratio of coherent to incoherent elastic production and the coherent and incoherent elastic $\langle p_T^2 \rangle$s. The ratio of inelastic to elastic production is not known for cascade J/ψ production. Thus the above variations were also performed for the cascade J/ψ production with the exception that the ratio of inelastic to elastic production was varied from all inelastic to all elastic.

Recall that for the decay of a polarized vector boson into two spin$-1/2$ particles,

$$1 \rightarrow \left(\frac{1}{2}\right)\left(\frac{1}{2}\right) \tag{5.45}$$

such as $J/\psi \rightarrow \mu^+\mu^-$, the decay angular probability density is

$$p(\cos\theta) = \frac{3}{4(2+\eta_L)}\Big[(1-\eta_L)(1+\cos^2\theta) + \eta_L \sin^2\theta\Big] \tag{5.46}$$

where θ is the direction of an emerging muon measured with respect to the direction of the incident photon, observed in the J/ψ centre–of–mass frame and $\eta_L \in [0,1]$, the ratio of the longitudinal (helicity–zero) J/ψ cross section to the total (transverse plus longitudinal) cross section, is

$$\eta_L = \frac{E d\sigma_{\psi_L}/d^3p}{E d\sigma_{\psi}/d^3p} \tag{5.47}$$

where $\sigma_\psi = \sigma_{\psi_L} + \sigma_{\psi_T}$. If η_L is $1/2$, then the J/ψ is unpolarized and the decay angular distribution is isotropic. For deep inelastic production η_L is given by

$$\eta_L^{(deep\ inel.)} = \frac{2z^2 p_T^2 m_\psi^2 \{[m_\psi^2(1-z) + p_T^2]^2 + z^2 p_T^4\}}{(m_\psi^2 + p_T^2)^2 \{[m_\psi^2(1-z)^2 + p_T^2]^2 + (1-z)^4(m_\psi^2 + p_T^2)^2 + z^4 p_T^4\}} \tag{5.48}$$

in the colour–singlet PGF model [Ber 81]. For elastic J/ψ production, the diffractive VMD model [Hum 77] predicts that the J/ψ is produced with maximal transverse polarization, $\eta_L = 0$, like the real incident photon via s channel helicity conservation (SCHC). To determine the systematic error in the dimuon trigger efficiency due to the uncertainty in the J/ψ polarization η_L was varied over the range $\eta_L \in \left[0, \eta_L^{(deep\ inel.)}\right]$ for inelastic production and over the range $\eta_L \in [0, 1/2]$ for elastic production. This systematic error was found to be $\pm 2\%$.

In addition, the systematic errors in the inelastic, deep inelastic and coherent and incoherent elastic cross sections included, in quadrature, the uncertainties in the measured ratios of the these production processes to the total J/ψ production

- $\Delta\varepsilon_{inelastic} \equiv$ the uncertainty in the inelastic production fraction
- $\Delta\varepsilon_{deep\ inel.} \equiv$ the uncertainty in the deep inelastic production fraction
- $\Delta\varepsilon_{coh.\ elastic} \equiv$ the uncertainty in the coherent elastic production fraction
- $\Delta\varepsilon_{incoh.\ elastic} \equiv$ the uncertainty in the incoherent elastic production fraction

The uncertainties in the above production fractions were sensitive to the photon energy and smearing corrections.

Included in the systematic errors in the deep inelastic and coherent and incoherent elastic cross sections per nucleon, in addition, in quadrature, were the uncertainties in the A^α dependence extrapolations from beryllium to hydrogen.

- $\Delta\alpha_{incoh.\ elastic,\ inelastic} \equiv$ the uncertainty in the incoherent elastic/inelastic A dependence exponent
- $\Delta\alpha_{coh.\ elastic} \equiv$ the uncertainty in the coherent elastic A dependence exponent.

The relative magnitudes of all the above systematic errors are listed in Table 5.20.

Table 5.20: Relative magnitudes of the systematic errors on the inelastic, deep inelastic, coherent and incoherent elastic J/ψ cross sections on beryllium and per nucleon.

Systematic Uncertainty	Relative Magnitude (%)
$(\Delta\varepsilon/\varepsilon)^{(J/\psi)}_{dimuon\ trigger}$	$\pm 15.$
$(\Delta\varepsilon/\varepsilon)^{(\psi')}_{dimuon\ trigger}$	$\pm 21.$
$(\Delta\varepsilon/\varepsilon)^{(\psi')}_{\pi^+\pi^-}$	± 3.5
$(\Delta\varepsilon/\varepsilon)_{polarization}$	± 2.0
$(\Delta BR/BR)_{J/\psi\to\mu^+\mu^-}$	$\pm 13.$
$(\Delta BR/BR)_{\psi'\to J/\psi\ anything}$	± 7.0
$(\Delta BR/BR)_{\psi'\to J/\psi\pi^+\pi^-}$	± 8.0
$(\Delta\sigma/\sigma)^{(Be)}_{TOT}$	± 4.6
$(\Delta\varepsilon/\varepsilon)_{inelastic}$	$+5.8, -1.9$
$(\Delta\varepsilon/\varepsilon)_{deep\ inelastic}$	$+5.7, -11.$
$(\Delta\varepsilon/\varepsilon)_{coh.\ elastic}$	$+6.7, -1.5$
$(\Delta\varepsilon/\varepsilon)_{incoh.\ elastic}$	$+5.6, -3.3$
$(\Delta\alpha/\alpha)_{incoh.\ elastic,\ inelastic}$	± 8.9
$(\Delta\alpha/\alpha)_{coh.\ elastic}$	$\pm 15.$

5.6 Comparison of Data and Monte Carlo

The Monte Carlo was used to correct the background subtracted data for E_{Xmiss}, smearing and acceptance. The corrected data were analyzed, the results were parametrized and fed back into the Monte Carlo. This procedure was iterated until values for $\langle E_{Xmiss} \rangle$ and the analysis results converged. Using this method, convergence of the analysis to the true physical point (within errors) in the ($\varepsilon_{coh.\ el.}$, a, b, $\varepsilon_{inel.}$, n_g) parameter space (see Equations 5.10, 5.23, 5.24, 5.26) and 5.27) depended on the Monte Carlo correctly simulating both the physics and the detector. Agreement between the data and the Monte Carlo was quantified by comparing the background subtracted data before corrections with the corresponding Monte Carlo distributions and calculating the χ^2 listed in Table 5.21. All the data and Monte Carlo distributions are in agreement to better than the 90% confidence levels corresponding to the number of degrees of freedom, n_D. The background subtracted inelasticity and transverse momentum squared data, before corrections for E_{Xmiss}, smearing and acceptance, are shown in Figures 5.22, 5.23, 5.24 and 5.25. The corresponding Monte Carlo distributions (solid lines —) are superimposed normalized to the data.

Table 5.21: Comparison of the χ^2 between the data and the Monte Carlo distributions with the respective 90% confidence levels corresponding to the number of degrees of freedom, n_D.

Distribution	χ^2	$\chi^2_{90\%\ CL}$	n_D
z_{rec}	2.5	9.24	5
x_{rec}, $0.10 < z_{rec} < 0.90$	1,3	6.25	3
p^2_{Trec}, $0.10 < z_{rec} < 0.90$	5.6	14.7	9
p^2_{Trec}, $0.99 < z_{rec} < 1.00$	18.	27.2	19

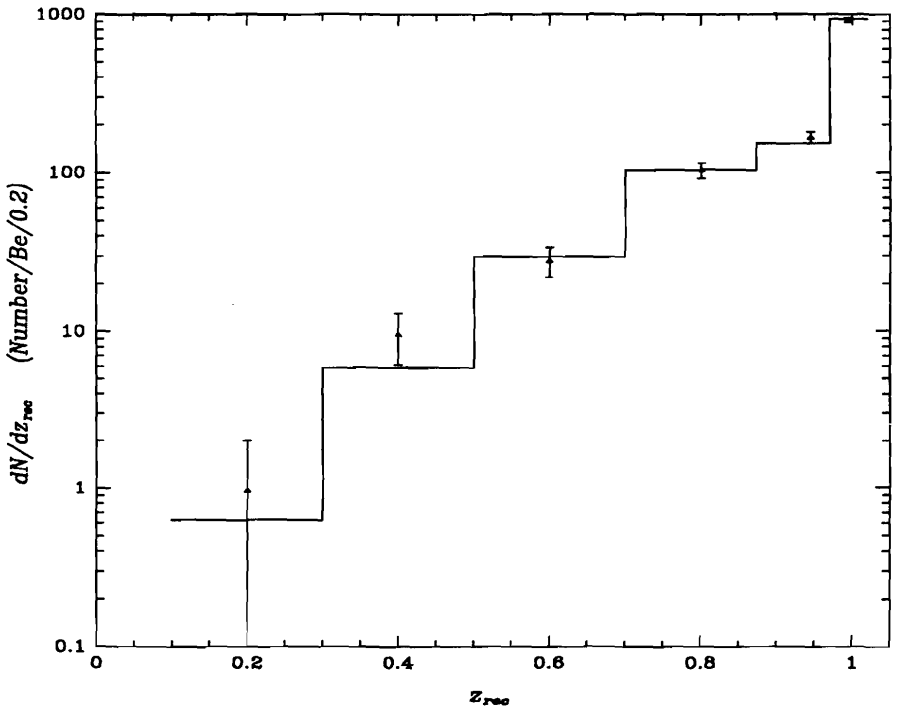

Figure 5.22: Comparison of the background subtracted z_{rec} data with the corresponding Monte Carlo distribution (solid line —).

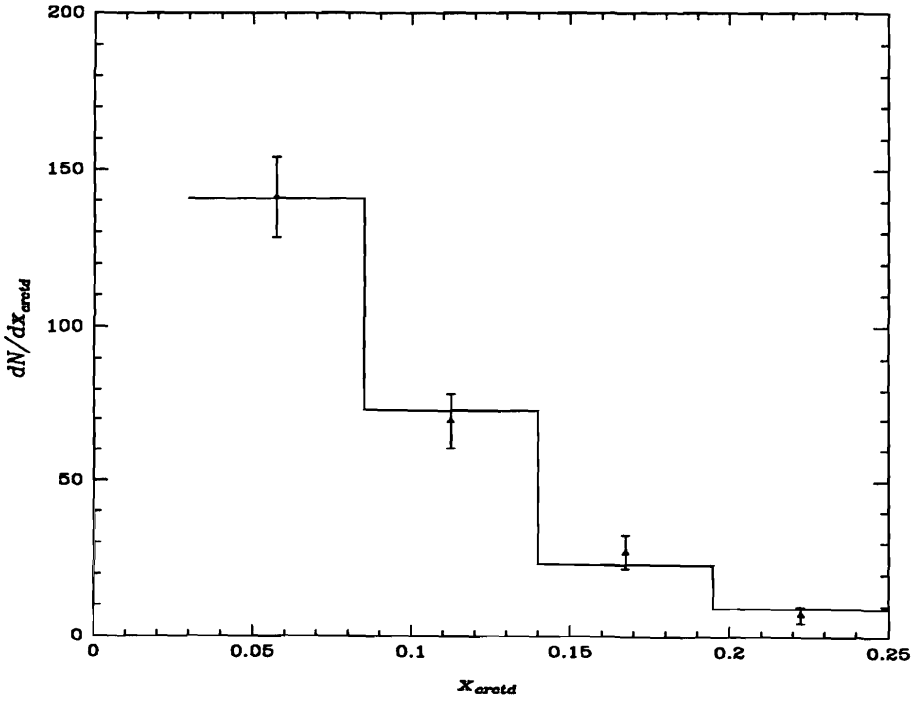

Figure 5.23: Comparison of the background subtracted x_{rec} data, for $0.10 < z_{rec} < 0.90$, with the corresponding Monte Carlo distribution (solid line —).

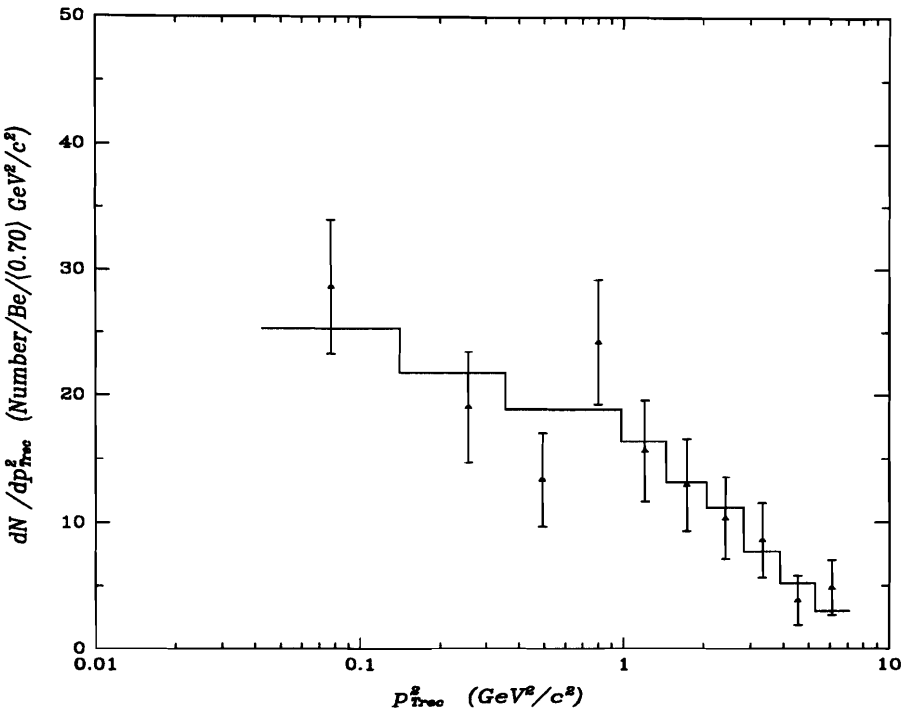

Figure 5.24: Comparison of the background subtracted p^2_{Trec} data, for $0.10 < z_{rec} < 0.90$, with the corresponding Monte Carlo distribution (solid line —).

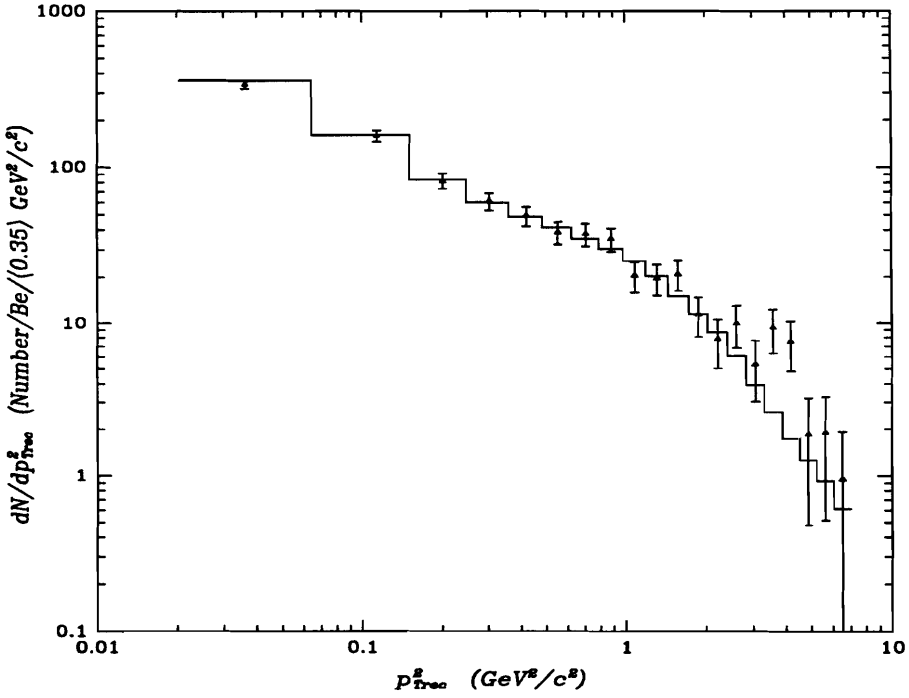

Figure 5.25: Comparison of the background subtracted p^2_{Trec} data, for $0.99 < z_{rec} < 1.00$, with the corresponding Monte Carlo distribution (solid line —).

5.7 Comparison of Data with Other Experiments

An extensive review of measurements from earlier J/ψ photoproduction and muoproduction experiments may be found in [Nas 83]. In Table 5.22, the E691 J/ψ data are compared with the data from E516, the previous photoproduction experiment performed at the Tagged Photon Laboratory, [Den 84]. The E691 data is characterized by increased statistics and smaller systematic uncertainties. Although these two set of data agree within errors, the trend of the central values suggest an increase in the deep inelastic production fraction with increasing energy.

The E691 measurement of gluon structure function, $xG(x)$, is compared, in Table 5.23, with the other most recent real and virtual photoproduction (muoproduction) measurements and a prompt photon measurement from WA70 [Bon 88]. Although the parametrization of the gluon structure function

$$xG(x) = (1-x)^{n_g} \tag{5.49}$$

is motivated by counting rules and is thus expected to be valid only at large x, the convention is to use this form over the entire range of x. The E691 J/ψ photoproduction measurement of $xG(x)$ is shown in Figure 5.14. The corresponding measurement from the E691 open–charm PGF analysis [Anj 90], shown in Figure 5.26, is more accurately stated as the measurement of $[dG(x)/dx]/G(x)$, at $x = 0.06$, for gluons in beryllium giving a value of -7.6 ± 2.3. The third result is the J/ψ virtual photoproduction (muoproduction) result of the European Muon Collaboration [Ron 90], shown in Figure 5.27. Note that the J/ψ real and virtual photoproduction data both extend over a range of x about 5.5 times larger than that of the open–charm real photoproduction data. The J/ψ virtual photoproduction data extend over a range of Q^2 about 10 times larger than that of the real photoproduction data but with a lower $\langle Q^2 \rangle$ of about 4 GeV^2 compared to value of about 21 GeV^2 for the real photoproduction data. However, all these results all agree within errors.

Table 5.22: Comparison of the E691 and other J/ψ photoproduction data.

Experiment	Target Material	$\langle E_\gamma \rangle$ (GeV)	Total $\sigma_{J/\psi}$ (nb/nucleon)	Total elastic $\sigma_{J/\psi}$ $z > 0.99$ (nb/nucleon)	Deep inelastic $\sigma_{J/\psi}$ $z < .9$ (nb/nucleon)	Deep inelastic production fraction
E516	H_2	100	$19.6 \pm 2.4 \pm 4.9$	$9.8 \pm 1.8 \pm 2.5$	$5.1 \pm 1.4 \pm 1.3$	$0.26 \pm 0.05 \pm 0.09$
E691	Be	145	$14.0 \pm 0.5 \pm 1.6$	$5.05 \pm 0.24 \pm 0.66$	$6.1 \pm 0.3 \pm 1.1$	$0.44 \pm 0.03 \pm 0.09$

Table 5.23: Reported measurements of the gluon structure function exponent.

Experiment	Production Mechanism	Q^2 (GeV^2)	x Range	n_g	Perturbative QCD Order
E691	$\gamma Be \to J/\psi X$	22	$[0.03, 0.25]$	6.5 ± 1.1 stat.$^{+1.0}_{-0.6}$ syst.	NLO
E691	$\gamma Be \to DDX$	20	$[0.04, 0.08]$	7.1 ± 2.2 (syst.)	NLO
EMC	$\mu(H_2, D_2) \to \mu' J/\psi X$	[0.1,10]	$[0.03, 0.25]$	5.1 ± 0.9 (stat.)	NLO
BCDMS	$\mu H_2 \to \mu' X$	5	$[0.06, 0.30]$	4.0 ± 1.3 (stat.) $^{+0.2}_{-0.3}$ (theo.) 8.1 ± 1.5 (stat.) $^{+0.2}_{-0.3}$ (theo.)	LO NLO $\overline{MS}$
EMC	$\mu Fe \to \mu' X$	5	$[0.30, 0.70]$	3.25 ± 0.4 (stat.) ± 0.6 (syst.)	LO
WA70	$pp \to \gamma X$	4	–	[4, 5]	NLO $\overline{MS}$

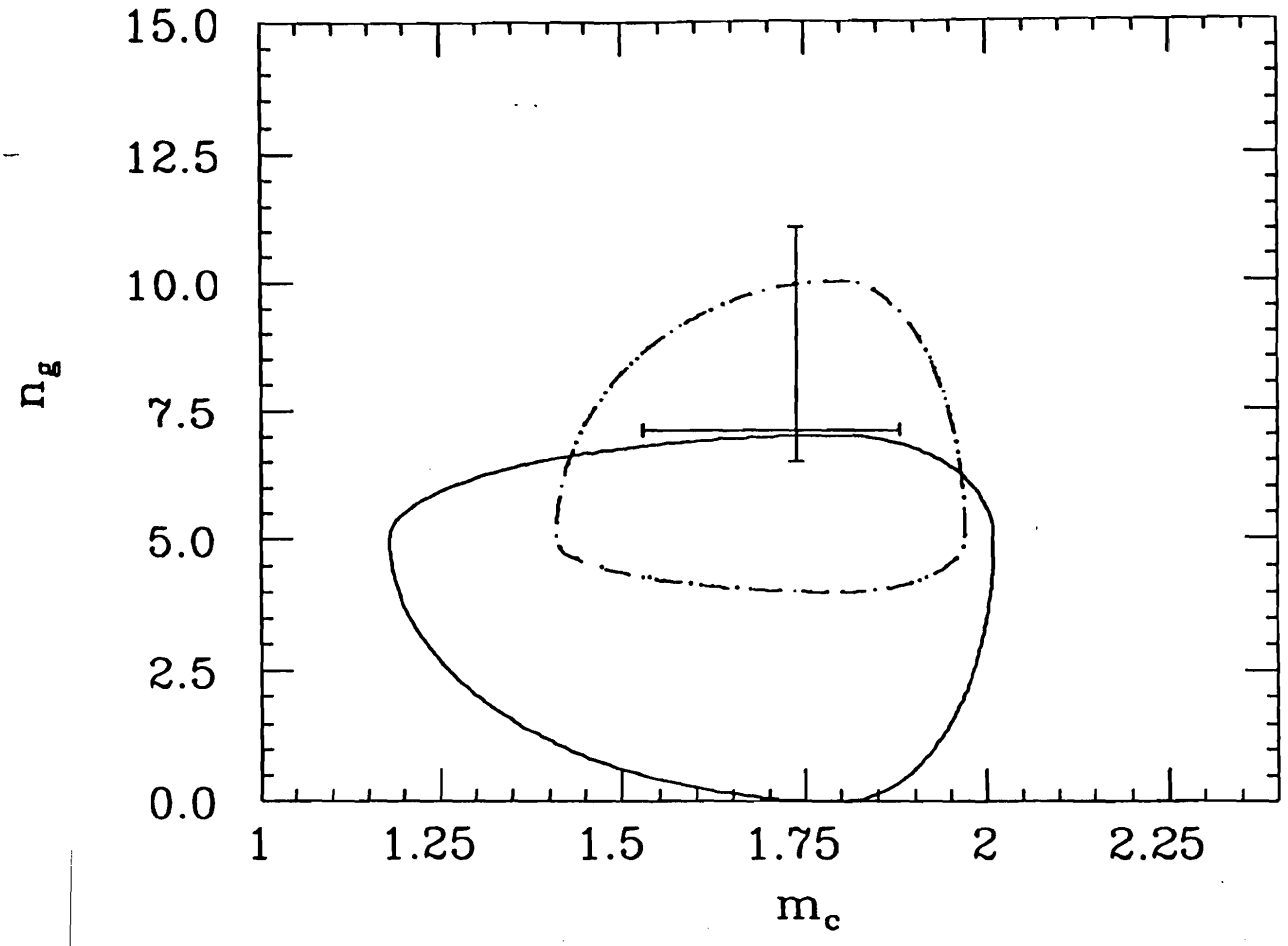

Figure 5.26: The 1σ limits for n_g and m_c from the photon–gluon fusion analysis of the E691 open–charm data. The horizontal line is for the total cross section measurement (n_g fixed at its combined–fit value of 7.1 ± 2.2) and the vertical line is for the rise of the total cross section with energy (m_c fixed at its combined–fit value of $1.74^{+0.13}_{-0.18}\mathrm{GeV}/c^2$). The dashed curve is for the p_T^2 fit and the solid curve is for the x_F fit. The combined fit result is at the intersection of the two lines.

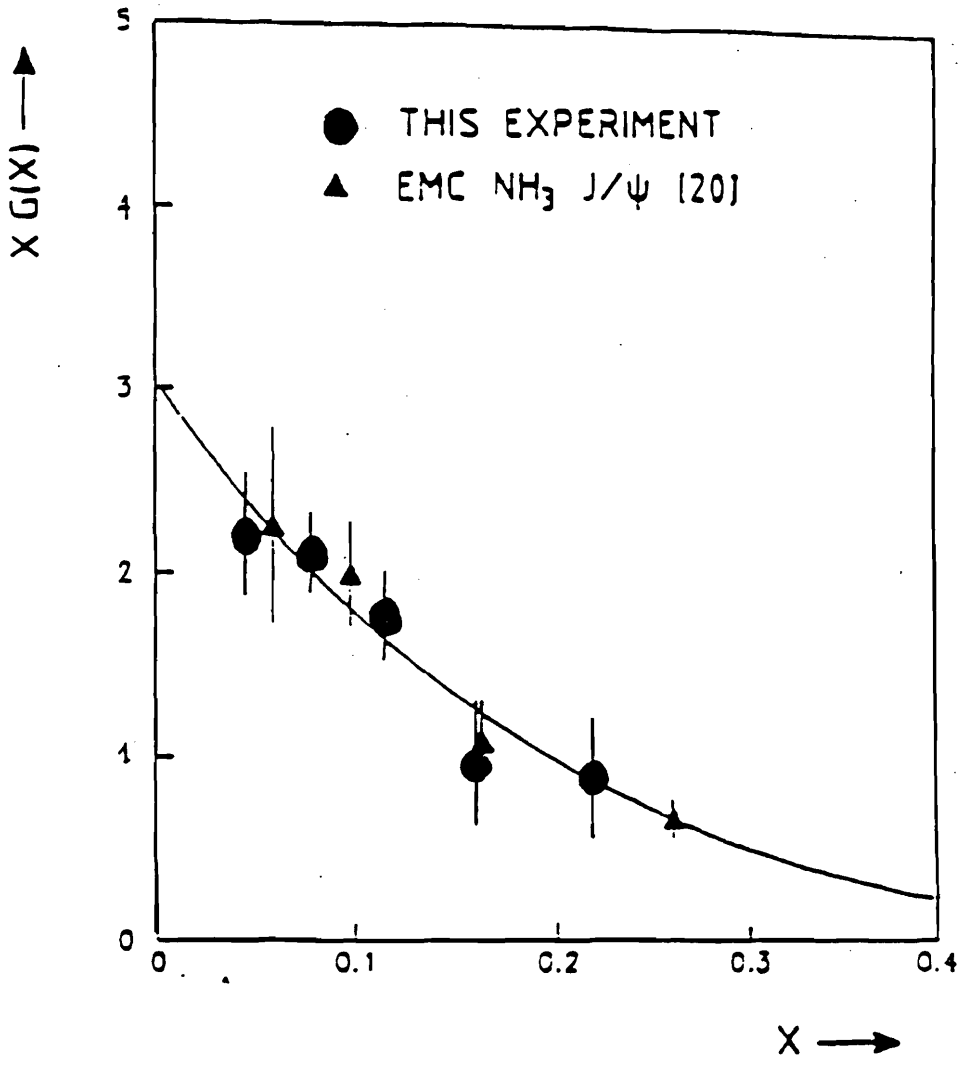

Figure 5.27: The EMC normalized nucleon gluon distribution distribution $xG(x)$ from hydrogen and deuterium data analyzed in the colour–singlet J/ψ photon–gluon fusion model. Also shown are earlier results from an EMC measurement on ammonia.

Chapter 6

Conclusions

In conclusion, the inelastic and elastic photoproduction on beryllium of 1225 ± 38 J/ψ particles from experiment E691 has been analyzed. The deep inelastic cross section was measured to be $48.3 \pm 2.0\ ^{+7.2}_{-8.6}$ nb/Be nucleus at $\langle E_\gamma \rangle = 145$ GeV. For elastic production, the coherent elastic cross section was measured to be $41.4 \pm 3.0 \pm 6.1$ nb/Be nucleus and the incoherent elastic cross section was measured to be $24.8 \pm 1.6 \pm 3.6$ nb/Be nucleus. The $d\sigma/dzdp_T^2$ distribution and energy dependence of the cross section for these production processes was also measured. For deep inelastic production, with $\langle z \rangle = 0.68 \pm 0.01\ ^{+0.03}_{-0.05}$, the mean p_T^2 was $1.20 \pm 0.05\ ^{+0.13}_{-0.17}$ GeV^2/c^2 and the ratio of cross sections at 200 and 100 GeV was $1.73 \pm 0.43\ ^{+0.41}_{-0.26}$, whereas for coherent and incoherent elastic production the mean p_T^2s are 0.070 ± 0.007 GeV^2/c^2 and 0.62 ± 0.05 GeV^2/c^2, respectively and the ratio of total (coherent plus incoherent) elastic cross sections at 200 and 100 GeV was 1.28 ± 0.15. All the measured quantities agree with the inelastic QCD and elastic VMD–Glauber Monte Carlo simulation that uses the Lund model for inelastic hadronization. The deep inelastic part of the J/ψ data was analyzed in the photon–gluon–fusion model. It was found that the rise of the cross section with energy and the $d\sigma/dzdp_T^2$ distribution are well described by a relatively soft gluon distribution, $xG(x) \propto (1-x)^{n_g}$, with $n_g = 6.5 \pm 1.1$ (stat.) $^{+1.0}_{-0.6}$ (syst.) at $\langle Q^2 \rangle = 22$ GeV^2, in agreement with the measurement from the open–charm E691 data, $n_g = 7.1 \pm 2.2$, at $\langle Q^2 \rangle = 20$ GeV^2.

The J/ψ colour–singlet photon–gluon fusion model should prove to be a powerful technique to extract the gluon structure function, $xG(x)$, for low x at HERA.

Appendix A

The Kinematics of J/ψ Photoproduction

A.1 Elastic J/ψ Photoproduction

For elastic J/ψ photoproduction, the kinematic variables of interest are the incident photon beam energy E_γ, the mass of the target beryllium nucleus m_{Be} or constituent nucleon m_N, the transverse momentum squared, p_T^2, of the J/ψ relative to the photon beam axis and the Lorentz invariant inelasticity, z, defined by

$$z = \frac{p_\psi \cdot p_N}{p_\gamma \cdot p_N}. \tag{A.1}$$

In the lab frame z corresponds to the fraction of the photon beam energy transferred to the J/ψ

$$z = \frac{E_\psi}{E_\gamma}. \tag{A.2}$$

The 4–momentum equation for incoherent elastic scattering is

$$p_\gamma + p_N = p_\psi + p'_N \tag{A.3}$$

Energy and momentum conservation constrains z and p_T^2. For a fixed E_γ there is only

one independent variable, z or p_T^2. This kinematic constraint may be derived, using the Mandelstam variables s, t and u, as follows.

$$s + t + u = 2m_N^2 + m_\psi^2 \tag{A.4}$$

$$\begin{aligned} s &= (p_\gamma + p_N)^2 && \text{(A.5)} \\ &= m_N^2 + 2p_\gamma \cdot p_N && \text{(A.6)} \\ &= m_N^2 + 2m_N E_\gamma && \text{(A.7)} \end{aligned}$$

$$\begin{aligned} u &= (p_\psi - p_N)^2 && \text{(A.8)} \\ &= m_\psi^2 + m_N^2 - 2p_\psi \cdot p_N && \text{(A.9)} \\ &= m_\psi^2 + m_N^2 - 2zp_\gamma \cdot p_N \\ &= m_\psi^2 + m_N^2 - z(s - m_N^2) && \text{(A.10)} \end{aligned}$$

where Equations A.1 and A.6 were inserted into Equation A.9 to obtain Equation A.10. Inserting Equation A.10 back into Equation A.4 gives

$$s + t - z(s - m_N^2) = m_N^2 \tag{A.11}$$

and solving for z yields

$$z = \frac{s + t - m_N^2}{s - m_N^2}. \tag{A.12}$$

The 4-momentum transfer t expressed in terms of z and p_T^2 is

$$\begin{aligned} t &= (p_\gamma - p_\psi)^2 && \text{(A.13)} \\ &= m_\psi^2 - 2p_\gamma \cdot p_\psi \\ &= m_\psi^2 - 2zE_\gamma^2 + 2E_\gamma p_{z_\psi} \end{aligned}$$

$$\begin{aligned} &= m_\psi^2 - 2zE_\gamma^2 + 2E_\gamma\sqrt{E_\psi^2 - p_T^2 - m_\psi^2} \\ &= m_\psi^2 - 2zE_\gamma^2 + 2E_\gamma\sqrt{(zE_\gamma)^2 - p_T^2 - m_\psi^2}. \end{aligned} \tag{A.14}$$

This expression can be simplified considerably by expanding t to second order,

$$\begin{aligned} t &\simeq m_\psi^2 - \frac{1}{z}(p_T^2 + m_\psi^2) - \frac{1}{4}\frac{(p_T^2 + m_\psi^2)^4}{z^3 E_\gamma^2} \\ &\simeq -p_T^2 - \frac{1}{4E_\gamma^2}(p_T^2 + m_\psi)^2. \end{aligned} \tag{A.15}$$

Note that, in the limit $p_T^2 \to 0$, t does not vanish but approaches a non–zero value t_{min}. Hence

$$t_{min} \simeq -\frac{m_\psi^4}{4E_\gamma^2} \tag{A.16}$$

and the maximum kinematically allowed value of z is alway less than one

$$z_{max} = \frac{s + t_{min} - m_N^2}{s - m_N^2} < 1\ . \tag{A.17}$$

Solving for z in terms of p_T^2 gives the constraint, in the lab frame,

$$\begin{aligned} z = &\Bigg\{\sqrt{(E_\gamma + m_N)^2\Big(m_N + \frac{m_\psi^2}{2E_\gamma}\Big)^2 - (2E_\gamma m_N + m_N^2)\Big[\Big(m_N + \frac{m_\psi^2}{2E_\gamma}\Big)^2 + p_T^2 + m_\psi^2\Big]} \\ &+ (E_\gamma + m_N)\Big(m_N + \frac{m_\psi^2}{2E_\gamma}\Big)\Bigg\}\Big/(2E_\gamma m_N + m_N^2). \end{aligned} \tag{A.18}$$

However, the expression for z is well approximated by inserting Equations A.7 and A.15 into Equation A.12 yielding

$$z \simeq 1 - \frac{p_T^2}{2m_N E_\gamma} - \frac{(p_T^2 + m_\psi^2)^4}{8m_N E_\gamma^3}. \tag{A.19}$$

From Equation A.19, one can now easily see that the inelasticity approaches its maximum value in the limit $p_T^2 \to 0$,

$$z_{max} \simeq 1 - \frac{m_\psi^4}{8 m_N E_\gamma^3} < 1 \tag{A.20}$$

Conversely, one can express p_T^2 in terms of z,

$$p_T^2 = (zE_\gamma)^2 - m_\psi^2 - \frac{1}{4E_\gamma^2}[2zE_\gamma^2 - (1-z)(2m_N E_\gamma + m_N^2) - m_\psi^2]^2. \tag{A.21}$$

The derivation for coherent elastic scattering is identical. One need only replace m_N by m_{Be} in the results.

A.2 Inelastic J/ψ Photoproduction

The 4–momentum equation at the parton scale for inelastic scattering is

$$p_\gamma + p_{g1} = p_\psi + p_{g2} \tag{A.22}$$

where g_1 is the gluon from the target nucleon and g_2 is the hard gluon radiated by the $c\bar{c}$ system in order that the J/ψ be a colour singlet. The fraction x of the target nucleon momenta carried by g_1 is defined (in the limit of the infinite momentum frame)

$$p_{g1} = x p_N \tag{A.23}$$

This introduces a new degree of freedom. For a fixed E_γ, two of the three variables z, p_T^2 and x are independent. Thus there is one degree of freedom for elastic scattering and two degrees of freedom for inelastic scattering. The kinematic constraint between

z, p_T^2 and x may be derived, analogously to elastic J/ψ scattering, using the parton Mandelstam variables $\hat{s}$, $\hat{t}$ and $\hat{u}$,

$$\hat{s} + \hat{t} + \hat{u} = m_\psi^2 \tag{A.24}$$

$$\begin{aligned} \hat{s} &= (p_\gamma + p_{g1})^2 && \text{(A.25)} \\ &= 2p_\gamma \cdot p_{g1} \\ &= 2xp_\gamma \cdot p_N \\ &= 2xm_N E_\gamma && \text{(A.26)} \end{aligned}$$

$$\begin{aligned} \hat{u} &= (p_\psi - p_{g1})^2 && \text{(A.27)} \\ &= m_\psi^2 - 2p_\psi \cdot p_{g1} \\ &= m_\psi^2 - 2xp_\psi \cdot p_N \\ &= m_\psi^2 - 2xzp_\gamma \cdot p_N \\ &= m_\psi^2 - z\hat{s}. && \text{(A.28)} \end{aligned}$$

Inserting Equation A.28 into Equation A.24 gives

$$z = 1 + \frac{t}{\hat{s}} \tag{A.29}$$

where $\hat{t} = (p_\gamma - p_\psi)^2 = t$. Comparing Equations A.7 and A.26, it is easily seen that for $E_\gamma \gg m_N$

$$\hat{s} \simeq xs. \tag{A.30}$$

Inserting Equation A.30 into Equation A.29 and solving for x gives the Lorentz invariant expression

$$x = -\frac{t}{(1-z)s}. \tag{A.31}$$

The lab frame expression for x is

$$x = \frac{-m_\psi^2 + 2zE_\gamma^2 - 2E_\gamma\sqrt{(zE_\gamma)^2 - p_T^2 - m_\psi^2}}{(1-z)(2m_N E_\gamma + m_N^2)}. \tag{A.32}$$

The variable x takes on its maximum value when all the momentum of the nucleon is carried by the gluon. Thus

$$x_{max} = 1 \tag{A.33}$$

In order to obtain a simple expression for the minimum value of x, the numerator of Equation A.32 is expanded out to first order

$$x \simeq \frac{(1-z)m_\psi^2 + p_T^2}{(1-z)(2m_N E_\gamma + m_N^2)} \tag{A.34}$$

valid for $(p_T^2 + m_\psi^2)/(zE_\gamma)^2 \ll 1$. Thus the gluon momentum fraction takes on it minimum value in the limit $p_T^2 \to 0$

$$x_{min} = \frac{m_\psi^2}{s} \tag{A.35}$$

and is independent of z to first order. The kinematic constraint on p_T^2 is found by rearranging Equation A.32. In the lab frame

$$p_T^2 = (zE_\gamma)^2 - m_\psi^2 - \frac{1}{4E_\gamma^2}[2zE_\gamma^2 - (1-z)(2xm_N E_\gamma + x^2 m_N^2) - m_\psi^2]^2. \tag{A.36}$$

A good approximation for Equation A.36 is obtained by rearranging Equation A.34

$$p_T^2 \simeq z(1-z)xs - (1-z)m_\psi^2. \tag{A.37}$$

The kinematic constraint on z is also obtained by rearranging Equation A.32. In the lab frame

$$z = \left\{\sqrt{(E_\gamma + xm_N)^2\left(xm_N + \frac{m_\psi^2}{2E_\gamma}\right)^2 - (2xE_\gamma m_N + x^2m_N^2)\left[\left(xm_N + \frac{m_\psi^2}{2E_\gamma}\right)^2 + p_T^2 + m_\psi^2\right]}\right.$$
$$\left. + (E_\gamma + xm_N)\left(xm_N + \frac{m_\psi^2}{2E_\gamma}\right)\right\} \Big/ (2xE_\gamma m_N + x^2m_N^2) \qquad \text{(A.38)}$$

As $x \to 1$, the z and p_T^2 kinematic constraints Equations A.38 and A.36 approach those of incoherent elastic scattering.

Appendix B

Background Subtraction

The signal region distribution for a kinematic variable x, denoted by $f_1(x)$, is a weighted sum of the true signal distribution, denoted by $f_S(x)$, and the true background distribution, denoted by $f_B(x)$,

$$f_1(x) = S_1 f_S(x) + B_1 f_B(x) \tag{B.1}$$

where S_1 and B_1 are the fractions of signal and background events in the signal region of the invariant mass plot. Similarly, the background region distribution, denoted by $f_2(x)$, is also a weighted sum of the true signal and the true background distributions,

$$f_2(x) = S_2 f_S(x) + B_2 f_B(x) \tag{B.2}$$

where S_2 and B_2 are now the fractions of signal and background events in the background region of the invariant mass plot (the regions adjacent to the signal).

Conversely, the true signal distribution may be expressed as a weighted sum of the signal region distribution and the background region distribution

$$f_S(x) = \alpha f_S(x) + \beta f_B(x). \tag{B.3}$$

Substituting Equations B.1 and B.2 into Equation B.3 and collecting terms

$$f_S(x) = (\alpha S_1 + \beta S_2) f_S(x) + (\alpha B_1 + \beta B_2) f_B(x) \tag{B.4}$$

yields two equations in the two unknowns α and β,

$$\alpha S_1 + \beta S_2 = 1 \tag{B.5}$$

$$\alpha B_1 + \beta B_2 = 0 \tag{B.6}$$

Equations B.5 and B.6 may now be inverted to give the α and β background subtraction parameters

$$\alpha = -\frac{B_2}{B_1 S_2 - B_2 S_1} \tag{B.7}$$

$$\beta = \frac{B_1}{B_1 S_2 - B_2 S_1} \tag{B.8}$$

of Equation B.3. Note that the method discussed above requires that all the distributions be normalized to unity

$$\int f_1(x) = \int f_2(x) = \int f_S(x) = \int f_B(x) = 1 \tag{B.9}$$

Appendix C

Fitting and Parameter Estimation

The N observed events, corrected for $E_{X miss}$ and smearing, were grouped into M bins (1–dimension) or cells (2–dimension or higher) with $n_{i(,j,k,...)}$ events in the ith bin or $i, j, k, \ldots th$ cell of the set of η kinematic variables

$$\vec{x} = \{x_1, \ldots, x_\eta\}. \tag{C.1}$$

The predicted number of events, $m_{i,j,k,...}$, in the $i, j, k, \ldots th$ cell is given by

$$m_{i,j,k,...}(\vec{\alpha}) = N \frac{\int_{i,j,k,...th\ cell\ in\ \vec{x}} f(\vec{x};\vec{\alpha}) A(\vec{x}) d\vec{x}}{\int_{all\ x} f(\vec{x};\vec{\alpha}) A(\vec{x}) d\vec{x}} \tag{C.2}$$

where

$$f(\vec{x};\vec{\alpha}) \equiv \frac{d\sigma}{d\vec{x}}(\vec{\alpha}) \tag{C.3}$$

is the differential physics cross section from theory with the set of ξ parameters

$$\vec{\alpha} = \{\alpha_1, \ldots, \alpha_\xi\} \tag{C.4}$$

and the weighting function $A(\vec{x}) \in [0, 1]$ is the overall detector geometric acceptance $\times$ efficiency. For grouped data, Poisson distributed in each cell, the likelihood is given by

$$\mathcal{L} = \prod_{i,j,k,\ldots=1}^{M} \frac{1}{n_{i,j,k,\ldots}!} [m_{i,j,k,\ldots}(\vec{\alpha})]^{n_{i,j,k,\ldots}} e^{-m_{i,j,k,\ldots}(\vec{\alpha})} \tag{C.5}$$

The best fit to theory is determined by searching the $\vec{\alpha}$ parameter space for the point $\vec{\alpha}_0$ (within errors) that maximizes $\mathcal{L}$. Estimation of $\vec{\alpha}_0$ by the maximum likelihood method is unbiased. The logarithm of the likelihood function attains its maximum value at the same point, $\vec{\alpha}_0$, as the likelihood function. It is computationally simpler to maximize the logarithm of the likelihood or to equivalently minimize the negative of the log–likelihood, $\mathcal{F}_l$, given by

$$\mathcal{F}_l = -2 \ln \mathcal{L} \tag{C.6}$$

$$= -2 \sum_{i,j,k,\ldots=1}^{M} [-n_{i,j,k,\ldots} \ln m_{i,j,k,\ldots}(\vec{\alpha}) - m_{i,j,k,\ldots}(\vec{\alpha}) - \ln n_{i,j,k,\ldots}!] \tag{C.7}$$

where the factor of 2 is introduced as a one σ error corresponds to a change of 1/2 in the value of $\mathcal{F}_l$. As the third term in Equation C.7 is independent of $\vec{\alpha}$, it may be subtracted out giving

$$\mathcal{F} = -2 \sum_{i,j,k,\ldots=1}^{M} [-n_{i,j,k,\ldots} \ln m_{i,j,k,\ldots}(\vec{\alpha}) - m_{i,j,k,\ldots}(\vec{\alpha})] \tag{C.8}$$

as the log–likelihood function to be minimized.

Estimation of $\vec{\alpha}_0$, $\vec{\sigma}(\vec{\alpha}_0)$ and the covariance matrix was performed via minimization of $\mathcal{F}$ using the variable metric method of Davidson, Fletcher and Powell [Jam 72] implemented in the MINUIT function minimization and error analysis package as the MIGRAD routine [Jam 83].

Appendix D

The Monte Carlo

D.1 The Photon Flux Generation

A QED–based Monte Carlo was used to calculate the photon beam bremsstrahlung energy spectrum for the 250 GeV electron beam incident on the 0.2 radiation length radiator. The detailed simulation included the finite thickness, Z dependence and inclination (with respect to the electron beam) of the copper radiator, pair production and multiple bremsstrahlung. The resulting photon energy spectrum is shown in Figure 3.3.

D.2 The Inelastic and Elastic J/ψ Event Generation

A photon flux uniform over 70 GeV to 250 GeV was generated. The upper kinematic limits for z scattering coherently from a Be nucleus, $z_{Be\ max}$, and incoherently from a nucleon, $z_{N\ max}$ were calculated using Equation A.20. The p_T^2 was then calculated from the kinematic constraints. For coherent elastic scattering m_{Be} was substituted for m_N. A z distribution uniform over all z would have had too few events in the elastic region, $z > 0.99$, relative to the inelastic region, $z < 0.99$, with respect to the data. Thus, events were generated as follows

Elastic Production 60% of the generated events, uniform random $z \in (0.99, z_{Be\ max}]$ (Equation A.20)

- Coherent Elastic: $z \in [z_{N\ max}, z_{Be\ max}]$, $p_T^2 = f(E_\gamma, z, m_{Be})$ (Equation A.21)
- Incoherent Elastic and Quasi–elastic: $z \in (0.99, z_{N\ max}]$, $p_T^2 = f(E_\gamma, z, m_N)$ (Equation A.21)

Inelastic Production 40% of the generated events, uniform random $z \in [0.10, 0.99]$ (Equation A.20)

- PGF: uniform random $x \in [m_\psi^2/s, 1.00]$, $p_T^2 = f(E_\gamma, z, x, m_N)$ (Equation A.36)
- Quasi–elastic: for study of systematics, $p_T^2 = f(E_\gamma, z, m_N)$ (Equation A.21)

The events were first weighted to have uniform densities over the elastic (E_γ, z, p_T^2) phase space and over the inelastic (E_γ, z, p_T^2, x) phase space, then were secondly weighted by the relative photon flux and the probability densities parametrizing the physical theory, Equations 5.26 and 5.27. The physical theory parameters were varied until the Monte Carlo distributions agreed with the reconstructed data to better than the 90% CL.

From the generated E_γ, z and p_T^2 variables the J/ψ lab frame 4-momenta components ($E_\psi = zE_\gamma$, $p_{x_\psi} = p_T \cos\theta$, $p_{y_\psi} = p_T \sin\theta$, $p_{z_\psi} = \sqrt{E_\psi^2 - p_T^2}$) were calculated. The random variable θ was taken to be uniform over [0, 2π]. Thus all projections of p_T^2 on the x and y axes were equiprobable.

To conserve the event 4–momenta for elastic/inelastic production the (photon, nucleus/nucleon, J/ψ) system was boosted to the photon–nucleus/nucleon centre-of-mass frame. For coherent elastic production the boost is $(\beta_x, \beta_y, \beta_z) = (0, 0, -E_\gamma/(E_\gamma + m_{Be}))$ and the recoil Be nucleus was assigned the 4–momenta

$$E'_{Be} = E_\gamma + E_{Be} - E_\psi \quad \text{(D.1)}$$

$$p'_{x_{Be}} = -p_{x_\psi} \quad \text{(D.2)}$$

$$p'_{y_{Be}} = -p_{y_\psi} \quad \text{(D.3)}$$

$$p'_{z_{Be}} = -p_{z_\psi} \quad \text{(D.4)}$$

and for incoherent elastic production the analogous boost is $(\beta_x, \beta_y, \beta_z) = (0, 0, -E_\gamma/(E_\gamma + m_N))$ with the recoil nucleon 4–momenta

$$E'_N = E_\gamma + E_N - E_\psi \quad \text{(D.5)}$$

$$p'_{x_N} = -p_{x_\psi} \quad \text{(D.6)}$$

$$p'_{y_N} = -p_{y_\psi} \quad \text{(D.7)}$$

$$p'_{z_N} = -p_{z_\psi} \quad \text{(D.8)}$$

Incoherent quasi-elastic production has the same boost β as incoherent elastic production but with the 4–momenta and rest mass

$$E'_{N^*} = E_\gamma + E_N - E_\psi \quad \text{(D.9)}$$

$$p'_{x_{N^*}} = -p_{x_\psi} \quad \text{(D.10)}$$

$$p'_{y_{N^*}} = -p_{y_\psi} \quad \text{(D.11)}$$

$$p'_{z_{N^*}} = -p_{z_\psi} \quad \text{(D.12)}$$

$$m_{N^*} = \sqrt{E^2_{N^*} - p^2_{N^*}} \quad \text{(D.13)}$$

The N^* was decayed according to phase space with isospin conservation. The decays are listed in Table D.1.

The inelastic production has the additional kinematic degree of freedom, x, the gluon momentum fraction given by Equation A.32. The Lorentz boost to the photon–

Table D.1: The quasi-elastic production and decay of the N^*.

N^* Production and Decay Mode	B.R. (%)
$p \rightarrow N^{*+} \rightarrow n\pi^+$	67
$p \rightarrow N^{*+} \rightarrow p\pi^0$	33
$n \rightarrow N^{*0} \rightarrow p\pi^-$	67
$n \rightarrow N^{*0} \rightarrow n\pi^0$	33

gluon (γg_1) centre of mass frame is $(\beta_x, \beta_y, \beta_z) = (0, 0, -(E_\gamma - xm_N)/(E_\gamma + xm_N))$. For inelastic production, the 4-momenta conservation is

$$E'_{g2} = \sqrt{p_{x_\psi} + p_{y_\psi} + p_{z_\psi}} \quad \text{(D.14)}$$

$$p'_{x_{g2}} = -p_{x_\psi} \quad \text{(D.15)}$$

$$p'_{y_{g2}} = -p_{y_\psi} \quad \text{(D.16)}$$

$$p'_{z_{g2}} = -p_{z_\psi} \quad \text{(D.17)}$$

where g_2 is the radiated gluon. All final state particles must be colourless. For the J/ψ, this requirement is satisfied by the radiation of g_2. To ensure overall colour neutrality, g_2 must interact with the nucleon target fragments to hadronize into colourless final states.

D.3 Inelastic Fragmentation

To satisfy the condition that all final state particles have no net colour – all are colour singlet systems, the radiated gluon – nucleon target fragment system must hadronize or fragment. The fragmentation was done using the LUND string model Monte Carlo JETSET (version 6.2). The string model is most easily visualized for the production of a back–to–back $q\bar{q}$ pair. In this model a colour flux tube links the two partons. As the q and $\bar{q}$ move apart, the potential energy stored in the relativistic string increases linearly as κr. From phenomenology, the string constant or linear

energy density κ is known to be on the order of 1 GeV/fm. When the string energy is greater than the mass of a $q\bar{q}$ pair, then the string may break by the production, at the break, of a new $q'\bar{q}'$ pair from the vacuum. Thus the initial $q\bar{q}$ system has split into two colour singlet systems $q\bar{q}'$ and $q'\bar{q}$. If the invariant mass of either of these systems is large enough, then further breaks may occur until only hadrons remain. All the $q'\bar{q}'$ breaks are space–like separated; they are causally disconnected. However two adjacent breaks are constrained by the requirement that the in between hadron be real – on the mass shell. In the string model, gluons correspond to kinks (carrying energy and momentum) on the string spanning a $q\bar{q}$ pair. JETSET also simulates the decays of unstable particles using a phase space distribution for most and a weak decay distribution for few. The identity, parentage and 4–momenta of the initial partons along with their fragmentation–decay chains were stored in a list. An interaction point in the target was chosen and the particles were propagated from the photoproduction point through the spectrometer simulation.

For inelastic J/ψ production, the target fragments are modelled as a quark–diquark, qDq, system. Once the J/ψ 3–momenta was balanced by that of the radiated gluon, Equations D.15 to D.17, the remaining energy and momenta were assigned to the qDq pair as follows

$$E'_{qDq} = E_\gamma + E_N - E_\psi - E_{G1} \tag{D.18}$$

$$p'_{z_q} = f_q(p_{z_\gamma} + p_{z_N}) \tag{D.19}$$

$$p'_{z_{Dq}} = (1 - f_q)(p_{z_\gamma} + p_{z_N}) \tag{D.20}$$

$$p'^2_{T_q} = \frac{1}{4}E'^2_{qDq} + \frac{1}{4E'^2_{qDq}}(p'^2_{z_{Dq}} - p'^2_{z_q} + M^2_{Dq} - M^2_q)^2 \tag{D.21}$$

$$- \frac{1}{2}(p'^2_{z_{Dq}} + p'^2_{z_q} + M^2_{Dq} + M^2_q) \tag{D.22}$$

$$= p'^2_{T_{Dq}} \tag{D.23}$$

$$p'_{x_q} = -p'_{x_{Dq}} \tag{D.24}$$

$$p'_{y_q} = -p'_{y_{Dq}} \tag{D.25}$$

where the longitudinal momentum fraction f_q carried by the quark in the qDq system was generated randomly over $[0,1]$ subject to the constraints

$$p'^2_{T_q} \geq 0 \tag{D.26}$$

$$E'_{qDq} \geq p'_{qDq} \tag{D.27}$$

$$E'_{\psi} + E'_q + E'_{Dq} + E'_{g1} = E_\gamma + E_N \tag{D.28}$$

If no such real value of f_q was found to exist (typically for $z > 0.9$), then the fragmentation was changed to quasi–elastic $N^* \rightarrow N\pi$. If the rest mass of the pseudo N^* was less than that of the $N\pi$ system (again, typically for $z > 0.9$), then the fragmentation was changed to kinematically elastic. Equations D.18 to D.25 taken together with Equations D.15 to D.17 and the constraints, Equations D.26 to D.28 ensured overall energy and momentum conservation for the inelastic system.

D.4 The E691 Tagged Photon Spectrometer Simulation

A detailed simulation of the Tagged Photon Spectrometer followed the J/ψ photoproduction and X fragmentation simulations. This simulation modelled the interactions, with the detectors, of a particle passing through the spectrometer. The relevant physical parameters for each detector were incorporated into the simulation. These included the detector geometries and the number of radiation and interaction lengths for each. The generated particles were moved each detector simulation in turn. Both multiple scattering of charged particles and secondary interactions with detector materials were taken into account. The charged particles were swum through the fields of the M1 and M2 analyzing magnets. Emission of Cherenkov light in the C1 and C2 threshold detectors was simulated by random photon radiation on the Cherenkov light cone of the charged particle according to the intensity law given by Equation 3.14.

The paths of these photons were traced using the measured mirror and Winston cone positions giving the total number of photons incident on each phototube. Electromagnetic showering of electrons, positrons, photons and neutral pions ($\pi^0 \rightarrow \gamma\gamma$) were simulated in the SLIC using a parametrization of the EGS (full QED) Monte Carlo. Hadronic showering, in both the SLIC and the Hadrometer, was modelled using a simple average parametrization of the shower depth and width. Passage of a muon through one of the scintillation counters of the back muon wall was recorded.

The Monte Carlo simulation data for each event was then collected, formatted and output as a Truth Table. This Truth Table included the positions of all the charged particles at each SMD and drift chamber plane, the amount of light incident at each Cherenkov phototube, the shower energy deposited in each calorimeter module, the position of a muon at the back muon wall and the full LUND list of generated particles and their decay chains. The Truth Table data was then input into a Digitization program that converted the Monte Carlo information into the raw data digital format produced the the actual data acquisition system of the detector. Thus the Monte Carlo data could then be passed through the identical data reconstruction and analysis program chain in order to extract trigger and reconstruction efficiencies and to study systematics. The Digitizer modelled detector inefficiencies, hot and dead channels, cross–talk between channels and noise. The dimuon, $B \cdot H$ and E_T triggers were also generated.

Appendix E

The E691 Tagged Photon Spectrometer

E.1 The Silicon Microstrip Detector

For a 145 GeV photon beam, the energy of a forward D meson is typically greater than 50 GeV giving a mean decay path $\gamma c\tau$ in the lab of several millimetres. Therefore a vertex detector with a two–vertex resolution of several hundred microns was required. The E691 silicon microstrip detector (SMD) met this criteria, revolutionizing fixed–target charm physics.

The $c\tau$ values of the D^0, D^+ and D_S^+ are 126 microns, 318 microns and 133 microns. Primary interaction region vertexing was essential for the extraction of the open–charm signal by resolving between the (primary) production vertex and the charm decay (secondary) vertex. The SMD is briefly described here because of its importance to the complementary open–charm production analysis and to the charm decay studies.

The SMD consisted of nine planes. These planes were grouped into three assemblies of three planes each. In each assembly the planes were oriented in one of three views; in the upstream to downstream order X, Y and V in the first and third assemblies and Y, X and V in the second assembly. The V view planes were oriented at -20.5° to the $y-$axis looking downstream. The arrangement of the nine SMD planes

is shown in Figure E.1. The positions of the planes along the $z-$axis are listed in Table E.1. The three planes of In the first (upstream) assembly the three planes each had an active area of 2.5 $\times$ 2.5 cm^2. These planes were manufactured by Enertec Schlumberger (France). The six planes of the remaining two assemblies each had an active area of 5.0 $\times$ 5.0 cm^2. They were manufactured by Micron Semiconductor (England). The angular acceptance of the SMD detector was about 100 milliradians. All planes had a 50 μm pitch (strip spacing).

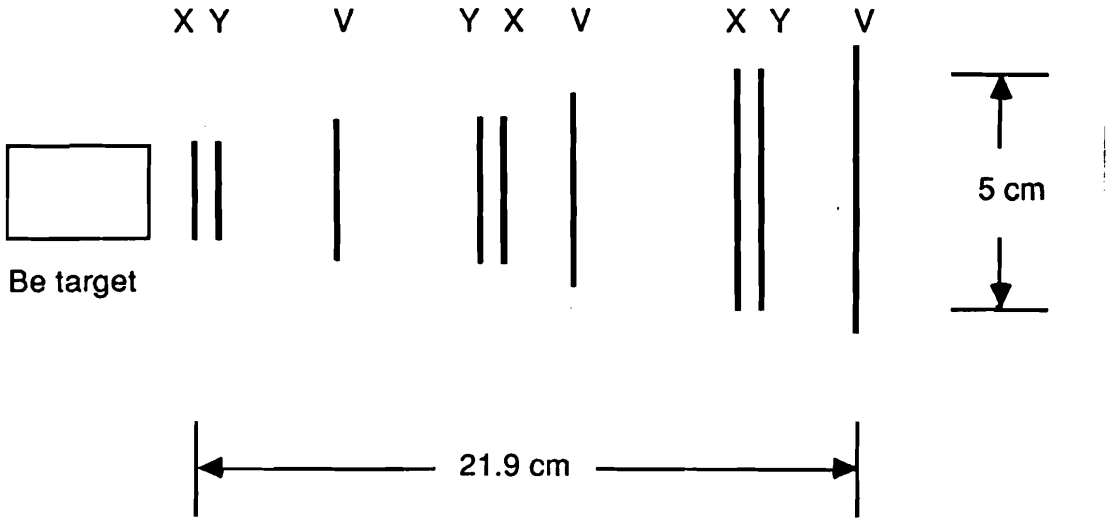

Figure E.1: The Silicon Microstrip Detector layout.

A schematic of a SMD plane is shown in Figure E.2. Each plane was constructed by ion-implanting one side of a 300 μm n–type silicon wafer with Arsenic (V) to form a continuous heavily–doped n–type layer. On the other surface, Boron (III) was implanted in strips along one direction. This procedure formed a surface layer with an alternating pattern of intrinsic and heavily doped p–type strips. Aluminum was deposited over the p–strips and the n–layer to provide for external connections. The resulting structure was a monolithic strip array of PIN diodes. The SMD contained a total of 6840 strips. Each strip was read out as an SMD channel. The number of

strips in each plane is listed in Table E.1.

When a minimum ionizing particle traversed an SMD wafer about 32500 electron–hole pairs (3.75 femtocoulombs) were created. The electrons and holes drifted in opposite directions in the electric field produced by the DC reverse–bias voltage of 90 V. This reverse–bias voltage depleted almost the entire p–n junction and thereby greatly reduced the leakage current. There was no charge multiplication in the silicon, unlike the drift chambers requiring the location of low noise preamplifiers, in well shielded enclosures, close to the SMD wafers. The preamplifiers used were Laben MSD2 hybrids. The MSD2 had a current gain factor of about 200, a rise time of about 3 ns and an equivalent noise charge of 1600 electrons (RMS) for a 10 pF input capacitance and a 40 ns gating time. These preamps were connected directly to the printed circuit fanout and were mounted on the detector assembly so as to achieve a linear density of 40 channels per 2.54 cm. The MSD2s gave an output of about 1 mV for a minimum ionizing signal traversing the silicon strip. These pulses were propagated on a 3.66 m long, flat, shielded transmission line cable with a nominal impedance of 28 ohms. The cables were assembled from a commercially produced nine strip inner conductor surrounded on both sides by an adhesive backed foam dielectric and an outer aluminum foil shield. At both ends of the cable, the foil was electroplated with copper to provide good electrical contact with the connector pin. Alternate centre conductor strips were used for signal and ground.

The cables fanned out the preamplified signals to discriminator/readout cards mounted with a linear density of 11 channels per 2.54 cm. These cards were modified Nanosystems eight-channel MWPC shift register readout cards. They were modified by adding a one-transistor amplifier in each channel. This amplifier inverted the positive silicon signal and had a potentiometer for adjusting the effective discriminator threshold. Because the signal–to–noise ratio at the discriminator input was about 10, the threshold had to be set much more accurately than in a wire chamber system. About 1% to 3% of the channels in each plane were hot, a hot channel being one which fired during virtually every triggered event. The noise rate, defined as the probability

of a false hit per strip per triggered event, was less than 0.1%. Each channel was equipped with a monostable delay and a trigger gate. The shift registers in each card were read out serially by a Nanosystem Camac scanner. A detailed description of the SMD theory, fabrication, mounting and operation is contained in [Bro 88].

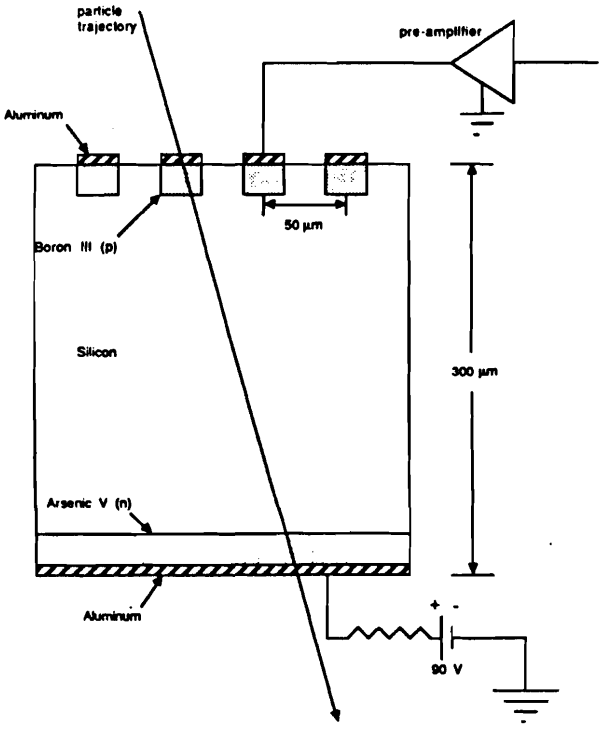

Figure E.2: A schematic cross-sectional view of a plane of the Silicon Microstrip Detector.

In a position sensitive detector like the SMD, the intrinsic resolution in the direction perpendicular to the beam is

$$\sigma^2_{intr} = \frac{\int_{-d/2}^{-d/2} x \; dx}{\int_{-d/2}^{-d/2} dx} = \frac{d^2}{12} \tag{E.1}$$

where d is the strip pitch (spacing). The strip pitch in the SMD was 50 μm. Thus the predicted intrinsic transverse resolution is $50/\sqrt{12}$ μm = 14 μm. The measured value in E691 was 16 μm. The theoretical track intercept (transverse) resolution is the sum of three independent effects

$$\sigma^2_{trans} = \sigma^2_{intr} + \sigma^2_{mult} + \sigma^2_{angl} \tag{E.2}$$

where $\sigma_{intr\ x(y)} = 13(16)\ \mu$m. The second term in Equation E.2 is due to multiple scattering

$$\sigma_{mult} = \frac{50\ (\mu m)}{p\ (GeV)} \tag{E.3}$$

and is a significant effect only for tracks with momenta less than 5 GeV. The third term in Equation E.2 is the error due to the angular resolution

$$\sigma_{ang} \simeq \frac{\sigma^2_{intr}}{3}\frac{L_1^2}{L_2^2} \tag{E.4}$$

where L_1 is the distance from the first triplet assembly to the secondary vertex and L_2 is the length of the vertex telescope. In E691, L_1/L_2 was about 0.25, so the contribution from σ_{angl} could be neglected.

The two–vertex resolution may be estimated by considering Figure E.3 where the parameters for a two track vertex in the xz–plane are shown. The vertex position along the z–axis is

$$z_v = \frac{x_{02} - x_{01}}{s_{x2} - s_{x1}} \tag{E.5}$$

and the associated error is

$$\sigma^2(z_v) = \frac{1}{(s_{x2} - s_{x1})^2}[\sigma^2(x_{01}) + 2\sigma(x_{01}, s_{x1})z_v + \sigma^2(s_{x1})z_v^2 \tag{E.6}$$

$$+ \sigma^2(x_{02}) + 2\sigma(x_{02}, s_{x2})z_v + \sigma^2(s_{x2})z_v^2] \tag{E.7}$$

where correlations between the errors in the two tracks are assumed to be negligible. For a set of N planes, each with transverse resolution σ_x, the error in the track intercept is

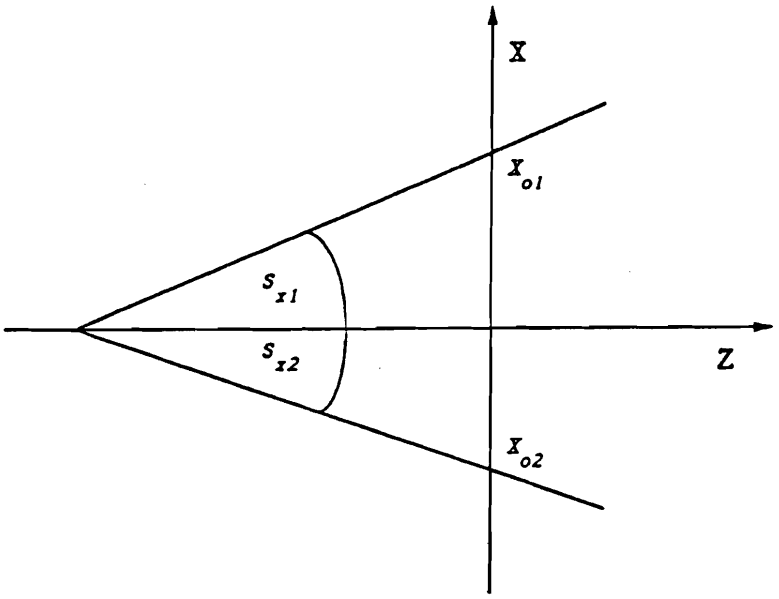

Figure E.3: The vertex parameters for a two track vertex in the $xz-$plane.

$$\sigma(x_0) = \frac{2\sigma_x}{\sqrt{N}} \tag{E.8}$$

For E691, $\sigma(x_0) \simeq 10$ μm, $\sigma(s_x) \simeq 100$ μrad and z_v is at most 10 cm. Thus the error in the vertex is dominated by the errors in the track intercepts. Using the above derivation, one estimates $\sigma(z_v) \sim 300$ μm for E691. The measured E691 most probable value is $\sigma(z_v) \sim 370$ μm while $\langle\sigma(z_v)\rangle \sim 420$ μm. As more tracks are added to a vertex, the resolution improves. The improvement in the resolution of an n–track vertex over a 2–track vertex is well estimated by

$$\sigma_n \simeq \frac{\sigma_2(z_v)}{\sqrt{n-1}} \tag{E.9}$$

The two-vertex resolution is

$$\sigma_{\Delta z} = \sqrt{\sigma^2(z_{v1}) + \sigma^2(z_{v2})} \tag{E.10}$$

For two 2-track vertices, one estimates $\sigma_{\Delta z} \sim 420$ μm. The E691 measured two-vertex resolution for a 3-track secondary vertex had a most probable value $\sigma_{\Delta z} \sim 360$ μm and $< \sigma_{\Delta z} > \sim 440$ μm. With

$$\frac{\Delta z}{\sigma_{\Delta z}} \sim 6 \tag{E.11}$$

the SMD gave good two-vertex resolution, reducing the non-charm combinatoric background by a factor of 300 to 500. The SMD plane efficiencies were determined from reconstructed tracks and are listed in Table E.1. A fully reconstructed open-charm event is shown in Figure E.4.

Table E.1: The z coordinate positions, number of channels and efficiencies of the SMD planes. The efficiency of a given plane is the fraction of a sample of reconstructed charged tracks passing through the plane that registered a hit in the plane.

SMD Plane	z Position (cm)	Number of Instrumented Channels	Efficiency (%)
1st Assembly			
X	1.931	512	87.7 ± 1.5
Y	3.015	512	88.2 ± 2.8
V	6.684	512	89.1 ± 2.8
2nd Assembly			
Y	11.046	768	88.6 ± 5.5
X	11.342	768	90.5 ± 7.1
3rd Assembly			
X	19.915	1000	88.9 ± 0.8
Y	20.254	1000	94.0 ± 0.6
V	23.878	1000	88.7 ± 1.0

Calibration

Based on previous studies [Kar 85], the discriminator thresholds were originally set to about 30% of the minimum ionizing signal. The thresholds were then adjusted individually until the planes efficiencies were maximized while maintaining the noise rate to less than 0.1%.

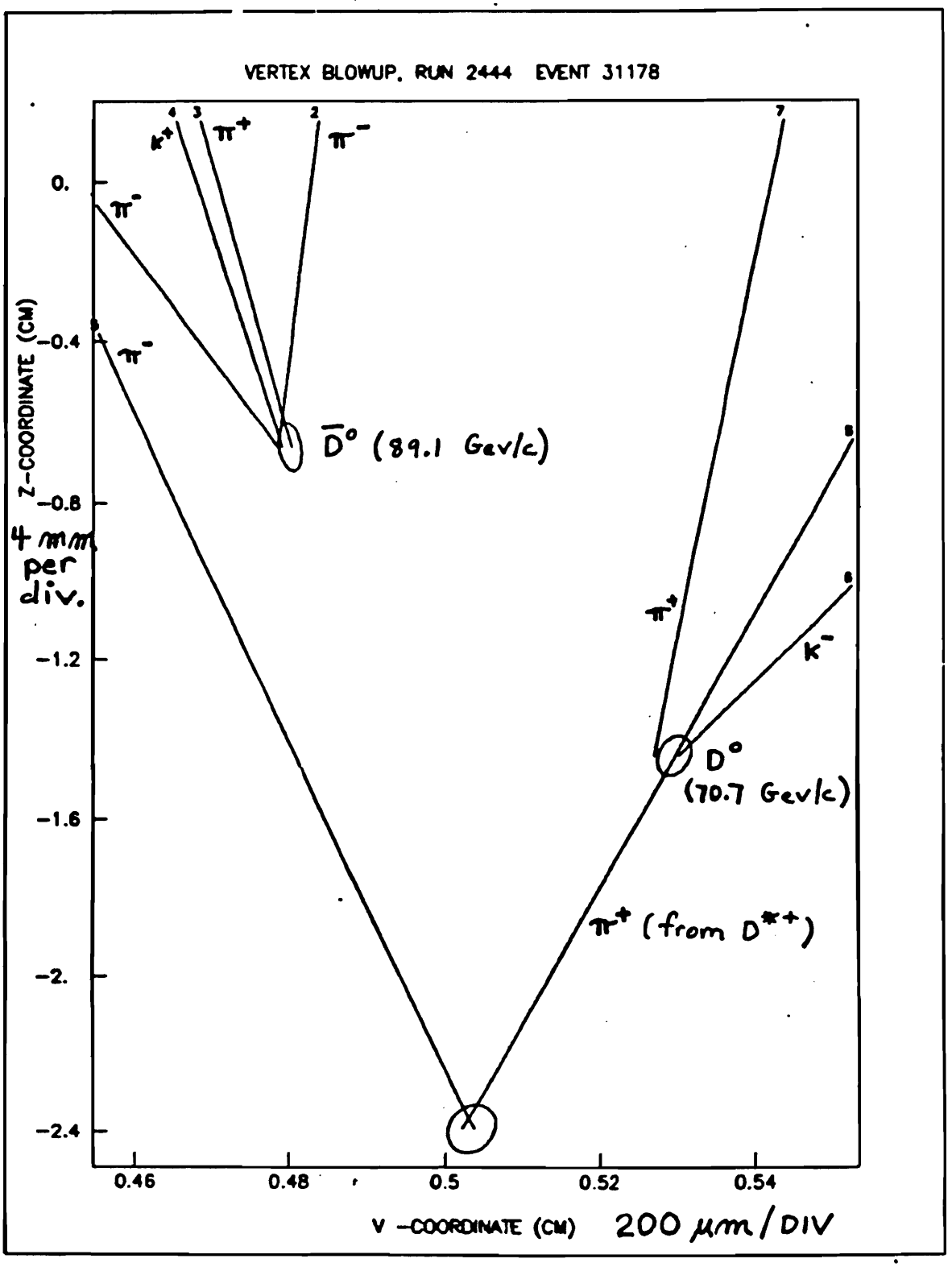

Figure E.4: An open-charm event with both secondary charm vertices fully reconstructed.

Reconstruction

The vertex reconstruction, a part of the second stage (PASS2) reconstruction, was used to find candidate primary vertices.

The vertex reconstruction consisted of three main subroutines. The first subroutine called SMDFIT was used to perform a refit of the tracks found by the first stage (PASS1) track reconstruction using only the SMD hit information. The second subroutine called MVTX1 was then used to find the candidate vertices. Finally, the third subroutine called PRIOUT ordered the candidate primary vertices according to their positions along the z axis.

Upon being called, MVTX1 first made a list of acceptable tracks based on the requirements that the tracks be at least category 3 with hits in at least the SMD and D2, have a good χ^2 per degree of freedom less than 5.0 and a good number of degrees of freedom greater than 2. The next step was to examine all pairs of good tracks and determine if they formed or were at least part of a primary vertex. MVTX1 called the subroutine VFIT1 to perform a linear constrained χ^2 fit to obtain the preliminary coordinates of the candidate vertex. The fit was linear because only the track intercepts were varied and not the track slopes. The vertices with a χ^2 per degree of freedom less than 3.0 were kept. Tracks were then added, one at a time, to the pair. MVTX1 called the subroutine VFIT5 to perform a non-linear constrained χ^2 fit where both the intercepts and the slopes of all the tracks were varied. Vertices with a χ^2 per degree of freedom less than 3.0 were kept. PRIOUT was then called to order the candidate primary vertices with the most upstream vertex being identified as the first. PRIOUT also recorded the vertex with the greatest number of tracks.

E.2 The Analyzing Magnets and the Drift Chambers

Two large aperture copper coil magnets were used to bend the charged particle paths (provide a p_T kick) for measurement of their momenta. The magnetic fields were in the $-y$ direction and bent positive charged particles in the $+x$ direction (towards the right side of the spectrometer looking downstream). The magnet properties are listed in Table E.2. The magnetic fields were parametrized by a sum of orthogonal polynomials consistent with Maxwell's equations. This parametrization was then adjusted to give agreement between the measured and accepted values of the K_S mass (from $K_S \to \pi^+\pi^-$) to better than $\pm$ 0.1 MeV.

Table E.2: Properties of the E691 Momentum Analyzing Magnets.

Magnet	M1	M2
z at Centre (cm)	286.6	620.6
Length along z (cm)	165.	208.
$x \times y$ at Entrance (cm)	154. $\times$ 73.	154. $\times$ 69.
$x \times y$ at Exit (cm)	183. $\times$ 91.	183. $\times$ 86.
Horizontal Angular Acceptance (mrad)	$\pm$ 240	$\pm$ 120
Vertical Angular Acceptance (mrad)	$\pm$ 120	$\pm$ 60
Current (amps)	2500.	1800.
p_T Kick (MeV)	212.4	320.7
$\int Bdl$	-0.71 T–m	-1.07 T–m

During the experiment the stability of the magnetic fields was continuously monitored in two independent ways. The currents supplied to M1 and M2 were 2500 amps and 1800 amps respectively. These currents levels were monitored by the beamline computer. During a spill the currents of M1 and M2 varied by no more than 0.1%. A Hall probe glued onto the pole face of each magnet was used to directly monitor the magnetic field. The ouput voltages from the Hall probe electronics (F. W. Bell Model 620 Gaussmeters; rated accuracy 0.25%) were amplified by ultra-low offset voltage operational amplifiers (Precision Monolithics OP-07AJ) and digitized by 12 bit Le Croy 2232 ADCs. The digitized voltages were written onto the data tapes once per

beam spill as part of the calibration event record. A warning was issued by the online monitoring alarm system if either of the magnetic fields drifted outside of acceptable values.

Charged particle tracking and momentum analysis was performed using the SMD and the four drift chamber (DC) stations (D1, D2, D3 and D4) consisting of 35 planes. These planes were grouped into assemblies, an assembly being a set of planes which completely determines the (x, y, z) co-ordinates of a single point on a charged particle trajectory. The time information cannot differentiate as to whether the charge cloud drifted to a sense wire from the right–hand or left–hand side. To resolve this left–right ambiguity, two planes U and V tilted $\mp 20.5°$ with respect to the vertical (looking downstream) were used. These three planes formed a D2, D3 or D4 UXV triplet assembly. In D1 an additional X′ plane, identical to the X plane but offset by half a cell, was added to help resolve the right–left ambiguities in the highest track density region. These four planes formed a XX′UV quadruplet assembly. Two views of the drift chamber assemblies are shown in Figures E.5 and E.6.

D1 was located upstream of the of the first bend magnet, providing an initial measurement of the track trajectory. In addition, D1 helped identify poorly constrained SMD track segments and eliminate false SMD track candidates. D2 was located between the first and second analyzing magnets providing the first space points and track segments after the momentum separation by M1. The efficiency in the central region of D2 was greatly degraded (by $\sim$ 50%) by the large number of e^+e^- pairs. M1 spread these pairs out horizontally resulting in a deadened region (called the D2 hole) $\pm$ 1 cm wide in the vertical and $\pm$ 10 cm wide in the horizontal. D3 was located downstream of the second analyzing magnet providing space point and track segments for tracks sufficiently stiff (large momentum) to have passed through both M1 and M2. D4 was located just upstream of the electromagnetic calorimeter. The long lever arm advantage of D4 was negated by spurious hits from the albedo of the electromagnetic showers and hardware problems resulting in a much degraded resolution.

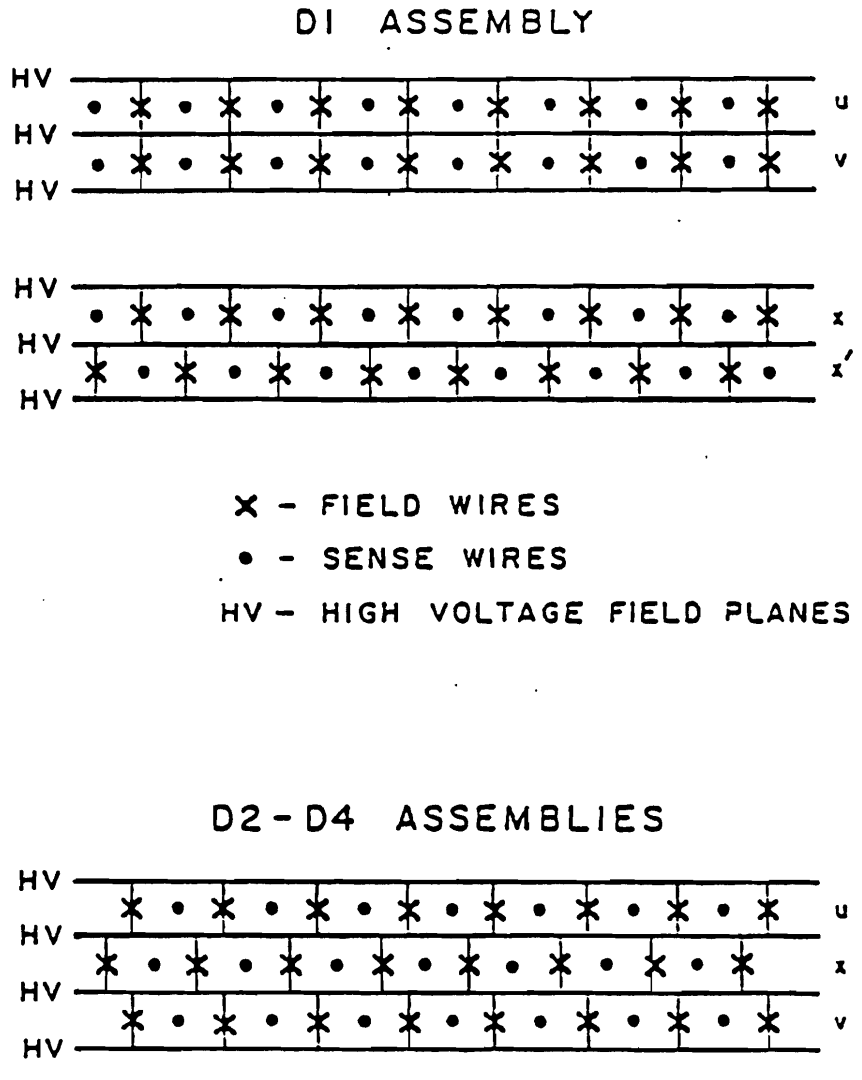

Figure E.5: The xz–plane view of the cell structure of the drift chambers.

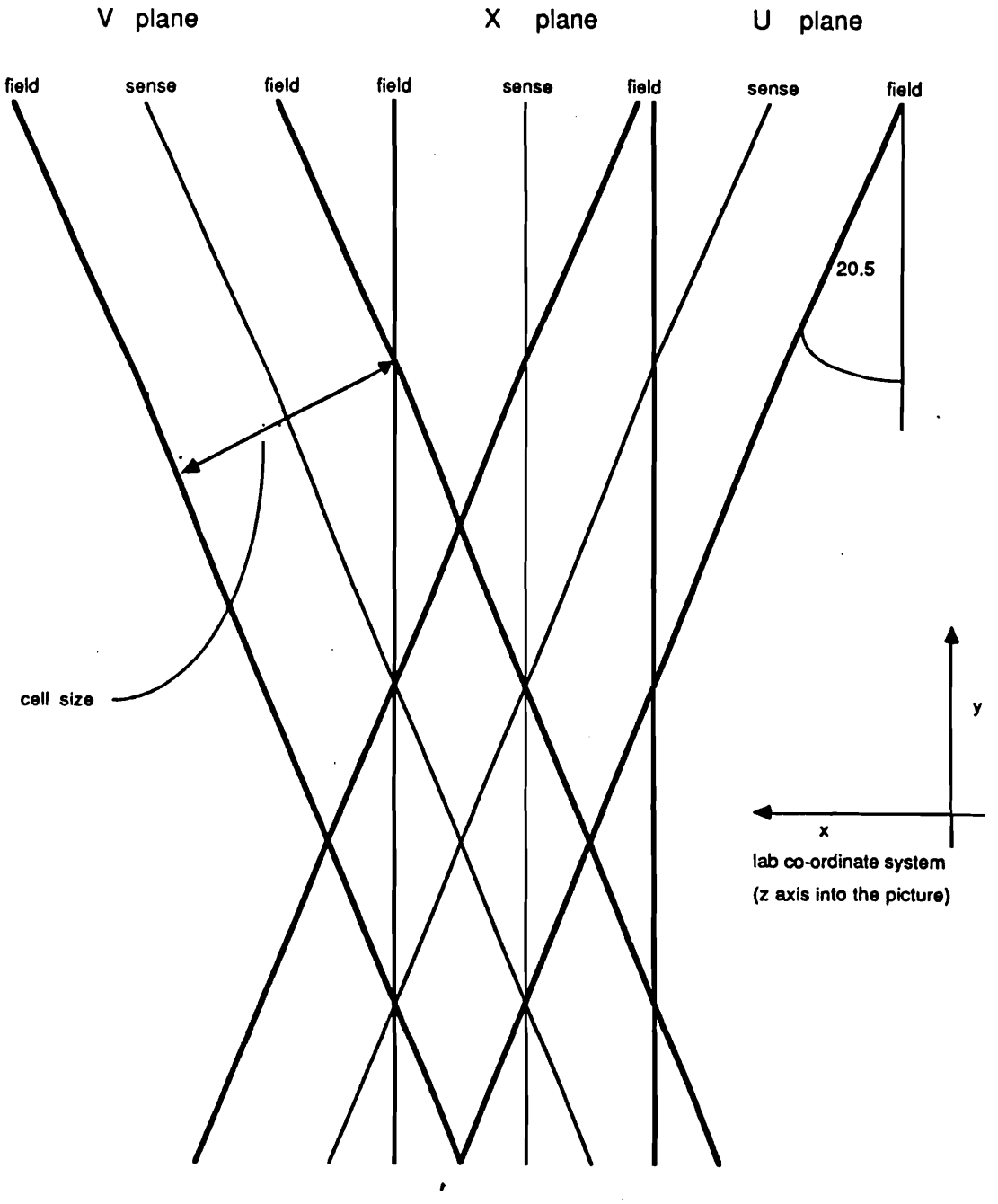

Figure E.6: The xy–plane view of the drift chamber cell structure.

Table E.3: Properties of the E691 Drift Chambers.

Drift Chamber	1	2	3	4
Sense Wire Voltage (kV)	0	0	0	+ 2.9
Field Wire Voltage (kV)	-1.6	-2.0	-2.0	-0.2
Cathode Plane Voltage (kV)	-2.3	-2.4	-2.4	0.0
U/V Cell Size (mm)	4.46	8.92	14.87	29.74
X/X′ Cell Size (mm)	4.76	9.53	15.88	31.75
Number of U + V Wires	896	1536	1280	256
Number of X + X′ Wires	640	848	672	160
Resolution (μm)	350	300	300	800

In D1 to D3 a drift chamber assembly was constructed of alternating layers of sense wire planes and high voltage field wire planes. A sense wire plane consisted of alternating sense wires and field wires. The sense wires were 25 μm diameter gold–plated tungsten and the field wires were 127 μm hard copper. Each sense wire plane was situated between two high voltage field wire planes which consisted solely of field wires stretched (horizontally in D1 and vertically in D2 and D3) across a G–10 frame. The sense wires were held at ground potential and the field wires were held at high negative potentials between -2 and -3 kV. The spacing between the field wires in these planes was 3 mm. The field wires determined the shape of the field across a cell. The negative potentials of the field wires in the sense and field wire planes were chosen to give as uniform a drift velocity as possible and to thereby minimize the low field dead spaces within each cell. The sizes of the U and V cells were smaller than the X cells by a factor of $\cos 20.5°$.

In D4 the analogs of the field wire planes were the ground planes. The ground planes consisted of aluminum sheets bonded to Hexcel backings for rigidity. The field planes and the field wires in the sense planes were held at ground potential and the sense wires were held at high positive potentials of between 2 and 3 kV. The field wires in the sense planes were held at a small positive potential to adjust the field shape in the cells if necessary.

All the drift chamber planes were enclosed in gas–tight aluminum containers with

flexible windows, composed of 2 mil Aclar and 5 mil Mylar, covering the active areas. To achieve a drift velocity nearly independent of the electric field strength a gas mixture containing equal parts of argon and ethane was used at a pressure of about 0.254 cm of water above the atmospheric pressure. A 1.5% admixture of ethanol was added to deter quenching and retard chamber aging [Est 86]. The DC system operated with a 2×10^5 gas gain and a typical drift velocity of 40 μm/ns. The pulse produced in a sense wire by the passage of a charged particle through the cell was processed by a signal card situated at the top of the drift chamber box. A signal card consisted of an amplifier followed by a discriminator. Each signal card processed sixteen cells. The output of the signal card was an ECL signal which propagated to the digitization system along a twisted pair cable. The ECL signal was used to provide a start signal to a channel of a Le Croy 4291 TDC system. Low level triggers provided the common stop signal for all cards. The digitized times were stored in a Le Croy 4299 memory buffer and then written to tape. Positions and efficiencies of the 35 drift chamber planes are listed in Table E.4. A detailed description of the drift chamber system is contained in [Men 86].

Calibration

The fields of the two magnets were mapped out before the start of the experiment. The mapping was carried out using a FNAL computer controlled magnetic field mapping machine. This machine measured the three field components over a grid of points 8.96 cm $\times$ 4.48 cm $\times$ 1.145 cm. M1 was mapped at 1800 amps and 2500 amps. M2 was mapped at 900 amps, 1800 amps and 2500 amps. The magnetic fields were measured to an accuracy of 0.1%.

The field measurements were then fitted to a set of polynomials ([Lec 69, Win 69, Win 70]) that satisfied Maxwell's equations in a current free region. By fitting to these functions, the average magnetic field deviations were found to be no more than 0.1%. To optimize CPU usage, this set of polynomials was converted to a set of Chebyshev polynomials for use in the swimming routine of the charged track reconstruction

program. The overall normalizations of the two magnetic fields were adjusted by less than 2% to give good agreement between the measured masses of well known particles, such as the K_S, with their Particle Data Handbook values.

The preliminary absolute alignment of the drift chamber planes relative to the spectrometer coordinate system was obtained from an on-site optical survey of the apparatus. Tolerances on the wire-laying process were maintained within acceptable limits so that the external survey accurately gave the actual positions of the drift cells.

The cells within each drift chamber plane were calibrated relative to each other such that two hits at the same distance from the sense wires in any two cells gave the same number of TDC counts. Before the beginning of every new run, the data acquisition system (DA) sent a message to the Le Croy 4298 crate controller that 'external autotrimming' was to be performed. The 4298 then sent a message to the pulser box to produce a 5 to 20V calibration pulse. The calibration pulse was split by impedance matched inductive pulse splitters with a 2.22 cm diameter ferrite core (material 3E2A). The output voltage from a splitter was $1/\sqrt{N}$ of the input voltage, where N was the number of outputs. Two 49–way splitters were used to pulse D1. Four 49–way splitters were used to pulse D2, one per assembly. Three 36–way splitters were used to pulse D3, again one per assembly. One 36–way splitter was used to pulse the assembly of D4. The splitters were pulsed one at a time. All unused outputs were terminated with 50 ohms. The calibration pulse from a splitter output was inductively coupled to the 16 sense wires of a card by an insulated copper strip antenna at the wire solder pads. The antennas were 50 ohm terminated. This arrangement was found to give single output pulses from all the channels on a card with negligible crosstalk into neighboring cards. The 4298 crate controller adjusted the relative time offsets (RT_0s) of the pulsed channels until all the pulsed channels gave the same number of TDC counts. A schematic of the drift chamber electronics is shown in Figure E.7.

A χ^2 minimization procedure was used to find the optimum values of the absolute

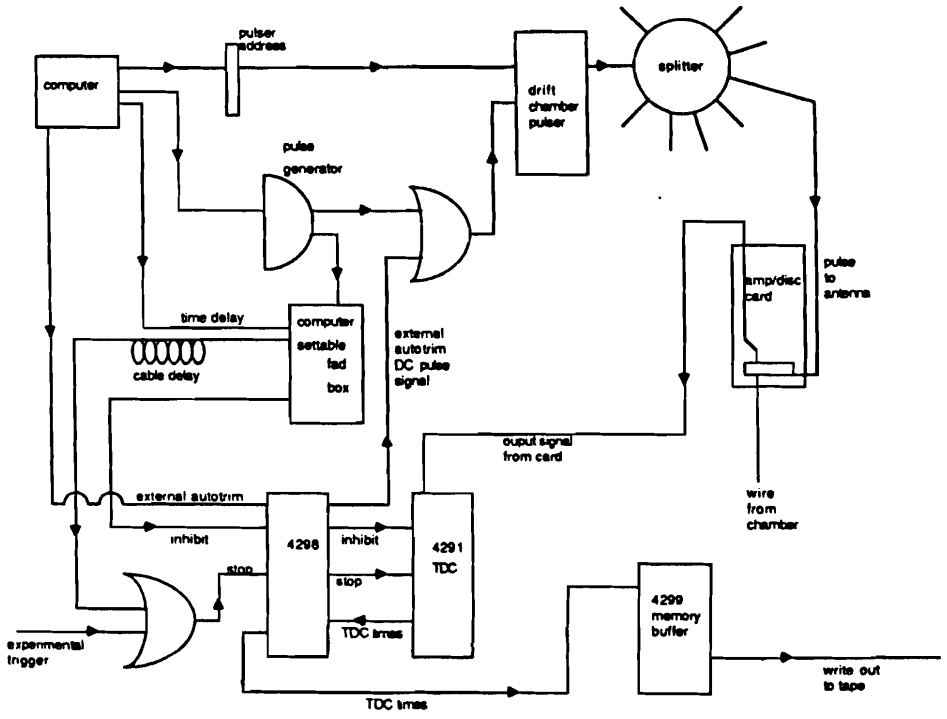

Figure E.7: A schematic of the drift chamber TDC calibration system logic.

time offsets (AT_0), the electron drift velocities (V_{drift}) and the absolute alignment constants. The tracks used in the χ^2 minimization routine were obtained during special calibration runs. During such a run the analyzing magnets were turned off and the beam stop, a lead absorber, was inserted into the path of the electron beam. Thus only the muon halo created at the primary target reached the detector. A calibration trigger, called the DC paddle trigger, was used to trigger on these muons. This trigger required a coincidence between the two paddle counters positioned in line parallel to the z–axis behind the muon wall. The two counters were separated by about 1 m.

The muon tracks obtained during these runs were used to minimize the expression

$$\chi^2 = \sum_i \chi_i^2 \tag{E.12}$$

where

$$\chi_i^2 = \sum_m \omega_m r_{im}^2 \tag{E.13}$$

denoted the χ^2 for the ith track and the mth plane, $1/\sqrt{\omega_m}$ denoted the plane resolution and r_{im} denoted the plane residual.

The residual of a plane was defined as the difference between the position of a track in that plane and the actual position of the hit in the plane that was associated with the track. It was given by

$$r_{im} = W_{im} + V_{drift}(t_{abs} - t_{TDC}) + d_a - \sum_j Q_{mj}\alpha_{ij} \tag{E.14}$$

where W_{im} was defined as the distance of the hit cell from the centre of the drift chamber plane in the drift chamber coordinate system. This distance was given by the number of cells the hit cell was from the plane centre multiplied by the cell size in the plane. The distance of the hit from the sense wire in the hit cell was given by $V_{drift}(t_{abs} - t_{TDC})$. The distance of the drift chamber coordinate system from the spectrometer coordinate system, the drift chamber alignment constant, was denoted by d_a. The α_{ij}'s were the five track parameters, the x and y intercepts, the x and y slopes and $1/p$. The Q_{mj}'s were the geometric factors required to obtain a hit position from the track parameters.

The RT_0s were not used in Equation E.14 because virtually all were zero. Thus they were not used in the offline drift chamber calibration or the track reconstruction.

Reconstruction

The event charged track reconstruction, denoted by PASS1, was performed by a FORTRAN program called SESTR. SESTR consisted of two programs that performed the charged track reconstruction in two stages: first program S1234 performed SMD–drift chamber reconstruction, then program ESTR performed drift chamber–only reconstruction. S1234 attempted to form tracks from the hits in the 9 SMD planes and the 35 drift chamber planes. ESTR then attempted to from tracks from only the remaining hits, those not identified with a track by S1234, in the 35 drift chamber planes. The momentum vectors of all the tracks were then estimated.

S1234 consisted of four subroutines. The first subroutine called was REGUN1 which attempted to reconstruct charged tracks from the hits in the SMD and D1. The region between the target and M1 containing the SMD and D1 was called Region 1. Track reconstruction was initiated in the SMD and D1 for the following reasons:

1. The 17 SMD and D1 planes were the most efficient.
2. The SMD and D1 planes had the least noise.
3. The 17 SMD and D1 planes gave the highest redundancy in the any of the field free regions of the spectrometer.
4. The region immediately downstream of the target was the region were the physics of interest occurred and the most tracks were found in the region where track reconstruction was initiated.

For a line of hits to be accepted as a track in Region 1, there had to be at least seven of a possible nine hits in the SMD planes with at least one hit per XYV assembly. If two tracks were nearly duplicate the one with the greater number of SMD hits was kept. If nearly duplicate tracks had the same number of SMD hits, then the track with the smaller χ^2 from a fit of the hits to a trajectory was kept.

The second subroutine called was TATL (Track and Triplet Linker) which attempted to match a track candidate in Region 1 with a hit in at least one of the eight UXV triplet assemblies that comprised D2 and D3. Since the major components of the M1 and M2 magnetic fields were aligned with the (negative) y–axis, the trajectory of a charged particle that passed through the aperture(s) of the magnet(s) was not appreciably bent in the y direction. Thus only triplets in the Y-band consistent with a straight line extrapolation of the candidate SMD–D1 track had to be examined, resulting a great saving of time. In the TATL pattern recognition the single bend point approximation was used for each analyzing magnet. The resulting trajectory, formed by the SMD–D1 candidate track at one end and the hit triplet at the other, was accurate to about 2 mm in D2 and D3. Thus the error on the trajectory was

smaller than the D2 and D3 cell sizes. This allowed drift chamber hit arrays for the 24 D2 and D3 planes to be used to test the hypothesis that a given triplet belonged to a given SMD track. If the pattern recognition picked up enough hits, then the SMD–drift chamber candidate track was kept, otherwise a new triplet was tried.

TATL was first used to try and match candidate SMD–D1 tracks with D3 triplets. The matching was done first with D3 for two reasons. Fewer tracks reached D3 than D2 and the ones that did reach D3 were spread out more than in D2 because of the additional p_T kick they received from M2. This reduced hit congestion made the candidate SMD–D1 track–D3 triplet matching more efficient than that for D2 triplets. Duplicate candidate tracks were weeded out by choosing the track with the greater number of hits or better χ^2 fit for duplicate tracks with equal numbers of hits. TATL was then used to try and match candidate SMD–D1 tracks with the remaining D2 triplets that were not consistent with a candidate SMD–D1–D3 track. Again duplicate tracks were weeded out.

All tracks were categorized according to whether or not they had hits in D1, D2, D3 and D4. Bit 0 of the variable JCATSG was allocated for tracks that had hits in D1, bit 1 to D2 hits, bit 2 to D3 hits and bit 3 to D4 hits. Tracks with at least seven SMD hits were assigned bit 1 along with D1.

All accepted candidate tracks were checked to make sure that D1 hits and D4 hits if any were added to the tracks. This completed the S1234 SMD–drift chamber 44 plane track reconstruction.

The third subroutine called was BTRFIT which improved the estimate of an accepted track's momentum vector by replacing the single–bend–point approximation by a momentum fit which incorporated the detailed M1 and M2 magnetic field parametrizations. This improved the momentum resolution of the drift chamber planes downstream of M1 by about a factor of five. This was done for tracks found either by TATL or ESTR. This enabled BTRFIT to perform the last pattern–recognition task, that of limited migration whereby hits were swapped or dropped in those planes were TATL or ESTR initially supplied hits and hits were added back in

the remaining planes that TATL and ESTR had initially missed.

The fourth subroutine call was STRKE which attempted to eliminate fake TATL tracks by rejecting tracks with excessively large χ^2 fits or tracks that shared too many hits in the SMD, D1, D2 or D3 with other good χ^2 tracks. STRKE also listed SMD-only category 1 tracks that had 8 or 9 unused SMD hits such as those left by charged strange particles the decay between the SMD and D1.

In PASS1 production running, S1234 subroutines were called by subroutine ESTR of SESTR. ESTR then proceeded to reconstruct any leftover tracks with no SMD hits such as those from K_S and Λ decays or tracks missed by S1234. ESTR saved a large amount of time by not looking at hits that had been used by S1234.

Table E.4: The plane positions and efficiencies of drift chambers D1, D2, D3 and D4.

Plane	z Position (cm)	Efficiency (%)
D1A X	153.6141	93.1 ± 0.6
X'	154.5666	92.9 ± 0.6
U	158.6941	92.2 ± 0.4
V	159.6466	91.9 ± 0.6
D1B X	188.7144	88.0 ± 0.5
X'	189.6669	92.7 ± 0.5
U	193.7918	82.9 ± 0.9
V	194.7443	91.1 ± 2.4
D2A U	382.3691	85.8 ± 0.3
X	383.9566	84.3 ± 0.3
V	385.5411	82.2 ± 0.4
D2B U	424.9090	78.7 ± 1.2
X	426.4965	82.0 ± 0.4
V	428.0840	80.2 ± 0.6
D2C U	466.6463	81.1 ± 1.3
X	468.2338	81.1 ± 0.4
V	469.8213	75.5 ± 1.5
D2D U	466.6463	89.7 ± 0.3
X	499.3081	83.1 ± 0.3
V	500.9058	81.1 ± 1.1
D3A U	928.2963	83.7 ± 0.8
X	929.8838	86.8 ± 2.8
V	931.4713	85.1 ± 1.4
D3B U	970.8413	79.9 ± 2.3
X	972.4288	82.0 ± 1.9
V	974.0163	77.9 ± 2.3
D3C U	1012.5862	87.8 ± 1.2
X	1014.1737	89.7 ± 0.7
V	1015.7612	87.3 ± 1.3
D3D U	1044.3963	91.7 ± 0.2
X	1045.9669	90.9 ± 0.6
V	1047.5646	89.9 ± 1.7
D4A U	1737.8959	67.7 ± 1.7
X	1743.5855	62.8 ± 1.9
V	1749.2751	45.8 ± 5.4

E.3 The Cherenkov Threshold Detectors

Two gas–filled Cherenkov threshold counters, C1 and C2, were used to distinguish between the charged π, K and p hadrons. The upstream counter, C1, was located behind and partly inside the second analyzing magnet M2 and the downstream counter, C2, was located behind the third drift chamber station D3.

The half–angle θ_C of the Cherenkov light cone for a particle with velocity β in a medium with index of refraction n is

$$\theta_C = \cos^{-1}\left(\frac{1}{n\beta}\right) \tag{E.15}$$

giving a threshold velocity $\beta_t = 1/n$ for Cherenkov light production. The number of Cherenkov photons N_γ produced per interval of path length is

$$\frac{dN_\gamma}{dl} = 2\pi\alpha \int \left[1 - \frac{1}{\beta^2 n^2(\lambda)}\right] \frac{d\lambda}{\lambda^2} \tag{E.16}$$

where λ is the emitted photon wavelength. Table E.5 lists the properties of C1 and C2. The lengths of the counters were determined by the requirement that a charged π emit 10 photoelectrons on average in traversing the counters. The different indices of refraction for the two counters meant that the Cherenkov emission thresholds were different in the two counters for a given particle.

Table E.5: The properties of the two E691 threshold Cherenkov counters C1 and C2.

Counter	C1	C2
Gas Mixture	N_2 100 %	N_2 20 % He 80 %
$\pi^\pm$ θ_C (mrad)	24.	13.
$n-1$	2.9×10^{-4}	8.6×10^{-5}
z Length (cm)	370.	660.
Mirror Plane z Position (cm)	866.	1653.4
Number of Cells	28	32

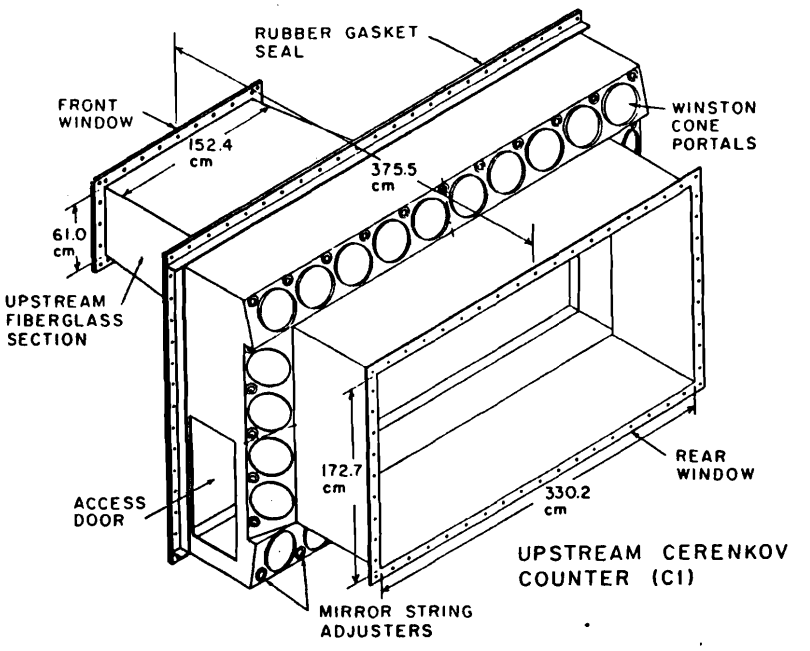

Figure E.8: A diagram of the upstream threshold Cherenkov detector C1.

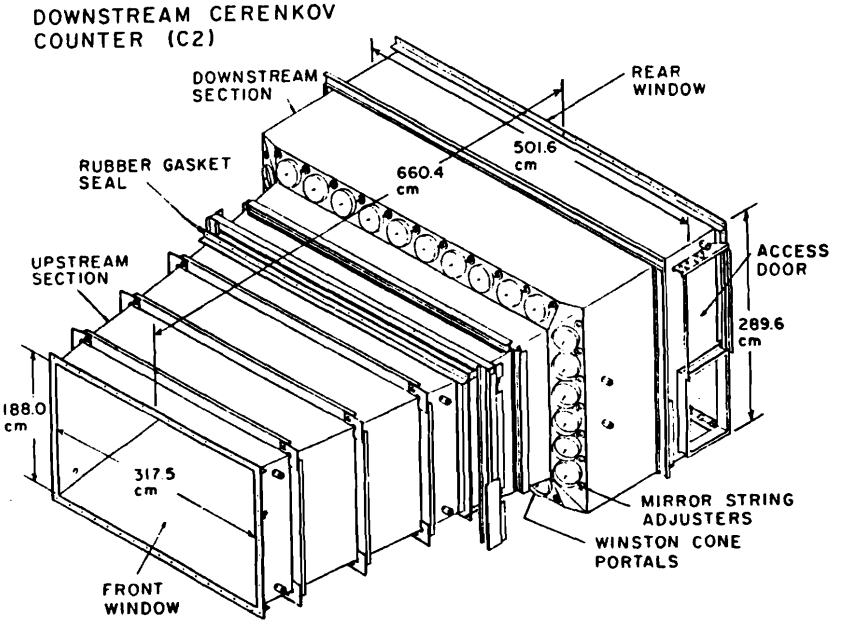

Figure E.9: A diagram of the downstream threshold Cherenkov detector C2.

Diagrams of C1 and C2 are shown in Figures E.8 and E.9. The C1 and C2 optics are shown in Figure E.10. Each counter contained a set of primary mirrors; 28 in C1 and 32 in C2. Each mirror focussed and reflected the Cherenkov light into a Winston cone. The Winston cones were used to collect the light from the primary mirrors and transmit it to the phototubes. The partial insertion of C1 into M2 made it necessary to collect the light from the downstream end of the counter. A set of secondary plane mirrors was used to reflect the light from the primary mirrors to the downstream Winston cones.

Both sets of primary mirrors possessed quadrant symmetry, with each C1 quadrant containing seven mirrors and each C2 quadrant containing eight mirrors. The layouts of the C1 and C2 primary mirrors are shown in Figures 3.6 and 3.6. These C1 and C2 mirror segmentations were an optimization of two opposing requirements; that the light from a single particle be completely collected in a single mirror and that the number of Cherenkov rings overlapping at a mirror be minimal. The Cherenkov light rings had a maximum radii of 8.4 cm in C1 and 8.7 cm in C2. Mirror sizes ranged from 15.0 cm $\times$ 25.0 cm at the C1 centre to 95.0 cm $\times$ 50.0 cm at the outer part of C2. Overlapping rings at the C1 centre occurred in about 7 – 11% of the events and at the outer C1 mirrors in less than 2% of the events. In C2, overlapping rings at the centre occurred for about 3 – 7% of the events and at the outer mirrors for less than 1% of the events. To avoid collecting light produced by the large midplane flux of electron pairs a 3.0 cm gap was left between the upper and lower halves of both sets of primary mirrors and baffles consisting of a set of black strips 3.81 cm in width recurring at 45.72 cm intervals were suspended across the midplanes.

The spherical primary mirrors were made from slump-molded glass with a thin film aluminum coating deposited on the front surface. The focal length was measured to be 1.98 m and the reflectivity, for 252.2 nm light, was measured to be $>$ 85 %. Each mirror in C1 was held in place with seven (8.1 kg test Dacron line) strings. A string support system provided a method for positioning the mirrors without placing any massive structures in the active beam region of the counters. The three strings

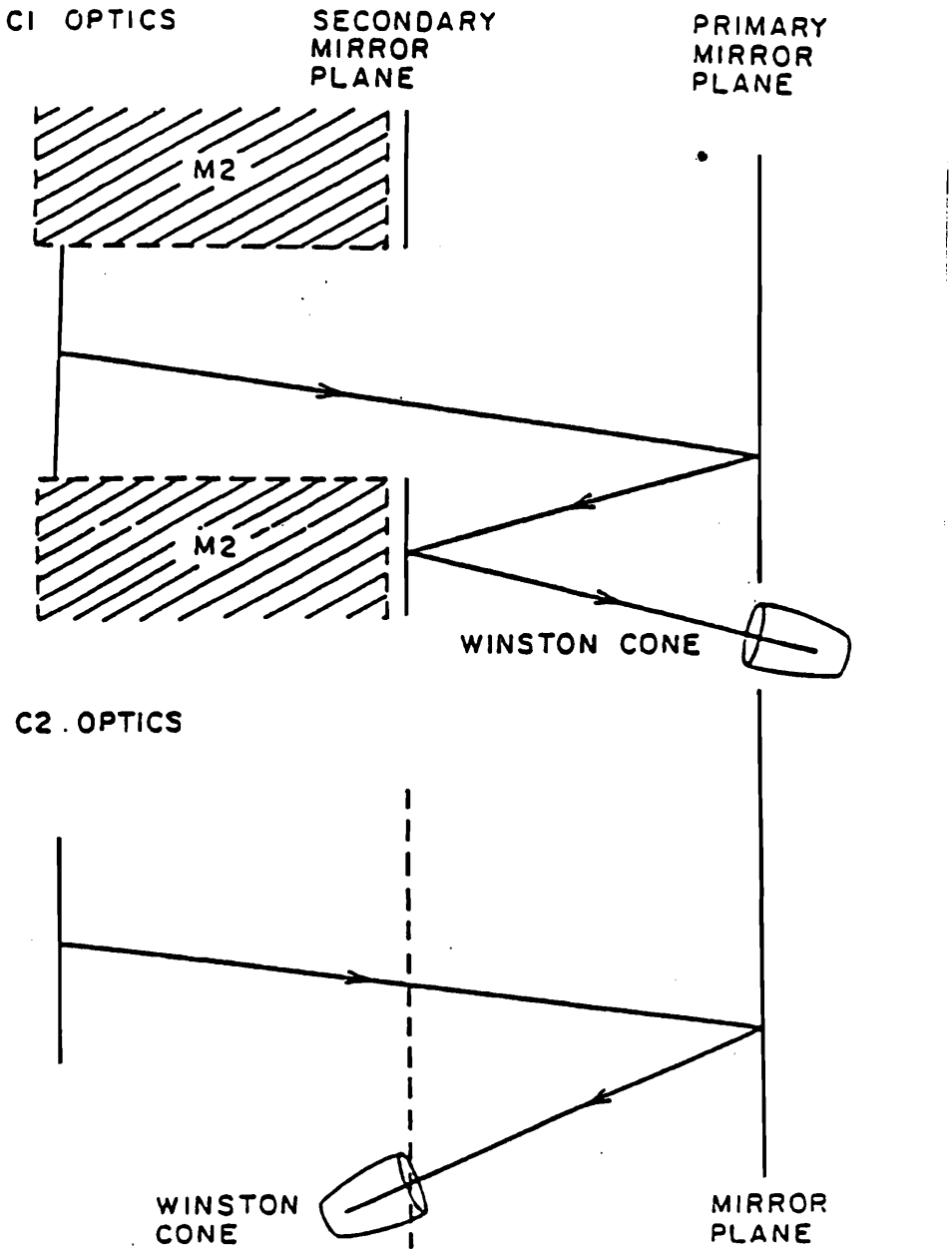

Figure E.10: The C1 and C2 optics.

fastened to the upstream face of the mirror were adjustable, permitting alignment of the mirror by vertical and horizontal rotations about an axis defined by the downstream strings. The C2 mirrors were held in place by a rectangular grid of aluminum tubing. Tight universal ball joints connected to rods were mounted on the back of the mirrors. The rods were set into the vertices of the grid.

The Winston cones were formed by spinning epoxy on a polished steel mandrel and then coating the inner surface with aluminum. The curvature of their reflecting surfaces was defined as a rotation of an off centre ellipse. The large and small openings of the cones were 38.1 cm and 12.7 cm respectively. The Winston cones were designed to focus Cherenkov light entering at an aperture angle of less than 20° into the phototubes with at most a single reflection. Light rays entering at higher angles were reflected back out after multiple bounces. The normal reflectivity of the cones, for 252.2 nm light, was 88%.

Light was transmitted from the Winston cones to the high gain 12.7 cm RCA 8854 phototubes via an aluminum coated lucite collar. A phototube output pulse is proportional to the incident number of photons or equivalently photoelectrons. The high gain cesium gallium phosphide first dynode enabled the single photoelectron peak to be clearly separated from the quiescent pedestal level. To take advantage of the higher phototube detection efficiency at short wavelengths the outer glass surfaces of the phototubes were coated with p–terphenyl (pTP). This compound absorbs light in the 160 – 250 nm range and re-emits in the 350 – 500 nm range; the region of highest phototube efficiency. The Winston cone–phototube assemblies are shown in Figure E.11. Magnetic shielding for the phototubes was provided by a cast steel outercasing and a mu–metal magnetic shield. The signals from the phototube anodes were digitized by a Le Croy 2249 ADC system and were written to tape as part of the physics events. The phototube dynode signals were used in the dimuon trigger.

The body of C1 was built from two sections. The downstream main body was made from 0.635 cm sheet aluminum. An access opening was installed on one side. Twenty-eight circular openings were cut out along the transverse perimeter. These

were used as Winston cone portals. To increase its rigidity the main body was reinforced with aluminum I-beams. The Winston cone mounting assemblies were clamped to these I-beams. The upstream section of C1 was situated inside M2. In order to avoid destructive eddy currents the upstream section of C1 was fabricated from 0.953 cm fiberglass. To provide a gas-tight volume, the ends of the counter were sealed with a flexible window. The window material chosen was a 0.51 mm laminate of black vinyl on the inside with aluminum foil covered by mylar on the outside.

C2 was also built from two sections. This was done to make the counter more easily transportable. Each section was fabricated from 0.635 cm sheet aluminum reinforced with aluminum I-beams. An access door was installed and thirty-two Winston cone portals were cut out along the transverse perimeter. The two ends of C2 were sealed with the same material as was used in C1. Both counters were mounted on a set of rails which enabled the counters to be rolled transverse to the beamline.

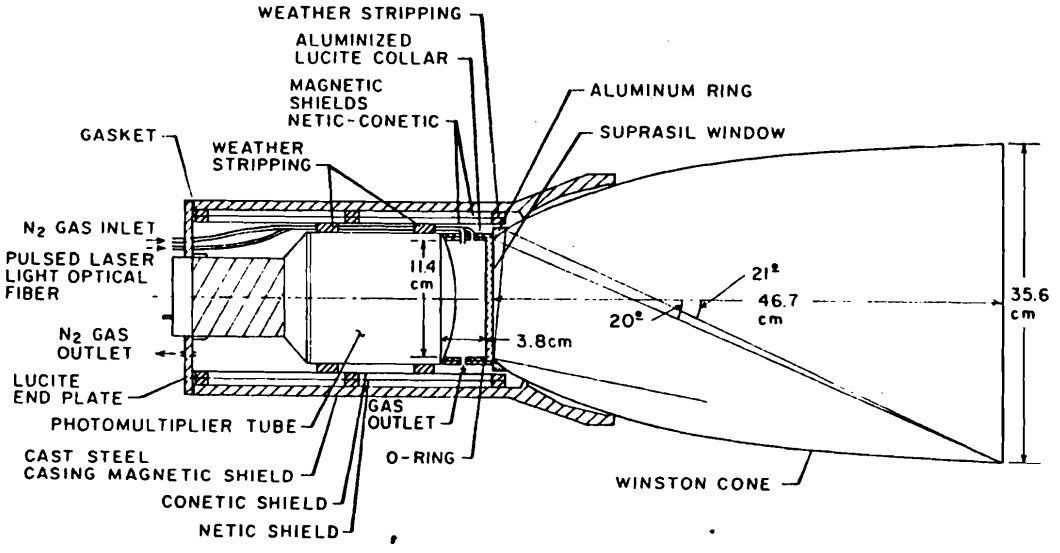

Figure E.11: The Winston cone–phototube assembly.

The gas mixtures were maintained by a gas cart which regulated the flow of the

helium and nitrogen. The gas pressures were held at just above atmospheric pressure and were checked about once every eight hours. The gas cart removed traces of oxygen and water vapor. The gas composition was monitored with a gas chromatograph. A nitrogen purge line was used to provide a circulation to remove water vapor and helium from the phototube environment; otherwise helium would have diffused into the phototubes and produced after-pulsing.

Calibration

The preliminary alignment of the mirrors and Winston cones was performed by positioning an ordinary light bulb at the target and adjusting the orientations of the mirrors and Winston cones so that the light from the bulb was reflected by the mirrors into their corresponding Winston cones. The final alignment was performed by positioning a laser at the target position, pointing the beam at the centre of each mirror and adjusting the orientations of the mirrors and Winston cones so that the beam reflected from the mirrors would pass through their corresponding Winston cones along the Winston cones' axes of symmetry.

Before the counters were sealed and filled with gas, an optical survey of the physical mirror boundaries was performed. From the target position the horizontal and vertical angles of all four corners of each mirror were measured using a theodolite. The distance from the centre line to the x and y coordinates of the mirror corners was then calculated and written to a calibration file for use in the event reconstruction.

A nitrogen laser light pulser system was used to generate Cherenkov single photoelectron peak (SPEP) calibration events. These events were used to determine the number of ADC counts that corresponded to a single photon striking a phototube. A diagram of the laser system is shown in Figure E.12. The nitrogen laser injected a pulse of coherent light into the light distribution system. A photodiode measured the intensity of a light pulse before and after it passed through a transmission filter wheel containing various neutral density filters. The transmission coefficient of the

filter wheel could be changed by rotating the filter wheel. The light pulse was then distributed to the C1 and C2 phototubes via a fiber optics network. The filter wheel was set to transmit light at an intensity that produced an average of about 1/2 a photoelectron in a phototube. This light level produced a SPEP about one half of the time along with the pedestal and also produced small two and occasionally three photoelectron peaks. After the run, the E_T data was used to determine the SPEP of each phototube.

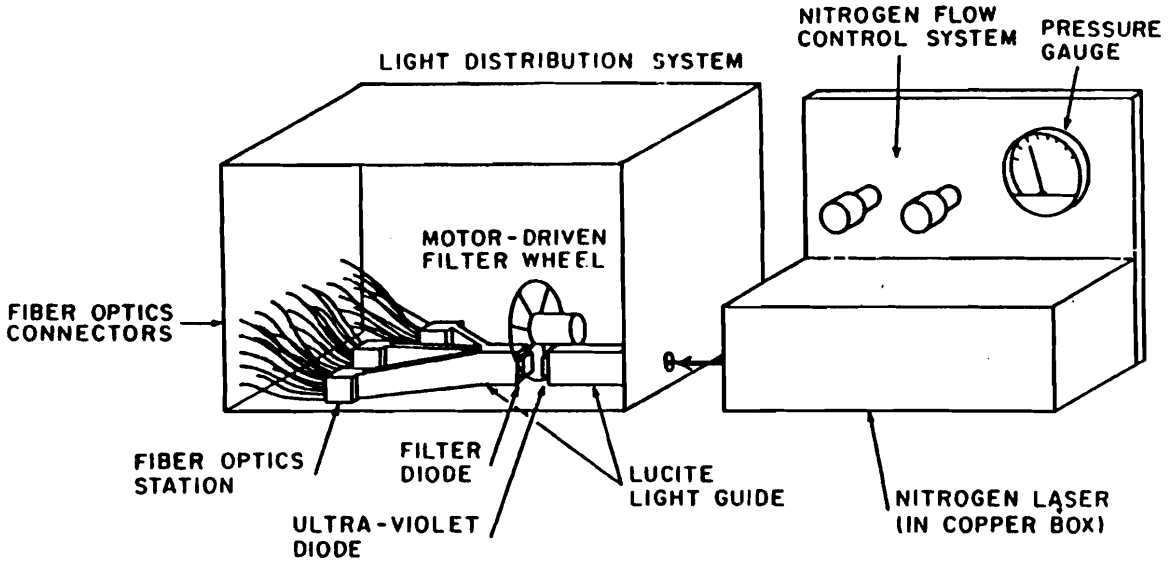

Figure E.12: The nitrogen laser light pulser system.

The E_T data was also used to determine the absolute value of the plateau region of the Cherenkov threshold curves. The pion, kaon and proton threshold curves are shown in Figure E.13. Tracks with momentum greater than 10 GeV that were well separated from other tracks were chosen. A track was considered to be well separated from the other tracks if the set of mirrors that its cone of Cherenkov light struck were not struck by the Cherenkov light from other tracks. The track was then assumed to be a pion and Equation E.15 was used to calculate the fraction of the light cone that intersected each mirror. The number of photons for a mirror in the set was taken to

be the total number of photons emitted multiplied by the fraction of the Cherenkov cone that fell on the mirror. The total number of photons emitted was given by integrating

$$\frac{dN_\gamma}{dl} = 2\pi\alpha \int \left[1 - \frac{1}{\beta^2 n^2(\lambda)}\right] \epsilon(\lambda) \frac{d\lambda}{\lambda^2} \tag{E.17}$$

where $\epsilon(\lambda)$ is the detector efficiency at the wavelength λ. This was converted to the number of photoelectrons produced by a phototube, given by

$$\frac{dN_{pe}}{dl} = N_0 \sin^2 \theta_c \tag{E.18}$$

where N_0 denoted a number determined by the efficiency of the light collection system, the conversion efficiency of the photocathode which was a function of the incident photon spectrum and the collection efficiency of the first dynode. A compound Poisson distribution was used to fit this data to give a mean and a width for the plateau region which was used for the entire threshold curve in the Cherenkov reconstruction.

Reconstruction

The threshold Cherenkov reconstruction, a part of the PASS2 reconstruction, was used to determine the probability that a charged track found in the PASS1 reconstruction was an electron, muon, proton or charged pion or kaon.

The first step was to predict for a given charged track the amount of Cherenkov light that would strike the C1 mirrors for each particle mass hypothesis. This was done by stepping the candidate particle through the magnetic field of M2 in C1, including the fringe field. A maximum of ten steps was used. Each step was a circular arc in the bend (xz)–plane. The value of the magnetic field at the centre of the arc was used. The sum along z of the field values at each step was normalized to the nominal value of $\int B(0,0,z)\ dz$. At each step Cherenkov photons were generated for each of the five particle mass hypotheses ($e^\pm$, $\mu^\pm$, $\pi^\pm$, $K^\pm$ or $p^\pm$). The total number of photons

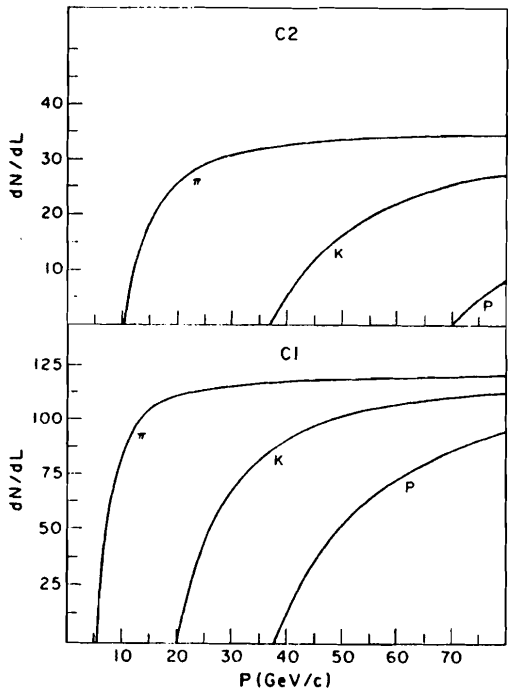

Figure E.13: The C1 and C2 pion, kaon and proton Cherenkov threshold curves.

generated for a given mass hypothesis was divided equally amongst the steps. These photons were projected along the Cherenkov cone to the C1 primary mirrors. The intersection of the Cherenkov cone with a subset of primary mirrors formed an ellipse. The amount of light that hit a mirror in that subset was determined analytically by taking it to be proportional to the fraction of the ellipse that it intersected. The total amount of light that hit a mirror in the subset, for a given mass hypothesis, was found by summing over the steps. A similar procedure was then performed for C2, the major differences being that C2 was in a field free region. Finally the mirror hits were mapped to the PMT hits.

The next step was to first use the single photoelectron gains from the calibration data to convert the pulse heights from the ADCs to the number of photoelectrons in the PMTs. Then the initial mass hypotheses for the charged tracks were set up. First a check was made to see if the track was associated with a SLIC shower. If that was the case, then the track was first labelled an electron. If the shower in the

SLIC and Hadrometer was hadronic then the track was relabelled a pion unless there was a high probability of it being a muon based on the Hadrometer signal and/or a hit in the appropriate section of the muon wall. If no calorimetry reconstruction information was available then the track was called a pion by default. The number of photoelectrons predicted in the PMTs for a given mass hypothesis–track combination was then compared against the number of photoelectrons measured in the PMTs. If the predicted and measured values did not agree then the mass hypothesis was modified to a particle that gave better agreement between the values. The procedure was halted at any stage if the mass hypotheses did not change. This gave the final set of mass hypotheses expressed as consistency probabilities. Thus the Cherenkov reconstruction assigned to each track a probability of the track being an electron, muon, pion, kaon or proton. For about 15% of nearby tracks the Cherenkov cones overlapped and reconstruction was not possible. In such cases, the apriori particle probability, defined as the fraction of particles of a particular type found in a typical hadronic event, was used. The apriori probabilities for electrons, muons, pions, kaons and protons were 0.02, 0.01, 0.81, 0.12 and 0.04. The effectiveness of the Cherenkov particle identification is illustrated in Figure E.14 where the $\phi(1020)$ is obtained by a cut requiring the product of the Cherenkov kaon probabilities for the two tracks to be greater than 5%.

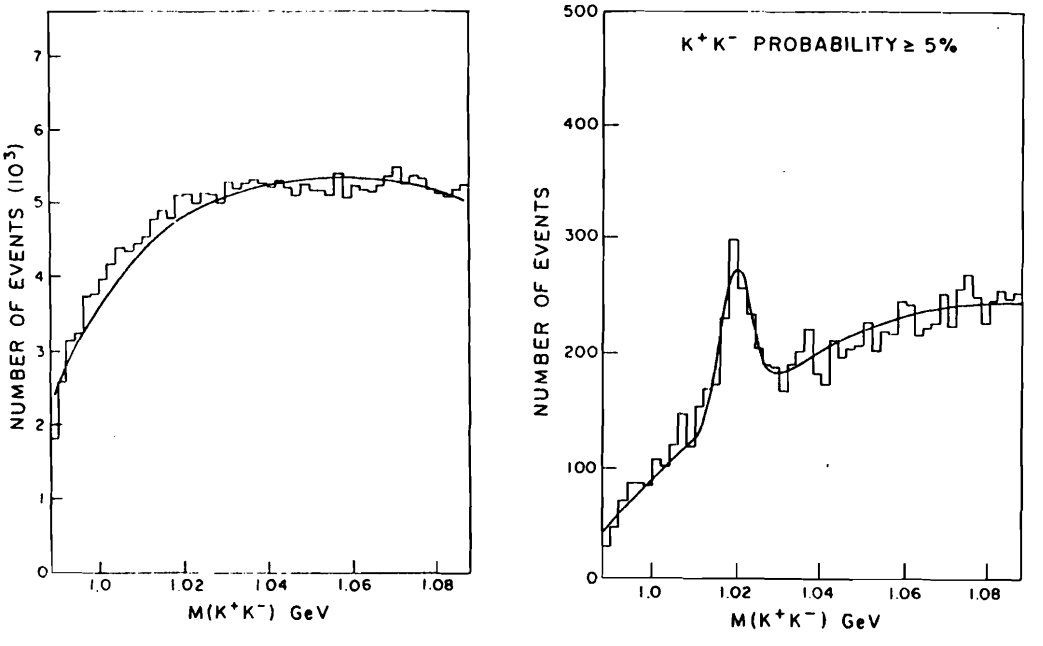

Figure E.14: The $\phi(1020) \rightarrow K^+K^-$ mass plot before and after the joint probability Cherenkov cut.

E.4 The Electromagnetic Calorimeter

The electromagnetic calorimeter, the Scintillator Lead Interleaved Calorimeter (SLIC) [Bha 85], was used to measure the energy, position and direction of electromagnetic showers produced by photons, electrons and positrons. It was also used in conjunction with the hadronic calorimeter, situated immediately downstream, to detect hadronic showers produced by neutral hadrons. Both the SLIC and the hadronic calorimeter were used in the E_T (global transverse energy) trigger. A cut-away diagram of the SLIC is shown in Figure E.15.

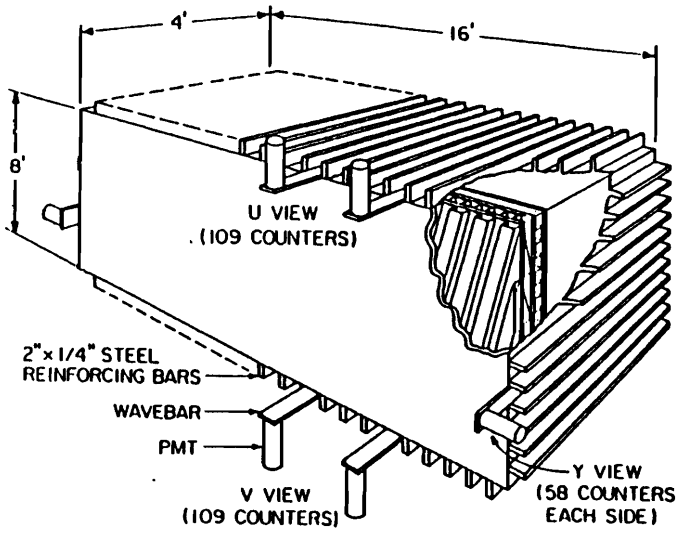

Figure E.15: A cut-away view of the SLIC, the E691 electromagnetic calorimeter.

The properties of the SLIC are listed in Table E.6. The SLIC consisted of 60 layers of lead alternating with 60 layers of liquid scintillator (Nuclear Enterprises NE235A). Each layer consisted of a 0.318 cm lead sheet laminated between two 1.0 mm thick sheets of aluminum, followed by a 1.27 cm liquid scintillator layer. A particle travelling parallel to the z–axis penetrated 21.5 radiation lengths and 2.07

interaction lengths. It was necessary to isolate the lead from the scintillator fluid as lead is a known liquid scintillator poison. Each scintillator layer was divided into 3.18 cm wide light channels by 0.041 cm thick Teflon coated aluminum bent into square wave corrugations. The Teflon index of refraction, n = 1.38, was lower than that of the liquid scintillator, n = 1.47. Thus the light in the channels was totally internally reflected for angles of incidence less than 20 degrees.

Table E.6: The properties of the SLIC.

SLIC Property	Value
(x, y, z) Dimensions (cm)	243.84 × 121.92 × 487.68
z Upstream Position (cm)	1839.
z Downstream Position (cm)	1961.
Number of Layers	60
Number of Channels	334
Pb Layer Thickness (cm)	0.3175
Al Sandwich Thickness (cm)	0.01016
Scintillator Layer Thickness (cm)	1.27
Single Counter Width (cm)	3.175
Radiation Lengths	21.5
Interaction Lengths (nucleon)	2.1
Energy Resolution	$21\%/\sqrt{E\ (GeV)}$
Vertical Acceptance (mrad)	about ±66
Horizontal Acceptance (mrad)	about ±133

Each lead–liquid scintillator layer was oriented in one of three possible ways. The twenty Y layers were horizontal. The twenty U and twenty V layers were oriented $\mp$ 20.5 degrees, looking downstream, with respect to the vertical. Three views were used in order to better resolve ambiguities in complicated events. The layers were cyclically arranged in the order U, V and Y. The Y view light channels were divided into two parts by means of mirrors inserted in the middle of the channels. Mirrors were also placed at the ends of the U and V view light channels to minimize light loss. The construction of a lead–liquid scintillator layer is shown in Figure E.16.

The lead–liquid scintillator layers were contained within a tank which was designed to withstand high hydrostatic pressures. The upstream and downstream faces were

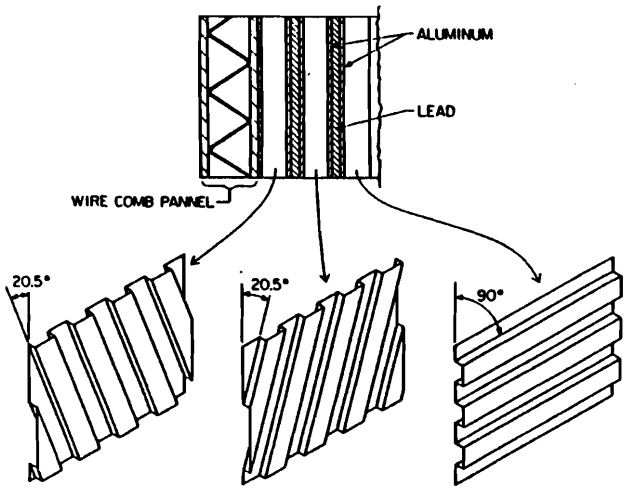

Figure E.16: The construction of a lead–liquid scintillator layer.

fabricated from opaque wirecomb panels. The top, bottom, east and west sides were fabricated from transparent rectangular lucite windows, separated by O–ring edge seals and held in place by window grates made from 5.08 × 0.625 cm steel bars laid on edge. The ends of the lead–liquid scintillator strips fitted into the spaces between the bars. The upstream face of the SLIC was 1849. cm downstream of the origin.

Lucite waveshifter bars, here called wavebars, were placed between the window bars. The wavebars were oriented longitudinally along the top, bottom, east and west sides of the SLIC. Each wavebar collected the light from twenty or forty light channels of one of the three views. In the U and V views, each of the thirty-eight central sets of twenty light channels were optically coupled to a wavebar. The outer seventy-one sets were coupled two to a wavebar. In the Y view, the central forty sets of twenty light channels on the east and west sides were singly coupled to a wavebar, while the outer eighteen on both sides were doubly coupled. The single width wavebars were 3.18 cm wide and the double width wavebars were 6.35 cm

wide. The light channel–wavebar coupling is shown in Figure E.17. The wavebars absorbed blue light from the window bars and re-emitted it as green light thereby maximizing the transmission to the phototubes. Each wavebar was optically coupled to a phototube. The phototubes were mated to the wavebars at a 45 degree angle to maximize the transmission efficiency. The single width wavebars were coupled to 5.1 cm RCA 4900 phototubes and the double width wavebars were coupled to 7.6 cm RCA 4902 phototubes.

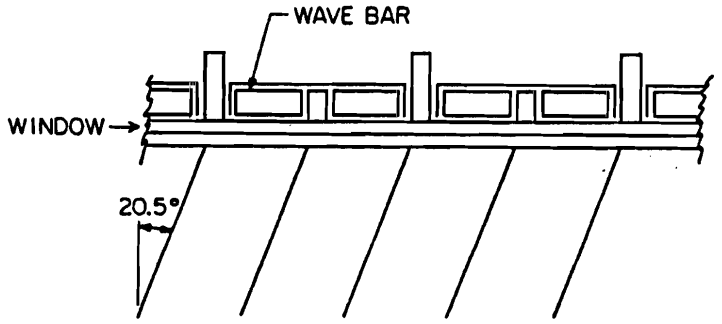

Figure E.17: The wavebar–light channel coupling.

The phototube anode signals were digitized by a Le Croy 2285 ADC system and written to tape as part of the event records. The phototube dynode signals were summed to form the SLIC component of the hadronic interaction trigger B·H. The weighted sum of dynode signals was used as the SLIC component of the E_T trigger.

The pair–plane was an array of 19 shower counters mounted on a shelf directly in front of the SLIC. It was used to intercept e^+e^- beam pairs thus reducing reconstruction confusion in the central region of the SLIC due to track congestion. Properties of

the pair–plane are listed in Table E.7. The pair-plane was not used in the calorimetric reconstruction due to miscalibration.

Table E.7: The properties of the pair–plane.

Pair–Plane Property	Value
(x, y) Dimensions (cm)	174. × 12.5
z Upstream Position (cm)	1829.
z Downstream Position (cm)	1839.
Number of Channels	19
Tungsten–Lucite	$C_{counter}$, C_{East}, C_{West}
Counters	$XE1 - XE3$, $XW1 - XW3$
Lead–Lucite Counters	$XE4 - XE8$, $XW4 - XW8$
W Layer Thickness (cm)	2.54
Pb Layer Thickness (cm)	5.1
Pb Brick Layer Thickness (cm)	0.95
Single Counter Widths (cm)	6.35, 12.7
Radiation Lengths	30.
Interaction Lengths (nucleon)	1.1

Calibration

The laser light pulser system was used to generate SLIC calibration events during the interspill by pulsing the SLIC channels five times at the beginning of a spill and one time at the end. These events were used to monitor the drift in the phototube gains. A broadening of the digitized pulse height distribution in a channel indicate that the phototube assembly was failing. A set of optical fibers transmitted the light pulses from the pulser system to each of the wavebar–photomultiplier tube assemblies. The pedestals were also monitored during the interspill by generating false gates.

At the start of the run and every couple of months thereafter special e^+e^- calibration runs were taken. During such a run the pair plane was lowered, and the tracks of e^+e^- pairs produced in the target were projected into the SLIC and a search for a shower in the in the region of the track was made. By this method the U and V channels, except for the central and edge counters, were calibrated. The Y channels

were calibrated using muons from the primary target. The calibration procedure is discussed in detail in [Raa 87].

The calibration was checked by measuring the mean value and width of the π^0 mass peak. The correct π^0 mass peak was obtained if the photon showers were isolated, but a correction was required for congested showers.

Reconstruction

The SLIC reconstruction, a part of the second stage (PASS2) reconstruction, was used to identify electron and positron showers and photon showers from π^0 decay.

The energy resolution of the SLIC was measured to be about $21\%/\sqrt{E\ (GeV)}$. Typical electron showers deposited about 60% of their energy within a single counter width; such showers were almost completely contained within 5 counter widths. Hadronic showers were broader; about twice as wide. Electromagnetic showers deposited almost all of their energy within the 21.5 radiation lengths of the SLIC but a large fraction of the energy of a hadronic shower passed out of the SLIC and into the hadronic calorimeter immediately behind. It was found that the energy deposited by a hadronic particle that showered in the SLIC was about 0.71 times the energy deposited by an electron or photon of the same initial energy. A major source of background was the satellite showers produced by hadronic interactions that mimic low energy photons or π^0s. Muons do not shower in the SLIC but leave narrow ionization trails depositing only about 0.5 GeV with a Landau tail.

The first stage of the SLIC reconstruction began by identifying energy deposits due to charged tracks. Candidate electromagnetic showers were distinguished from hadronic showers using E/p ratios and Hadrometer channel pulse heights. Since the wavebars integrated the light from the counters of a given view in lines parallel to the z–axis, the only information available about a shower was its transverse shape in the xy–plane. A contiguous group of counters in a given view whose individual energies were above an energy threshold were denoted as a cell. The counters adjacent to a

cell whose energies were below the energy threshold were denoted as the boundaries of the cell. A cell could contain the transverse energy distributions of two or more (overlapping) showers. Such cells were subdivided into sectors, each sector containing the individual showers. The criteria for a cell to be partitioned into sectors was that at least two non–adjacent counters in the cell have significantly more energy that their nearest neighbours. If a charged track was known to have passed through the central counter of a sector then its energy cut was lowered. The shower energy weighted mean of a sector was determined from the central counter and its two adjacent counters. This position was then adjusted for the known transverse shape of electromagnetic showers to give sector shower positions in the xy–plane.

A stepwise regression fit was then used to determine which of the candidate sectors were significant and how the total cell energy should be distributed amongst the significant sectors. An energy error σ_{Ei} and weight,

$$w_i = \frac{1}{\sigma_{Ei}^2} \tag{E.19}$$

were assigned to each ith sector. The sector energy error was determined from shower statistics, photoelectron statistics, whether the incident particle was thought to be a lepton, photon or hadron, and the energy deposited.

The next step was to use a stepwise multiple regression, a linear least squares fitting technique, to try to determine whether the sector shower was produced by a charged or neutral particle. The first step was to project the charged track trajectories that had been found by SESTR during PASS1 into the SLIC and to look for a sector in each of the U, V and Y views whose energy was consistent with that of a charged track. Such sectors were labelled ± 1 according to the charge of the track. The second step was to attempt to match the remaining sectors in the three views to identify showers from neutral particles. Such sectors were labelled by 0. The two major problems in matching sectors were partitioning the energy in a counter that had more than one hit with the corresponding sectors in the other views and determining with which set

of sectors in the other views a counter with one hit that intersected more than one set of sectors should be matched.

The final step was to perform the π^0 reconstruction. The invariant mass of all pairs of photons found in the above reconstruction was calculated. The agreement between the π^0 mass and the $\gamma\gamma$ mass was parametrized by

$$\chi^2 = [(M^2_{\gamma\gamma} - M^2_{\pi^0})/\Delta M^2]^2 \tag{E.20}$$

where ΔM^2 is the error on the $\gamma\gamma$ mass squared. The quantity ΔM^2 is the error obtained by taking the photon energy errors and the opening angle errors in quadrature. The χ^2 provided a measure of the likelihood that the difference between the $\gamma\gamma$ mass and the π^0 mass was consistent with the photon four–momentum errors. A probability was calculated for each π^0 candidate based on the χ^2 and the background under the π^0 peak. This probability was refined by requiring that candidate π^0s not share photons, by adjusting the energies of both photons to make the $\gamma\gamma$ mass equal to the π^0 mass. The SLIC was able to resolve shower centroids to within 3 mm. Two photons from a 20 GeV π^0 decay are separated by about 25 cm at the front face of the SLIC. This stage of the SLIC reconstruction is discussed in detail in [Sum 84]. The reconstruction efficiency for a π^0 in the mode $D^0 \rightarrow K^-\pi^+\pi^0$ was about 15%.

In the second stage of the SLIC reconstruction, the transverse SLIC pulse height distributions were compared with the expected theoretical QED distributions of the same energy. The library of theoretical showers was generated using the EGS electromagnetic shower Monte Carlo. This stage helped distinguish nearby hadronic showers from noise thus improving the energy resolution and providing additional information for assigning a probability as to whether the shower was electromagnetic.

E.5 The Hadronic Calorimeter

The hadronic calorimeter, the Hadrometer [App 86], was designed to measure that part of the energy from hadronic showers that was not measured by the SLIC. Less than 1% of the energy of electromagnetic showers from the SLIC reached the Hadrometer. The Hadrometer was used for the detection, identification and energy and angle measurements of neutral hadrons in multiparticle events. It was also a component, along with the SLIC, of the total hadronic cross-section trigger ($B \cdot H$) and the global transverse energy (E_T) trigger. The Hadrometer is shown in Figure E.18.

The Hadrometer consisted of 36 layers of steel plate alternating with 36 layers of plastic scintillator. The active cross–sectional area of the Hadrometer was 2.7 m high by 4.9 m wide. The front face of the Hadrometer was located 1962. cm downstream of the origin. It was 5.85 interaction lengths parallel to the z–axis. The steel plates were 2.5 ± 0.3 cm thick. They were stacked on edge on a 15 cm thick steel slab. Orthogonal strips of X (vertical) and Y (horizontal) scintillator were placed in alternating order into the the 36 gaps. The scintillator was polymethyl methacrylate doped with 1% naphthalene, 1% PPO and 0.01% POPOP. This material was selected as the best compromise between the conflicting requirements of maximum light output and a long light attenuation length. The plastic scintillator was nominally 1 cm thick with variations of up to $\pm$ 25%. These variations were systemic, the edges being thinner.

The Hadrometer was separated by a 5.08 cm gap into upstream and downstream modules each consisting of 18 steel–plastic scintillator layers. Each layer contained 33 X strips and 38 Y strips. The Y strips met at the mid XZ plane. The scintillator strips were 14.3 cm wide. Each module contained 33 X and 38 Y Hadrometer channels. A channel collected light from 9 X or Y strips, in line along the beam axis, using an undoped acrylic (Type G) light guide. The light guides were optically connected to 12.7 cm RCA 6342 phototubes.The phototube anode signals were digitized by a Le Croy 2280 ADC system and were written to tape as part of the event records. The properties of the Hadrometer are summarized in Table E.8.

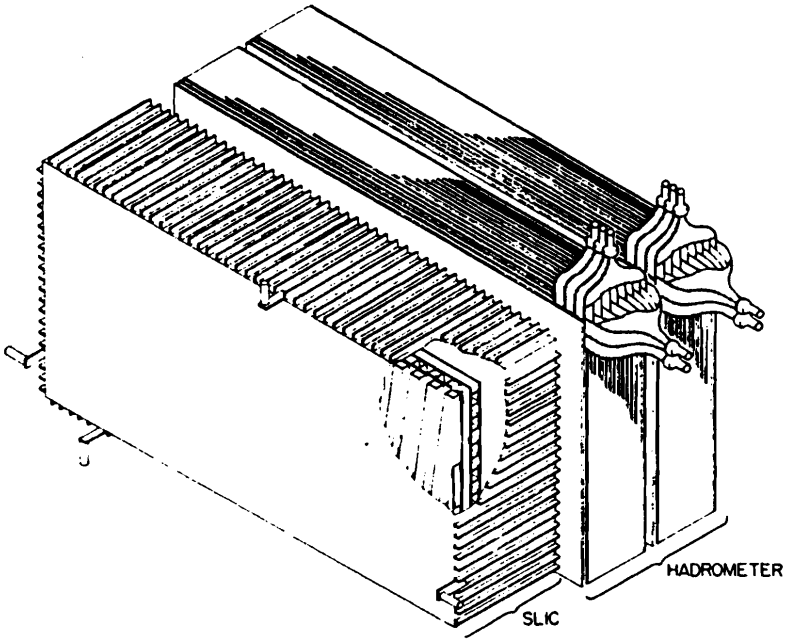

Figure E.18: A schematic view of the SLIC and the Hadrometer.

Calibration

The laser light pulser system was used to generate Hadrometer calibration events, to monitor the drift in the phototube gains, by pulsing the Hadrometer channels five times before the start of a spill and once after. A set of optical fibers transmitted the light pulses from the pulser system to each of the photomultiplier tube assemblies.

The absolute calibration of the 142 Hadrometer channels was maintained using halo muon tracks obtained during the special muon calibration runs. A parametrization curve was obtained for the light signal attenuation in the scintillator strip of each channel as a function of the distance of the hit from the phototube.

The absolute overall calibration of the Hadrometer was obtained by the above method was check by minimizing the energy resolution of the combined SLIC and Hadrometer, for isolated charged hadron showers from the E_T data, with the constraint that the combined signals equaled the measured momentum. Thus the χ^2

Table E.8: Properties of the E691 hadronic calorimeter, the Hadrometer.

Hadrometer Properties	Value
(x, y) Dimensions (cm)	270. × 490.
z Upstream Position (cm)	1962.
z Downstream Position (cm)	2120.
Number of Layers	18
Steel Layers Thickness (cm)	2.54.
Scintillator Layers Thickness (cm)	0.95
Total Steel Thickness (cm)	91.4
Total Scintillator Thickness (cm)	34.3
Single Counter Width (cm)	14.48
Radiation Lengths	52.8
Interaction Lengths (nucleon)	5.9
Energy Resolution	$75\%/\sqrt{E\ (GeV)}$

expression

$$\chi^2 = [pq - (G_S E_S + G_H E_H)]^2 \tag{E.21}$$

was minimized to obtain the SLIC and Hadrometer calibration constants, G_S and G_H, where E_S and E_H denoted the attenuation corrected energies and p denoted the measured momentum. The absolute calibration was insensitive to the angle of incidence of the hadron.

Reconstruction

The Hadrometer reconstruction, a part of the second stage (PASS2) reconstruction, was used to identify charged and neutral hadronic showers. The energy resolution of the Hadrometer was found to be $75\%/\sqrt{E\ (GeV)}$ and the intrinsic position resolution was less than 5.08 cm.

The first step in the reconstruction was to make a list of the Hadrometer channels that had registered a hit; those whose pulse heights were significantly greater than the pulse heights of their neighbouring counters.

The second step was to project the trajectories of the charged tracks found in PASS1 into the Hadrometer and attempt to match them with a pair of hits in the X and Y views. If such a match was made then an average hadronic shower shape was used to subtract out the energy of the charged particle. The subtracted energy was corrected for the energy deposited in the SLIC. The SLIC energy that was subtracted was constrained not to exceed the energy deposited in the Hadrometer. Also, a correction was made for the attenuation of the scintillator light as a function of the distance to the photomultiplier tubes.

The final step was to search for remaining pairs of X view and Y view hits from neutral hadrons in the sums of the upstream and downstream halves of the Hadrometer. These X and Y hits from neutral hadrons were matched according to their energies. A maximum of two neutral hadrons could be reconstructed on each side of the Hadrometer.

E.6 The Front and Back Muon Walls

The back muon wall was a planar array of twelve 45.7 cm and three 61.0 cm wide vertical plastic scintillator strips perpendicular to the beam. The arrangement of the strips in the muon wall is shown in Figure 3.8. These strips provided an X view only for the muon hit. The muon wall was 2234. cm downstream of the origin. Its geometric centre was located at $x = 2.69$ cm and $y = -3.68$ cm. The strips were connected to 12.7 cm EMI 9791B photomultiplier tubes via lucite light pipes. The signals from the photomultiplier tubes were discriminated. The output logic signals were used to set latch bits and as inputs to the dimuon trigger. Typical noise rates in the muon counters were 1–2 MHz.

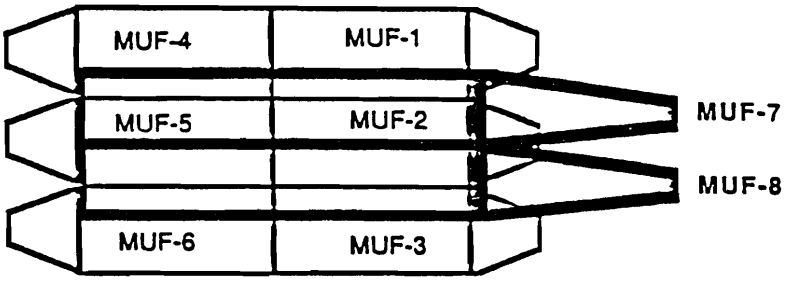

Figure E.19: The Front Muon Wall as seen by an incoming muon.

The front muon wall, located at the beam entrance to the experimental hall, was used to signal for the presence. These external muon were produced in the E691 beamline and in upstream experiments. The front muon wall is shown in Figure E.19.

The counters were manufactured from 1.5' by 4' or 8' sections of scintillator with lucite light guides.

Calibration

The back muon counter efficiencies were measured with the DC paddle counter telescope which was placed behind each counter at about $y = 0$. The efficiencies of the counters are listed in Table E.9.

Table E.9: The efficiencies of the back muon counters. The statistical errors on these efficiencies are less than $\pm$ 1%.

Muon counter	Efficiency (%)
2	95.
4	90.
6	94.
8	93.
10	94.
12	96.
14	93.
16	95.
18	95.
20	97.
22	95.
24	94.
26	95.
28	93.
30	97.

Bibliography

[Alt 77] G. Altarelli and G. Parisi, Nucl. Phys **B126**, 298 (1977).

[And 83] B. Andersson, G. Gustafson, G. Ingelman and T. Sjöstrand, Phys. Rep. **97**, 33 (1983).

[Anj 90] J. C. Anjos *et al.*, Phys. Rev. Lett. **65**, 2503 (1990). The data are described in J. C. Anjos et al., Phys. Rev. Lett. **62**, 513 (1989).

[App 86] J. A. Appel *et al.*, Nucl. Instr. and Meth. **A243**, 361 (1986).

[Art 83] X. Artu, Phys. Rep. **97**, 147 (1983).

[Aub 74] J. J. Aubert et al., Phys. Rev. Lett. **33**, 1404 (1974)

[Aug 74] J. E. Augustin et al., Phys. Rev. Lett. **33**, 1406 (1974)

[Aur 89] P. Aurrenche et al., Phys. Rev. **D39**, 3275 (1989)

[Bab 78] J. Babcock, D. Sivers and S. Wolfram, Phys. Rev. **D 18**, 162 (1978).

[Bar 87] R. Barate *et al.*, Z. Physik **C33**, 505 (1987).

[Bar 87] D. Bartlett *et al.*, Nucl. Instr. and Meth. **A260**, 55 (1987).

[Bau 78] T. H. Bauer, R. D. Spital, F. M. Pipkin and D. R. Yennie, Rev. Mod. Phys., **50**, 261 (1978).

[Ber 81] E. L. Berger and D. Jones, Phys. Rev. **D 23**, 1521 (1981).

[Bha 85] V. K. Bharadwaj *et al.*, Nucl. Instr. and Meth. **228**, 283 (1985).

[Bin 82] M. Binkley *et al.*, Phys. Rev. Lett. **48**, 73 (1982).

[Bon 88] M. Bonesini *et al.*, Z. Physik **C38**, 371 (1988).

[Bjo 69] J. D. Bjorken and E. A. Paschos, Phys. Rev. **185**, 1975 (1969).

[Bro 88] T. E. Browder, Ph. D. Thesis, University of California, Santa Barbara, 1988 (unpublished).

[Cab 63] N. Cabibbo, Phys. Rev. Lett. **10**, 531 (1963).

[Cal 69] C. G. Callan Jr. and D. Gross, Phys. Rev. Lett. **22**, 156 (1969).

[Cal 78] D. O. Caldwell *et al.*, Phys. Rev. Lett. **40**, 1222 (1978).

[Cal 79] D. O. Caldwell *et al.*, Phys. Rev. Lett. **42**, 553 (1979).

[CCF 84] The CCFRR collaboration, D. B. MacFarlane *et al.*, Z. Phys. **C26**, 1 (1984).

[CDH 84] The CDHSW collaboration, P. Berge *et al.*, CERN-EP/89-103 (1989).

[CHA 83] The CHARM collaboration, F. Bergsma *et al.*, Phys. Lett. **123B**, 269 (1983).

[Clo 79] F. E. Close, *An Introduction to Quarks and Partons* (Academic Press, New York, 1979), p. 234.

[Con 89] J. S. Conway *et al.*, Phys. Rev. **D 39**, 92 (1989); J. Badier *et al.*, Phys. Lett. **117B**, 372 (1982); G. Altarelli, G. Parisi and R. Petronzio, Phys. Lett. **76B**, 351 (1978).

[Den 84] B. H. Denby *et al.*, Phys. Rev. Lett. **52**, 795 (1984); B. H. Denby, Ph. D. Thesis, University of California, Santa Barbara, 1984 (unpublished).

[Dun 82] A. Duncan, Ph. D. Thesis, University of Colorado, 1982 (unpublished).

[Est 86] P. Estabrooks, E691 Internal Memo, 1986.

[Ell 89] R. K. Ellis and P. Nason, Nucl. Phys. **B312**, 551 (1989).

[Far 74] G. R. Farrar, Nucl. Phys. **B 77**, 429 (1974).

[Fey 49] R. P. Feynman, Phys. Rev. **76**, 769 (1949).

[Fey 72] R. P. Feynman, *Photon–Hadron Interactions*, (W. A. Benjamin Inc., Reading, Mass., 1972)

[Fie 78] R. D. Field and R. P. Feynman, Nucl. Phys. **B 136**, 1 (1978).

[Fri 73] H. Fritzsch, M. Gell–Mann and H. Leutwyler, Phys. Lett. **47B**, 365 (1973).

[Fri 78] H. Fritsch and K. H. Streng, Phys. Lett. **72 B**, 385 (1978).

[Gel 64] M. Gell–Mann, Phys. Lett **8**, 214 (1964).

[Gla 69] R. J. Glauber, in *High–Energy Physics and Nuclear Structure*, edited by S. Devons (Plenum Press, New York, 1970), p. 207.

[Gla 61] S. L. Glashow, Nucl. Phys. **22**, 579 (1961)

[Gla 70] S. L. Glashow et al., Phys. Rev. **D2**, 1285 (1970)

[Glu 78] M. Gluck and E. Reya, Phys. Lett. **79 B**, 453 (1978).

[Gro 73] D. Gross and F. Wilczek, Phys. Rev. Lett **30**, 1343 (1973).

[Gun 74] J. F. Gunion, Phys. Rev. **D 10**, 242 (1974).

[Hig 66] P. W. Higgs, Phys. Rev. **145**, 1156 (1966).

[Hof 63] R. Hofstadter, in *Electron Scattering and Nuclear and Nucleon Structure*, edited by R. Hofstadter (W. A. Benjamin, New York, 1963), p. 220

[Hol 85] S. D. Holmes, W. Y. Lee and J. E. Wiss, Ann. Rev. Nucl. Part. Sci., **35**, 397 (1985).

[Hum 77] B. Humpert and A. C. D. Wright, Phys. Rev. **D 15**, 2503 (1977).

[JAD 79] The JADE Collaboration, W. Bartel et al., Phys. Lett., **91B**, 142 (1980).

[Jam 72] F. James, in *The Proceedings of the 1972 CERN Computing and Data Processing School*, CERN 72–21 (1972).

[Jam 83] F. James and M. Roos, *MINUIT, A System for Function Minimization and Analysis of the Parameter Errors and Correlations*, CERNLIB D506, CERN (1977).

[Jon 78] L. M. Jones and H. W. Wyld, Phys. Rev. **D 17**, 759 (1978).

[Kar 85] P. Karchin et al., IEEE Trans. on Nucl. Sci. **NS–32**, 612 (1985).

[Kob 73] M. Kobayshi and M. Maskawa, Prog. Theo. Phys. **49**, 652 (1973).

[Lec 69] C. Lechanoine et al., *Method for Efficient Magnetic Analysis in an Inhomogeneous Magnetic Field*, Nucl. Instr. and Meth. **69**, 122 (1969).

[Lee 56] T. D. Lee and C. N. Yang, Phys. Rev. **104**, 254 (1956).

[MAR 79] The MARK J Collaboration, D. P. Barber et al., Phys. Rev. Lett., **43**, 830 (1979).

[Mar 88] For recent results on $xG(x)$, see A. D. Martin, R. G. Roberts and W. J. Stirling, Phys. Rev. **D 37**, 1161 (1988) and references therein. Also, A. C. Benvenuti *et al.*, Phys. Lett. **B223**, 490 (1989).

[Mca 56] R. W. McAllister and R. Hofstadter, Phys. Rev., **102**, 851 (1956)

[Men 86] S. R. Menary, M. Sc. Thesis, University of Toronto, Toronto, 1986 (unpublished).

[Nam 66] Y. Nambu, in *Preludes in Theoretical Physics*, edited by de Shalit (North–Holland, Amsterdam, 1966).

[Nas 83] T. Nash, in *Proceedings of the International Symposium on Lepton and Photon Interactions at High Energies, Ithaca, New York,* edited by D. G.

Cassel and D. L. Kreinick (Newman Laboratory of Nuclear Studies, Cornell University, Ithaca, 1983).

[Nas 88] P. Nason, S. Dawson, and R. K Ellis, Nucl. Phys., **B303**, 607 (1988)

[PDG 90] Particle Data Group, Phys. Lett. **239 B**, (1980).

[Per 74] M. L. Perl, *High Energy Hadron Physics* (J. Wiley & Sons, New York, 1974), p. 11.

[Clo 79] F. E. Close, *An Introduction to Quarks and Partons* (Academic Press, New York, 1979), p. 234.

[Pil 90] E. Pilon, in *Proceedings of the XXVIth Rencontre de Moriond, Les Arcs, Savoie, France,* edited by J. Trân Thanh Vân (Editions Frontieres, France, 1991), 113.

[PLU 79] The PLUTO Collaboration, Ch. Berger et al., Phys. Lett., **86B**, 418 (1979).

[Pol 73] H. D. Politzer, Phys. Rev. Lett. **30**, 1346 (1973).

[Pou 74] J. S. Poucher *et al.*, Phys. Rev. Lett. **32**, 118 (1974).

[Pur 87] M. V. Purohit and A. B. Stundžia, private communication.

[Raa 87] J. R. Raab, Ph. D. Thesis, University of California, Santa Barbara, 1987 (unpublished).

[Raa 88] J. R. Raab *et al.*, Phys. Rev. **D 37**, 2391 (1988).

[Ron 90] E. Rondio, in *Proceedings of the XXVIth Rencontre de Moriond, Les Arcs, Savoie, France,* edited by J. Trân Thanh Vân (Editions Frontieres, France, 1991), 225.

[Roy 80] D. P. Roy, Phys. Lett. **96 B**, 189 (1980).

[Rut 11] E. Rutherford, Phil. Mag. **21**, 672 (1911).

[Sal 68] A. Salam, in *Elementary Particle Physics (Nobel Symp No. 8* edited by N. Svartholm, Almquist and Wilsell , Stockholm.

[Shi 76] M. A. Shifman, A. I. Vainstein and V. I. Zakharov, Phys. Lett. **65 B**, 255 (1976).

[Sjo 84] T. Sjöstrand, Phys. Lett. **142 B**, 420 (1984). T. Sjöstrand, Nucl. Phys. **B 248**, 469 (1984). T. Sjöstrand, Z. Physik **C 26**, 235 (1984).

[Sjo 85] T. Sjöstrand, *The Lund Monte Carlo for Jet Fragmentation and* e^+e^- *Physics - JETSET version 6.2*, LU TP 85-10, University of Lund, Sölvegatan 14A, S-223 62 Lund, Sweden.

[Sli 85] K. Sliwa et al., Phys. Rev. **D 32**, 1053 (1985).

[Sok 86] M. D. Sokoloff *et al.*, Phys. Rev. Lett. **57**, 3003 (1986).

[Sum 84] D. J. Summers, Ph. D. Thesis, University of California, Santa Barbara, 1984 (unpublished).

[Sum 85] D. J. Summers, Nucl. Instr. and Meth. **228**, 290 (1985).

[TAS 79] The TASSO Collaboration, R. Brandelik et al., Phys. Lett., **86B**, 243 (1979).

[Tsa 69] L. W. Mo and Y. S. Tsai, Rev. Mod. Phys., **41**, 205 (1969); Y. S. Tsai, SLAC–848, (1971).

[Win 69] H. Wind, *Where Should a Magnetic Field be Measured?*, IEEE Transactions on Magnetics **MAG–5**, 269 (1969).

[Win 70] H. Wind, *Evaluating a Magnetic Field from Boundary Observations Only*, Nucl. Instr. and Methods **84**, 117 (1970).

[Wei 67] S. Weinberg, Phys. Rev. Lett., **19**, 1264 (1967).

[Wei 73] S. Weinberg, Phys. Rev. Lett., **31**, 494 (1973).

[Zwe 64] G. Zweig, CERN report no. 8182/TH 401, (1964).

Statement of Contribution to E691

Date	Location	Status	Project	Advisor
May 1989 – May 1992	Toronto & Fermilab	Ph. D. Student	**Thesis** *Analysis of Inelastic and Elastic J/ψ Photoproduction On Beryllium.*	G. J. Luste[1] & M. V. Purohit[2]
Sept. 1989 – Sept. 1991	Fermilab	"	Implementation of J/ψ elastic and inelastic photoproduction generators for the E691 Monte Carlo. Development of 4-momenta conserving hadronization algorithm for use with LUND in the missing forward energy studies. Monte Carlo modelling of E691 dimuon trigger.	Independent
Dec. 1989 – May 1990	"	"	Study of E691 drift chamber damage due to high intensity charged particle flux	M. V. Purohit
May 1989 – Sept. 1990	"	"	Supervision of E691 Monte Carlo data production.	Independent
May 1989 – Sept. 1989	"	"	Study of E691 photon beam tagging system using elastic $\rho \rightarrow \pi^+\pi^-$.	M. V. Purohit
Jan. 1987 – Sept. 1988	"	"	Vector and tensor polarization study of E691 $D^{*+} \rightarrow D^0\pi^+$ data.	"
Jan. 1987 – Sept. 1988	"	"	Monte Carlo modelling of E691 Cherenkov detector properties.	"
Jan. 1987 – Sept. 1988			Scalar counters study for cross section normalization.	"
May 1986 – Sept. 1986	"	M. Sc. Student	**Thesis.** *Results on the Photoproduction of Two–Charm Events.*	M. V. Purohit & G. J. Luste
May 1986 – Sept. 1986	"	"	Monte Carlo modelling of E691 drift chamber properties.	"
Sept. 1984 – Sept. 1985	"	"	Implementation and upgrade of E691 data acquisition online monitoring system.	S. B. Bracker[3]
Sept. 1984 – Sept. 1985	"	"	Design and implementation of E691 dimuon trigger.	M. Witherell[4]
May 1984 – Sept. 1984	"	Summer Student	Design of E691 data acquisition online monitoring system.	S. B. Bracker

[1] University of Toronto

[2] Princeton University

[3] Fermi National Accelerator Laboratory and the University of Toronto

[4] University of California at Santa Barbara